University of London
Imperial College of Science, Technology and Medicine
Department of Mechanical Engineering

Assessment of LES sub-grid models for turbulent reacting flows.

A. Papoutsakis

Submitted in fulfilment of the requirements for the degree of
Doctor of Philosophy of the University of London and
the Diploma of Imperial College, October 2007

I herby declare that the work presented in this thesis is my own.

London, 30 November 2007.

Andreas Papoutsakis

Abstract

The research reported in this thesis focuses on the assessment of modelling techniques for the sub-grid scale quantities incorporated in Large Eddy Simulations (LES) of turbulent reacting flows.

Direct Numerical Simulation (DNS) has been utilised for the model free solution of methane combustion in a turbulent flow field, i.e. a time evolving planar jet and also in decaying homogeneous and isotropic turbulence. The algorithm uses a high-accuracy pseudo-spectral method for the solution of the transport equations for the mixture fraction and the momentum. A finite difference methodology is used for the solution of the reacting scalars. The numerical algorithm has been parallelised in order to meet the computational power demands of the simulations. Finally, a four step chemistry mechanism has been used to capture extinction and re-ignition in methane combustion.

The resulting DNS database is used for the evaluation of micromixing modelling in LES. In particular, zero equation models for the scalar dissipation rate and the scalar variance are compared to the results from the DNS simulations. Both quantities serve as a coupling between the LES flow field solution and standard mixture fraction based combustion modelling approaches. In addition, the methane combustion simulation is used for the investigation of extinction and re-ignition modelling by the Conditional Moment Closure (CMC) methodology. Doubly conditioned CMC equations have been introduced to model the local extinction and re-ignition phenomena, which cannot be captured by singly conditioned CMC. In this study, the doubly conditioned CMC equations are solved, and the performance of this methodology is tested and compared to the singly conditioned CMC and DNS results.

Acknowledgements

I would like to express my sincere gratitude to my supervisor Dr. Andreas Kronenburg for his guidance, encouragement, understanding and professionalism. I would also like to thank my co-supervisor Prof. William Jones for his continuous support throughout the period of my studies at Imperial College. In addition, Prof. George Bergeles at NTUA is acknowledged for encouraging me to start this project.

Very special thanks are due to Dr. Salvador Navarro Martinez for his vital help. Many thanks are also due to my colleagues and friends in Imperial College, including Dr. Stefano Bondi, Elias Chronopoulos, Markus Hartinger, Anthony Jefferies, Dr. John Keays, Markus Kostka, Pierre Le Fur, Idalina Gomez, Nikos Soulopoulos, Maria Spathopoulou, Konstantina Vogiatzaki, Konstantinos Zargoulidis and Konstantinos Zegos, for their support and specifically for their important help proofreading this thesis.

At this point, I would like to praise the important support I have received by my close friends in London and back home, specifically to Georgios Anastasakis, Ziad Adwan, Hara Gavra, Maria Kakaroglou, Sergio Kobogiorgas, Georgios Kritsotakis, and Hara Papadaki. In addition, I have to express my gratitude to Tania Mpatzoglou for inspiring me to take the plane, and also for her constant healing support all these years. I thank you.

This work would have not been possible without the help of my family. Leuteri, Elleni, Maria and Gianni, this thesis is dedicated to you.

Dedication

Στον αδελφό μου Γιάννη.

'Rage, rage against the dying of the light.'

Dylan Thomas

Nomenclature

Roman symbols

Symbol	Description
A	Pre-exponential factor
a	Proportionality of the model predictions
C	Model constant
C_p	Constant pressure heat capacity
c	Correlation of the model predictions
D	Molecular diffusion coefficient
E_a	Activation energy
E_k	Turbulent kinetic energy spectrum
e	Efficiency, Energy
G	LES filter function
h	Enthalpy
h_t	Total enthalpy
h_s	Sensible enthalpy
J	Diffusion in conditional space
K	Arrhenius forward constant
k	Turbulent kinetic energy
$\mathcal{L}$	Leonard term

L	Jet width
ℓ_0	Large turbulent scales
M	Number of species, timesteps
$\mathcal{M}$	Model term
N	Square of the mixture fraction gradient, number of nodes
$\boldsymbol{NL}$	Non linear terms vector
$\boldsymbol{X}$	Spectral solver unknowns
P	Probability Density Function
$\mathcal{P}$	Probability
p	Pressure
Q	Heat release
Q_k	Conditional average
R	Ideal gas constant
R	Autocovariance
R_{ij}	Two-point correlation
S	Rate of strain
s	Mass stoichiometry ratio
T	Temperature
T_a	Activation temperature
t	Time
u, v, w	Velocity
V	Diffusion velocity
W	Molecular weight
X	Species molar concentration
x, y, z	Spatial coordinates
x_i, y_j, z_k	Spatial coordinates on the DNS mesh
X_i, Y_j, Z_k	Spatial coordinates on the filtering mesh
Y	Species mass fraction
z_A, z_B	Control points transverse coordinate

z_1, z_2	Shear layer transverse positions

Greek symbols

Symbol	Description
α	Thermal diffusion coefficient
δ_{ij}	Kronecker's delta
$\delta_{0.9}$	Shear layer thickness
δ_m	Shear layer momentum thickness
Δ	Filter width
ϵ	Dissipation of turbulent kinetic energy
ζ	Enthalpy sample space, similarity transverse distance
η	Kolmogorov length scale, mixture fraction sample space
Θ	Non-dimensional enthalpy
κ	Wavenumber magnitude
κ	Wavenumber vector
Λ	Integral length scale
λ_T	Taylor length scale
λ	Thermal conductivity coefficient
μ	Viscosity
ν	Stoichiometry coefficient, kinematic viscosity
ξ	Mixture fraction
Π	Dynamic pressure
ρ	Density, autocorelation function
ρ_{ij}	Two-point corelation coefficient
τ	Timescale
τ_{ij}	Stress tensor
Φ	Arbitrary scalar field

χ	Scalar dissipation rate
ψ	Fine-grained Density Function
ω	Source term
ω	Vorticity

Superscripts

Symbol	Description
*	Non dimensional
′	Turbulent fluctuation
0	Initial stream
b	Backward
f	Forward

Subscripts

Symbol	Description
0	Reference value
ad	Adiabatic
d	Diffusion
F	Fuel
O	Oxidiser
P	Product
r	Reaction, Resolved
S	Smagorinsky
T	Taylor scale

t	Turbulent

Abbreviations

Symbol	Description
CFFT	Complex Fast Fourier Transform
CMC	Conditional Moment Closure
DFFT	Discrete Fourier Transform
DNS	Direct Numerical Simulation
DCMC	Doubly Conditioned Moment Closure
FDF	Fine-grained Density Function
FFT	Fast Fourier Transform
LES	Large Eddy Simulation
MMC	Multiple Mapping Conditioning
NS	Navier Stokes
PDF	Probability Density Function
RFFT	Real Fast Fourier Transform
RANS	Reynolds Averaged Navier-Stokes
SGS	Sub-Grid Scale
SCMC	Singly Conditioned Moment Closure

Operators

Symbol	Description
$\langle\cdot\rangle$	Reynolds average
$\widetilde{\langle\cdot\rangle}$	Favre Reynolds average
$\bar{\cdot}$	LES filter

$\widetilde{\cdot}$	Favre filter
$\widehat{\cdot}$	Test filter
$\widetilde{\widehat{\cdot}}$	Favre test filter
$\langle \cdot \vert \eta \rangle$	Conditional average
$\overline{\cdot}^{\eta}$	Conditional filtering
$\widetilde{\cdot}^{\eta}$	Conditional Favre filtering
$\langle \cdot \vert \eta \rangle$	Double conditional average
$\overline{\cdot}^{\eta,\zeta}$	Double Conditional filtering
$\widetilde{\cdot}^{\eta,\zeta}$	Double Conditional Favre filtering
$[\cdot]_{z=z}$	Averaging over homogeneous directions

Non-dimensional numbers

Symbol	Description
Da	Damköhler number
Re	Reynolds number
Sc	Schmidt number
Pr	Prandtl number
St	Strouhal number

Contents

List of Tables

List of Figures

Chapter 1

Introduction

Combustion remains the most common way to exploit the chemical energy of fossil fuels [1]. In a flame, oxidiser, usually the oxygen in the air, reacts with fuel. The resulting exothermic reaction produces thermal energy that can then be used either "as is", or be transformed to another form of energy with the help of a thermal engine.

In modern economies, combustion is inevitably related to energy production, with 90% of the energy consumed in the United Kingdom being produced by the combustion of fossil fuels [2]. Combustion-free energy production, such as energy from nuclear and hydroelectric power or from renewables, is mainly used in electricity production. However, in the UK 72% of the electricity production comes from the combustion of fossil fuels. This can be split into contributions from natural gas (37%), coal (34%) and oil with just 1%.

The main challenge that energy production faces is the reduction of its effect on the planet. Although the atmospheric pollution due to the energy production is mainly caused by the combustion generated energy, the contribution of fossil fuels to energy production is not expected to reduce. In fact, fossil fuels are expected to increase their contribution to the electricity production reaching 75% in the UK until 2020 [2], due to the expected increase of energy consumption. In the developing world the increase of energy production is expected to be much higher. The second crucial challenge for the UK energy policy is the security of the energy supply, threatened by the depletion of hydrocarbon resources. This condition is promoting domestically available coal-fired

generation of electricity and demands an increased efficiency of the energy production. Given the importance of combustion in energy production both now and in the future, research on combustion should provide the technology for cleaner, more efficient and more secure energy supply.

Combustion is responsible for the emission of pollutants which cause a series of effects on the environment. Acid rain, reduction of atmospheric visibility, production of tropospheric ozone and depletion of stratospheric ozone is caused by sulfur and nitrogen oxides found in the exhaust gases during fossil fuel combustion [3]. In addition, the above mentioned pollutants along with fine organic and inorganic particulates pose a threat to the public health. The scientific evidence that climate change and more precisely global warming is augmented by the anthropogenic carbon dioxide emissions continues to strengthen [2]. The emission of carbon dioxide cannot be dealt with by any other means than achieving high thermodynamic efficiency of energy production from hydrocarbons [3], and by devising ways to apply carbon capturing methods on energy plants [4]. In response to the environmental challenges, research in combustion aims to reduce the emissions of pollutants by means of understanding the mechanism of their formation , and at the same time to provide technologies for efficient energy use [5] and production [6].

Given that the vast majority of combustion applications, especially in energy production, take place in a turbulent flowfield [7], combustion needs to be understood as a complex phenomenon that involves interactions with the turbulent flow field, turbulent mixing of the reactants, chemistry and the thermodynamics in a flame. This set of phenomena is summarised under the term of "turbulent combustion" where the oxidiser and the fuel transport, mix, and react in a turbulent flowfield. Scientific research in turbulent combustion, intends to solve the combustion problem challenges by deriving models to predict the performance of combustion applications, and to understand and to manipulate the mechanisms of pollutants formation.

Combustion modelling in practical applications of non-premixed combustion requires the mastering of turbulence [7]. In pursuit of modelling the effect of turbulence on combustion, or rather the interaction between the two, several conceptual approaches have emerged. The mixing control concept argues that non-premixed com-

bustion is controlled by the reactants' mixing, and the flame lies in the areas where the reactants have mixed to stoichiometric proportion [8]. This perception leads to the very common mixture fraction based modelling approaches.

The concept of laminar flamelets appeared in the early 1980s [9]. Following this approach, species transport is locally modelled by a Stationary Laminar Flamelet (SLFM) equation. The underlying idea is that the reaction regions are thin compared to the turbulent scales, and the reactions take place in a laminar flowfield. Then, the effect of turbulence on the flame is characterised by the scalar dissipation rate that appears explicitly in the SLFM formulation. The SLFM method has now evolved to incorporate a Lagrangian viewpoint [10], and also to include transient effects [11].

Occurrences of compositions outside those assumed by the SLFM equations are common for hydrocarbon flames. In response to that, the Probability Density Functions (PDF) methodology provided a more general modelling approach to the fluctuations of compositions [12, 13]. PDF methods make the representation of the independent turbulent fluctuations feasible for each one of the species concentrations.

Conditional Moments Closure (CMC) [14, 15] is based on the observation that fluctuations of the species mass fractions and the temperature are low among the values that correspond to the same mixture fraction. First order CMC neglects the conditional variations, whereas second order closures [16] can be incorporated in CMC providing better modelling in flames with significant local extinction and re-ignition. A more direct approach to model the physics of ignition and re-ignition in turbulent combustion is the Doubly Conditional Moments Closure (DCMC) [17, 18] which includes a second conditioning dimension, preferably sensible enthalpy, reducing the magnitude of the doubly conditioned fluctuations caused from local extinction of the flame.

An effort to unify the PDF and CMC concepts results in the Multiple Mapping Conditioning (MMC) [19]. Instead of using a single conditioning variable as in CMC, MMC considers a set of reference variables. MMC lies between the one- or two-dimensional approach for the dimensionality of the composition space as implied by SLFM and CMC, from the one side, and the full dimensions description introduced by PDF methods, on the other side, however many issues such as the modelling of the diffusion coefficients in reference space remain unsolved.

The modelling of turbulent flow is a formidable task by itself [7]. Given the additional computational cost of combustion modelling by either SLFM, CMC, MMC or PDF methods, Reynolds Averaged Navier-Stokes (RANS) equations have been broadly used for the simulation of the turbulent flowfield. However, the implementation of the current combustion models has started to be coupled with Large Eddy Simulation (LES) during the last decade. This transition to LES is not straightforward. The two methodologies, RANS and LES, incorporate different modelling strategies, thus new techniques must be provided for the coupling between LES and a combustion model.

DNS and experimental work is expected to address some crucial questions on the spatial structure of premixed and non premixed flames. Very accurate, simultaneous measurements of all species and flow structures are necessary to assess the validity of closures and modelling assumptions needed for CMC, and hence, DNS is better suited than experimental measurement for evaluation [7].

The aim of this study is to investigate the accuracy of the zero equation models used in LES to model crucial unclosed quantities related to the turbulent micromixing and the performance of the CMC methodology in modelling local extinction and reignition phenomena. In order to achieve this, the tools for creating a DNS database of isotropic and non-isotropic turbulent flames, characterised by Reynolds numbers as realistic as possible and by incorporating a chemistry mechanism that can account for extinction have been derived.

The main contributions of this study can be summarised as follows:

1. The realisation of a parallel pseudospectral DNS code which is capable of dealing with the discretisation problem arising from the introduction of exponential chemistry source terms. A crucial criterion for the design of the code was the necessity to keep a balance between memory allocation demands and speed of calculations. This balance enables the computation of demanding turbulence simulations given the current computational power available.

2. The assembly of a DNS database designated to identify the mechanisms of the interaction between turbulence, mixing, and combustion. This DNS database

consists of two families of flows, i.e. homogeneous isotropic turbulence and planar jet cases which transit to turbulence and can be characterised by two different Reynolds numbers. A simple mixing scenario and different scenarios of reacting flows with varying degrees of extinction have been simulated individually for each of the two flow field families.

3. The assessment of zero equation models used in LES for the closure of the sub-grid scalar dissipation rate and the scalar variance, and the evaluation of the underlying assumptions. The modelling of both quantities is crucial for the coupling between the flowfield solutions and the combustion modelling in CMC.

4. Doubly conditioned CMC equations have been introduced to model the local extinction and re-ignition phenomena which cannot be captured by singly conditioned CMC. In this study we solve the doubly conditioned CMC equations and test its performance in relation to the singly conditioned CMC and the DNS results.

This thesis begins with a review of the fundamentals of turbulent combustion modelling. In particular, emphasis is given to the evolution of DNS in turbulence and combustion research, and the current status that DNS has reached. Further the CMC methodology is presented for both single and double conditioning.

The third chapter presents the numerical approach to the problem of solving a turbulent flow field with DNS. The pseudospectral methodology utilised and the challenges associated with the parallelisation of pseudospectral codes are discussed in detail.

The next chapter is an introduction to the numerical experiments carried out for the investigation of the modelling methodologies in turbulent combustion. Here both mixing and reacting problems are discussed in parallel, and the details of each separate case are outlined. A short evaluation of the results is shown.

The fifth chapter comprises a discussion of the computed pure mixing cases. At this point the problem of micromixing modelling is addressed and the accuracy of standard sub-grid scale mixing models is investigated. The sixth chapter deals with the modelling of extinction and re-ignition in turbulent reacting flows by the CMC

methodology, where the single and double conditioning approaches of CMC are discussed. For this the singly and doubly conditioned CMC equations are solved and the results are compared with the DNS solution. Finally, chapter seven summarises the findings of the previous chapters.

Chapter 2

Background

Fluid mechanics is the science of the mechanics of liquids and gases which is based on the same fundamental principles employed in the solid mechanics. Following a segregation equivalent to the branches of solid mechanics, fluid mechanics may be divided in statics, fluid kinematics and fluid dynamics. Hydrostatics deals with the study of forces and pressure fields in fluids at rest. Fluid kinematics studies the velocity and the streamlines in fluid flows, using the kinematic constrains of a fluid flow, regardless of force and energy distribution. Finally, fluid dynamics studies the flow of a flow field representing the kinematic part in relation to the energy and pressure distribution of the flow field. This relation between forces and kinematics in mechanics is expressed with the momentum transport, or the equivalent momentum impulse law used in solid dynamics. The analytical formulation of the momentum transport, mass transport and energy transport provides a closed system of equations for the velocity, density, temperature and pressure fields of a fluid.

2.1 Governing equations

A gaseous flame is governed by the transport equations of the momentum, mass, species and energy. The chemical mechanism will provide the source terms in the transport equations of the species and the heat release of the reactions. The governing equations are presented and used here in differential formulation in orthogonal Carte-

sian coordinates for a three-dimensional flow field. The Cartesian coordinates of a vector are denoted by a numeric subscript, i.e. u_1, u_2, u_3 for the three components of the velocity $\boldsymbol{u}$ along the x_1, x_2 and x_3 axis, respectively. Also, throughout this thesis the Einstein notation is followed, implying addition over all terms where an index is repeated. The mass conservation in differential form is expressed by the equation

$$\frac{\partial \rho}{\partial t} + \frac{\partial \rho u_i}{\partial x_i} = 0 \,, \tag{2.1}$$

where ρ is the density of the fluid, which may be a single phase mixture of several species and, in general, may vary over space and time.

The transport of momentum in fluid mechanics is modelled by the Navier-Stokes equations. For a three-dimensional flow, the momentum transport is modelled as

$$\frac{\partial \rho u_i}{\partial t} + \frac{\partial \rho u_j u_i}{\partial x_j} = -\frac{\partial p}{\partial x_i} + \frac{\partial \tau_{ij}}{\partial x_j} \quad \text{for } i = 1,2,3 \,, \tag{2.2}$$

where no body forces, such as gravity, electromagnetic or centrifugal forces, are considered. In equation (2.2), p is the pressure field and τ_{ij} represents the i,j-element of the viscous part of the stress tensor. The stress tensor τ includes the viscous forces due to the velocity gradients, and it can be expressed for a Newtonian fluid as a function of the spatial gradients of the velocity field $\boldsymbol{u}$ as

$$\tau_{ij} = -\frac{2}{3}\mu \frac{\partial u_k}{\partial x_k}\delta_{ij} + \mu\left(\frac{\partial u_i}{\partial x_j} + \frac{\partial u_j}{\partial x_i}\right) \,, \tag{2.3}$$

where $\mu = \rho\nu$ is the viscosity and ν is the kinematic viscosity of the fluid. An alternative formulation of the stress tensor T, can be defined to include the normal forces of the pressure, $T_{ij} = \tau_{ij} - \delta_{ij}p$. It is common practice that the stress tensor τ is rearranged as,

$$\tau_{ij} = 2\mu S_{ij} - \frac{2}{3}\mu\delta_{ij}\frac{\partial u_k}{\partial x_k} \,. \tag{2.4}$$

Here the terms containing the normal and the cross derivatives have been segregated. The tensor S_{ij} is rate of strain, and expresses the viscous forces in the momentum transport,

$$S_{ij} = \frac{1}{2}\left(\frac{\partial u_i}{\partial x_j} + \frac{\partial u_j}{\partial x_i}\right) . \tag{2.5}$$

Using the expression of the stress tensor for a Newtonian fluid, the Navier-Stokes equations are obtained, viz.

$$\frac{\partial \rho u_i}{\partial t} + \frac{\partial \rho u_i u_j}{\partial x_j} = -\frac{\partial p}{\partial x_i} + \frac{\partial}{\partial x_j}\left[\mu\left(\frac{\partial u_i}{\partial x_j} + \frac{\partial u_j}{\partial x_i} - \frac{2}{3}\delta_{ij}\frac{\partial u_k}{\partial x_k}\right)\right] \quad \text{for } j = 1, 2, 3 . \tag{2.6}$$

Turbulent combustion problems also involve the transport and mixing of the reacting species. The species involved in a flame are largely defined, by the compositions of the fuel and the oxidiser. Furthermore, the chemistry kinetic mechanism, which is utilised to model the reactions taking place, introduces a number of intermediate species. The reaction rate for each one is also provided by the mechanism itself. In addition to the mass and momentum transport equations, the transport equations for non-reactive and reactive scalars need to be solved so that the modelling of the transport phenomena taking place in a flame is closed. The transport equation of the k-th species in a mixture of M species can be written in the following form:

$$\frac{\partial \rho Y_k}{\partial t} + \frac{\partial}{\partial x_i}(\rho(u_i + V_{k,i})Y_k) = \omega_k \quad for \quad k = 1, M . \tag{2.7}$$

Here, Y_k is the mass fraction of the k-th species in the mixture, V_k is its diffusion velocity, and ω_k is the source term, which represents the production and depletion of the scalar due to chemical reactions. The diffusion velocities are defined by the solution of the algebraic system,

$$\nabla X_l = \sum_{k=1}^{M} \frac{X_l X_k}{D_{l,k}}(V_k - V_l) + (Y_l - X_l)\frac{\nabla P}{P} \quad for \quad l = 1, M , \tag{2.8}$$

where $D_{l,k}$ is the binary mass diffusion coefficient of the species l into the species k, and X_k is the mole fraction of the k-th species in the mixture and the volume forces are neglected [20]. The derivation of the above system of equations can be found in Kuo [21]. In this formulation, the diffusion of mass due to temperature gradients, which is known as the Soret effect, is neglected. In addition, the complex expression in equation

(2.8) is not implemented in most codes. According to the common practice, the much simpler Fick's law is employed for the approximation of the diffusion velocity. The simplified expression of the diffusion velocities can be written as

$$V_{k,i}Y_k = -D_k \frac{\partial Y_k}{\partial x_i} , \tag{2.9}$$

where the diffusion velocity is proportional to the concentration gradient. The coefficient D_k is the diffusion coefficient of species k into the mixture. Finally, a simplified expression of the species transport equation is obtained,

$$\frac{\partial \rho Y_k}{\partial t} + \frac{\partial \rho u_i Y_k}{\partial x_i} = \frac{\partial}{\partial x_i}\left(\rho D_k \frac{\partial Y_k}{\partial x_i}\right) + \omega_k \quad for \quad k = 1, M . \tag{2.10}$$

The energy transport problem is modelled by the enthalpy h transport equation

$$\frac{\partial \rho h}{\partial t} + \frac{\partial}{\partial x_i}(\rho u_i h) = \frac{\partial p}{\partial t} + \frac{\partial}{\partial x_i}\left[\lambda \frac{\partial T}{\partial x_i} - \rho \sum_{k=1}^{M} (h_k V_{k,i} Y_k)\right] + \tau_{ij}\frac{\partial u_i}{\partial x_j} + \rho \sum_{k=1}^{M} (Y_k f_{k,i} V_{k,i}) , \tag{2.11}$$

where λ is the thermal conductivity of the mixture, and $T(\boldsymbol{x}; t)$ is the temperature field. For the derivation of equation (2.11) it has been assumed that heating due to viscous forces, the heat source term due to radiative fluxes, and the body forces are not taken into account. Although the enthalpy may be defined in multiple ways in order to include various forms of energy contained in the fluid, a form of the enthalpy h is related to an equivalent form of energy e as

$$h = e + p/\rho , \tag{2.12}$$

showing that the enthalpy includes the dynamic energy of the fluid due to its pressure. The total enthalpy h_t quantifies the thermal energy of the fluid due to its temperature, the dynamic energy due to its pressure, the chemical energy of its species and the kinetic energy due to its velocity

$$h_t = \int_{T_0}^{T} C_v dT + p/\rho + \sum_{k=1}^{N} \Delta h^0_{f,k} Y_k + \frac{1}{2} u_i u_i . \tag{2.13}$$

The energy due to the fluid pressure is usually merged with the thermal energy as $\int_{T_0}^{T} C_p dT$, where the constant pressure heat capacity C_p of the mixture is used instead of the constant volume heat capacity C_v. The enthalpy difference $\Delta h_{f,k}^{O}$ is the enthalpy of formation, which is the energy needed for the formation of the species k at standard conditions P_0 and T_0.

Sensible enthalpy h_s can also be used for the modelling of the energy transport problem and is defined as

$$h_s = h - \sum_{k=1}^{N} \Delta h_{f,k}^{0} Y_k \,. \tag{2.14}$$

The transport equation for the sensible enthalpy can be formed from the enthalpy transport equation (2.11), using the definition (2.14), as

$$\frac{\partial \rho h_s}{\partial t} + \frac{\partial}{\partial x_i}(\rho u_i h_s) = \omega_T + \frac{\partial p}{\partial t} + \frac{\partial}{\partial x_i}\left[\lambda \frac{\partial T}{\partial x_i} - \rho \sum_{k=1}^{M} (h_{s,k} V_{k,i} Y_k)\right] + \tau_{ij}\frac{\partial u_i}{\partial x_j} + \rho \sum_{k=1}^{M} (Y_k f_{k,i} V_{k,i}) \,, \tag{2.15}$$

where ω_T is the heat release due to combustion, thus, the enthalpy formulation (2.11) is preferred in CFD applications since it is a conserved scalar, i.e. it lacks a source term.

For the derivation of modelling methodologies in turbulent combustion, but also for the solution of simplified flows, the enthalpy transport equation can be replaced by the following temperature transport equation, where constant heat capacity C_p and conductivity λ, equal for all the species of the mixture has been assumed,

$$\frac{\partial \rho T}{\partial t} + \frac{\partial \rho u_i T}{\partial x_i} = + \frac{\partial}{\partial x_i}\left(\alpha_t \frac{\partial T}{\partial x_i}\right) + \omega_T \,, \tag{2.16}$$

where α_t is the thermal diffusion coefficient

$$\alpha_t = \frac{\lambda}{\rho C_p} \,. \tag{2.17}$$

The temperature transport equation can be derived from the sensible enthalpy transport equation (2.15) for constant pressure and low speed flames, where all heat

capacities $C_{p,k}$ of the species k are assumed to be equal, i.e. $C_{p,k} = C_p$.

Equations (2.6, 2.8, 2.11) provide a set of differential equations for the modelling of reacting flows. However, this system can be solved analytically only for a small number of simple problems. The objective of Computational Fluid Dynamics (CFD) is the computational solution of the mathematical model of a fluid using numerical methods.

Significant simplification for models in turbulent combustion occur when all species and the temperature diffuse equally, thus the ratio of Schmidt and Prandtl numbers known as the Lewis number,

$$Le = \frac{Sc}{Pr}, \tag{2.18}$$

is equal to unity. The number $Sc = \frac{D_k}{\nu}$ is the Schmidt number, and expresses the relation between the diffusion of the momentum due to viscous forces and the diffusion of the species due to molecular diffusion. Also the Prandtl number, $Pr = \frac{a_t}{\nu}$, in equation (2.18), quantifies the relation between the diffusion of temperature and the dissipation of momentum. In fact, in hydrocarbon flames with high Reynolds numbers the molecular and the atomic hydrogen are the only species with a Lewis numbers deviating significantly from unity. However, their concentrations are low, since they are intermediate species in hydrocarbon flames, and unity Lewis number assumptions do not affect significantly the flame structure.

2.2 Turbulence

In most engineering applications, the combustion process is turbulent [1]. It is now quite important to present some of the characteristics of the turbulent flow, so as to ensure a better understanding of some of the characteristic phenomena that take place in a turbulent flame, and also to better describe the methods used in CFD for the modelling of turbulent combustion.

Any of the variables $f(\boldsymbol{x}; t)$ of a turbulent flow field, i.e. the velocity components, the species concentration and the temperature field, can be expressed as the summation of a mean plus a turbulent contribution [22]

$$f(\boldsymbol{x};t) = \overline{f}(\boldsymbol{x};t) + f' \,, \tag{2.19}$$

where in the above expression, the bar $\bar{\cdot}$ denotes an average value. The single prime $\cdot'$ represents the fluctuation so that u', Y_i' and T' are the fluctuations around the average value of $\overline{u}$, $\overline{Y}_i$ and $\overline{T}$ respectively. The averaging operation can be either defined in time or in space [22].

Richardson [23] introduced a conceptual approach to the understanding of turbulence, where he suggested that turbulence can be understood as a superposition of coherent flow structures, i.e. eddies of different sizes. The size is the principal characteristic of the structure and eddies can therefore be classified according to their characteristic length scale [24].

Generally speaking, turbulence is generated by velocity gradients [25]. The fundamental process responsible for the existence of different scales in turbulence is the energy cascade [26]. The velocity gradients can be regarded as the large scale eddies. The large scale eddies break up producing eddies of smaller size. According to the same mechanism the eddies break up to smaller and smaller sizes until they dissipate since the viscous effects increase disproportionately with decreasing size. As a consequence of this common mechanism of production, cascade and, finally, dissipation of turbulence, it can be expected that equally sized eddies should have a similar intensity.

Apart from the intensity of the turbulent motion, eddies of the same order of size tend to exhibit some other similarities. Such similarities apply to the homogeneity of the motion, to the effect on the scalar mixing and to the dissipation of the turbulent kinetic energy. As a result, it becomes quite evident that the size of the eddies can be a characteristic property, according to which the turbulent motion could be categorised into turbulent scales. Therefore, a specific length scale, l, and a velocity $u(l)$ can characterise an eddy. A characteristic time τ can be derived from the above quantities and can be expressed as $\tau(l) = l/u(l)$.

Transition to turbulence occurs at high Reynolds numbers. Considering a macroscopic turbulent flow, e.g. grid turbulence or a shear layer with a characteristic velocity U and length scale L, the Reynolds number $Re = UL/\nu$ should be large and the effect of viscosity minimal. The biggest scales in a turbulent flow field, namely ℓ_0, are compara-

ble to the scale of the macroscopic flow. Their characteristic velocity u_0 is comparable to the amplitude of the turbulent fluctuations u' and it is usually expressed by the r.m.s of the fluctuations, $\overline{u'^2}^{1/2}$. The r.m.s. of the fluctuations is also related to the turbulent kinetic energy k,

$$k = \frac{1}{2}u_1'^2 + \frac{1}{2}u_2'^2 + \frac{1}{2}u_3'^2 = \frac{3}{2}u'^2 \,. \tag{2.20}$$

This energy, rather than dissipating directly to heat due to the viscosity, cascades to smaller eddies. In these large energy containing scales, the Reynolds number $Re_0 = \frac{\ell_0 u_0}{\nu}$ is quite big, comparable to Re , for the viscosity to have an effect. The amount of the dissipation of the kinetic energy from the large scales to the smaller scales is proportional to the energy of the large scales divided by their time scale

$$\epsilon \sim \frac{u_0^2}{\tau_0} = \frac{u_0^3}{\ell_0} \,. \tag{2.21}$$

In general, the dissipation rate ϵ expresses the loss of the kinetic energy of the fluid to heat due to the work of viscosity and is given by the expression

$$\epsilon = 2\nu\left(S_{ij}S_{ij}\right) = \nu\left(\frac{\partial u_i}{\partial x_j}\frac{\partial u_i}{\partial x_j} + \frac{\partial u_i}{\partial x_j}\frac{\partial u_j}{\partial x_i}\right) \tag{2.22}$$

The above definition of the kinetic energy dissipation rate is accurate since it has been derived as the work of the viscous forces. If the turbulent kinetic energy of the large scales was dissipating, rather than cascading to smaller scales, then the dissipation would have been proportional to $\nu u_0^2/\ell_0^2$, following a dimensional analysis based on the equation (2.22). Instead, by identifying the small scales as the scales at which the dissipation takes place, expression (2.21) is obtained. This is done by assuming that the rate in which the energy cascades from the large scales equals the rate that the energy dissipates in the small scales. This underlines the importance of Richardson's ideas.

The physics of the small scales of a turbulent flow field can be investigated by the local isotropy hypothesis and by the two similarity hypotheses introduced by Kolmogorov [27]. The isotropy hypothesis states that the small scales of a turbulent flow with sufficient high Reynolds number are isotropic. The important consequence of this

hypothesis is the loss of any directional information of macroscopically non-isotropic flows as the turbulent scales become smaller. Thus, there is a universal behaviour of a turbulent field whether it is found in a jet or in grid turbulence. The first similarity hypothesis states that the small scale motion has a universal form defined by the energy dissipation, ϵ, and the viscosity, ν. The dissipation rate expresses the amount of the energy transfer from the large scales to the smaller ones. The characteristic length, time and velocity are called Kolmogorov scales and dimensional analysis gives,

$$\eta = \frac{\nu^{3/4}}{\epsilon^{1/4}} , \tag{2.23}$$

$$\tau_\eta = \frac{\nu^{1/2}}{\epsilon^{1/2}} , \tag{2.24}$$

and,

$$u_\eta = \nu^{1/4}\epsilon^{1/4} . \tag{2.25}$$

It can easily be seen that the Kolmogorov Reynolds number is $Re_\eta = \eta u_\eta/\nu = 1$. This implies that the viscous forces are significant at the Kolmogorov scale, leading to the dissipation of the turbulent fluctuations to heat. As a result, the Kolmogorov scale is synonymous with the smallest scale of a turbulent flow field. The ratio of the Kolmogorov scale to the large energy containing length-scales expresses the range of scales, and can be derived using expression (2.21) and (2.23) giving,

$$\frac{\eta}{\ell_0} = Re^{-3/4} . \tag{2.26}$$

The ratio of the two limits provides the range of scales in a turbulent field. This is a very important parameter since, ideally, all scales must be resolved in computational mechanics and therefore it defines the computational complexity of the problem to be analysed. As the Reynolds number increases more computational power is required for the simulation of such a flow field.

2.2.1 The turbulent kinetic energy spectrum

If a turbulent flow field is transformed into spectral space, it can be argued that the wavenumber denotes the size of an eddy. Consequently it is advantageous to study the characteristics of the turbulent scales in wavenumber space. However, the association of Fourier modes with instantaneous eddies should be treated with some skepticism, given that eddies are localised structures, whereas Fourier modes are not [29].

The Fourier, or spectral space, is a three-dimensional space defined by the wavenumber vector $\kappa = \{\kappa_1, \kappa_2, \kappa_3\}$. Given that the wavenumber is closely related to the size of the eddies, each turbulent scale can be characterised separately. A definition of the velocity spectrum can be based on the correlation function R_{ij}, which provided by the following equation [26],

$$R_{ij}(\boldsymbol{r}, \boldsymbol{x}; t) = \overline{u_i'(\boldsymbol{x}; t)u_j'(\boldsymbol{x} + \boldsymbol{r}; t)} \, . \tag{2.27}$$

The velocity spectrum tensor Φ_{ij} is the three-dimensional Fourier transform of the corresponding two-point correlation function. Other formulations for the derivation of the turbulent kinetic energy spectrum are based on the time correlation [26]. This temporal spectrum is often used in experimental research and in studies in RANS methodology. However, for non-stationary flow fields spectra expressed on the wavenumber space should be used instead of the frequency space [28]. The velocity spectrum tensor is a Fourier transform pair with the two-point correlation function

$$\Phi_{ij}(\boldsymbol{\kappa}; t) = \frac{1}{(2\pi)^3} \iiint_{-\infty}^{\infty} R_{ij}(\boldsymbol{r}; t) e^{-i\boldsymbol{\kappa}\boldsymbol{r}} d\boldsymbol{r} \, , \tag{2.28}$$

which varies in time for a non-stationary turbulent flow field, but remains unchanged in time for stationary fields. The above equation transforms the flow field correlation function from the three-dimensional physical space $\boldsymbol{r} = \{r_1, r_2, r_3\}$ to the three-dimensional wavenumber space $\boldsymbol{\kappa} = (\kappa_1, \kappa_2, \kappa_3)$. The three-dimensional turbulent kinetic energy spectrum can be derived from the velocity spectrum tensor Φ_{ij}, according to the equation

$$E_k(\kappa) = \oint_{|\boldsymbol{\kappa}|=\kappa} \frac{1}{2}\Phi_{ii}(\boldsymbol{\kappa})d\mathcal{S}(\kappa) \,, \tag{2.29}$$

where κ is the magnitude of the wavenumber vector, i.e. $\kappa = |\boldsymbol{\kappa}| = \sqrt{\kappa_1^2 + \kappa_2^2 + \kappa_3^2}$. The idea behind equation (2.29) is that the energy contribution $\frac{1}{2}\Phi_{ii}$ of each wavenumber combination is added up for each of the combinations that have the same three-dimensional wavenumber $\boldsymbol{\kappa}$. In the Fourier space all these points are located in a sphere with radius equal to κ.

The turbulent scales can be divided into four categories, which can be best illustrated in spectral space. A typical appearance of a three-dimensional energy spectrum is depicted in figure 2.1. In the same figure the relative position of the large scales $\frac{1}{\ell_0}$ and Kolmogorov scale $\frac{1}{\eta}$ is presented for homogeneous turbulence in wavenumber space. According to Von Kármán, the energy per wavenumber for small κ, i.e. the large scales, increases as κ^4 [30], whereas the Kolmogorov spectrum gives a κ^2 dependence [31] for the same region. Nevertheless, this area of the energy spectrum is numerically resolved, rather than modelled both in LES and in RANS. The latter methodology though, does not fully resolve the energy containing scales. However, the inner structure of this part of the energy spectrum is subject to the boundary conditions and other macroscopic factors and therefore it is not global. As a result, the modelling methodologies introduced in RANS do not have a global character [32].

The energy containing scales with characteristic length equal to ℓ_0 lie close to the area of the maximum turbulent kinetic energy in the energy spectrum. The smallest and least energy containing range consists of the viscous subrange. This scale starts at the area of the viscous cutoff, commonly characterised by the Kolmogorov scale η. In this area, the energy per wavenumber decreases exponentially with respect to the wavenumber. Finally between the energy containing range and the Kolmogorov scale lies the inertial subrange, and is characterised by a decline of the turbulent kinetic energy with respect to the wavenumber following the $\kappa^{-\frac{5}{3}}$ law. This law can be derived from dimensional analysis for the turbulent kinetic energy and applying the second similarity hypothesis of Kolmogorov.

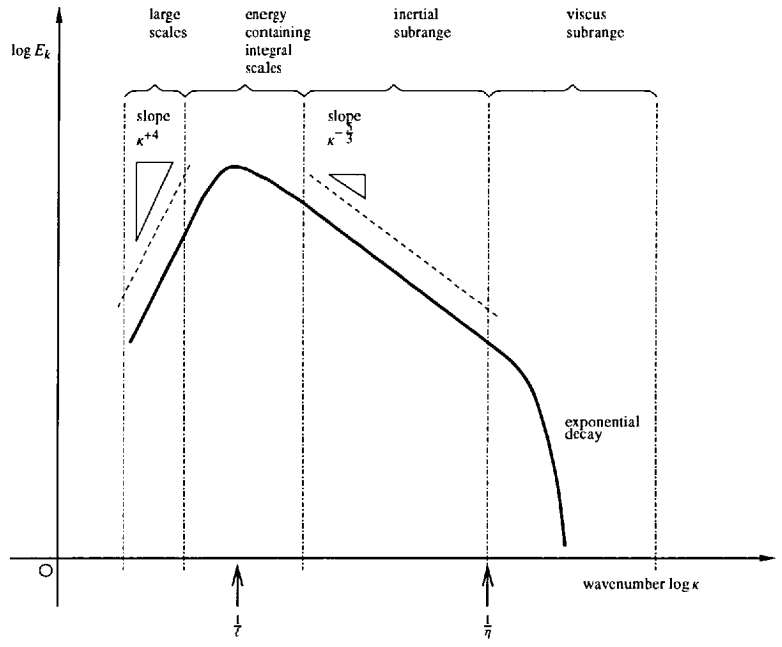

Figure 2.1: Turbulent kinetic energy spectrum and turbulent length scales. Adapted from Tennekes and Lumley [25]

2.2.2 The spectral distribution of a scalar quantity

Turbulence affects any scalar field which is transported by the flow field and it therefore creates not only velocity fluctuations but also induces the fluctuations of the scalar field. This scalar field can be the temperature or the concentrations of chemically inactive or reactive species. The definition of the spectral representation of turbulence can be extended to any scalar quantity that is transported by a turbulent flow field. The autocorrelation coefficient formulation and the spatial spectrum are identical to the corresponding definitions used for the derivation of the velocity spectrum. Generally speaking, the scalar energy spectrum follows the scales of the turbulent velocity field. The viscosity, ν, controls the turbulent velocity scales that in turn control the convection of the scalar field. In contrast, the diffusivity, D, controls the diffusion of the scalar and the dissipation of its fluctuations. The ratio of the viscosity over the diffusivity governs the divergence of the scalar spectrum from the velocity spectrum [25]. This ratio is non dimensional and is given by the Prandtl number, $Pr = \nu/\alpha_t$, for thermal diffusivity, or the Schmidt number, $Sc = \nu/D$, for the molecular diffusion

coefficient.

In the case of high Prandtl or Schmidt numbers, such as dyes in liquids [26], a fifth characteristic range for length scales can be identified [25]. It is called viscous convective subrange and extents to even finer scales than the Kolmogorov length scale. In this case, i.e $D < \nu$ or $\alpha_t < \nu$, the smallest scales of the scalar fields are characterised by the Batchelor microscale [33], which can be expressed as a fraction of the Kolmogorov microscale as,

$$\eta_B = \eta\, Sc^{-1/2} . \tag{2.30}$$

When the Prandtl number is smaller than unity, i.e $D > \nu$ or $\alpha_t > \nu$, then the scalar diffuses faster than the momentum. This would create a less fine structure for the scalar than for the velocity field itself. In this case the smallest scales of the scalar fields are characterised by the Oboukhov-Corrsin scale [34, 35] given by the equation,

$$\eta_{OC} = \eta\, Sc^{-3/4} . \tag{2.31}$$

A graphical representation of the scalar energy spectra for cases of scalar fields with high and low Prandtl numbers is provided in figure 2.2.

2.3 Chemical kinetics

A flame is the result of an exothermic reaction between fuel and oxidiser. The structure of flame is described and modelled by a chemical mechanism. In most gaseous flames the fuel consists of hydrogen, carbon monoxide and gaseous hydrocarbons. The oxidiser in most industrial applications is air. Air is a mixture of oxygen, nitrogen and some trace species such as Ar, CO and CO_2. The main products of a hydrocarbon flame are carbon dioxide and water. However, other products depending on the fuel may be carbon monoxide, sulfur oxides, nitrogen oxides, soot and unburnt hydrocarbons. While carbon dioxide is unavoidable, all other harmful emissions can in theory be reduced. Increasing the efficiency of the combustion process, understanding the mechanisms responsible for the formation of pollutants and eliminating their

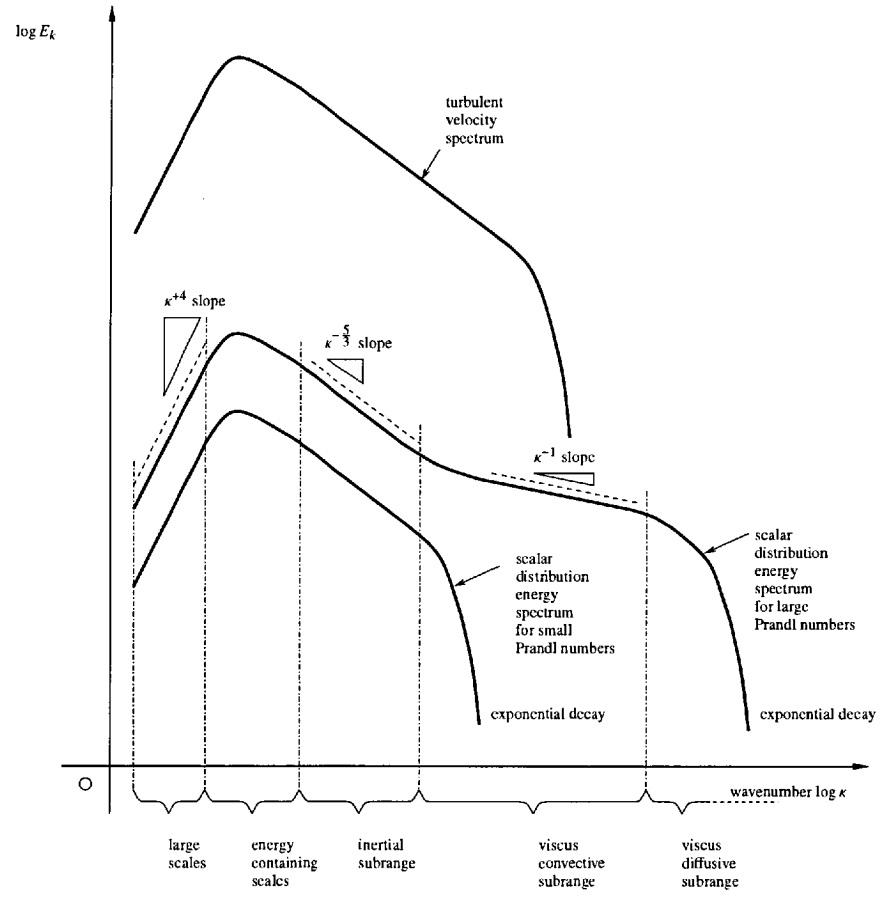

Figure 2.2: Three dimensional energy spectrum for a scalar quantity. Adapted from Tennekes and Lumley [25]

emissions is the main goal of combustion modelling. In addition to fuel, oxidiser and products, intermediate species are produced by the combustion process but they are usually found in very small concentrations in the final products. However, they play an important role in the chemical mechanism itself and are crucial for sustaining the combustion process. The chemical mechanism provides a set of n reactions for the chemical conversion of all m species, M_k:

$$\begin{aligned}
\nu_{11}^1 M_1 + \ldots + \nu_{k1}^1 M_k + \ldots + \nu_{m1}^1 M_m &\rightleftharpoons \nu_{11}^2 M_1 + \ldots + \nu_{k1}^2 M_k + \ldots + \nu_{m1}^2 M_m \\
&\vdots \\
\nu_{1j}^1 M_1 + \ldots + \nu_{kj}^1 M_k + \ldots + \nu_{mj}^1 M_m &\rightleftharpoons \nu_{1j}^2 M_1 + \ldots + \nu_{kj}^2 M_k + \ldots + \nu_{mj}^2 M_m \\
&\vdots \\
\nu_{1n}^1 M_1 + \ldots + \nu_{kn}^1 M_k + \ldots + \nu_{mn}^1 M_m &\rightleftharpoons \nu_{1n}^2 M_1 + \ldots + \nu_{kn}^2 M_k + \ldots + \nu_{mn}^2 M_m \,.
\end{aligned} \tag{2.32}$$

In the above set of reactions, the stoichiometric mass coefficients ν_{ij}^1 and ν_{ij}^2 define the amount of moles consumed or produced by each reaction. The reaction rate ω_j of each reaction is related to the reaction rate ω_k of each species M_k, by

$$\omega_k = \sum_{j=1}^{n} (\nu_{kj}^1 - \nu_{kj}^2)\omega_j. \tag{2.33}$$

The reaction rates for each reaction j are functions of the forward and backward rate constants K_j^f and K_j^b, the species molar concentrations $[X_k] = \frac{\rho Y_k}{W_k}$ and of the absolute temperature T,

$$\omega_j = K_j^f \left[\rho\frac{Y_1}{W_1}\right]^{\nu_{1j}^1} \cdot \ldots \cdot \left[\rho\frac{Y_k}{W_k}\right]^{\nu_{kj}^1} \cdot \ldots \cdot \left[\rho\frac{Y_m}{W_m}\right]^{\nu_{mj}^1} - K_j^b \left[\rho\frac{Y_1}{W_1}\right]^{\nu_{1j}^2} \cdot \ldots \cdot \left[\rho\frac{Y_k}{W_k}\right]^{\nu_{kj}^2} \cdot \ldots \cdot \left[\rho\frac{Y_m}{W_m}\right]^{\nu_{mj}^2}, \tag{2.34}$$

where W_k is the molecular weight of species M_k. The calculation of the forward rate constant, K_j^f, is usually based on the Arrhenius formulation,

$$K_j^f = A_j^f T^{b_j} e^{-\frac{E_{a,j}}{RT}} \,. \tag{2.35}$$

In the above equation the pre-exponential factor A_j^f, the exponent b_j and the activation energy $E_{a,j}$ depend on the reaction and are parameters provided by the reaction mechanism. The activation energy is directly related to the activation temperature $T_{a,j} = \frac{E_{a,j}}{R}$. Also R is the universal gas constant. The backward rate constant K_j^b is computed from the reaction equilibrium as a function of the forward constant K_j^f [36].

$$K_j^b = \frac{K_j^f}{\left(\frac{p_a}{RT}\right)^{\sum_{k=1}^{N} \nu_{kj}} e^{\left(\frac{\Delta S_j^0}{R} - \frac{\Delta H_j^0}{RT}\right)}} . \tag{2.36}$$

Where, ΔS_j^0 and ΔH_j^0 refer to the entropy and enthalpy changes for the $j-th$ reaction.

2.4 Flame structure

Gaseous flames are divided in two major categories, premixed and non-premixed flames. In premixed flames, the oxidiser and the fuel react after they are well mixed and have formed a homogeneous mixture. The topology of a premixed flame is presented in figure 2.3(**a**) [37]. In premixed combustion, a flame front propagates towards the unburned mixture and combustion products or burnt gases are left behind. Figure 2.3(**a**) shows is one of a typical Bunsen burner, which represents one of several typical setups for premixed combustion. In other cases, there is no mean flow of the reactants, instead the flame propagates into a stagnant mixture of fuel and oxidiser after being ignited by a spark. Such a scenario is typical for a gasoline engine [1].

In non-premixed or diffusion flames, the fuel and the oxidiser are kept separated before entering the combustion chamber. Then, the two are mixed in the reaction region. As a result, mixing must be done fast enough for combustion to proceed [20]. Mixing plays a major role in non-premixed flames since it is the conversion rate controlling step. The topology of a typical diffusion flame is presented in figure 2.3(**b**). Other topologies of diffusion flames include the combustion of fuel spray in cylinders of diesel engines or jet engine combustors. In the combustor shown in figure 2.3(**b**) the fuel is issues from the orifice at a certain speed. The oxidiser enters the combustor and the two start mixing. The fuel stream forms a jet where the concentration of the fuel is high along the centreline. The reaction region is located on the surface, where the reactants have mixed to a stoichiometric mixture. In the vicinity of that surface, the oxidiser and the fuel are fully burnt, and the temperature is expected to be the highest [1]. Therefore, the reaction region in the diffusion flame is formed by a thin layer located around the stoichiometric surface.

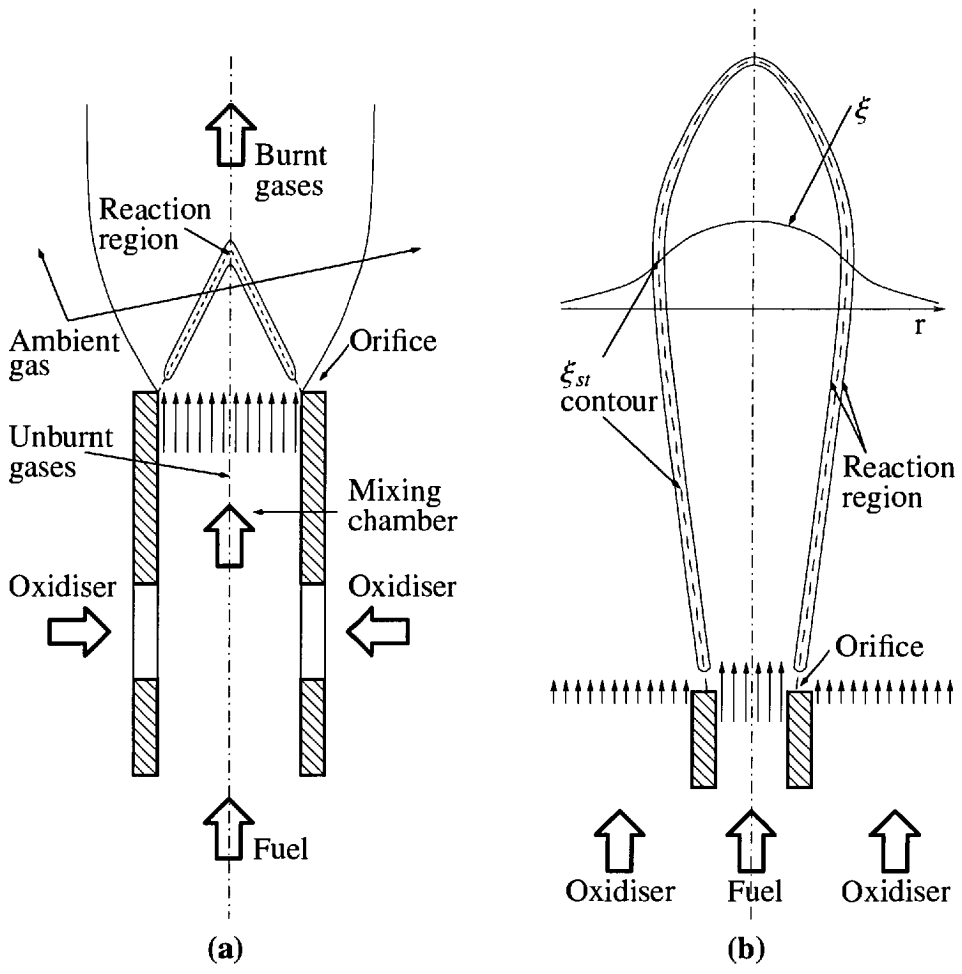

Figure 2.3: (a) Topology of a premixed flame. (b) Topology of a non-premixed flame

When modelling a combustion process, a first rather crude but computationally cheap approximation is often used. A simple one-step reaction of fuel, F, oxidiser, O, and products P, is assumed and the chemical conversion can be expressed by the reversible reaction

$$\nu_F F + \nu_O O \rightleftharpoons \nu_P P + Q\,, \tag{2.37}$$

where ν_F moles of fuel and ν_O moles of oxidiser react to ν_P moles of products and vice versa. The symbol Q denotes the amount of heat produced per ν_F moles of fuel burnt, and is a positive quantity for an exothermic reaction. The values of ν_F, ν_O and ν_P result from the necessary quantity of oxidiser for the stoichiometric combustion of

ν_F moles of fuel.

In non-premixed combustion, the mixing of the reactants is quantified by a scalar variable, which is the mixture fraction ξ, and is defined in a such way that it is not affected by the chemistry of the phenomenon. Mixture fraction is defined as a linear combination of the reacting species in a flame, so that the reaction rate is eliminated. The transport equations for the mass fractions of fuel, Y_F, and oxidiser, Y_O, can be written as,

$$\frac{\partial \rho Y_F}{\partial t} + \frac{\partial \rho u_i Y_F}{\partial x_i} = \frac{\partial}{\partial x_i}\left(\rho D \frac{\partial Y_F}{\partial x_i}\right) + \omega_F \ , \tag{2.38}$$

and

$$\frac{\partial \rho Y_O}{\partial t} + \frac{\partial \rho u_i Y_O}{\partial x_i} = \frac{\partial}{\partial x_i}\left(\rho D \frac{\partial Y_O}{\partial x_i}\right) + \omega_O \ . \tag{2.39}$$

From the stoichiometry of reaction (2.37) and the molecular weights of the oxidiser and the fuel W_O and W_F respectively, the relation between the reaction rates is given by

$$\omega_O = s\omega_F \ , \tag{2.40}$$

where s is the mass stoichiometry ratio $s = \frac{\nu_O W_O}{\nu_F W_F}$. From equations (2.38) and (2.39) it is obvious that the linear combination $\beta = sY_F - Y_O$ is a scalar, which varies from sY_F^0 in the pure fuel region to $-Y_O^0$ in the pure oxidiser region. Also, its chemical source term is zero. The mass fraction Y_F^0 stands for the mass fraction of the fuel in the pure fuel or initial stream, which is equal to unity unless it is diluted. Whether the diluted fuel is considered as the fuel F in reaction (2.37) or not is a matter of definition. The same is valid for the oxidiser, where Y_O^0 stands for the mass fraction of the oxidiser in the pure oxidiser region. Thus, in both cases, the zero exponent stands for the stage where the fuel and the oxidiser are not mixed. The scalar β can be normalised by constraining its value between 0 and 1,

$$\xi = \frac{sY_F - Y_O + Y_O^0}{sY_F^0 + Y_O^0} \ . \tag{2.41}$$

The variable ξ is the mixture fraction. It quantifies the mixing between the fuel and the oxidiser, and it is a conserved scalar because it is neither produced nor consumed by chemical reactions. The transport equation of the mixture fraction ξ can be expressed by the following non-dimensional expression,

$$\frac{\partial \rho \xi}{\partial t} + \frac{\partial \rho u_i \xi}{\partial x_i} = \frac{\partial}{\partial x_i}\left(\rho D \frac{\partial \xi}{\partial x_i}\right), \tag{2.42}$$

where constant properties have been assumed.

The values of ξ vary from unity, identifying the areas of pure fuel, to zero for the areas of pure oxidiser. Figure 2.3(b) shows the expected distribution of mixture fraction ξ across a typical diffusion flame. Along the centreline of the jet, the concentration of the mixture fraction is expected to be high. Therefore, the value of the mixture fraction should be closer to unity, while it reduces to zero in areas distant from the centreline where the oxidiser has larger concentrations.

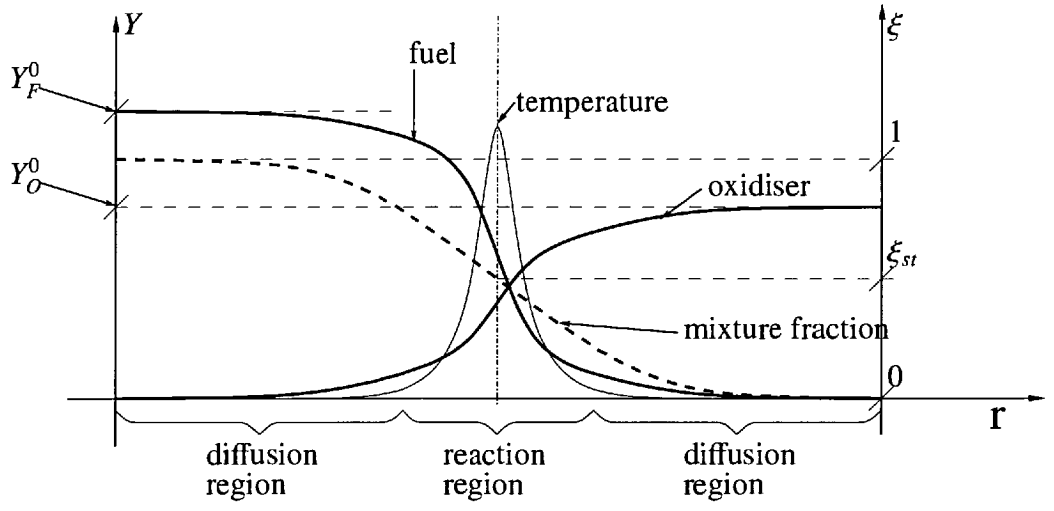

Figure 2.4: Distribution of temperature and reactants across a flame front in a diffusion flame.

Figure 2.4 shows the flame structure in a diffusion flame in more detail. The coordinate r represents the distance from the centreline for a jet flame. At the stoichiometric surface the fuel mass fraction equals $Y_F = sY_O$. From expression (2.41) the corresponding value for the mixture fraction at the stoichiometric point is found to be

$$\xi_{st} = \frac{Y_O^0}{sY_F^0 + Y_O^0} \,. \tag{2.43}$$

Provided that the mixture fraction quantifies the mixing between the reactants in a flame, and that the mixing controls a diffusion flame, it is common practice in non-premixed combustion to express the variables of a diffusion flame in mixture fraction space. In order to make this feasible, one must make the assumption that the mass fraction of the species and the temperature have the same one-dimensional structure across the flame front in each cross-section of the flame. Assuming that species and temperature are functions of ξ and time only, $T = T(\xi, t)$ and $Y_k = Y_k(\xi, t)$, the species mass fraction transport equation (2.10) can be expressed in mixture fraction space [1] as,

$$\rho\frac{\partial Y_k}{\partial t} = \omega_k + \rho D\left(\frac{\partial \xi}{\partial x_i}\frac{\partial \xi}{\partial x_i}\right)\frac{\partial^2 Y_k}{\partial \xi^2} \,, \tag{2.44}$$

and the temperature equation (2.17) is rearranged to,

$$\rho\frac{\partial T}{\partial t} = \omega_T + \frac{\alpha_t}{D}\rho D\left(\frac{\partial \xi}{\partial x_i}\frac{\partial \xi}{\partial x_i}\right)\frac{\partial^2 T}{\partial \xi^2} \,. \tag{2.45}$$

Where the convective term has been neglected, assuming that the flame structure is constant in space. This formulation introduces the scalar dissipation rate term χ, that is defined by

$$\chi = 2\rho D\frac{\partial \xi}{\partial x_i}\frac{\partial \xi}{\partial x_i}, \tag{2.46}$$

which expresses the effect of mixing on the structure of a diffusion flame.

Equations (2.44) and (2.45) are known as the flamelet equations. A flamelet is an elementary flame which is laminar with a one-dimensional structure akin to the one depicted in figure 2.4 and depends only on the axis perpendicular to the flame front, i.e. on the mixture fraction. Equations (2.44) and (2.45) can be simplified further following some assumptions. A first assumption made is the steady state assumption $\frac{\partial \cdot}{\partial t} = 0$, which leads to the steady flamelet concept,

$$\omega_k = -\frac{1}{2}\chi\frac{\partial^2 Y_k}{\partial\xi^2}\,, \tag{2.47}$$

and,

$$\omega_T = -\frac{1}{2}\chi\frac{\partial^2 T}{\partial\xi^2}\,. \tag{2.48}$$

The introduction of the mixture fraction can be viewed as a coordinate transformation from physical to mixture fraction space. The flame structure is projected on the mixture fraction space, as shown in figure 2.5, rather than in the physical space shown in figure 2.4. Under the CMC concept the mixture fraction space is known as the η-space.

The simplest scenario for the structure of a steady flamelet is the "frozen" chemistry scenario. In this case, the reaction rates are zero. Although this is a non combusting case, it can nevertheless be observed in areas of the flame that are extinct and the reactants just mix without reaction. For $\omega_k = 0$, and $\omega_T = 0$ equations (2.47) and (2.48) reduce to $\frac{\partial^2 Y_k}{\partial\xi^2} = 0$ and $\frac{\partial^2 T}{\partial\xi^2} = 0$ throughout the mixture fraction space, thus Y_ξ is a linear function of ξ. In this pure mixing case, the mass fractions of the species and the temperature are the mean of the respective values in pure oxidiser and pure fuel weighted by the mixture fraction, as can be seen in figure 2.5.

The complement to the frozen chemistry structure is the fast irreversible chemistry shown in mixture fraction space in figure 2.5. In this model, the chemistry is much faster than the mixing. The flame has an infinitesimally small thickness where the reaction rates are non zero, and is located on the stoichiometric mixture fraction contour. Because of the irreversibility of the chemistry the reactants do not coexist. The oxidiser is zero on the rich side of the flame, where $\xi > \xi_{st}$, and the fuel is zero on the lean side of the flame, where $\xi < \xi_{st}$. The reaction rates outside the flame front are zero, thus the distribution of the mass fractions and the temperature is linear with a discontinuity of the first derivative at stoichiometric. The maximum temperature equals the adiabatic temperature T_{ad} [20], because in the fast chemistry scenario the mixing rates are small compared to the reaction rates,

$$T_{ad} = T_F^0 \xi_{st} + T_O^0 (1 - \xi_{st}) + \frac{Q}{C_p} Y_F^0 \xi \,. \tag{2.49}$$

The above expression is the sum of the temperature of the un-burnt mixture at the stoichiometric mixture fraction, and the increase of the temperature due to the heat released by the exothermic reaction. Assuming that a diffusion flame takes place under constant pressure, the specific heat C_p for the burnt gases can be used in expression (2.49).

When the chemistry and the time scales are comparable, the flame structure becomes more complex and depends on the effects of the flow on the chemical conversion rates. This condition lies between the frozen and the fast chemistry scenarios [20]. and the reaction region is characterised by a finite flame thickness, as shown in figure 2.5

2.4.1 Flame thickness

Figure 2.6 depicts a schematic topology of a flame front in a turbulent non premixed flame. The reaction zone is characterised by a finite width, ℓ_r, surrounding the stoichiometric mixture fraction contour. The reaction takes place within the diffusion region where the oxidiser and the fuel are mixed, having a width equal to ℓ_d.The diffusion and reaction thicknesses can be projected into the mixture fraction space as ℓ_d^η and ℓ_r^η respectively, as shown in the figure 2.5. Several authors have proposed ways to define a characteristic length for diffusion flames.

The procedure, is however, not as straightforward as in premixed flames where the flame speed provides a characteristic velocity magnitude [1]. Following Vervisch [38] the width of the diffusion region is controlled by the mixture fraction distribution and can be estimated as

$$\ell_d \sim \frac{1}{|\nabla \xi|_{st}} \,, \tag{2.50}$$

from the spatial gradient of ξ on the stoichiometric mixture fraction. Another approach is based on the diffusion coefficient and the velocity strain rate a, $\ell_d \sim \left(\frac{D}{a}\right)$, [1]. In η space the diffusion thickness ℓ_d^η can be extracted from ℓ_d,

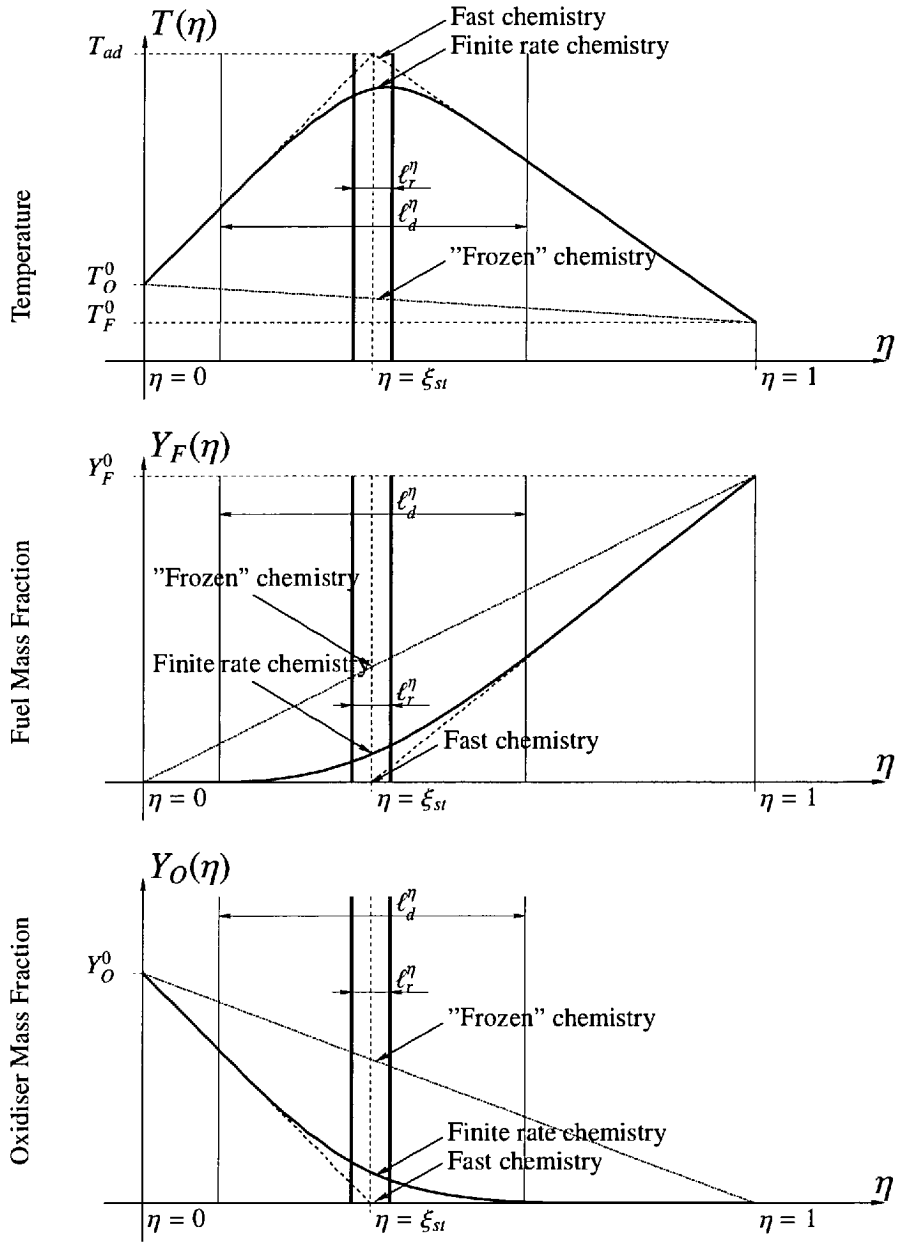

Figure 2.5: Distribution of temperature and reactants along the mixture fraction space.

$$\ell_d^\eta = |\nabla Z|_{st} \ell_d \,, \tag{2.51}$$

which is equivalent to expression (2.50), assuming that the diffusion thickness expands throughout the mixture fraction space, $\ell_d^\eta = 1$. The width of the reaction region ℓ_r depends on both the chemistry time scales and the scalar mixing. As mentioned

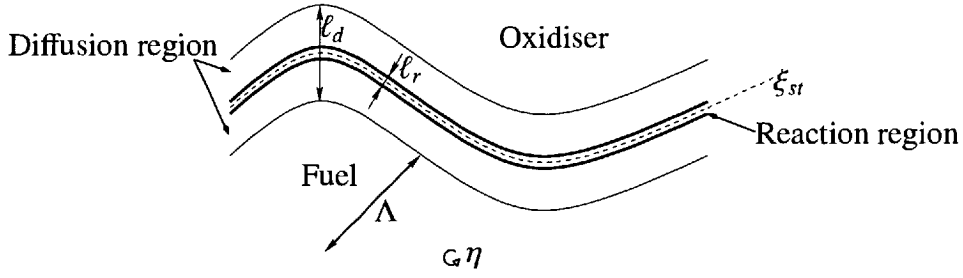

Figure 2.6: Diffusion and reaction lengths in a non premixed reaction zone.

above, the reaction region for a fast chemistry scenario is infinitensimaly thin, whereas the reactions occur in a confined area around the stoichiometric mixture fraction when the diffusion times become comparable to the chemistry time scales. The Damköhler number quantifies the ratio of the turbulent flow time scales τ_t to the chemistry time scales τ_r, i.e. $Da = \frac{\tau_t}{\tau_r}$. The inverse of scalar dissipation rate on the stoichiometric mixture fraction ξ_{st} is used for the definition of the flow or of the mechanical time scale τ_t for the turbulent mixing. The chemical time scale is often based on the inverse of maximum reaction rate. According to Liñan and Crespo [39] and Cuenot and Poinsot [40], the general formulation of the Damköhler number is,

$$Da = \frac{32\nu_F A^f s^{\nu_O} \rho^{\nu_O+\nu_F-1} s^{\nu_O}(1-\xi_{st})^2 \left(\frac{Y_F^0}{W_F}\right)^{\nu_F-1} \left(\frac{Y_O^0}{W_O}\right)^{\nu_O} \left(\frac{T_{ad}^2 C_p}{T_{ac} Q Y_F^0}\right) e^{-\frac{T_{ac}}{T_{ad}}}}{\frac{1}{\rho}\chi_{st}}, \qquad (2.52)$$

where the numerator in the above fraction is the maximum reaction rate for the specific reaction mechanism, calculated as the reaction rate for the stoichiometric mixture burning at adiabatic temperature. Simpler definitions of the Damköhler number use the pre-exponential factor to estimate the maximum reaction rate [41],

$$Da = \frac{A^f T_{ad}^b e^{-T_{ac}/T_{ad}}}{\frac{1}{\rho}\chi_{st}}, \qquad (2.53)$$

for the maximum temperature T_{ad}. Having defined the Damköhler number, the thickness of the reaction zone can then be determined as a fraction of the diffusive zone width [38],

$$\ell_r \sim \ell_d Da^{\frac{-1}{\nu_F+\nu_O+1}}, \tag{2.54}$$

for the simple one-step chemical mechanism (2.37).

2.5 Direct Numerical Simulation in CFD

The aim of Computational Fluid Dynamics is to predict the evolution of a flow field by the numerical integration of the governing equations, as they appear in section (2.1). The most straightforward approach to this problem is the Direct Numerical Simulation (DNS) where a direct numerical solution of the governing equations is carried out. This approach is common practice in laminar stationary flow fields. However, a turbulent flow field presents a great variety of scales which extend to much smaller length scales than the scales of the boundary conditions and the macroscopic characteristics of the flow. A simulation of a turbulent flow field must account for all the scales of turbulent fluctuations, thus the numerical discretisation must be smaller than the smallest turbulent scale. Following equation (2.26), the number of grid nodes in each direction is a function of the flow Reynolds number.

2.5.1 Computational cost of DNS

The computational cost of a DNS is proportional to the number of the mesh nodes used for the discretisation of the computational domain for the proper resolution of a turbulent flow field. Considering a cubic domain with edges of length $\mathcal{L}$, and an equally spaced discretisation with N nodes in each direction, the grid spacing in physical space Δx is simply $\mathcal{L}/N$. According to Pope [26], the mesh spacing Δx needed for resolving the smallest turbulent scales represented by a Kolmogorov length scale η is

$$\Delta x \approx 2.1\eta. \tag{2.55}$$

This formulation derives from the observation that the spectrum of the dissipation of energy, for wavenumbers of the fluctuations k bigger than $1.5/\eta$ [42, 43] reduce dramatically. Given that the corresponding length spacing in physical space for the

wavenumber k is π/k, equation (2.55) is formed. For a model free simulation of homogeneous isotropic turbulence the appropriate size of the computational domain is defined by the integral length scale. Pope states that the computational domain should be eight times the integral length scale. Following Pope [26], this constrain can be expressed as

$$\mathcal{L} \approx 8\Lambda \approx 3.6\ell_0 \,. \tag{2.56}$$

For the derivation of the above expression it has been assummed that in homogeneous isotropic turbulence of high Reynolds number the longitudinal integral scale asymptotically reaches a constant fraction of ℓ_0. This results in the following estimate for the number of nodes needed to resolve a turbulent flow field

$$N = \frac{\mathcal{L}}{\Delta x} \approx \frac{8\Lambda}{2.1\eta} \approx 1.6\frac{\ell_0}{\eta} = 1.6Re_0^{3/4} \,. \tag{2.57}$$

Another estimate for the required total number of nodes in three dimensions is provided by Reynolds [44] and Givi [45],

$$N^3 \approx 0.1Re_\lambda^{9/2} \,, \tag{2.58}$$

and is based on the Taylor Reynolds number. Using the relation $Re_0 \sim \frac{3}{20}Re_\lambda^2$ between Re_λ and the turbulent Reynolds number Re_0, rule (2.57) can be expressed as,

$$N^3 \approx 0.06Re_\lambda^{9/2} \,. \tag{2.59}$$

Although both rules are estimates of the resolution requirements for a DNS calculation, a comparison of the two rules (2.58) and (2.59) shows that (2.59) is stricter.

The total number of nodes $N^3 \sim 0.06Re_\lambda^{9/2}$ defines the memory requirements of a three-dimensional DNS simulation. The time needed for a DNS calculation depends on the number of time steps M required for the integration of the governing equations. A typical duration, for a DNS of homogeneous isotropic turbulence, varies from three to four τ, where τ is the eddy-turnover time. This observation can provide an estimate of the total computational time depending on the Courant number. The Courant num-

ber formulation constrains the computational time step Δt so that each fluid element will move only a fraction of the grid spacing each time step. Several formulations of this constrain have been proposed for DNS [26]. An expression can be based on the turbulent kinetic energy

$$\frac{\Delta t k^{1/2}}{\Delta x} = \frac{1}{20}, \tag{2.60}$$

or the turbulent time scale τ_η,

$$\frac{\Delta t}{\tau_\eta} = \frac{1}{10}. \tag{2.61}$$

The number of time steps M needed for a duration of four eddy-turnover times, is

$$M \sim 9.2 Re_\lambda^{3/2}, \tag{2.62}$$

or alternatively, following equation (2.61),

$$M \sim 15.5 Re_\lambda. \tag{2.63}$$

From the above analysis it is evident that there is a steep increase of the computational power demands with increasing turbulent Reynolds number. Furthermore, the primary aim of DNS calculations is to investigate real life turbulence in order to facilitate the research on turbulence modelling. Flows in real life applications are highly turbulent, making the effort to apply DNS to realistic turbulent flow regimes a computationally challenging task. In order to succeed in shifting the field of DNS research from low Reynolds turbulence to the simulation of more realistic cases, a DNS calculation should be set up in a such way that makes most of the computational power available and to achieve the highest Reynolds number possible. This relation between turbulent Reynolds number and the corresponding computational cost is presented in table (2.1) adapted from Pope [26].

This table shows three numerical examples of the analysis presented in this section for the computational cost of DNS. The CPU time, is estimated assuming 1000 operations for each node and each time step. The presumed processor is able of

Table 2.1: Estimations of CPU time, memory, and number of nodes for a DNS, as a function of the turbulent Reynolds number.

Re_λ	Re_0	N	N^3	M	N^3M	CPU time	Memory allocation
30	135	64	$2.3 \cdot 10^5$	$1.5 \cdot 10^3$	$4.0 \cdot 10^8$	$10m$	$6Mbytes$
120	2145	512	$1.3 \cdot 10^8$	$1.2 \cdot 10^4$	$1.6 \cdot 10^{12}$	$20days$	$3Gbytes$
478	34325	4,096	$6.8 \cdot 10^{10}$	$9.6 \cdot 10^4$	$6.6 \cdot 10^{15}$	$200years$	$1.5Tbytes$

1 *GigaFLOPS* (Floating Operations Per Second), a number close to the capabilities of modern processors assuming double precision numerics. For the memory allocation, double precision is also assumed, and refers to the three components of the velocity field, thus 3×8 bytes per node. It must be mentioned that table (2.1) accounts for the integration of the momentum equation only. Depending on the numerical method used, the flow field is stored in the computer memory for more than one time, and the computational demands shown in table (2.1) are expected to be higher, for example accounting for the previous and the current time step, pressure terms or spatial derivatives.

As it will be seen in the next section, the characteristics of the DNS presented in literature deviate from the values provided in the table 2.1. It must be noted that the information of this table is indicative of the computational costs involved in the DNS of turbulent flows and of their dependence to the turbulent Reynolds number. Given that these values are theoretical estimates, the resolution of a DNS simulations is assessed by the analysis of the statistics of the final solutions. In addition, numerical techniques like the forcing of the large scales, that models the effect of the energy containing scales, relax the constrains for the upper limit of the spatial resolution of DNS simulations. On the other hand, DNS of flows other than the homogeneous isotropic turbulence have special characteristics such as the total time of the simulation, which may be significantly larger, and cause divergence from the theoretical analysis provided in this section.

2.5.2 Review of DNS

Given that the computational cost in terms of both CPU-time and memory allocation is the bottleneck of DNS, an efficient and accurate algorithm is needed. Such a choice makes most of the memory used, and the accuracy leads to bigger time steps reducing the computational time. Spectral algorithms were the only choice of CFD engineers for DNS applications until the mid nineties. They offered a reduced need for memory allocation and permitted larger time steps compared to a finite differences code [45].

The numerical methods that have been proposed in DNS have to deal with four main features: the spatial representation and approximation of the spatial derivatives; the treatment of the boundary conditions; the time evolution algorithm; and the technical part of the computer implementation. The features mentioned above refer to the treatment of the velocity field of the a turbulent flow. However, a numerical simulation can be enhanced to include other phenomena which interact with turbulence. as is the case with DNS of pollutants transport, flames , and two phase flows.

The foundations of DNS were laid in the late sixties when a simulation of decaying isotropic and homogeneous turbulence in a box was carried out by Orszag and Patterson [46, 47]. This first simulation was also the first implementation of a Galerkin spectral algorithm for the integration of the Navier-Stokes equations. The calculations were performed on a CDC 6000 computer, allowing a realistic simulation of a homogeneous isotropic turbulent flow field with a maximum Taylor scale Reynolds number of about $\lambda_T = 35$ on a computational mesh consisting of a cube with 32 nodes in each direction [45]. After this first stage there was a steady increase of the number of grid nodes and consequently simulations of higher turbulent Reynolds numbers aided by an equivalent increase of computational power. By the early eighties, calculations using 64^3 nodes for homogeneous isotropic turbulence had become common, starting with Patterson and Siggia in 1981, [48] and then Brachet *et* al. in 1983 [49] and Kida and Murakami in 1987 [50]. During this period, the next big step in DNS after Orszag was taken by Rogallo in 1981. Rogallo's study examined the effects of mean shear, irrotational strain, and rotation on homogeneous turbulence and compared simulations with theory and experimental data. The algorithm used by Rogallo was an extension of the Orszag and Patterson spectral method, combined with a transformation of the govern-

ing equations. Subsequent DNS have essentially been based on Roggalo's algorithm [51], including the code utilised in this study. At that time Rogallo [52] and later Kerr [42] had performed numerous 128^3 simulations. A flow Reynolds number simulation of $Re = 3000$ had been achieved by Brachet *et* al. [49] at as early as 1983. However this was achieved by exploiting the symmetries of the Taylor-Green vortex reaching to an effective but not actual resolution of 256^3 nodes. A DNS with an actual resolution of 256^3 nodes was carried out by Vincent and Meneguzzi in 1991 [53]. The increase of the computational power made available to researchers induced the next step of bigger simulations with 512^3 nodes, from Chen [54], Jimenez [55, 56, 57] and Meneguzzi [53] in the mid-nineties. The codes used for homogeneous isotropic turbulence were, following Rogallo, all pseudospectral, with periodic boundary conditions and a low storage Runge-Kutta algorithm for the integration time [58]. In the mid-eighties the primary goal of researchers was the investigation of the inertial range of turbulence. The inertial scale had been established experimentally, but for Reynolds numbers not less than 10,000. Seeking to establish a subrange, researchers were directed to the technique of the external forcing of the low wavenumbers [59]. The energy provided to the large scales allowed the evolution of the smaller scales before they dissipate, leading to a developed inertial subrange. One should note the contrast to LES where the large scales are simulated and the small scales are modelled. In forced DNS the small scales are directly simulated, while the energy cascade from the large scales is modelled with the forcing [51].

During the next decade, DNS computations that incorporate meshes of large sizes have been witnessed. Fukayama and Gotoh carried out homogeneous turbulence simulations on a mesh of 1024^3 nodes and Taylor Reynolds numbers between of 38 and 478. The results were published in 2000, and among other conclusions the inertia subrange was established and the universality of the fluctuations was discussed [60]. The biggest simulation of homogeneous isotropic turbulence was announced by Kaneda *et* al. [61]. The mesh used is the finest resolution ever used reaching to up to 4096^3 nodes. The Earth Simulator supercomputer was employed for this task.

The increase of the computational power not only lead to an increase of the size of the meshes employed, but also caused an enrichment of the variety of the turbulence

phenomena studied with DNS. As a result DNS has evolved from the computation of homogeneous isotropic turbulence for relatively small Reynolds numbers to turbulent flows of more complicated geometries such as boundary layers and wall interactions, jets and mixing layers. Furthermore, researchers have started studying interactions between turbulence and other phenomena as species transport, compressible flows or combustion.

During the seventies the computational power available did not allow DNS of wall bounded flows; however, coarse grid computations of free-shear layers were available at the end of the decade [62]. The simplest wall bounded flow and also the first to be studied with DNS was the plane channel flow by Mosser and Moin [63], and Kim *et* al. [64]. These turbulent flows presented at least one homogeneous direction. This setup makes the use of periodic boundary conditions, possible. Later advances in the development of inflow boundary conditions led to DNS of flows with more complicated geometries. Such examples are either the backward facing step simulation of Le and Moin [65], or the turbulent boundary layer with an adverse pressure gradient and separation of Na and Moin [66].

DNS of mixing layers and scalar mixing have been widely used for the study of in-homogeneous turbulence [67, 68, 69] featuring a three-dimensional mesh of maximum $128 \times 128 \times 257$ nodes. The DNS of Rogers *et* al. [70, 71] was the first three-dimensional simulation with adequate resolution of the turbulent scales. The Reynolds number based on the momentum thickness was $Re_\delta = 500$. However, the scope of this simulation was the study of the instability mechanism leading to transition, rather than the developed turbulence itself. A more detailed simulation of Rogers and Moser [72] involved the study of the inhomogeneous turbulent flow field induced by a mixing layer. A Galerkin spectral methodology was utilised for the integration of the governing equations on a mesh of $512 \times 210 \times 192$ spectral nodes. In addition to the simulation of momentum transport, the evolution of a passive scalar with unity Schmidt number was also simulated. The boundary conditions were periodic in the streamwise direction, leading to a temporal evolving shear layer. Another DNS of a spatially evolving mixing layers had been utilised for deriving tools for LES [73].

Other examples of fundamental shear flows simulated with DNS are wakes and

planar or cylindrical jets. A DNS setup closer to the mixing layer rather than the classical cylindrical jet is the planar jet, incorporating two parallel shear layers. A temporal evolving planar jet simulation, characterised by a bulk Reynolds number of $Re_D = 6800$, was used for the derivation and assessment of a turbulent viscosity dynamic model, carried out by Akhavan *et* al. [74]. The discretisation used involved 128 Chebysev nodes in the transverse direction, whereas 128×258 Fourier nodes where used in the spanwise and streamwise directions. The DNS results where evaluated and compared with the planar jet experiments of Wygnanski and Fiedler [75]. Results from the planar jet DNS of Klein *et* al. [76] were published in 2003. The orifice Reynolds number for this simulation ranges from 1000 to 6000, and the Navier-Stokes equations were integrated on a mesh of $360 \times 128 \times 512$ grid points. The jet was spatially evolving, and the effect of inlet boundary conditions was assessed. A laborious DNS of a spatially evolving planar jet was undertaken by Stanley *et* al. [77] with an flow Reynolds number of 3000 providing comparisons with equivalent experimental results.

An original DNS setup of an inhomogeneous mixing layer is the simulation of Knaepen *et* al. [78]. This simulation deals with scalar mixing in stratified turbulence, where the flow is a shear free mixing layer characterised by a zero mean streamwise velocity. DNS of circular jets were carried out by Brachet in the mid-nineties [79] where the vortex induction in circular jets was studied. In addition, other simulations of circular jets were the DNS of Verzicco with a orifice Reynolds number of $Re_D = 1500$ on a cylindrical mesh of $48 \times 128 \times 128$ [80] and the similar setup of Mathew and Basu [81].

As mentioned above, DNS, apart of more complicated geometries, has also been extended to cover the study of the interaction between turbulence and other phenomena. The study of the effect of compressibility on turbulence was initiated with DNS of homogeneous isotropic turbulence by Feiereisen in 1981 [82], whereas buoyancy generated turbulence, was simulated by Girimaji in 1997 [83]. The interactions between turbulence and reactive scalars, transported in a turbulent flow field, are of great interest for combustion modelling. The understanding of these interactions is expected to provide better predictions and more precise modelling of combusting systems. Since the mid-eighties DNS has played a significant role in studying the structure of flames.

Reactive flows present a major difficulty for the full resolution of all the scales of the combined turbulence-combustion problem. A complete DNS solution for practical devices, is not possible and modelling methodologies, such as RANS and LES, are utilised instead. However, the need of DNS simulations that will provide the simultaneous spatial structure of a flame has led to DNS of artificial turbulent flames [38] incorporating various levels of assumptions [20]. Such flames are test cases set up in such a way that the range of scales, from macroscopic to Kolmogorov and flame thickness, are all resolved. Starting with the first attempt of Hill in 1979 [45], there has been a long list of researchers who carried out DNS of turbulent flames.

The assumptions employed in combustion DNS deal with the modelling of density variations, the range of the Lewis numbers among the reactants, the dependence of the diffusivity coefficients and the viscosity of the mixture on temperature variations and, finally, the simplified chemistry mechanisms involved.

Most of the DNS of pure mixing and scalar transport use incompressible constant density formulations. In DNS, the modelling of flame density variations may be omitted in cases of minimal heat release. Such an assumption is valid in the case of a fuel diluted in a passive gas as described by Mell [84]. The next step is the low Mach number assumption where the density depends solely on temperature. Finally, a fully compressible code can be used in DNS, leading to long computational times due to the CFL restrictions for the time advancement.

The chemical kinetics mechanism determines the number of species to be solved, having a direct effect on the computational cost of the simulation. It is claimed that a realistic computation requires at least twenty species for the modelling of hydrocarbon oxidisation [36]. The numerical issues arising from a such complicated chemistry mechanism lead to a prohibitive computational cost.

The flow field chosen for combustion DNS may vary from homogeneous isotropic turbulence case to more complicated inhomogeneous cases, mirroring the variety of DNS simulations for non-reacting flows. Jets and mixing layers can be treated either as time evolving with periodic boundary conditions or as spatially evolving where the inlet boundary conditions should be treated accordingly. For spatially evolving simulations significant difficulties arise for the treatment of the inlet boundary conditions

which should be precise solutions of the Navier-Stokes equations [85]. An example of a Lagrangian DNS of a mixing layer was the simulation of de Bruyn Kops *et* al. [86] where a parallel pseudospectral code had been used for a mesh of $512 \times 512 \times 1024$ nodes and the flame was modelled with a single step reaction mechanism. The first effort to model an reacting inhomogeneous turbulent flow, was the reacting mixing layer DNS of Riley *et* al. [87]. The chemistry was also modelled using a single step mechanism and negligible heat release was assumed. This, combined with a low Mach number assumption, led to constant density, viscosity, and diffusion coefficients. The low resolution of the simulation with the finest grid reaching $64 \times 64 \times 64$ did not allow the computations to develop further than the transitional period. Pantano [88] performed a DNS simulation that deals with a reacting inhomogeneous flow involving relatively few assumptions. The flow field was a spatially evolving planar jet. The flow Reynolds number was $Re_D = 3000$ and the mesh utilised consists of $1024 \times 512 \times 192$ nodes in the streamwise, transverse, and spanwise, directions respectively. The inflow boundary conditions were artificially synthesised with a procedure described by Stanley [77]. The heat release was not negligible and the density variations due to temperature are treated using a fully compressible algorithm. The fuel consists of methane and the chemistry mechanism employed accounts for eight species in total, i.e. two final products, three intermediate species, one passive scalar, the oxidiser and the fuel. Furthermore, the Lewis number vary for each species, and both diffusivity and viscosity change with temperature. A temporal configuration of a planar jet of a CO/H_2 flame had been simulated by Hawkes *et* al. [89]. The chemical mechanism utilised is incorporating eleven species, thus being able to account for extinction and re-ignition. The flow field is integrated by a fully compressible CFD code and the numerical resolution can handle flow Reynolds numbers from 2510 to 9079. An explicit differentiation scheme based on 8th-order finite difference had been used while a fourth order Runge-Kutta is utilised for the time advancement.

One way of drastically reducing the computational cost in a DNS is to perform two dimensional computations [90]. Such an approach sacrifices the realistic simulation of the three dimensional turbulent structure, but, on the other hand, it allows detailed chemistry mechanisms. Depending on the priorities and the nature of the study, two

dimensional simulations have been proved quite useful for the parametric analysis for turbulent combustion modelling.

Premixed flames have also been studied with DNS. A detailed literature review of the simulations carried out for premixed flames can be found in the book of Poinsot and Veynante [20].

2.6 Modelling methodologies for turbulence in CFD

In the previous section it became clear that the computational cost of a direct simulation of a real life turbulent flow is prohibitive. The need for numerical simulations of turbulent flows with high Reynolds number in complicated geometries had led to modelling methodologies such as the Reynolds Averaged Navier-Stokes simulations (RANS) or the more demanding Large Eddy Simulation (LES). Both approaches are based on the idea of solving for either an averaged or a filtered turbulent flow field. Such a flow field contains less information and its variables exhibit a much smaller range of turbulent scales compared to the unfiltered and instantaneous values found in the governing equations.

2.6.1 Reynolds Averaged Navier-Stokes equations (RANS)

One way to reduce the resolution requirements for the integration of the governing equations of a turbulent flow field is to apply a time averaging operation on the velocity and the scalar field. This averaging operator $\langle\cdot\rangle$ for the field variable $f(\boldsymbol{x};t)$, is defined as

$$\langle f\rangle(\boldsymbol{x}) = \lim_{\Delta t\to\infty}\frac{1}{\Delta t}\int_{t_0}^{t_0+\Delta t} f(\boldsymbol{x};t)dt\,, \tag{2.64}$$

where (2.64) is the Reynolds average of the turbulent field variable, while the operation itself is the Reynolds averaging operation. In the present study the brackets are used to denote Reynolds averaging in order to avoid confusion with the filtering operation introduced in the next section for the LES methodology. For a statistically stationary flow field, $\langle f\rangle(\boldsymbol{x})$ is expected to be independent of time. The properties of

the Reynolds averaging operator can be easily derived from (2.64) and be summarised as

$$\begin{aligned} \langle a \rangle &= a \\ \langle aF \rangle &= a\langle F \rangle \\ \langle F + G \rangle &= \langle F \rangle + \langle G \rangle \\ \langle \langle F \rangle \rangle &= \langle F \rangle \\ \langle \langle F \rangle G \rangle &= \langle F \rangle \langle G \rangle \\ \langle \frac{dF}{dx} \rangle &= \frac{d\langle F \rangle}{dx} \end{aligned} , \tag{2.65}$$

where F and G are random variables, whereas a denotes a constant parameter.

The RANS equations can be derived by applying the averaging operator to the Navier-Stokes equations (2.2) and making use of the averaging operator properties (2.65)

$$\frac{\partial \langle \rho \rangle \langle \widetilde{u_j} \rangle}{\partial t} + \frac{\partial (\langle \rho \rangle \langle \widetilde{u_i} \rangle \langle \widetilde{u_j} \rangle)}{\partial x_i} = -\frac{\partial \langle p \rangle}{\partial x_j} + \frac{\partial \langle \tau \rangle_{ij}}{\partial x_i} - \frac{\partial \langle \rho \rangle (\langle \widetilde{u_i u_j} \rangle - \langle \widetilde{u_i} \rangle \langle \widetilde{u_j} \rangle)}{\partial x_i} \quad \text{for } j = 1, 2, 3 , \tag{2.66}$$

where $\langle \tau_{ij} \rangle$ is the averaged viscous stress tensor provided by the equation (2.3). The operator $\langle \widetilde{\cdot} \rangle$ is the Favre average [91], introduced for variable density flows and is defined as

$$\langle \widetilde{f} \rangle = \frac{\langle \rho f \rangle}{\langle \rho \rangle} , \tag{2.67}$$

which reduces to the Reynolds average operator $\langle \cdot \rangle$, if constant density is assumed. Here it must be noted that the notations of the Reynolds averaging and the Favre averaging operators are not the common notations found in RANS literature. However, these averaging operations are incorporated in this study in order to avoid any confusion with the equivalent LES filtering operations which is dealt with in the next section.

The average of the velocity product $\langle u_i u_j \rangle$ that appears in equation (2.66) is a part of the Reynolds stresses, $\langle \widetilde{u_i' u_j'} \rangle = \langle \widetilde{u_i u_j} \rangle - \langle \widetilde{u_i} \rangle \langle \widetilde{u_j} \rangle$, which expresses the dissipation of turbulent kinetic energy due to turbulent fluctuations. This term remains unclosed and its closure is the aim of RANS modelling. This is a task of enormous complexity,

given that all the scales of the turbulent flow field, from the highly anisotropic inertial scales to the smallest more uniform scales remain unmodeled and have to be captured by the models employed. RANS modelling remains a successful methodology for the simulation of turbulent reactive flows and has been the subject of a vast literature [92]. In comparison to DNS the computational cost of RANS is much smaller, given that the resolution requirements are more relaxed for the averaged flow field, and, the flow field may be treated as stationary. In addition, taking advantages of the symmetries of the flow, the flow field can also be simulated with two-dimensional computations. According to Jones [92] the inadequacies of RANS modelling stems from the implicit attempt to parametrise all the scales of the turbulence energy spectrum using a single length scale and a single time scale.

2.6.2 Large Eddy Simulation

A new approach to the problem of simulating turbulent flows has come to the fore during the past four decades. It aims to improve the description of turbulent scales based on the ideas of scale separation. The large turbulent scales are strongly affected by the macroscopic characteristics of the specific flow. Specifically, these scales are governed by the interaction with walls, boundaries, recirculation regions and shear layers, thus making it very difficult to derive a global model which could describe them. On the other hand, the smaller scales, according to Kolmogorov's ideas, are characterised by a universal structure making them ideal for parametrisation. Large Eddy Simulation (LES) is based on the idea of directly solving the bigger scales while providing models for the effect of the smallest dissipative scales on the flow. This can be achieved by applying a spatial filter which cuts off the turbulent scales with small wavenumbers, and then solving the governing equations for the time dependent problem of the filtered flow field. The effect of the smaller scales enters the filtered equations in the form of unclosed terms. However, because of their global character, their modelling is expected to be simpler.

The computational cost is much bigger compared to the equivalent cost for the RANS methodology. Some part of the turbulence spectrum is solved for, making LES strictly time dependant, even for statistically stationary fields. The symmetries of the

boundary conditions or of the macroscopic problem cannot be exploited, ever since the large scales may exhibit non symmetric instabilities. Finally, taking into account that the large scales are highly three-dimensional, two-dimensional LES is simply inaccurate. However, because the small scales comprise most of the range in a turbulent spectrum, their modelling leads to significant savings in the computational cost when compared to DNS.

In contrast to RANS time averaging, LES filtering is applied in space rather than in time. The governing equations for LES are derived by applying the filtering operator $\bar{\cdot}$ to the Navier-Stokes equations. The spatial filtering for a variable of a turbulent field, $f(\boldsymbol{x};t)$, is expressed as its convolution with a filter function G [93],

$$\overline{f(\boldsymbol{x_0};t)} = \int_{x\in V} G(\boldsymbol{x_0}-\boldsymbol{x},\Delta(\boldsymbol{x_0}))f(\boldsymbol{x};t)dV\ . \tag{2.68}$$

The integration is applied for the whole flow field denoted by, the volume, V. The filter function $G(\boldsymbol{x_0}-\boldsymbol{x},\Delta(\boldsymbol{x_0}))$ is normalised in a such way that its integral equals to unity,

$$\int_{x\in V} G(\boldsymbol{x_0}-\boldsymbol{x},\Delta(\boldsymbol{x_0}))dV = 1\ \forall \boldsymbol{x_0}\in V\ . \tag{2.69}$$

The parameter Δ is the filter width, which may vary in space. Usually the filter function is defined as a product of three one-dimensional filters,

$$G(\boldsymbol{r},\Delta) = \prod_{i=1}^{3} G_i(r_i;\Delta_i(x_i))\ . \tag{2.70}$$

The filter width is the length scale that separates the large from the smallest scales. Applying a filtering operation with filter width Δ will smoothen the flow field by cutting off the small scales with wave number smaller than π/Δ, while having a negligible effect to the large scales. Given that the turbulent scales appear in the turbulent kinetic energy spectrum, the effect of the filtering operation can be investigated in spectral space. The Fourier transform of the filtered field f, for wavenumber κ is,

$$\hat{\bar{f}}(\kappa) = \frac{1}{2\pi}\hat{G}(\kappa)\hat{f}(\kappa)\ , \tag{2.71}$$

Table 2.2: LES filter functions [26].

Filter	Filter function $G(r)$	Transfer function $\frac{1}{2\pi}\hat{G}(\kappa)$
Box	$\frac{1}{\Delta}H(\frac{1}{2}\Delta - \lvert r\rvert)$	$\frac{\sin(\frac{1}{2}\kappa\Delta)}{\frac{1}{2}\kappa\Delta}$
Gaussian	$\left(\frac{6}{\pi\Delta^2}\right)^{\frac{1}{2}} e^{-\frac{6r^2}{\Delta^2}}$	$e^{-\frac{\kappa^2\Delta^2}{24}}$
Sharp spectral	$\frac{sin(\frac{\pi r}{\Delta})}{\pi r}$	$H(\frac{\pi}{\Delta} - \lvert\kappa\rvert)$

making use of the convolution identity for the Fourier transform. The "hat" symbol denotes the Fourier transform. The expression $\frac{1}{2\pi}\hat{G}(\kappa)$ is the transfer function of the filtering operation. In spectral space, the filter width corresponds to a critical wavenumber $\kappa_c = \frac{\pi}{\Delta}$. The shape of the filtering function is not strictly defined, however, there are three types of filters which are commonly used: the spectral cutoff, the Gaussian and the spatial box filter. The details of the three LES filters are shown in table (2.2), where $H(r)$ is the step function being zero for negative values and unity for positive values.

The spectral cutoff filter eliminates all the eddies with wavenumbers bigger than the one corresponding to the filter width Δ while the box filter simply averages the field values within a box of width Δ. Figure 2.7 shows the shapes of the three, one-dimensional filter functions in physical space and the corresponding transfer functions.

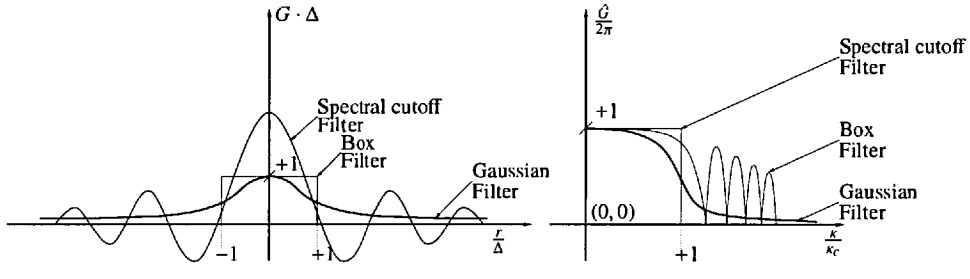

Figure 2.7: The shapes of the filtering functions and the transfer functions.

The derivation of the LES governing equations is based on the mathematical properties of the filtering. The rules for manipulating the filtering operator can be easily proven using the definition (2.68), the properties of the filtering operator are:

$$\begin{aligned} \overline{a} &= a \\ \overline{aF} &= a\overline{F} \\ \overline{F+G} &= \overline{F}+\overline{G} \\ \overline{\frac{dF}{dt}} &= \frac{d\overline{F}}{dt}\,, \end{aligned} \tag{2.72}$$

for the constant value a, the field variables $F(\boldsymbol{x};t)$ and $G(\boldsymbol{x};t)$

The above properties are also valid for the RANS averaging operator. However, not all properties of RANS averaging are valid for LES, i.e.,

$$\begin{aligned} \overline{\overline{F}} &\neq \overline{F} \\ \overline{\overline{F}G} &\neq \overline{FG} \\ \overline{\frac{dF}{dx}} &\neq \frac{d\overline{F}}{dx} \end{aligned} \quad . \tag{2.73}$$

In general, as seen in the set on inequalities (2.73), filtering does not commute with the spatial derivative. In fact, the spatial derivative of a field variable is found to be,

$$\frac{d\overline{F}}{dx_i} = \overline{\frac{\partial F}{\partial x_i}} + \int F(\boldsymbol{x}-\boldsymbol{r};t)\frac{\partial G(\boldsymbol{x}-\boldsymbol{r};t)}{\partial x_i}d\boldsymbol{r}\,. \tag{2.74}$$

However, if a homogeneous filter function is used, i.e. $\frac{\partial G(x-r;t)}{\partial x_i} = 0$, which does not change within the flow field, then the integral on the r.h.s. of equation (2.74) becomes equal to zero and the spatial derivatives commute with spatial differentiation. Taking into account that LES is generally used for inhomogeneous turbulent flows, it is common to use a filter width that follows the length scales of turbulence, and varies along the domain. In such a realisation the filter width should vary modestly in space to keep the commutation error to a minimum [93].

An alternative way of filtering has been derived in order to deal with variable density flows. In turbulent reacting flows such as flames, large density variations occur and must be accounted for. Conventional filters lead to an explicit treatment for the sub-grid terms arising from the density fluctuations. In response to this problem the

fluctuations are weighted with the local density,

$$\widetilde{f}(\boldsymbol{x};t) = \frac{\overline{\rho f}}{\overline{\rho}} \,. \tag{2.75}$$

The filter introduced by equation (2.75) is known as Favre filtering. For constant density flows, Favre filtering becomes identical to the simple filter, shown in equation (2.68). Imposing the filtering operation on the Navier-Stokes equations (2.2), making use of the filtering operator properties listed in equation (2.72) and assuming the commutation with spatial derivatives, equation (2.74), the momentum transport for a filtered flow field can be expressed as

$$\frac{\partial \bar{\rho}\widetilde{u}_j}{\partial t} + \frac{\partial(\bar{\rho}\widetilde{u}_i\widetilde{u}_j)}{\partial x_i} = -\frac{\partial \bar{p}}{\partial x_j} + \frac{\partial \bar{\tau}_{ij}}{\partial x_i} - \frac{\partial \bar{\rho}(\widetilde{u_i u_j} - \widetilde{u}_i\widetilde{u}_j)}{\partial x_i} \quad \text{for } j = 1,2,3 \,. \tag{2.76}$$

The same procedure is followed for the transport equations of any scalar field subject to turbulence. Following the same rules as for the Navier-Stokes equations, the transport equations for the filtered mass fractions of the reacting species can be derived by filtering the species transport equations (2.7) and can then be expressed as,

$$\frac{\partial \bar{\rho}\widetilde{Y}_k}{\partial t} + \frac{\partial}{\partial x_i}(\bar{\rho}\widetilde{u}_i\widetilde{Y}_k) = \frac{\partial}{\partial x_i}\left[\overline{V_{k,i}Y_k} - \bar{\rho}\left(\widetilde{u_i Y_k} - \widetilde{u}_i\widetilde{Y}_k\right)\right] + \overline{\omega}_k \quad for \quad k = 1,N \,. \tag{2.77}$$

Using the same procedure, the mixture fraction and enthalpy transport equations can be written as

$$\frac{\partial \bar{\rho}\widetilde{\xi}}{\partial t} + \frac{\partial}{\partial x_i}(\bar{\rho}\widetilde{u}_i\widetilde{\xi}) = \frac{\partial}{\partial x_i}\left[\overline{V_{k,i}\xi} - \bar{\rho}\left(\widetilde{u_i\xi} - \widetilde{u}_i\widetilde{\xi}\right)\right] \,, \tag{2.78}$$

and,

$$\frac{\partial \bar{\rho}\widetilde{h}}{\partial t} + \frac{\partial}{\partial x_i}(\bar{\rho}\widetilde{u}_i\widetilde{h}) = \frac{\partial \bar{p}}{\partial t} + \overline{u_i\frac{\partial p}{\partial x_i}} + \frac{\partial}{\partial x_i}\left[\overline{\lambda\frac{\partial T}{\partial x_i}} - \bar{\rho}\left(\widetilde{u_i h} - \widetilde{u}_i\widetilde{h}\right)\right] + \overline{\tau_{ij}\frac{\partial u_i}{\partial x_j}} - \frac{\partial}{\partial x_i}\left(\overline{\rho\sum_{k=1}^{N} V_{k,i}Y_k h_k}\right) \tag{2.79}$$

The above set of equations (2.76) to (2.79) is used to describe the evolution of the LES filtered flow fields in turbulent combustion. However, due to the filtering operation, new unclosed terms have appeared. These terms account for the effect of the small scales of turbulence on the flow field. In LES, the unclosed terms are known as unresolved or sub-grid scales. Although the grid size in a LES simulation is not directly connected to the filtered width which separates the resolved from the unresolved scales, the term "sub-grid" is commonly used in LES literature. The closure of the unresolved terms is the subject of the LES sub-grid scale modelling.

In the previous description of the LES approach no reference has been made to the discretisation for the numerical solution of equations (2.76) to (2.79). Having assumed that the LES solution should directly account for all scales larger than Δ, the discretisation should employ a grid spacing smaller or equal to Δ. Following Deardorff [94] the grid spacing is quantified by a characteristic length based on the volume of the computational cell $(\Delta x_1 \Delta x_2 \Delta x_3)^{1/3}$. The usual practice is to keep the grid spacing equal to the separation length Δ, therefore keeping computational cost to a minimum. As a result, the grid spacing and the filter width are practically treated as identical entities. It can be stated that a LES numerical representation is accomplished in two stages, at first, the filter is applied and secondly a discretisation is supposed, making sure that the length scales of the filtered flow field are fully resolved. Figure 2.8 depicts the effect of the filtering operation on a fluctuating variable. The filtered field is defined continously across the one-dimensional space. Ideally the discretisation of the flow field should be such that 80% of the energy fluctuations are resolved [95, 96, 26]. However, the equations (2.76) to (2.79) are accurate for the filtered values $\overline{f(x)}$ which are defined continously across the field. Inevitably, the commutation of the spatial derivatives with the filtering operator is affected by the discretisation error introduced by expressing the filtered field with a finite number of values on a grid [93].

2.7 Sub grid scale modelling in LES

The unresolved Reynolds stresses $\tau_{ij}^{u} = -\rho(\widetilde{u_i u_j} - \widetilde{u}_i \widetilde{u}_j)$ appear in the momentum transport equation of the LES filtered field (2.76), and need closure. The name "stress"

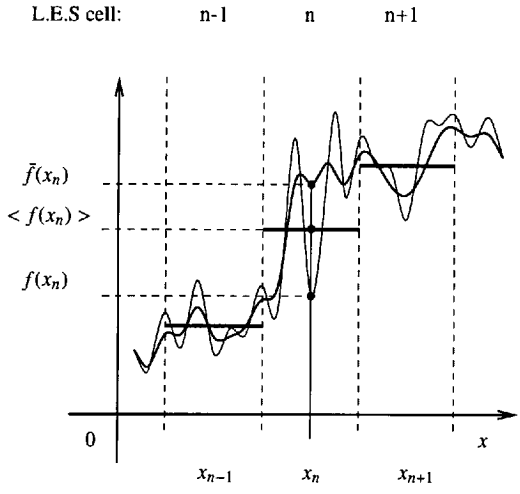

Figure 2.8: The filtering and the discretisation of a fluctuating quantity on one dimension

stems from the way τ_{ij}^u is treated in LES modelling rather than from its physical nature [20]. Reynolds stresses express the momentum flux due to the small eddies. The earliest and most commonly used model for the closure of the Reynolds stresses is the Smagorinsky model [97]. The Smagorinsky model belongs to the "family" of eddy viscosity models. In this family of models the effect of the unresolved Reynolds stress is described by an increase of the fluid viscosity due to the sub-grid turbulent motion, and for a constant density simulation it is expressed as,

$$\tau_{ij}^u - \frac{1}{3}\tau_{kk}^u \delta_{ij} = \mu_t \left(\frac{\partial \widetilde{u}_i}{\partial x_j} + \frac{\partial \widetilde{u}_j}{\partial x_i} - \frac{2}{3}\delta_{ij}\frac{\partial \widetilde{u}_k}{\partial x_k} \right) = 2\mu_t \left(\widetilde{S}_{ij} - \frac{1}{3}\widetilde{S}_{kk} \right) . \tag{2.80}$$

The above expression is common for all the eddy viscosity models introduced by Boussinesq [22, 98]. The parameter $\mu_t = \rho \nu_t$ is the turbulent viscosity, a quantity introduced to model the effects of the small scale eddies as a virtual increase of the viscosity. Prandtl's formulation provides an approximation of the kinematic eddy viscosity [22] as:

$$\mu_t \sim \rho \ell \mathcal{U} . \tag{2.81}$$

where $\mathcal{U}$ and ℓ are a velocity and a length scale respectively. The integral length scale is chosen for eddy viscosity models and the filter width Δ is mainly taken as a

measure of the representative length scale ℓ in LES [94]. For the characteristic velocity $\mathcal{U}$ the turbulent kinetic energy of the fluctuations is used and $\mathcal{U}$ is approximated by $\mathcal{U} \sim \sqrt{\frac{2}{3}k_{SGS}}$. The term k_{SGS} in a LES context is a measure of the turbulent kinetic energy of the sub-grid fluctuations, and is directly related to the trace of the Reynolds stress tensor, $k_{SGS} = \frac{1}{2}\widetilde{u_k u_k} - \frac{1}{2}\tilde{u}_k\tilde{u}_k\frac{2}{\rho}\tau^u_{kk}$. Thus, the turbulent viscosity can be expressed as $\mu_t = C\rho\Delta\sqrt{k_{SGS}}$, introducing a proportionality coefficient C.

Solving a transport equation for the sub-grid kinetic energy has been practised in LES [99], however, it has been commented that it is against the "philosophy" of the LES methodology. Such an approach increases the already significant computational cost, but it does not exploit the benefits of LES modelling, where only the small sub-grid scales are left unresolved [32]. The Smagorinsky model is a zero equation model based on the assumption that the energy provided to the small scales is equal to the dissipation of energy to heat. The *"production equals dissipation"* assumption stems from turbulent kinetic energy transport equation, where local equilibrium for k_{SGS} is assumed. This can be expressed by

$$\tau_{ij}\tilde{S}_{ij} = -\rho\epsilon_{SGS} \ . \tag{2.82}$$

The dissipation of the sub-grid scales, ϵ_{SGS}, is then expressed as the sub-grid kinetic energy over a time scale, i.e. $\Delta/\mathcal{U}$, that provides a dissipation term which corresponds to $\mathcal{U}$ and Δ. Using the constant C_ϵ, the expression of the dissipation is,

$$\epsilon_{SGS} \simeq C_\epsilon\frac{k_{SGS}^{3/2}}{\Delta} \ . \tag{2.83}$$

From the Boussinesq approximation (2.80) and assuming incompressibility, $\tilde{S}_{kk} = 0$ and $\tilde{S}_{ij} = \bar{S}_{ij}$, an expression for the residual stress can be derived,

$$\tau^u_{ij} - \rho\frac{1}{3}k_{SGS}\delta_{ij} = -2C\rho\Delta k_{SGS}\tilde{S}_{ij} \ . \tag{2.84}$$

This expression, along with equation (2.83), can then be introduced to equation (2.82),

$$\left(\frac{1}{3}\delta_{ij}\rho k_{SGS} - 2C\sqrt{k_{SGS}}\rho\Delta\tilde{S}_{ij}\right)\tilde{S}_{ij} = -\rho C_\epsilon \frac{k_{SGS}^{3/2}}{\Delta} . \tag{2.85}$$

For constant density flows equation (2.85) can provide a model for k_{SGS} based on the filtered flow field,

$$k_{SGS} = C_S^2\Delta|\widetilde{S}| , \tag{2.86}$$

where the constant C_S is the so called Smagorinsky constant and $|\widetilde{S}| = \sqrt{2\widetilde{S}_{ij}\widetilde{S}_{ij}}$ is the magnitude of the resolved rate of the strain tensor. Although expression (2.86) is valid for constant density flows only, it is widely used for variable density flows [32]. Equation (2.86) can now be used to provide the Smagorinsky model for the eddy viscosity, as

$$\mu_t = C_S^2\rho\Delta^2|\widetilde{S}| . \tag{2.87}$$

A typical value for the Smagorinsky constant is $C_S = 0.2$, as determined by Lilly [100] using theoretical arguments. The same value has been proposed by Clark *et* al. [101] using computational results and Kwak *et* al. [102] using experimental results on decaying turbulence. On the other hand, it has been argued by Deardoff [94] and Schumann [99] that a value of 0.2 for the Smagorinsky constant is too dissipative in simulations of channel flows and proposed a smaller value of $C_S = 0.1$ [24].

Turbulent viscosity expresses the effect of the small eddies on momentum transport along the fluid and can also be used for the closure of the scalar transport equation. The unclosed term $\widetilde{u_iY_k} - \widetilde{u}_i\widetilde{Y}_k$ appears in the transport equations of both reacting and passive scalars (see equations (2.77) and (2.78)) and also in the enthalpy transport equation (2.79). This term, known as the turbulent flux of the scalar Y_k can closed with a turbulent viscosity model as,

$$\widetilde{u_iY_k} - \widetilde{u}_i\widetilde{Y}_k = \frac{\nu_t}{Sc_t}\frac{\partial\widetilde{Y}_k}{\partial x_i} , \tag{2.88}$$

where Sc_t is the turbulent Schmidt number, which taken as constant, [103, 104, 105]. The introduction of a turbulent Schmidt number implies that the sub-grid scale

flux of the momentum and the scalar have similar length and velocity and velocity scales, thus Sc_t must be close to unity [105]. For the LES simulation of Pitch [103]Sc_t is taken as equal to 0.4, whereas it is taken as equal to 0.7 for the LES of Branley *et* al. [32]. For the DNS of Kops *et* al. [104] Sc_t is assumed equal to unity. The above equation (2.88) is the classical gradient assumption for the modelling of the scalar fluxes [106] through an eddy diffusivity D_t which can be introduced instead of the turbulent viscosity, and is given by

$$D_t = \frac{\nu_t}{Sc_t} . \tag{2.89}$$

2.8 LES of turbulent reacting flows

The LES modelling approach for the integration of a turbulent flow field and the solution of the transport equations for the energy and all species has been described in the previous section. However, two aspects of the turbulent combustion have to be addressed. Firstly, the closure of the reaction rate terms ω_k and ω_T based on the filtered values and secondly, the treatment of the complexity of the chemical mechanism. A chemical mechanism may model the combustion process incorporating up to hundreds of species. Solving the LES transport equations for all the species in a turbulent flame leads to prohibitive computational cost. Flamelet modelling, Conditional Moment Closure and PDF methods address the problem of capturing the inner structure of a flame front. At the same time SLFM and CMC simplify the solution of the species transport equations [7].

2.8.1 Flamelet modelling

Flamelet modelling is based on the idea that a small instantaneous flame element embedded in a turbulent flow field has the structure of a laminar flamelet. This assumption requires that the reaction region is significantly thinner than the smallest turbulent scales so that the combustion occurs in laminar flow even for a turbulent flame. The flame structure can be described by the distribution of the temperature $T(\xi)$ and the mass fractions of the species $Y_k(\xi)$, together with the corresponding source terms $\omega_k(\xi)$

and $\omega_T(\xi)$, for ξ defined along the mixture fraction space η. Following the flamelet methodology, the structure of a laminar one-dimensional flame is governed by equations (2.47) and (2.48). Together with the boundary conditions for $Y_k(\xi = 0)$, $Y_k(\xi = 1)$, $T(\xi = 0)$ and $T(\xi = 1)$ the flamelet equations constitute a boundary value problem for the unknown flame structure.

Following the Stationary Laminar Flamelet Modelling (SLFM) methodology, the effect of the scalar mixing on the flame structure is introduced by the distribution of scalar dissipation rate $\chi(\xi)$, where χ is a function of the mixture fraction. For a laminar, one-dimensional flame this distribution can be parametrised with one degree of freedom. The distribution of $\chi(\xi)$ is expressed as a function of the scalar dissipation rate at the stoichiometric mixture fraction, ξ_{st}, viz.

$$\chi(\xi) = \chi(\xi_{st})\frac{F(\xi)}{F(\xi_{st})}\,, \tag{2.90}$$

where $F(\xi) = e^{-2[erf^{-1}(1-2\xi)]^2}$

represents the function for the dependence of χ in η-space [20]. Solving the boundary value problem for the steady flamelet equations (2.47) and (2.48), for fixed value of χ_{st}, one can come up with solutions for the species distribution $Y_k(\xi)$ and temperature $T(\xi)$ in mixture fraction space. The solution for the mass fractions and the temperature can be tabulated in a so called "flamelet library" as $Y_k(\xi, \chi_{st})$ and $T(\xi, \chi_{st})$ respectively. The derived flamelet library is dependent on the specific chemistry mechanism.

Assuming that the flame structure within a LES cell is represented by laminar flamelets, the filtered mass fractions and the temperature can be related to the integral of the equivalent distributions along the mixture fraction space as

$$\bar{\rho}\widetilde{Y_k} = \int_0^{+\infty}\int_0^1 \rho Y_k(z, \chi_{st}) P(\xi, \chi_{st}) d\xi d\chi_{st}\,, \tag{2.91}$$

and,

$$\bar{\rho}\widetilde{T} = \int_0^{+\infty}\int_0^1 \rho T(z, \chi_{st}) P(\xi, \chi_{st}) d\xi d\chi_{st}\,. \tag{2.92}$$

where P is the joint Probability Density Function (PDF) for the scalar dissipation

rate and the mixture fraction [1]. If ξ and χ_{st} are statistically independent, P can be expressed as the product of the two probabilities $P(\xi,\chi_{st}) = P(\xi) \cdot P(\chi_{st})$ [20]. The mixture fraction PDF is presumed using a β-function, defined by two degrees of freedom

$$P(\xi) = \frac{\Gamma(a+b)}{\Gamma(a)\Gamma(b)}\xi^{a}(1-\xi)^{b-1} . \tag{2.93}$$

The two degrees of freedom a and b are defined in a such way that the presumed PDF corresponds to the mean value $\widetilde{\xi}$ and the variance $\widetilde{\xi''^2}$ of the mixture fraction,

$$a = \widetilde{\xi}\left[\frac{\widetilde{\xi}(1-\widetilde{\xi})}{\widetilde{\xi''^2}} - 1\right] , \tag{2.94}$$

$$b = \frac{a}{\widetilde{\xi}} - a . \tag{2.95}$$

As far as the PDF of the scalar dissipation rate is concerned, two different approaches are normally utilised in LES combustion. Firstly there is a detailed approach where a lognormal distribution is assumed [107, 20],

$$P(\chi_{st}) = \frac{1}{\chi_{st}\sigma\sqrt{2\pi}} e^{-\frac{(\ln\chi_{st}-\mu)^2}{2\sigma^2}} . \tag{2.96}$$

The lognormal PDF is characterised by two degrees of freedom which are defined by the values of the mean scalar dissipation rate at stoichiometric and its variance. The parameter μ in equation (2.96) is related to the filtered scalar dissipation $\widetilde{\chi_{st}}$ as [108],

$$\mu = ln\widetilde{\chi}_{st} - \frac{\sigma^2}{2} , \tag{2.97}$$

whereas the parameter σ is related to the variance of the scalar dissipation logarithm,

$$\sigma^2 = ln\frac{\widetilde{\chi''^2_{st}} + \widetilde{\chi}^2_{st}}{\widetilde{\chi}^2_{st}} . \tag{2.98}$$

Several models for σ or the variance of the scalar dissipation have been proposed, although σ is often assumed constant and equal to unity. The parameter σ can also be

related to the turbulent Reynolds number $\sigma = 0.5 \ln(0.1 Re_t^{1/2})$ [109]. However, it is stated that the influence of the scalar dissipation variance does not have a significant effect on the final results.

The second and simpler approach for the modelling of the PDF of the scalar dissipation rate is a Dirac-delta function [110, 20], i.e.

$$P(\chi_{st}) = \delta(\chi_{st} - \widetilde{\chi_{st}}) \,. \tag{2.99}$$

Having defined the PDF of the scalar dissipation and the mixture fraction in equations (2.91) and (2.92), the values for the reactive species and the temperature can be retrieved by utilising the flamelet libraries $Y_k(\xi, \chi_{st})$ and $T(\xi, \chi_{st})$. The implementation of flamelet modelling within a LES algorithm requires the LES solution of the momentum transport and the mixing problem as described by equations (2.76) and (2.78), respectively. In flamelet modelling the unsteady and random nature of the turbulent flow field is introduced to the combustion mechanism by the mixing problem. The LES of the scalar mixing explicitly provides the filtered mixture fraction $\widetilde{\xi}$. However, the mixture fraction variance $\widetilde{\xi''^2}$, the scalar dissipation on the stoichiometric mixture fraction $\widetilde{\chi_{st}}$, and the filtered scalar dissipation rate $\widetilde{\chi}$ remain unclosed. The three unclosed values can be reduced to two, providing the following model for the scalar dissipation rate at the stoichiometric mixture fraction

$$\widetilde{\chi} = \widetilde{\chi}_{st} \int_0^1 \frac{F(\xi)}{F(\widetilde{\xi}_{st})} P(\xi) d\xi \,. \tag{2.100}$$

The above relation between $\widetilde{\chi_{st}}$ and $\widetilde{\chi}$ derives from the integration of (2.90) over the mixture fraction space.

2.8.2 Micromixing modelling in LES

Closures for $\widetilde{\chi}$ and $\widetilde{\xi''^2}$ cannot be based solely on the filtered scalar field $\widetilde{\xi}$. The scalar dissipation rate and the variance are unresolved, and depend on the sub-grid fluctuations of the mixture fraction, caused by the interaction of the fine turbulent scales with the mixing problem.

Scalar variance is a measure of the intensity of the mixture fraction fluctuations,

$$\widetilde{\xi''^2} = \widetilde{\xi^2} - \tilde{\xi}^2 \,. \tag{2.101}$$

$\widetilde{\xi''^2}$ can be regarded as the sub-grid scalar energy, where ξ^2 represents the magnitude of the energy of the mixture fraction fluctuations. The filtered scalar dissipation rate $\widetilde{\chi}$ is decomposed into the dissipation of the filtered field χ_r, i.e. the resolved scalar dissipation, plus the tine scale, or sub-grid contribution χ_{SGS},

$$\underbrace{2D\bar{\rho}\widetilde{\frac{\partial\xi}{\partial x_i}\frac{\partial\xi}{\partial x_i}}}_{\widetilde{\chi}} = \underbrace{2D\bar{\rho}\frac{\partial\tilde{\xi}}{\partial x_i}\frac{\partial\tilde{\xi}}{\partial x_i}}_{\chi_r} + \underbrace{2D\bar{\rho}\widetilde{\frac{\partial\xi'}{\partial x_i}\frac{\partial\xi'}{\partial x_i}}}_{\chi_{SGS}} \,. \tag{2.102}$$

The first term of the right hand side in equation (2.102) can be evaluated from the filtered flow field. However, the sub-grid part is unresolved and has to be modelled in LES.

The two quantities $\widetilde{\xi''^2}$ and $\widetilde{\chi_{SGS}}$, describe the same phenomenon; the effect of the small scales of the turbulent fluctuations on the mixture fraction distribution. Thus, these two terms can be related through dimensional analysis arguments. In fact, scalar dissipation rate and scalar variance provide the time scale of the sub-grid scale mixing, τ_ξ,

$$\tau_\xi = \frac{\widetilde{\xi''^2}}{\frac{1}{\bar{\rho}}\widetilde{\chi_{SGS}}} \,. \tag{2.103}$$

An estimate for the time scale τ_ξ can be retrieved from RANS modelling [106, 111, 112], where it is related to the filtered turbulent kinetic energy $\bar{k}$ and the filtered kinetic energy dissipation rate $\bar{\epsilon}$. In LES, an approximation for τ_ξ can be based on the resolved rate of strain $|\bar{S}|$ [105],

$$\frac{1}{\tau_\xi} \sim C\frac{\bar{\epsilon}}{\bar{k}} \sim C|\bar{S}| \,, \tag{2.104}$$

where the constant C is introduced in order to provide a relation between the sub-grid scale τ_ξ and the turbulent time scale $\frac{\bar{k}}{\bar{\epsilon}}$.

An insight into the physics of turbulent micromixing is obtained from the scalar variance transport equation. The starting point for the derivation of this equation, is

the mixture fraction transport equation (2.42). The transport equation for the square of the mixture fraction derives from equation (2.42), using the identity $\frac{\partial \xi^2}{\partial t} = 2\xi\frac{\partial \xi}{\partial t}$, and assuming constant density for the mixing problem, viz.

$$\underbrace{\rho\frac{\partial \xi^2}{\partial t}}_{\text{Rate}} + \underbrace{\rho u_i\frac{\partial \xi^2}{\partial x_i}}_{\text{Convection}} = \underbrace{D\rho\frac{\partial^2 \xi^2}{\partial x_i^2}}_{\text{Diffusion}} - \underbrace{2D\rho\frac{\partial \xi}{\partial x_i}\frac{\partial \xi}{\partial x_i}}_{\text{Dissipation}} . \tag{2.105}$$

The transport equation for $\overline{\xi^2}$ derives from the transport equation for the filtered mixture fraction $\overline{\xi}$ by applying the same procedure used for the derivation of equation (2.105) and this results in

$$\underbrace{\overline{\rho}\frac{\partial \overline{\xi}^2}{\partial t}}_{\text{Rate}} + \underbrace{\overline{\rho u_i}\frac{\partial \overline{\xi}^2}{\partial x_i}}_{\text{Convection}} = \underbrace{D\overline{\rho}\frac{\partial \overline{\xi}^2}{\partial x_i^2}}_{\text{Diffusion}} - \underbrace{2D\overline{\rho}\frac{\partial \overline{\xi}}{\partial x_i}\frac{\partial \overline{\xi}}{\partial x_i}}_{\text{Dissipation}} - \underbrace{2\frac{\partial \overline{\xi}\tau_i}{\partial x_i}}_{\text{SGS Diffusion}} + \underbrace{2\tau_i\frac{\partial \overline{\xi}}{\partial x_i}}_{\text{SGS Dissipation}} , \tag{2.106}$$

where $\tau_i = \overline{\rho}(\overline{u_i\xi} - \overline{u_i}\overline{\xi})$ is the turbulent flux for the mixture fraction. Finally, from equations (2.105) and (2.106) the scalar variance transport equation is obtained,

$$\begin{aligned}\underbrace{\overline{\rho}\frac{\partial\left(\overline{\xi^2} - \overline{\xi}^2\right)}{\partial t}}_{\text{Rate}} + \underbrace{\overline{\rho}\overline{u_i}\frac{\partial \overline{\xi^2}}{\partial x_i} - \overline{u_i}\frac{\partial \overline{\xi}^2}{\partial x_i}}_{\text{Convection}} &= \underbrace{D\overline{\rho}\frac{\partial^2\left(\overline{\xi^2} - \overline{\xi}^2\right)}{\partial x_i^2}}_{\text{Diffusion}} \\ \underbrace{-2D\overline{\rho}\left(\overline{\frac{\partial \xi}{\partial x_i}\frac{\partial \xi}{\partial x_i}} - \frac{\partial \overline{\xi}}{\partial x_i}\frac{\partial \overline{\xi}}{\partial x_i}\right)}_{\text{Dissipation}} &+ \underbrace{2\frac{\partial \overline{\xi}\tau_i}{\partial x_i}}_{\text{Diffusion of large scales}} - \underbrace{2\tau_i\frac{\partial \overline{\xi}}{\partial x_i}}_{\text{Production by large scales}} .\end{aligned} \tag{2.107}$$

Equation (2.107) is a typical transport equation where the energy of the sub-grid fluctuations for the mixture fraction $\overline{\xi^2} - \overline{\xi}^2$ convects, diffuses, and dissipates along the turbulent flow field. The effect of the resolved flow field is represented by the last two terms of equation (2.107), i.e. the diffusion of large scales and the production by large scales [113].

The main step for the derivation of zero equation models for LES is the local equilibrium assumption which is supposed to be valid for the small sub-grid scales of a LES. This requires that the turbulent flow field is stationary, homogeneous and isotropic, thus all the linear combinations of the spatial gradients and the time rates reduce to zero. Assuming local equilibrium for the equation (2.107) all the terms but the *production by large scales* and the *dissipation* are negligible and the equation reduces to

$$\underbrace{2D\overline{\rho}\left(\overline{\frac{\partial\xi}{\partial x_i}\frac{\partial\xi}{\partial x_i}}-\frac{\partial\overline{\xi}}{\partial x_i}\frac{\partial\overline{\xi}}{\partial x_i}\right)}_{\chi_{SGS}}=2\tau_i\frac{\partial\overline{\xi}}{\partial x_i}\,. \tag{2.108}$$

Equation (2.108) is the expression of the *production equals dissipation* assumption for the energy of the turbulent fluctuations of the mixture fraction and is valid under a local equilibrium assumption. The scalar flux τ_i in equation (2.108) can be modelled using the gradient model shown in equation (2.88), for the mixture fraction, i.e. $\tau_i = D_t\overline{\rho}\frac{\partial\overline{\xi}}{\partial x_i}$. This leads to a first model for the sub-grid scalar dissipation rate,

$$\widetilde{\chi}_{SGS}=2\overline{\rho}D_t\frac{\partial\widetilde{\xi}}{\partial x_i}\frac{\partial\widetilde{\xi}}{\partial x_i}\,, \tag{2.109}$$

where the turbulent diffusivity D_t is modelled as

$$D_t=\frac{(C_s\Delta)^2}{Sc_t}|\widetilde{S}|\,. \tag{2.110}$$

The model described by equations (2.109) and (2.110) provides an explicit, zero equation closure for the scalar dissipation rate. A decomposition of the total scalar dissipation rate leads to the same conclusion as shown by Girimaji and Zhou [112]

A closure for the scalar variance can be obtained from the relation between $\widetilde{\xi''^2}$ and $\widetilde{\chi_{SGS}}$ shown in equation (2.103). The estimate for the time scale of the sub-grid scale mixing in equation (2.104) is inserted into equation (2.103). Using the gradient model for χ_{SGS} yields a gradient model for the scalar variance, viz.

$$\widetilde{\xi''^2}=2C_v\Delta^2\frac{\partial\widetilde{\xi}}{\partial x_i}\frac{\partial\widetilde{\xi}}{\partial x_i}\,, \tag{2.111}$$

the constant C_v can be calculated, assuming the Oboukhov-Corrsin spectrum for the scalar fluctuations [105]. This leads to a value of $C_v = 0.2$ for the constant of the scalar variance model (2.111) [104, 114, 20].

The closures for the scalar dissipation rate (2.109) and scalar variance (2.111) mentioned above incorporate constant coefficients, C_S and C_v. This leads to nonzero sub-grid values for χ_{SGS} and $\widetilde{\xi''^2}$, when the gradient of the scalar distribution $\nabla\xi\nabla\xi$ is not zero. However, in the transitional area of turbulent jets the mixture fraction gradients are large while the flow field remains laminar, and the sub-grid fluctuations are not yet developed. The constant model coefficient should vary depending on the flow type, the Reynolds number and the characteristics of the filter [115]. In practice, the Smagorinsky constant has to be changed in different flows for optimal performance, it cannot limit its effect close to walls or in laminar shear flows [115]. In order to treat these deficiencies, the dynamic modelling technique was developed [116, 117].

The concept of test filtering is introduced for the implementation of the dynamic modelling procedure. A test filter is applied on the LES filtered field, and it is characterised by the test filter width $\hat{\Delta}$ which in general is larger larger than the LES filter width. Typically, the test filter width is taken twice the size of the grid filter width, i.e. $\hat{\Delta} = 2\Delta$ [118]. The test filtering operator $\hat{}$, is then defined as

$$\widehat{\widetilde{f(\boldsymbol{x}_0;t)}} = \int_{x\in V} \widehat{G}(\boldsymbol{x}_0 - \boldsymbol{x}, \hat{\Delta}(\boldsymbol{x}_0))\widetilde{f}(\boldsymbol{x};t)dV\,, \tag{2.112}$$

where the test filter $\hat{G}$ is applied to the already filtered LES field variable $\widetilde{f}$. For variable density flows an alternative definition of the test filtered field which includes Favre averaging is introduced,

$$\breve{\widetilde{f}} = \frac{\widehat{\overline{\rho}\widetilde{f}}}{\hat{\overline{\rho}}} \tag{2.113}$$

Following the procedure for the closure of the scalar dissipation rate (2.109), the derivation of a dynamic model starts from the modelling of the scalar fluxes τ_i. For the singly filtered LES flow field, the scalar fluxes are defined as

$$\tau_i = \widetilde{\overline{\rho}u_i\xi} - \overline{\rho}\widetilde{u_i}\widetilde{\xi}\,, \tag{2.114}$$

whereas, for the doubly filtered flow field the unresolved scalar fluxes T_i are

$$T_i = \widehat{\check{\bar{\rho}}\widetilde{u_i\xi}} - \check{\hat{\bar{\rho}}}\check{\tilde{u}}_i\check{\tilde{\xi}} . \tag{2.115}$$

A gradient model for the closure of the scalar fluxes for the filter and the test filtered flow fields can be expressed as

$$\tau_i = C\bar{\rho}\Delta^2 \left|\widetilde{S}\right| \frac{\partial\widetilde{\phi}}{\partial x_i} , \tag{2.116}$$

$$T_i = C\hat{\bar{\rho}}\hat{\Delta}^2 \left|\check{\tilde{S}}\right| \frac{\partial\check{\tilde{\phi}}}{\partial x_i} . \tag{2.117}$$

It must be noted that in the gradient models shown in (2.116) and (2.117), the Schmidt number and the Smagorinsky constant have been included in the model constant C. The aim of dynamic modelling is to provide an estimate of the constant C, calculated for the specific flow type, and spatial location. According to the dynamic modelling procedure [116], the model constant C must be the same for both closures shown in equations (2.116) and (2.117). The system of equations (2.116) and (2.117) is solved by test filtering equation (2.116) and subtracting the result from equation (2.117). Assuming that C varies slowly in space, so that $\widehat{C\tilde{f}} = \hat{C}\hat{\tilde{f}} = C\hat{\tilde{f}}$ the following expression for the model constant C is obtained,

$$\mathcal{L}_i = C\mathcal{M}_i , \tag{2.118}$$

where the Leonard term, $\mathcal{L}_i$, and the model term, $\mathcal{M}_i$, appear. The Leonard term is expressed as

$$\mathcal{L}_i = \widehat{\bar{\rho}\tilde{u}_i\tilde{\xi}} - \hat{\bar{\rho}}\check{\tilde{u}}_i\check{\tilde{\xi}} , \tag{2.119}$$

while, the model term is equal to

$$\mathcal{M}_i = \Delta^2\widehat{\left(\bar{\rho}\left|\tilde{S}\right|\frac{\partial\tilde{\phi}}{\partial x_i}\right)} - \hat{\Delta}^2\hat{\bar{\rho}}\left|\check{\tilde{S}}\right|\frac{\partial\check{\tilde{\phi}}}{\partial\hat{\tilde{x}}_i} . \tag{2.120}$$

Expression (2.118) consists of three equations, suggesting that the definition of

C is overdetermined. Thus, the the least squares method [119] is used to provide the value of the dynamic coefficient C,

$$C = \frac{\mathcal{L}_i \mathcal{M}_i}{\mathcal{M}_j \mathcal{M}_j} . \tag{2.121}$$

The constant C may take negative values which in some LES realisations need to be neglected, due to stability reasons [120]. This is called a "clipped" dynamic model. Another practice [120, 114] to avoid negative turbulent diffusion is to average the dynamic constant along homogeneous directions of the flow and assume a unique value for C among them.

It shall be noted that the derivation for the dynamic model started from the scalar flux closure. Even though an appropriate scaling law for the scalar dissipation rate can be derived, the dynamic procedure cannot be applied directly to this problem given that all the dissipation occurs at the smallest scales [114]. Thus, an indirect approach is utilised for the dynamic modelling of the scalar dissipation rate, based on the production equals dissipation assumption.

The starting point for the derivation of the dynamic scalar variance model of Pierce *et* al. [114], is the expression of the gradient model for $\widetilde{\xi''^2}$,

$$\bar{\rho}\widetilde{\xi''^2} = C\Delta^2 \bar{\rho} \frac{\partial \widetilde{\xi}}{\partial x_i} \frac{\partial \widetilde{\xi}}{\partial x_i} \tag{2.122}$$

Applying the dynamic procedure following the equation (2.121), the Leonard $\mathcal{L}$ term can be obtained from

$$\mathcal{L} = \widehat{\bar{\rho}\tilde{\xi}^2} - \hat{\bar{\rho}}\,\breve{\xi}^2 , \tag{2.123}$$

while the model term $\mathcal{M}$ is defined by expression,

$$\mathcal{M} = \Delta^2 \widehat{\bar{\rho} \frac{\partial \widetilde{\xi}}{\partial x_i} \frac{\partial \widetilde{\xi}}{\partial x_i}} - \hat{\Delta}^2 \widehat{\bar{\rho}} \frac{\partial \breve{\xi}}{\partial x_i} \frac{\partial \breve{\xi}}{\partial x_i} . \tag{2.124}$$

Finally the dynamic coefficient is calculated from the single equation,

$$C = \frac{\mathcal{L}}{\mathcal{M}} , \tag{2.125}$$

which will provide a dynamic coefficient for the gradient model shown in equation (2.122).

Another family of models, applicable to the closure of the scalar variance, consists of the scale similarity models. This methodology employs to the fractal nature of turbulence and assumes that the small scale statistics can be inferred from somewhat larger scale structures [121] as shown in figure 2.9.

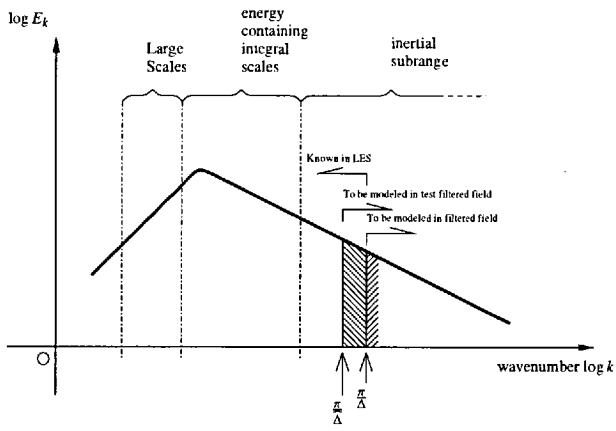

Figure 2.9: Scale similarity modelling

According to the similarity model, the scalar variance is taken as proportional to the difference of the energy of the scalar fluctuations between the filtered and the test filtered scalar field,

$$\widetilde{\xi''^2} = C_z\left(\widehat{(\tilde{\xi}^2)} - \left(\widehat{\tilde{\xi}}\right)^2\right) . \tag{2.126}$$

Here the constant C_z, can be assumed constant [121, 122, 123]. In fact, a value of $0.2\frac{\hat{\Delta}}{\Delta}$ is proposed for C_z where the typical value for the Smagorinsky constant C_s is assumed. According to Germano *et* al. [116] the constant C_z depends on the size of the degree of resolution for a specific LES. Cook *et* al. [123] propose a methodology for the calculation of the constant C_z, for a similarity model of the unresolved turbulent kinetic energy in LES. According to this model, the parameter C_z can be calculated numerically as a function of the test filter width $\hat{\Delta}$ and the integral length scale Λ_ξ. At first, the following form, for the scalar energy spectrum is assumed,

$$E_\xi(k) \sim k^{-5/3} e^{-1.73(k\Lambda_\xi)^{-4/3} - 2.25(k\eta_Z)^{4/3}}, \tag{2.127}$$

as proposed by Corrsin [124]. Following the analysis of Cook [123], where a similarity model of the unresolved turbulent kinetic energy is derived, the unclosed terms in the expression of the similarity model in equation (2.126) can be modelled as

$$\widetilde{\xi''^2} = 2 \int_0^\infty (1 - \hat{G}^2(k;\Delta)) E_\xi(k) dk \,, \tag{2.128}$$

and,

$$\widehat{(\tilde{\xi}^2)} - \left(\widehat{\tilde{\xi}}\right)^2 = 2 \int_0^\infty (1 - \hat{G}^2(k;\hat{\Delta})) \hat{G}^2(k;\Delta) E_\xi(k) dk \,, \tag{2.129}$$

where, $\hat{G}^2(k;\hat{\Delta})$ and $\hat{G}^2(k;\Delta)$ are the transfer functions for the test and the LES filters respectively, shown in the table 2.2. Following the equation (2.126), the similarity coefficient C_z can be computed as the ratio of the above integrals (2.128) and (2.129).

The range of values for C_z is between 0.5 and 1.75 [125], and shows a weak dependence on the integral length scale Reynolds number (2.127), with increasing values for larger Reynolds numbers. Furthermore, it shows a stronger dependence on the ratio between the integral length scale and the filter width, ℓ/Δ.

Pierce *et* al. [114] showed the relation between similarity and dynamic modelling assumptions, where the similarity model is simply expressed as

$$\widetilde{\xi''^2} = C_z \mathcal{L} \tag{2.130}$$

The above model for scalar variance has also been investigated by Jimenez *et* al. [106] where for the similarity model expressed by equation (2.126), the dynamic constant C in equation (2.125) was used.

2.8.3 Conditional Moment Closure

The underlying hypothesis in CMC methods is that most of the turbulent fluctuations of the scalars can be associated with the fluctuation of at least one key quantity [15]. Specifically for non-premixed flames, the concentrations of the species and the temper-

ature can be related to the mixture fraction variable ξ. Assuming that the mass fraction Y_k of species k in a turbulent flame is a stochastically fluctuating variable, its properties are characterised by its probability. A Probability Density Function (PDF), $P_k(y)$, is defined for the concentration Y_k so that

$$\mathcal{P}(Y_k < y) = \int_{-\infty}^{y} P_k(y')dy' , \tag{2.131}$$

where y and y' take values along the domain of Y_k, and $\mathcal{P}(Y_k < y)$ is simply the probability of Y_k being smaller than y [15]. For the definition of a mean for Y_k conditioned on a reference variable, the joint-PDF $P(y, \eta)$ is utilised. Using the mixture fraction as a reference variable, $P(y, \eta)$ is defined so that

$$\mathcal{P}(Y_k < a \vee \xi < \eta) = \int_{-\infty}^{y}\int_{-\infty}^{\eta} P(y_0, \eta_0)d\eta_0 dy_0 , \tag{2.132}$$

where $\mathcal{P}(Y_k < a \vee \xi < \eta)$ is the joint cumulative probability for $(Y_k < a \vee \xi < \eta)$ to be valid. Although definitions (2.131) and (2.132) have been provided for Y_k, and ξ, this does not mean that they cannot be applied to any other variable.

The conditional mean of the concentration Y_k, conditioned on the mixture fraction space η is defined as, [15]

$$\langle Y_k|\xi = \eta\rangle = \langle Y_k|\eta\rangle = \langle Y_k|\xi = \eta\rangle = \frac{1}{P(\eta)}\int_{-\infty}^{+\infty} yP(y, \eta)dy . \tag{2.133}$$

where, η is the mixture fraction space coordinate. CMC is based on the integration of the transport equations for the conditional means $\langle Y_k|\eta\rangle$. The derivation of the CMC equations can be achieved either with the decomposition method presented by Bilger [126, 127] or with the joint PDF method by Klimenko [14].

According to the decomposition method, the instantaneous value of the mixture fraction $Y_k(\boldsymbol{x}; t)$ for the reacting species k at a point $\boldsymbol{x}$ of the flow field and at time t can be expressed as

$$Y_k(\boldsymbol{x}; t) = Q_k(\xi(\boldsymbol{x}; t), \boldsymbol{x}, t) + Y_k''(\boldsymbol{x}; t) . \tag{2.134}$$

Here the conditional fluctuation Y_k'' is the fluctuation with respect to the conditional

mean. The conditional mean Q_k, is defined on the physical space of the flow field plus the mixture fraction space at a specific time. Many implementations of the method in the context of the RANS methodology can be found in literature [128, 129, 130, 131, 16].

For the LES methodology, the conditionally filtered representation is used instead [132, 133]. The definition of the conditional filtering operation is based on the Fine-grained Density Function (FDF), ψ_η. The FDF is defined for each point of the physical space and expands to a fourth dimension, i.e. the mixture fraction space. For singly conditioned CMC, its formulation is based on the mixture fraction of the combustion problem at specific point of the physical space, viz.

$$\psi_\eta = \psi(\boldsymbol{x}; t, \eta) = \delta\left(\eta - \xi(\boldsymbol{x}; t)\right) \ , \tag{2.135}$$

The symbol δ represents the Dirac function, which is a generalised function, thus it is implicitly defined by the convolution with a *good* function [15],

$$\int_{-\infty}^{+\infty} F(\xi)\delta(\xi)d\xi = F(0) \ . \tag{2.136}$$

The term *good* function is used to describe real functions with two properties: $F(\eta)$ must be a smooth enough function, C^n, thus having as many derivatives as needed, and it must tend to zero when $\eta \to \pm\infty$.

As seen in (2.135) the fine-grained density function is also a generalised function. For the derivation of the transport equations for the FDF, the differentiation of generalised functions needs to be addressed, given that the definition of the derivative of a generalised function is not straightforward. The following identities regarding the differentiations of FDF for single conditioning are presented in [15],

$$\frac{d\psi}{dt} = -\frac{\partial}{\partial\eta}\left(\psi\frac{d\xi}{dt}\right) \tag{2.137}$$

$$\nabla\cdot(f\psi) = \psi\cdot\nabla f + f\nabla\cdot\psi \tag{2.138}$$

$$\frac{d\psi f}{dt} = f\frac{d\psi}{dt} + \psi\frac{df}{dt} \tag{2.139}$$

$$\nabla\psi = -\frac{\partial}{\partial\eta}(\psi\nabla\xi) \tag{2.140}$$

$$\nabla^2\psi = -\frac{\partial\psi\nabla^2\xi}{\partial\eta} + \frac{\partial^2\psi\nabla\xi\cdot\nabla\xi}{\partial\eta\partial\eta}, \tag{2.141}$$

for f being a C^1 real function. The derivatives shown in equations (2.137) to (2.141) are not valid under the mathematical definition of a derivative in real analysis. They rather serve as definitions of the differentiation for the generalised function ψ. However, the above properties are valid when convoluted with a *good* function. In fact, the above properties will be used for the derivation of the transport equation of the conditionally filtered variables. Two more identities used for the derivation of the transport equations in CMC include the density and diffusivity coefficients,

$$\nabla\cdot(\rho D\nabla\psi) = \nabla\cdot(\nabla(\psi\rho D)) - \nabla\cdot(\psi\nabla(\rho D)) \tag{2.142}$$

$$\nabla\cdot(\psi\rho D\nabla\xi) = \psi\nabla\cdot(\rho D\nabla\xi) - \frac{\partial}{\partial\eta}(\psi\rho D(\nabla\xi\cdot\nabla\xi)) . \tag{2.143}$$

CMC combustion modelling in LES can be applied using the conditionally filtered variables instead of the conditional means. If the filter function G has a width Δ, the unconditionally filtered field for an arbitrary field function Φ is

$$\overline{\Phi}(\boldsymbol{x};t) = \int_{\boldsymbol{x}'\in V'} \Phi(\boldsymbol{x}';t)G(\boldsymbol{x}-\boldsymbol{x}',\Delta)dV' \quad ,\boldsymbol{x}\in V , \tag{2.144}$$

and is defined for every LES cell. The conditionally filtered field introduced by the CMC methodology is defined as,

$$\overline{\Phi|\eta} = \frac{\int_V \Phi\psi_\eta(\xi(\boldsymbol{x}';t)-\eta)G(\boldsymbol{x}-\boldsymbol{x}',\Delta)dV'}{\overline{P}(\eta)} . \tag{2.145}$$

The variable Φ represents any scalar field transported in the flow field. Usually, this can be the mass fraction of any of the reacting species, the enthalpy or the temperature. Its transport equation can be written in a similar way to the equation (2.10), as

$$\frac{\partial \rho \Phi}{\partial t} + \frac{\partial \rho u_i \Phi}{\partial x_i} = \frac{\partial}{\partial x_i}\left(D\frac{\partial \Phi}{\partial x_i}\right) + \omega_\Phi \,, \tag{2.146}$$

The integration is done over a volume V depending on the domain of the filter function. Finally $\overline{P}(\eta)$ is the Filtered Probability Density Function (FPDF) for ξ. Given that in LES the filtering operation is governed by the filter function G rather than being a time average, the FPDF is a PDF weighted by the filter function,

$$\overline{P}(\eta) = \int_{x' \in V} \psi_\eta(\xi(\boldsymbol{x}';t) - \eta) G(\boldsymbol{x} - \boldsymbol{x}', \Delta) dV \,. \tag{2.147}$$

The coupling between the LES filtered field and the conditionally filtered field provides a relation between the conditionally filtered and the LES filtered value. This is achieved by integrating $\overline{\Phi|\eta}$ in η space and results in

$$\overline{\Phi} = \int_0^1 \overline{\Phi|\eta} \overline{P}(\eta) d\eta \,. \tag{2.148}$$

For variable density flows a Favre filtered value, $\tilde{\Phi}_\eta$, for conditional variables can be defined as

$$\overline{\rho}_\eta \tilde{\Phi}_\eta = \overline{\rho \Phi|\eta} \,, \tag{2.149}$$

where the notation for the Favre conditional filter has been simplified to $\tilde{\Phi}_\eta = \widetilde{\Phi|\eta}$. As for the conditional mean, the conditional filter of a turbulent flow field introduces an extra dimension to the description of the filtered fluctuation fields, but similar to CMC in the RANS context, it will allow improved closure of the filtered chemical source term.

The starting point of the derivation of the LES-CMC coupling are the transport equations for the fine grained PDF ψ and the product $\psi\Phi$, found in the expression of the conditionally filtered field in equation (2.145). To obtain the transport equation for ψ, the mass conservation equation (2.1) is multiplied by ψ and using the differentiation identities, the final equation is given by

$$\frac{\partial \rho \psi}{\partial t} + \nabla \cdot \rho \boldsymbol{v} \psi = -\frac{\partial^2}{\partial \eta^2}(\rho N \psi) - \frac{\partial}{\partial \eta} \nabla \cdot (\rho \psi D \nabla \xi) \,, \tag{2.150}$$

where, N is defined as $N = D\nabla\xi \cdot \nabla\xi$. Multiplying the generic scalar field Φ by ψ, the governing equation of $\Phi\psi$, can be obtained as

$$\frac{\partial \rho\Phi\psi}{\partial t} + \nabla\cdot\rho v\Phi\psi = \psi\omega_\Phi + \nabla\cdot(\rho D\nabla(\psi\Phi)) + \frac{\partial}{\partial\eta}\underbrace{[2\psi\rho D\nabla\xi\cdot\nabla\Phi - \frac{\partial}{\partial\eta}(N\Phi\psi)]}_{J_\Phi} . \quad (2.151)$$

Equations (2.150) and (2.151) are valid for any scalar Φ, where neither high-Reynolds number, nor incompressibility had been assumed. However, unity Lewis numbers are assumed for all scalars. The term J_Φ in equation (2.151), represents diffusion in η-space.

The LES filter is applied by integrating the above equations over a volume V weighted by the filter function G, i.e. by applying the operation $\int_V(\cdot)GdV$ to equation (2.151), while a constant filter width has been used. Applying identity (2.145) to the filtered $\Phi\psi$ transport equation, the full expression of the transport equation for the conditionally filtered scalar $\widetilde{\Phi}_\eta$ derives, viz.

$$\frac{\partial\bar{\rho}_\eta\bar{P}_\eta\widetilde{\Phi_\eta}}{\partial t} + \nabla\cdot(\bar{\rho}_\eta\bar{P}_\eta\widetilde{v\Phi}_\eta) = \bar{P}_\eta\overline{\omega_{\Phi\eta}} + \frac{\partial}{\partial\eta}\tilde{J}_\Phi + \nabla\cdot\left(\bar{\rho}_\eta\bar{P}_\eta\widetilde{D\nabla\Phi}_\eta - \frac{\partial}{\partial\eta}\left(\bar{\rho}_\eta\bar{P}_\eta\widetilde{D\nabla\xi\Phi}_\eta\right)\right) . \quad (2.152)$$

According to the above equation, the conditionally filtered scalar field $\widetilde{\Phi}_\eta$ transports and diffuses in a four dimensional space consisting of the physical space and the mixture fraction or η space. The conditionally filtered flux $\widetilde{J}_\Phi$ for equation (2.152) takes the form,

$$\tilde{J}_\Phi = 2\bar{\rho}_\eta(\widetilde{D\nabla\xi\cdot\nabla\Phi})_\eta\bar{P}_\eta - \frac{\partial}{\partial\eta}[\bar{\rho}_\eta\bar{P}_\eta(\widetilde{N\Phi})_\eta] . \quad (2.153)$$

The primary closure hypothesis assumes a Brownian nature for the diffusion in conditional space [15]. Thus, a closure for the conditional flux $\widetilde{J}_\Phi$ can be based on the following diffusion approximation as

$$\tilde{J}_\Phi = A\tilde{\Phi}_\eta + B\frac{\partial\widetilde{\Phi}_\eta}{\partial\eta} . \tag{2.154}$$

The values of A and B should be independent of $\widetilde{\Phi}_\eta$. Their value can be derived by applying the relations (2.153) and (2.154) for a conserved scalar $\Phi = a + b\xi$. The resulting model for the conditionally filtered flux J_Φ from equation (2.154) is then formulated as

$$\widetilde{J}_\Phi = -\frac{\partial}{\partial\eta}(\bar{\rho}_\eta\bar{P}_\eta\tilde{N}_\eta)\tilde{\Phi}_\eta + \bar{\rho}_\eta\tilde{N}_\eta\bar{P}_\eta\frac{\partial\widetilde{\Phi}_\eta}{\partial\eta} . \tag{2.155}$$

By introducing the model for the filtered flux (2.155) into equation (2.152) the leads to the final LES-CMC model [133], takes the form.

$$\frac{\partial\tilde{\Phi}}{\partial t} + \tilde{\boldsymbol{u}}_\eta \cdot \nabla\Phi = \tilde{\omega}_{\Phi,\eta} + \widetilde{N}_\eta\frac{\partial^2\tilde{\Phi}}{\partial\eta^2} + e_\Phi + e_D . \tag{2.156}$$

The term e_Φ accounts for the correlation of the conditional fluctuations for the velocity field and the scalar field of the mass fraction Φ.

$$\bar{\rho}_\eta\bar{P}(\eta)e_\Phi = \nabla\cdot[\overline{\rho(\nu\Phi}_\eta - \widetilde{\nu\Phi}_\eta)\bar{P}(\eta)] , \tag{2.157}$$

and e_D is defined as

$$\bar{\rho}_\eta\bar{P}_\eta e_D = \nabla\cdot\bar{\rho}_\eta\bar{P}(\eta)(\widetilde{D\nabla\Phi})_\eta - \frac{\partial}{\partial\eta}\nabla\cdot[\bar{\rho}_\eta\bar{P}_\eta(\widetilde{D\nabla\xi\Phi})] + \widetilde{\Phi}_\eta\frac{\partial}{\partial\eta}[\nabla\cdot\bar{\rho}_\eta\bar{P}_\eta(\widetilde{D\nabla\xi})_\eta] , \tag{2.158}$$

The unclosed terms in the above CMC formulation are the conditional distribution of the scalar dissipation rate, the conditional reaction rate ω_η, e_Φ and e_D. A first order closure is usually chosen for the closure of the conditional reaction rate, where the conditional means for the mass fractions and the enthalpy are employed in order to obtain the conditional reaction rate, from the chemical mechanism,

$$\widetilde{\omega}_\eta = \omega(\widetilde{Y_{k;\eta}}, \widetilde{h}_\eta) . \tag{2.159}$$

Although a first order closure does not account for the fluctuations around the

conditional mean, the expansion of the flame structure along the mixture fraction space introduced in CMC significantly reduces the fluctuations and the error of the prediction of the conditional reaction rate. The conditional fluctuation term e_Φ is modelled using a gradient-type approach similar to LES modelling of the sub-grid contributions,

$$e_\Phi = -\nabla \cdot (D_\eta \nabla Q) \,, \tag{2.160}$$

where D_η, the conditional turbulent diffusivity, can be taken as constant and equal to the turbulent diffusivity D_t. The term e_D is usually neglected in CMC implementations. The first of the three terms scales with Re^{-1} while the second term scales with $Re^{-1/2}N^{1/2}$. Thus, e_D is expected to become negligible for high Reynolds numbers. The conditional scalar dissipation rate modelling is based on the filtered values from the LES simulation $\widetilde{\chi}$. The conditionally filtered and the LES filtered scalar dissipation rates are related by

$$\widetilde{\chi} = \int \widetilde{\chi}_\eta \tilde{P}(\eta) d\eta \,, \tag{2.161}$$

and the modelling of $\widetilde{\chi}_\eta$ is based on the inversion of the above integral (2.153). The conditional distribution of χ can be assumed common for all LES cells contained in a larger CMC control volume [133]. The distribution of the pairs for the LES filtered values $[\widetilde{\chi}, \widetilde{\xi}]$ can then be interpolated to provide a smooth distribution for χ_η in the mixture fraction space. This approach is quite generic since it does not require a presumed PDF for the inversion of (2.153). This characteristic makes the method applicable to flows with intermediate local minima and maxima in the mixture fraction space such as lifted flames [133].

2.8.4 Double Conditioning

Although CMC remains one of the most promising combustion submodels [128, 134], simulations of methane-air flames show some discrepancies between predictions and experiments [16]. This behaviour is undisputedly credited to the inability of the CMC methodology to account for extinction and re-ignition of the flame [18] . Local extinction and re-ignition causes significant fluctuations of the temperature around its

conditional mean. However, the flame structure is considered as unique inside a CMC volume. This results to misleading predictions for the reaction rates. One approach to account for the fluctuations of the temperature and the diversity of the flame structure is the second order closure of the reaction rates. Expanding the temperature using a Taylor series, the temperature variance and the species-temperature correlations are used for the predictions of the reaction rates [135, 136].

An alternative approach dealing with the extinction and re-ignition of the flame in CMC has been proposed by Bilger [137, 15], introducing a second conditional coordinate to describe the flame structure. Bilger derived the transport equations for the reactive species conditioned on the mixture fraction and an appropriately chosen progress variable. Temperature, enthalpy or scalar dissipation can be chosen as conditioning variables [138, 132, 17, 18].

Following Kronenburg [18], the sensible enthalpy h_s, governed by the transport equation (2.15), is chosen as a second conditioning variable, while equation (2.42) governs the transport of the mixture fraction ξ. For double conditioning the conditional average of a reactive species Y_k is defined on a five dimensional space, consisting of the physical space $\boldsymbol{x}$, the mixture fraction space η, and the enthalpy sample space ζ,

$$Q_k(\boldsymbol{x}; t, \eta, \zeta) = \langle Y_k(\boldsymbol{x}; t) | \xi(\boldsymbol{x}; t) = \eta, h_s(\boldsymbol{x}, t) = \zeta \rangle \,, \tag{2.162}$$

at each instant t. The decomposition of the instantaneous mass fraction Y_k is expressed as

$$Y_k = Q_k(\xi, \eta, \boldsymbol{x}; t) + Y_k''(\boldsymbol{x}; t) \,, \tag{2.163}$$

where, Q_k is now the doubly conditioned average and Y_k'' the conditional fluctuation. The transport equation for the conditional average can be derived by substituting (2.163) into the species mass fraction equations (3.4) and taking the conditional average [18].

However, for the coupling of the CMC equations with the LES methodology the conditionally filtered values [133] are used instead. The derivation of the doubly conditioned filtered CMC equations can be based on the alternative derivation of the CMC

equations as proposed by Klimenko and Bilger [15]. At first, a fine grained PDF with $n = 2$ is assumed,

$$\psi_{\eta,\zeta} = \psi(\boldsymbol{x}; t, \eta, \zeta) = \delta(\eta - \xi(\boldsymbol{x}; t))\,\delta(\zeta - h_s(\boldsymbol{x}; t)) \ , \tag{2.164}$$

Using the above fine grained PDF, the doubly conditional filtered scalar field $\Phi_{\eta,\zeta}$ can be expressed as [132]

$$\overline{\Phi|\eta,\zeta} = \frac{\int_V \Phi\psi(\boldsymbol{x}'; t, \eta, \zeta)G(\boldsymbol{x} - \boldsymbol{x}', \Delta)dV'}{\overline{P}(\eta,\zeta)} \ . \tag{2.165}$$

$\overline{P}(\eta,\zeta)$ is the joint filtered density function

$$\overline{P}(\eta,\zeta) = \int_{x'\in V} \psi(\boldsymbol{x}'; t, \eta, \zeta)G(\boldsymbol{x} - \boldsymbol{x}', \Delta)dV \ , \tag{2.166}$$

defined in a similar way to the singly conditioned FPDF in equation (2.147).

$$\overline{\Phi} = \int_{-\infty}^{+\infty}\int_{-\infty}^{+\infty} \overline{\Phi|\eta,\zeta}\overline{P}(\eta,\zeta)d\eta d\zeta \ . \tag{2.167}$$

The coupling between the LES filtered field and the conditionally filtered field is achieved by integrating $\overline{\Phi|\eta}$ in η and ζ space in a similar way to equation (2.148), and results in

$$\overline{\Phi} = \int_0^1\int_0^1 \overline{\Phi|\eta,\zeta}\overline{P}(\eta,\zeta)d\eta d\zeta \ . \tag{2.168}$$

For variable density flows a Favre filtered value, $\tilde{\Phi}_{\eta,\zeta}$, for the doubly conditioned variable Φ can be defined as

$$\overline{\rho}_{\eta,\zeta}\tilde{\Phi}_{\eta,\zeta} = \overline{\rho\Phi|\eta,\zeta} \ . \tag{2.169}$$

The properties of the fine grained PDF for $n = 1$ shown in equation (2.137) can be extended for $n = 2$. The basic properties used for the derivation of the filtered CMC equations are

$$\frac{\partial\psi f}{\partial t} = f\frac{\partial\psi}{\partial t} + \psi\frac{\partial f}{\partial t} \ , \tag{2.170}$$

and,

$$\nabla\psi = -\frac{\partial}{\partial\eta}(\psi\nabla\xi) - \frac{\partial}{\partial\zeta}(\psi\nabla h_s) \; . \tag{2.171}$$

Furthermore, it must be noted that although the conditional values $\Phi_{\eta,\zeta}$, $\rho_{\eta,\zeta}$ and $\nu_{\eta,\zeta}$ are functions of the conditioning value η and ζ, the equivalent unconditioned stochastic fields (Φ, ρ, ν), depend solely on the coordinates of the physical domain x and t. Thus, the derivatives of the unconditioned fields with respect to η and ζ are zero.

For $n = 2$ and $Y_1 = \xi$, $Y_2 = h_s$, $Z_1 = \eta$, $Z_2 = \zeta$, $W_1 = 0$ and $W_2 = \omega_{h_s}$ the expression for the fine grained PDF, $\psi_{\zeta,\eta}$, gives

$$\frac{\partial\rho\psi}{\partial t} + \nabla\cdot(\rho\nu\psi) + \frac{\partial}{\partial\eta}(\psi\nabla\cdot(\rho D_\xi\nabla\xi)) + \frac{\partial}{\partial\zeta}(\psi\nabla\cdot(\rho\alpha_t\nabla h)) = \frac{\partial\psi\omega_{h_s}}{\partial\zeta} \; , \tag{2.172}$$

where no assumptions on the Lewis number have been made. As mentioned before, the present derivation follows the joint PDF method. Multiplying the expression (2.172) by Φ and taking into account the identities (2.170) and (2.171) for the differentiation of the double conditioning fine grained PDF, the evolution equation for $\rho\Phi\psi$ is obtained, viz.

$$\begin{aligned}\frac{\partial\rho\Phi\psi}{\partial t} + \nabla\cdot(\rho\nu\Phi\psi) \; + \; & \frac{\partial}{\partial\eta}(\Phi\psi\nabla\cdot(\rho D_\xi\nabla\xi)) + \frac{\partial}{\partial\zeta}(\Phi\psi\nabla\cdot(\rho\alpha_t\nabla h)) - \psi\nabla\cdot(\rho D\nabla\Phi) \\ = \; & \frac{\partial}{\partial\zeta}(\Phi\psi\omega_{h_s}) + \psi\omega_\Phi \; ,\end{aligned} \tag{2.173}$$

where the transport equation (2.146) for the generic scalar field Φ has also been taken into account.

Assuming unity Lewis numbers all diffusivity coefficients are equal, $D_\xi = D = \alpha_t$, and also equal to the thermal diffusivity. The last three terms of the lhs in equation (2.173) can be further expanded. The first two of the three can be expressed as

$$\frac{\partial}{\partial\eta}(\Phi\psi\nabla\cdot(\rho D_\xi\nabla\xi) + \frac{\partial}{\partial\zeta}(\Phi\psi\nabla\cdot(\rho\alpha_t\nabla h)) \; = \; -\frac{\partial}{\partial\eta}(\psi\rho D\nabla\Phi\cdot\nabla\xi) - \frac{\partial}{\partial\zeta}(\psi\rho D\nabla\Phi\cdot\nabla h)$$

$$-\nabla\cdot(\rho D\Phi\nabla\psi)+\frac{\partial^2}{\partial\eta\partial\eta}(\psi\rho D\Phi(\nabla\xi\cdot\nabla\xi)) + \frac{\partial^2}{\partial\zeta\partial\zeta}(\psi\rho D\Phi(\nabla h\cdot\nabla h)) + 2\frac{\partial^2}{\partial\eta\partial\zeta}(\psi\rho D\Phi(\nabla\xi\cdot\nabla h)) , \quad (2.174)$$

while the third term is expanded as

$$\psi\nabla\cdot(\rho D\nabla\Phi)=\nabla\cdot(\psi\rho D\nabla\Phi)+\frac{\partial}{\partial\eta}(\psi\rho D\nabla\Phi\cdot\nabla\xi)+\frac{\partial}{\partial\zeta}(\psi\rho D\nabla\Phi\cdot\nabla h) . \quad (2.175)$$

Both expressions (2.174) and (2.175) can be derived from the basic identities (2.170) and (2.171). The final equation for $\Phi\psi$ is obtained by inserting the expansions (2.174) and (2.175) into (2.173),

$$\begin{aligned}\frac{\partial\rho\Phi\psi}{\partial t}+\nabla\cdot(\rho v\Phi\psi) &+ \frac{\partial^2}{\partial\eta\partial\eta}(\psi\rho D\Phi(\nabla\xi\cdot\nabla\xi))+\frac{\partial^2}{\partial\zeta\partial\zeta}(\psi\rho D\Phi(\nabla h\cdot\nabla h))\\ &+ 2\frac{\partial^2}{\partial\eta\partial\zeta}(\psi\rho D\Phi(\nabla\xi\cdot\nabla h))\\ -\nabla\cdot(\rho D\nabla(\psi\Phi)) &- 2\frac{\partial}{\partial\eta}(\psi\rho D\nabla\Phi\cdot\nabla\xi)-2\frac{\partial}{\partial\zeta}(\psi\rho D\nabla\Phi\cdot\nabla h)\\ &= \frac{\partial}{\partial\zeta}(\Phi\psi\omega_{h_s})+\psi\omega_\Phi . \end{aligned} \quad (2.176)$$

Here, the last term on the lhs of equation (2.176) originates from the third term on the rhs of equation (2.174) and the first term on the rhs of equation (2.175), as

$$\nabla\cdot(\rho D\nabla(\psi\Phi))=\nabla\cdot(\rho D\psi\nabla\Phi)+\nabla\cdot(\rho D\Phi\nabla\psi) , \quad (2.177)$$

by using the identity (2.170).

Applying the filtering operator $\int_V(\cdot)GdV$, shown in equation (2.165), on the transport equation (2.176), it gives:

$$\frac{\partial\bar\rho_{\eta,\zeta}\widetilde{\Phi}_{\eta,\zeta}\bar P_{\eta,\zeta}}{\partial t}+\nabla\cdot(\bar\rho_{\eta,\zeta}\widetilde{\nu\Phi}_{\eta,\zeta}\bar P_{\eta,\zeta}) - \frac{\partial}{\partial\eta}\widetilde{J_{\Phi,1}}_{\eta,\zeta}-\frac{\partial}{\partial\zeta}\widetilde{J_{\Phi,2}}_{\eta,\zeta}-\nabla\cdot\left(\bar\rho_{\eta,\zeta}D\nabla\left(\bar P_{\eta,\zeta}\widetilde{\Phi}_{\eta,\zeta}\right)\right)$$

$$= \bar{P}_{\eta,\zeta}\frac{\bar{\omega}_\Phi}{\rho}_{\eta,\zeta}, \tag{2.178}$$

where the terms $\widetilde{J_{\Phi,1}}_{\eta,\zeta}$ and $\widetilde{J_{\Phi,2}}_{\eta,\zeta}$ are defined as

$$\widetilde{J_{\Phi,1}}_{\eta,\zeta} = -\frac{\partial}{\partial\zeta}\left(\bar{\rho}_{\eta,\zeta}\bar{P}_{\eta,\zeta}D\widetilde{\Phi\nabla\xi\cdot\nabla h}_{\eta,\zeta}\right) - \frac{\partial}{\partial\eta}\left(\bar{\rho}_{\eta,\zeta}\bar{P}_{\eta,\zeta}D\widetilde{\Phi\nabla\xi\cdot\nabla\xi}_{\eta,\zeta}\right) + 2\bar{\rho}_{\eta,\zeta}\bar{P}_{\eta,\zeta}D\nabla\Phi\cdot\nabla\xi \tag{2.179}$$

$$\widetilde{J_{\Phi,2}}_{\eta,\zeta} = -\frac{\partial}{\partial\eta}\left(\bar{\rho}_{\eta,\zeta}\bar{P}_{\eta,\zeta}D\widetilde{\Phi\nabla\xi\cdot\nabla h}_{\eta,\zeta}\right) - \frac{\partial}{\partial\zeta}\left(\bar{\rho}_{\eta,\zeta}\bar{P}_{\eta,\zeta}D\widetilde{\Phi\nabla h\cdot\nabla h}_{\eta,\zeta}\right) + 2\bar{\rho}_{\eta,\zeta}\bar{P}_{\eta,\zeta}D\nabla\Phi\cdot\nabla h$$
$$+ \bar{\rho}_{\eta,\zeta}\bar{P}_{\eta,\zeta}\widetilde{\left(\frac{\Phi\omega_{h_s}}{\rho}\right)}_{\eta,\zeta}. \tag{2.180}$$

And they can be modelled using the primary closure assumption with a similar way to the singly conditioned CMC equations. Assuming Brownian diffusion, the terms $\widetilde{J_{\Phi,1}}_{\eta,\zeta}$ and $\widetilde{J_{\Phi,2}}_{\eta,\zeta}$ should be defined as,

$$\widetilde{J_{\Phi_i}}_{\eta,\zeta} = A\widetilde{\Phi}_{\eta,\zeta} + B\frac{\partial\widetilde{\Phi}_{\eta,\zeta}}{\partial\eta} + \Gamma\frac{\partial\widetilde{\Phi}_{\eta,\zeta}}{\partial\zeta} \text{ for } i = 1,2 \tag{2.181}$$

and the constants A, B, and Γ must remain unchanged for every distribution of $\widetilde{\Phi}_{\eta,\zeta}$. Inserting a linear distribution $\widetilde{\Phi}_{\eta,\zeta} = \alpha + \beta\eta + \gamma\zeta$ into the expressions (2.179) and (2.181) for $\widetilde{J_{\Phi,1}}_{\eta,\zeta}$, and into the expressions (2.180) and (2.181) for $\widetilde{J_{\Phi,2}}_{\eta,\zeta}$, the values for A, B, and Γ can be defined providing the following expressions for the fluxes on the conditional space, viz.

$$\widetilde{J_{\Phi,1}}_{\eta,\zeta} = -\frac{\partial}{\partial\eta}\left(\bar{\rho}_{\eta,\zeta}\bar{P}_{\eta,\zeta}\widetilde{\nabla\xi\cdot\nabla\xi}_{\eta,\zeta}\right)\widetilde{\Phi}_{\eta,\zeta} - \frac{\partial}{\partial\zeta}\left(\bar{\rho}_{\eta,\zeta}\bar{P}_{\eta,\zeta}\widetilde{\nabla\xi\cdot\nabla h}_{\eta,\zeta}\right)\widetilde{\Phi}_{\eta,\zeta}$$
$$+\bar{\rho}_{\eta,\zeta}\bar{P}_{\eta,\zeta}\widetilde{\nabla\xi\cdot\nabla\xi}_{\eta,\zeta}\frac{\partial\widetilde{\Phi}_{\eta,\zeta}}{\partial\eta} + \bar{\rho}_{\eta,\zeta}\bar{P}_{\eta,\zeta}\widetilde{\nabla\xi\cdot\nabla h}_{\eta,\zeta}\frac{\partial\widetilde{\Phi}_{\eta,\zeta}}{\partial\zeta} \tag{2.182}$$

$$\widetilde{J_{\Phi,2}}_{\eta,\zeta} = -\frac{\partial}{\partial\eta}\left(\bar{\rho}_{\eta,\zeta}\bar{P}_{\eta,\zeta}\widetilde{\nabla\xi\cdot\nabla h}_{\eta,\zeta}\right)\widetilde{\Phi}_{\eta,\zeta} - \frac{\partial}{\partial\zeta}\left(\bar{\rho}_{\eta,\zeta}\bar{P}_{\eta,\zeta}\widetilde{\nabla h\cdot\nabla h}_{\eta,\zeta}\right)\widetilde{\Phi}_{\eta,\zeta}$$
$$+\bar{\rho}_{\eta,\zeta}\bar{P}_{\eta,\zeta}\widetilde{\nabla h\cdot\nabla h}_{\eta,\zeta}\frac{\partial\widetilde{\Phi}_{\eta,\zeta}}{\partial\zeta} + \bar{\rho}_{\eta,\zeta}\bar{P}_{\eta,\zeta}\widetilde{\nabla\xi\cdot\nabla h}_{\eta,\zeta}\frac{\partial\widetilde{\Phi}_{\eta,\zeta}}{\partial\eta} \tag{2.183}$$

$$+ \quad \bar{\rho}_{\eta,\zeta}\bar{P}_{\eta,\zeta}\widetilde{\left(\frac{\omega_{h_s}}{\rho}\right)}_{\eta,\zeta}\widetilde{\Phi}_{\eta,\zeta} \,. \tag{2.184}$$

After inserting the J_Φ terms the equation (2.178) can be further simplified using the fine grained PDF transport equation (2.172), which when filtered with the operator $\int_V(\cdot)GdV$ gives,

$$\begin{aligned}
&\frac{\partial\bar{\rho}_{\eta,\zeta}\bar{P}_{\eta,\zeta}}{\partial t} + \nabla\cdot(\bar{\rho}_{\eta,\zeta}\bar{P}_{\eta,\zeta}\widetilde{\boldsymbol{v}}_{\eta,\zeta}) \\
+\frac{\partial^2}{\partial\zeta\partial\zeta}(\bar{\rho}_{\eta,\zeta}\bar{P}_{\eta,\zeta}D\widetilde{\nabla h\cdot\nabla h}_{\eta,\zeta})) + \frac{\partial^2}{\partial\eta\partial\eta}(\bar{\rho}_{\eta,\zeta}\bar{P}_{\eta,\zeta}D\widetilde{\nabla\xi\cdot\nabla\xi}_{\eta,\zeta})) \quad &+ \quad 2\frac{\partial^2}{\partial\eta\partial\zeta}(\bar{\rho}_{\eta,\zeta}\bar{P}_{\eta,\zeta}D\widetilde{\nabla\xi\cdot\nabla h}_{\eta,\zeta})) \\
+\frac{\partial}{\partial\eta}(\nabla\cdot(\bar{\rho}_{\eta,\zeta}\bar{P}_{\eta,\zeta}D\widetilde{\nabla\xi}_{\eta,\zeta})) + \frac{\partial}{\partial\zeta}(\nabla\cdot(\bar{\rho}_{\eta,\zeta}\bar{P}_{\eta,\zeta}D\widetilde{\nabla h}_{\eta,\zeta})) \quad &= \quad \frac{\partial\bar{\rho}_{\eta,\zeta}\bar{P}_{\eta,\zeta}\widetilde{\frac{\omega_{h_s}}{\rho}}_{\eta,\zeta}}{\partial\zeta} \,.
\end{aligned} \tag{2.185}$$

Finally subtracting the equation (2.185), multiplied by $\widetilde{\Phi}_{\eta,\zeta}$, from the equation (2.178) the final doubly conditioned CMC-LES model can be written as,

$$\begin{aligned}
\underbrace{\bar{\rho}_{\eta,\zeta}\bar{P}_{\eta,\zeta}\frac{\partial\widetilde{\Phi}_{\eta,\zeta}}{\partial t}}_{TermI,\ Time\ rate} + \underbrace{\bar{\rho}_{\eta,\zeta}\bar{P}_{\eta,\zeta}\widetilde{\boldsymbol{v}}_{\eta,\zeta}\nabla\widetilde{\Phi}_{\eta,\zeta}}_{TermII,\ Convection} \quad &= \quad \underbrace{\bar{P}_{\eta,\zeta}\left(\frac{\bar{\omega}_\Phi}{\rho}\right)_{\eta,\zeta}}_{TermIII,\ Reaction\ rate} \\
&- \underbrace{\bar{\rho}_{\eta,\zeta}\bar{P}_{\eta,\zeta}\widetilde{\left(\frac{\omega_{h_s}}{\rho}\right)}_{\eta,\zeta}\frac{\partial\widetilde{\Phi}_{\eta,\zeta}}{\partial\zeta}}_{TermIV,\ Heat\ release} \\
&- \underbrace{\bar{\rho}_{\eta,\zeta}\bar{P}_{\eta,\zeta}(\rho D\widetilde{\nabla\xi\cdot\nabla\xi})\frac{\partial^2\widetilde{\Phi}_{\eta,\zeta}}{\partial\eta\partial\eta}}_{TermV,\ \xi\ dissipation} \\
&+ \underbrace{\bar{\rho}_{\eta,\zeta}\bar{P}_{\eta,\zeta}(\rho D\widetilde{\nabla h\cdot\nabla h})\frac{\partial^2\widetilde{\Phi}_{\eta,\zeta}}{\partial\zeta\partial\zeta}}_{TermV,\ h_s\ dissipation} \\
&+ \underbrace{2\bar{\rho}_{\eta,\zeta}\bar{P}_{\eta,\zeta}(\rho D\widetilde{\nabla\xi\cdot\nabla h})\frac{\partial^2\widetilde{\Phi}_{\eta,\zeta}}{\partial\eta\partial\zeta}}_{TermV,\ Cross\ dissipation} \\
&+ \underbrace{\nabla\left(\bar{\rho}_{\eta,\zeta}\bar{P}_{\eta,\zeta}(\widetilde{\boldsymbol{v}}_{\eta,\zeta}\widetilde{\Phi}_{\eta,\zeta} - \widetilde{\boldsymbol{v}\Phi}_{\eta,\zeta})\right)}_{TermVI,\ \bar{\rho}_{\eta,\zeta}\bar{P}_{\eta,\zeta}e_\Phi}
\end{aligned}$$

$$\underbrace{\nabla \cdot \left(\bar{\rho}_{\eta,\zeta} D \nabla \left(\tilde{P}_{\eta,\zeta} \widetilde{\Phi}_{\eta,\zeta}\right)\right) + \frac{\partial}{\partial \eta}(\nabla \cdot (\bar{\rho}_{\eta,\zeta} \tilde{P}_{\eta,\zeta} D \widetilde{\nabla \xi}_{\eta,\zeta})) + \frac{\partial}{\partial \zeta}(\nabla \cdot (\bar{\rho}_{\eta,\zeta} \tilde{P}_{\eta,\zeta} D \widetilde{\nabla h}_{\eta,\zeta}))}_{TermVII,\, \bar{\rho}_{\eta,\zeta} \tilde{P}_{\eta,\zeta} e_D} . \tag{2.186}$$

The above equation governs the transport of the filtered doubly conditioned value $\widetilde{\Phi}_{\eta,\zeta}$ for any arbitrary variable Φ governed by the transport equation (2.146). The formulation (2.186) presents some analogies to the equivalent transport equation (2.156) for the singly conditionally filtered field $\widetilde{\Phi}_{\eta}$. In particular, both equations include the time rate, the convection term, the source terms, the dissipation terms. Finally the term e_{Φ} which accounts for the corelation of the conditional fluctuations and the term e_D, which describes the diffusion of the conditionally filtered scalar field in physical space [133] are found in both expressions.

Chapter 3

The structure of the DNS code

In certain areas of CFD, spectral methods have become the prevailing numerical tool for large scale calculations [139]. More specifically, spectral methods are used for simulations of homogeneous turbulence, shear flows and global weather modelling as an alternative to finite differences and finite elements techniques. The spectral technique for solving partial differential equations can be traced back to the analytical methodologies introduced in the nineteenth century.

Meteorological applications of spectral Galerkin methods appeared in the mid-twentieth century with Blinova [140], Haurwitz *et* al. [141] and Silberman [142]. The expense of dealing with nonlinear terms was a severe drawback and was addressed with an the development of the transform methods introduced by Orszag [143]. In contrast to the spectral Galerkin methods where the unknowns are the expansion coefficients and the equations are solved by the techniques used in classical analysis, in the spectral collocation technique the unknowns are the values on an alternative discretisation of the physical space, and the spectral series expansion is used for the calculation of the derivatives [139].

The benefits of spectral solvers are mainly associated with reduced memory demands and high accuracy of the spectral representation, leading to larger time steps and smaller computational times [45]. This explains the popularity of these methods for the solution of large scale computational problems used in theoretical research on turbulence and transition. However, a wider application in practical cases is prevented due

to the difficulties arising from the geometrical restrictions of a spectral representation and the sensitivity to boundary conditions [139].

The structure of the computational code used for the present numerical experiments on turbulent mixing and combustion is discussed in this chapter. The Navier-Stokes solver uses a de-aliased pseudospectral algorithm [42]. The proposed technique for its parallelisation is also presented. Finally, the performance of the parallel code on a Linux computer cluster is assessed.

3.1 Governing equations

For the simulations presented in this study constant properties, i.e. density, viscosity, thermal conductivity and heat capacities have been assumed. This contradicts the observation of significant fluctuations of the mixture properties in flames due to the temperature variations and the mixing of the reactants characterised by different properties.

However, as it will be shown in the chapter four, following Swaminathan and Bilger [41] the composition of the fuel and the oxidiser streams are chosen so that both fuel and oxidiser have the same molecular weights and similar thermodynamic and chemical properties, close to those of air, making this configuration attractive to incompressible simulations. Density variations due to heat release are also neglected. Although density variations due to heat release plays a significant role in turbulent combustion, incompressible DNS of flames[45] can capture qualitatively important features of phenomena such as extinction [144]. However, the temperature field interacts with the reactive species transport through the chemistry mechanism and the modelling of the chemical source terms.

In a constant fluid property formulation, where the density is constant over time, $(\partial\rho)/(\partial t) = 0$ and space $(\partial\rho/\partial x_i) = 0$, the mass conservation equation (2.1) simplifies to

$$\frac{\partial u_i}{\partial x_i} = 0\,, \tag{3.1}$$

which is equivalent to the kinematic condition that the velocity field should be

a solenoidal field, $\nabla \cdot \boldsymbol{u} = 0$. For constant density and viscosity the Navier-Stokes equations (2.2) can be further simplified to

$$\rho\frac{\partial u_j}{\partial t} + \rho u_i\frac{\partial u_j}{\partial x_i} = -\frac{\partial p}{\partial x_j} + \mu\frac{\partial^2 u_j}{\partial x_i{}^2} \quad \text{for } j = 1,2,3\,, \tag{3.2}$$

using equation (3.1), while the viscous stress tensor reduces to

$$\tau_{ij} = 2\mu S_{ij}\,. \tag{3.3}$$

Finally, a simplified expression of the species transport equation is obtained,

$$\rho\frac{\partial Y_k}{\partial t} + \rho u_i\frac{\partial Y_k}{\partial x_i} = \rho D_k\frac{\partial^2 Y_k}{\partial x_i^2} + \omega_k \quad for \quad k = 1, M\,. \tag{3.4}$$

In addition, the energy transport can be modelled by the temperature transport equation (2.16), which simplifies to,

$$\frac{\partial T}{\partial t} + u_i\frac{\partial T}{\partial x_i} = +\alpha_t\frac{\partial^2 T}{\partial x_i^2} + \omega_T\,, \tag{3.5}$$

for a constant property simulation. The set of governing equations provided in this section will be used to model the momentum and species transport for a diluted methane flame and for scalar mixing simulations in turbulent flow fields. It is worth noting that variable density formulations have been used for the DNS of turbulent combustion [88, 145] however a such configuration has a dramatic effect on the computational cost and further restricts the resolution requirements of the simulations [41].

3.1.1 Non-dimensionalised transport equations

The reactive flow field solved in the present study is modelled by a non-dimensional set of equations. The momentum, species and temperature transport equations (3.2, 3.4, 3.5) can be non-dimensionalised. This is done by choosing a set of characteristic values for time, length, pressure and temperature. The non-dimensional variables are then given by

$$t^* = \frac{t}{L_0/u_0} \; ; \; x_i^* = \frac{x_i}{L_0} \; ; \; u_i^* = \frac{u_i}{u_0} \; ; \; p^* = \frac{p}{\rho u_0^2} \; ; \; T^* = \frac{T - T_0}{T_1 - T_0} \, , \tag{3.6}$$

where a unity Strouhal number, $St = \frac{L_0}{u_0 t_0}$, is implied. The variables denoted with an asterix $\cdot^*$ have no dimensions. Applying the substitutions in (3.6), the transport equations in a dimensionless form can be written as

$$\frac{\partial u_j^*}{\partial t^*} + u_i^* \frac{\partial u_j^*}{\partial x_i^*} = -\frac{\partial p^*}{\partial x_j^*} + \frac{1}{Re} \frac{\partial^2 u_j^*}{\partial x_i^{*2}} \, , \tag{3.7}$$

$$\frac{\partial Y_k}{\partial t^*} + u_i^* \frac{\partial Y_k}{\partial x_i^*} = \frac{1}{ScRe} \frac{\partial^2 Y_k}{\partial x_i^{*2}} + \frac{L_0}{u_0} \omega_k \, , \tag{3.8}$$

$$\frac{\partial T^*}{\partial t^*} + u_i^* \frac{\partial T^*}{\partial x_i^*} = \frac{1}{PrRe} \frac{\partial^2 T^*}{\partial x_i^{*2}} + \frac{L_0}{u_0 (T_1 - T_0)} \omega_T \, , \tag{3.9}$$

given that the mass fraction is a dimensionless variable. The Reynolds number, $Re = \frac{u_0 L_0}{\nu}$, expresses the ratio between the convection and viscous forces.

Given that a constant property simulation is assumed and the DNS solutions provide a qualitative analysis of the mixing and the turbulent combustion problem, the results presented in this thesis are expressed in non-dimensional form. However, it is worth noting that for the specific fuel and oxidiser composition, which resembles this of air, a dimensional configuration of the flow field can be provided as it will be seen in the next chapter, where the simulations set up is presented. Assuming that the time is provided in seconds, i.e. $t_0 = 1 sec$, and the kinematic viscosity of the air at 20^o can be taken as equal to $1.5 \cdot 10^{-5} \frac{m^2}{sec}$, the reference length L_0 is found to be equal to $3.87 cm$.

3.2 The numerical method

The DNS solver is based on the pseudospectral algorithm introduced by Rogallo [52]. Its main characteristic is the storage of the flow field information in a hybrid space consisting of both spectral and physical coordinates. This setup facilitates the transformation of the field to physical space and back to spectral space without having to store the information of the flow field more than once. The specific Rogallo pseudospectral

technique aims to minimise the memory storage the CPU time and the input/output costs of the pseudospectral algorithm [139].

3.2.1 Re-formulation of the governing equations

The momentum transport is modelled by an incompressible constant property formulation of the Navier-Stokes equations,(3.7). This formulation of the Navier-Stokes equations incorporates the vorticity field. Vorticity $\omega(x;t)$ is the field vector defined as a function of the velocity field,

$$\omega(x;t) = \nabla \times u(x;t) \,, \tag{3.10}$$

where '$\times$' is the cross product operator. Then, the convection term of the momentum transport equation (3.7) can be expressed as,

$$u_i \frac{\partial u_j}{\partial x_i} = [(u \cdot \nabla)u]_j = [\frac{1}{2}\nabla(|u|^2) - u \times \omega]_j \,, \tag{3.11}$$

making use of the identity

$$\nabla(u \cdot u) = 2\, u \times (\nabla \times u) + 2\, (u \cdot \nabla)u \,, \tag{3.12}$$

valid for any C^1 vector field u, where $\cdot$ is the inner product of two vectors. Applying the above transformations, the momentum transport equation (3.7) can be finally formulated as a system of the following three equations,

$$\frac{\partial u}{\partial t} = u \times \omega - \nabla\Pi + \frac{1}{Re}\nabla^2 u \,, \tag{3.13}$$

$$\nabla^2\Pi = \nabla(u \times \omega) \,, \tag{3.14}$$

$$\omega = \nabla \times u \,. \tag{3.15}$$

where Π is a scalar variable which includes the term $|u|^2$ arising from (3.12) and can be related to the dynamic pressure

$$\Pi = p + \frac{1}{2}|\boldsymbol{u}|^2 \,. \tag{3.16}$$

The first of the three equations, i.e. equation (3.13), derives directly from the momentum transport equation (3.7) using the expression (3.11) for the convection term. Equation (3.14) results, from the divergence of the momentum transport equation, and utilising the mass conservation equation. Finally, the last equation (3.15) is just the definition of the vorticity. The system of equations (3.13) to (3.15), constitute the rotational form of the incompressible Navier-Stokes equations. The rotational formulation is favoured in spectral methods because it guarantees the conservation of kinetic energy. According to Orszag [47] this is also important for numerical reasons, assuring that nonlinear instabilities will not occur if the time step advancement is kept below the stability limit.

An equivalent manipulation can be applied to the transport equations of the mixture fraction ξ, equation (2.42), the reactive species Y_k, equation (3.8), and the temperature, equation T (3.9). In fact, in the case of scalar transport in a turbulent flow, the derivation is somewhat simpler, since the governing equations are second order compared to the fourth order Navier-Stokes equations. For an arbitrary scalar field Φ the transport equation can be rearranged as:

$$\frac{\partial \Phi}{\partial t} = -(\boldsymbol{u} \cdot \nabla)\Phi + \frac{1}{ScRe}\nabla^2\Phi + \omega_\Phi \,. \tag{3.17}$$

If Φ represents temperature, the Schmidt number needs to be replaced by the Prandtl number, Pr.

The system of equations presented in this section is valid for an incompressible, constant property flow. For the description of a turbulent flame, the only unclosed terms are the reaction rates which are modelled as a function of the species mass fractions and temperature according to the chemical mechanism employed.

3.2.2 The Fourier transform of the flow field

In spectral methods, the field variables are represented by a weighted sum of eigenfunctions [139]. The unknowns, i.e. the weights, are calculated by integrating the

approximation series in space and using the orthogonality properties of the eigenfunctions. The differentiation of the field variables is obtained analytically from the derivatives of the eigenfunctions. For problems with periodic boundary conditions Fourier series are a natural choice [146].

In pseudospectral methods, a discretisation of the physical space is assumed. For the cubic computational domain of a turbulent flow field with edges of length 2π shown in figure (3.1)(a), the physical space (x_1, x_2, x_3) can be discretised as:

$$x_1^i = \frac{2\pi i}{N},\ x_2^j = \frac{2\pi j}{N},\ x_3^k = \frac{2\pi k}{N},\ for\ i,j,k = 0,\ldots N-1\ , \tag{3.18}$$

where N^3 collocation points are assumed, consisting a cubic, Cartesian, and uniform mesh in each direction of the computational domain. This discretisation can be expressed in spectral space with a series of three consecutive Discrete Fourier Transforms (DFT),

$$g(x_1^i, x_2^j, k_3, t) = \frac{1}{N}\sum_{k=0}^{N-1} f(x_1^i, x_2^j, x_3^k, t)e^{ix_3^k k_3} \tag{3.19}$$

$$h(x_1^i, k_2, k_3, t) = \frac{1}{N}\sum_{j=0}^{N-1} g(x_1^i, x_2^j, k_3, t)e^{ix_2^j k_2} \tag{3.20}$$

$$\hat{f}(k_1, k_2, k_3, t) = \frac{1}{N}\sum_{i=0}^{N-1} h(x_1^i, k_2, k_3, t)e^{ix_1^i k_1}\ . \tag{3.21}$$

In the above equation, i is the imaginary unit, g, h are the intermediate DFT of the field f, and $\hat{f}$ is the final DFT of f. Each Fourier node is characterised by a vector of three wavenumbers, $\boldsymbol{k} = [k_1^i, k_2^j, k_3^k]$, for each direction. Equations (3.19) to (3.21) impose a discretisation on the spectral space, which is expressed by using a finite number of N Fourier modes for each direction,

$$k_1^i = i,\ k_2^j = j,\ k_3^k = k,\ for\ i,j,k = 1 - N/2,\ldots N/2\ , \tag{3.22}$$

given that any higher wavenumber than $N/2$ can be aliased with the wavenumbers in the interval $[1 - N/2, N/2]$. The domain of the spectral representation is presented

in figure (3.1)(d). In the same figure, the domain for the intermediate representations g and h are shown in (b) and (c) respectively.

Using equations (3.19) to (3.21), the finite set of values $f(x_1^i, x_2^j, x_3^k, t)$ defined on discrete points in the physical space is transformed to a finite set of weights $\hat{f}(k_1^i, k_2^j, k_3^k, t)$ defined by a finite set of wavenumbers. Furthermore, the range of the real values $f(x_1^i, x_2^j, x_3^k, t)$ is tranformed to a complex space C. Given that f is a real function, it can be shown that the values of g for negative wavenumbers are defined by

$$g(x_1^i, x_2^j, k_3^k, t) = -g^*(x_1^i, x_2^j, k_3^{-k}, t) \; for \; k_3 = 1 - N/2, \ldots, -1 \tag{3.23}$$

where g^* is the conjugate of g. As a result the negative part of the domain of g is redundant and the upper part of the cube, highlighted in figures (3.1)(b) to (d), contains all the information needed for the reproduction of f in physical space. Also $g(x_1^i, x_2^j, k_3^0, t)$ and $g(x_1^i, x_2^j, k_3^N/2, t)$ must also be purely real numbers for f to be real.

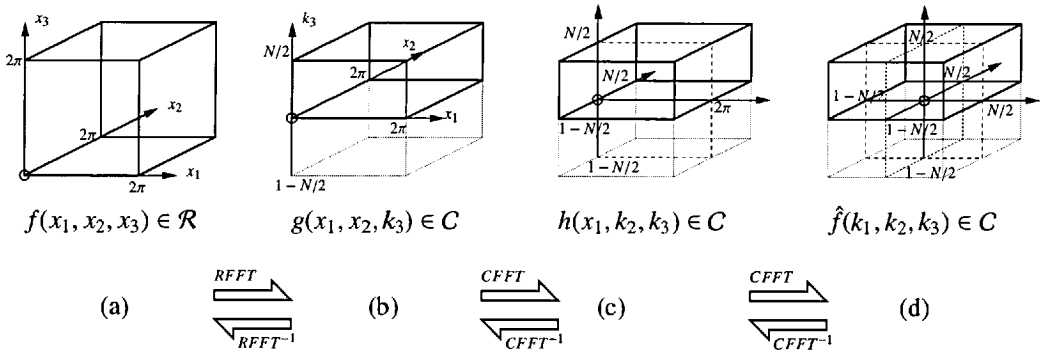

Figure 3.1: The flow field domain, defined on the **(a):** (x, y, z)-space, **(b):** (k_x, y, z)-space, **(c):** (k_x, k_y, z)-space, **(d):** (k_x, k_y, k_z)-space

The inverse Discrete Fourier Transform, denoted here as DFT^{-1}, provides the spatial discretised distribution of the three dimensional field f as a function of the eigenfunction weights $\hat{f}$. This can be expressed in a compact vectorised formulation as

$$f(\boldsymbol{x}^{i,j,k}; t) = \sum_{k=\{1-N/2,1-N/2,1-N/2\}}^{\{N/2,N/2,N/2\}} \hat{f}(\boldsymbol{k}; t) e^{i\boldsymbol{x}^{i,j,k} \cdot \boldsymbol{k}}. \tag{3.24}$$

Evaluating all the values of f demands N^2 operations for each direction. However, the introduction of the Fast Fourier Transform (FFT) by Cooley and Tukey [147]

reduced the computational cost to $Nlog(N)$ for both DFT and DFT^{-1}.

This procedure is summarised in figure (3.1), where a real FFT (RFFT) and two complex FFT (CFFT) are applied to provide the representation of the flow field in spectral space. The reverse is achieved by using the same series of inverse transforms, i.e. RFFT^{-1} and CFFT^{-1}, summing up to $N^3 \log^3 N$ operations. The alias errors occurring during the FT are removed using the 2/3 rule, where the high wavenumber part of the spectrum is removed [42].

3.2.3 Spatial representation

The interpolation of the unknowns, i.e. the velocities u_j, the dynamic pressure Π, the non-linear term $(\boldsymbol{u} \times \boldsymbol{\omega})$, the temperature T and the species mass fractions Y_ℓ, of the differential system, which describes the turbulent combustion problem, and consists of the equations (3.13), (3.14), (3.15), and (3.17), is expressed as:

$$u_j\left(\boldsymbol{x}^{i,j,k};t\right) = \sum_{k_1=1-\frac{N}{2}}^{\frac{N}{2}} \sum_{k_2=1-\frac{N}{2}}^{\frac{N}{2}} \sum_{k_3=1-\frac{N}{2}}^{\frac{N}{2}} \hat{u}_j(\boldsymbol{k};t) \cdot e^{\mathrm{i}\boldsymbol{k}\cdot\boldsymbol{x}^{i,j,k}} \quad \text{for} \quad j=1,2,3\,, \tag{3.25}$$

$$\Pi\left(\boldsymbol{x}^{i,j,k};t\right) = \sum_{k_1=1-\frac{N}{2}}^{\frac{N}{2}} \sum_{k_2=1-\frac{N}{2}}^{\frac{N}{2}} \sum_{k_3=1-\frac{N}{2}}^{\frac{N}{2}} \hat{\Pi}_i(\boldsymbol{k};t) \cdot e^{\mathrm{i}\boldsymbol{k}\cdot\boldsymbol{x}^{i,j,k}}\,, \tag{3.26}$$

$$(\boldsymbol{u}\times\boldsymbol{\omega})_j\left(\boldsymbol{x}^{i,j,k};t\right) = \sum_{k_1=1-\frac{N}{2}}^{\frac{N}{2}} \sum_{k_2=1-\frac{N}{2}}^{\frac{N}{2}} \sum_{k_3=1-\frac{N}{2}}^{\frac{N}{2}} \widehat{(\boldsymbol{u}\times\boldsymbol{\omega})}_j(\boldsymbol{k};t) \cdot e^{\mathrm{i}\boldsymbol{k}\cdot\boldsymbol{x}^{i,j,k}} \quad \text{for} \quad j=1,2,3\,, \tag{3.27}$$

$$T\left(\boldsymbol{x}^{i,j,k};t\right) = \sum_{k_1=1-\frac{N}{2}}^{\frac{N}{2}} \sum_{k_2=1-\frac{N}{2}}^{\frac{N}{2}} \sum_{k_3=1-\frac{N}{2}}^{\frac{N}{2}} \widehat{T}(\boldsymbol{k};t) \cdot e^{\mathrm{i}\boldsymbol{k}\cdot\boldsymbol{x}^{i,j,k}}\,, \tag{3.28}$$

$$Y_k\left(\boldsymbol{x}^{i,j,k};t\right) = \sum_{k_1=1-\frac{N}{2}}^{\frac{N}{2}} \sum_{k_2=1-\frac{N}{2}}^{\frac{N}{2}} \sum_{k_3=1-\frac{N}{2}}^{\frac{N}{2}} \widehat{Y_\ell}(\boldsymbol{k};t) \cdot e^{i\boldsymbol{k}\cdot\boldsymbol{x}^{i,j,k}} \quad \text{for} \quad k=1\ldots M\,. \tag{3.29}$$

The momentum transport equation can be expressed in spectral space by introducing the interpolations (3.25) and (3.26) in equations (3.13), (3.14),and (3.15). Applying the standard procedure imposed by the Strum-Louiville methodology, i.e. taking the

convolution of the eigenfunction e^{ikx} corresponding to a single wavenumber $\boldsymbol{k}$, integrating across the computational domain $\boldsymbol{x}$, and accounting for the orthogonality of the basis functions, the momentum transport is expressed by the following two equations:

$$\frac{\partial \hat{u}_j}{\partial t} = \widehat{(\boldsymbol{u} \times \boldsymbol{\omega})}_j - \mathbf{i} k_j \hat{\Pi} - \frac{1}{Re} |\boldsymbol{k}|^2 \hat{u}_j \quad \text{for} \quad j = 1, 2, 3 \,, \tag{3.30}$$

$$-|\boldsymbol{k}|^2 \hat{\Pi} = i k_\ell \widehat{(\boldsymbol{u} \times \boldsymbol{\omega})}_\ell \,. \tag{3.31}$$

In general, the main difficulty when integrating the Navier-Stokes equation is the elimination of the pressure term. To achieve this in equation (3.13) expression (3.14) must be integrated. However, expressing momentum transport with the system of the Navier-Stokes equations (3.30) and (3.31), the pressure can be eliminated analytically. In fact one of the advantages of spectral representation is that any differentiation can easily be expressed as a simple algebraic multiplication with the wavenumber. After the elimination of the pressure, the momentum transport equation in spectral space is written as

$$\frac{\partial \hat{u}_j}{\partial t} = \widehat{(\boldsymbol{u} \times \boldsymbol{\omega})}_j - k_j \frac{k_\ell \widehat{(\boldsymbol{u} \times \boldsymbol{\omega})}_\ell}{|\boldsymbol{k}|^2} - \frac{1}{Re} |\boldsymbol{k}|^2 \hat{u}_j \quad \text{for} \quad j = 1, 2, 3 \,. \tag{3.32}$$

Following an equivalent procedure, the transport equations for the temperature T and the species mass fractions Y_ℓ are given by

$$\frac{\partial \hat{T}}{\partial t} = \omega_T \widehat{-(u \cdot \nabla) T} - \frac{1}{PrRe} k^2 \hat{T} \,, \tag{3.33}$$

and, (3.34)

$$\frac{\partial \hat{Y}_\ell}{\partial t} = \omega_k \widehat{-(u \cdot \nabla) Y_k} - \frac{1}{ScRe} \alpha k^2 \hat{Y}_k \quad \text{for} \quad k = 1 \ldots M \,. \tag{3.35}$$

The governing equations (3.32) to (3.34), provide the numerical solution of the time evolution for a turbulent flow field based on a known initial distribution of the velocity, species and temperature field. The initial and boundary conditions which define the boundary value problem are to be discussed in the next section.

3.2.4 Initial and boundary conditions

The flow and scalar fields must be periodic in all directions. From the spectral representation (3.19), (3.20), and (3.21) it can be deduced that,

$$\begin{aligned} f(x_1, x_2, x_3) &= f(x_1 + 2\pi, x_2, x_3), \\ f(x_1, x_2, x_3) &= f(x_1, x_2 + 2\pi, x_3), \\ f(x_1, x_2, x_3) &= f(x_1, x_2, x_3 + 2\pi). \end{aligned} \tag{3.36}$$

Although the need of periodicity is a huge constraint of the Fourier representation, periodic boundary conditions do not prevent us from carrying out realistic simulations of turbulent flows. Indeed, producing artificial turbulence to simulate non-periodic inflow and outflow conditions is a complicated task [45] and may introduce inaccuracies.

On the other hand, artificial turbulent fluctuations are needed for the initial conditions. For homogeneous isotropic turbulence calculations, the spectral reconstruction method [42] is used. According to this methodology, the initial flow field is the result of the superposition of Fourier modes. Here, the intensity of the modes is defined by the energy spectrum used by Orszag and Paterson [47],

$$E(|\boldsymbol{k}|) = c|\boldsymbol{k}|^4 e^{-|k|^2/a^2} \tag{3.37}$$

where the constants c and a are suitably chosen, such that all the scales are well resolved [43]. The phase for each of these modes is then chosen randomly, subject to consistency with the mass conservation equation [139].

Another way of deriving initial conditions for turbulent flow-field is to assume a laminar initial field. If this flow field has a significantly high Reynolds number and is unstable, we can expect that it will develop to a fully turbulent field.

3.2.5 The time advancement

Starting from an initial flow field at time t the pseudospectral solver provides a numerical prediction of the flow field at the next time step $t + \Delta t$.

Following the typical factorisation method for linear homogeneous differential equations, the system consisting of the equations (3.32) to (3.34) is multiplied by $e^{\frac{1}{Re}|k|^2 t}$ and the linear terms of the right hand side can be factorised as,

$$\frac{\partial}{\partial t}(\mathcal{D}^T(t)\underbrace{\begin{bmatrix}\hat{u}_1\\ \hat{u}_2\\ \hat{u}_3\\ \hat{Y}_1\\ \vdots\\ \hat{Y}_M\\ \hat{T}\end{bmatrix}}_{\hat{X}(t)}) = \mathcal{D}^T(t)\underbrace{\begin{bmatrix}\widehat{(u\times\omega)_1 - k_1\frac{k_\ell(u\times\omega)_\ell}{k^2}}\\ \widehat{(u\times\omega)_2 - k_2\frac{k_\ell(u\times\omega)_\ell}{k^2}}\\ \widehat{(u\times\omega)_3 - k_3\frac{k_\ell(u\times\omega)_\ell}{k^2}}\\ \omega_1 - (u\cdot\nabla)Y_1\\ \vdots\\ \omega_M - (u\cdot\nabla)Y_M\\ \omega_T - (u\cdot\nabla)T\end{bmatrix}}_{\text{Nonlinear terms: } \widehat{NL}(t)}, \tag{3.38}$$

where the vector $\mathcal{D}$(t) is defined by

$$\mathcal{D}(t) = \begin{bmatrix} e^{\frac{1}{Re}k^2 t}\\ e^{\frac{1}{Re}k^2 t}\\ e^{\frac{1}{Re}k^2 t}\\ e^{\frac{1}{ScRe}k^2 t}\\ \vdots\\ e^{\frac{1}{ScRe}k^2 t}\\ e^{\frac{1}{PrRe}k^2 t}\end{bmatrix}. \tag{3.39}$$

Thus, a first order Taylor approximation of the field variables at time $t+\Delta t$ is given by

$$\mathcal{D}^T(\Delta t)\hat{X}(t+\Delta t) = \Delta t\widehat{NL}(t) + \hat{X}(t)\,. \tag{3.40}$$

The time advancement is achieved with the minimal storage time-advancement scheme for spectral methods of Wray [148]. The specific algorithm is a third order Runge-Kutta algorithm where three approximations of the flow field at three different intermediate time steps are used to provide a final prediction of $\hat{X}$ at the time step $\Delta t+t$. The special characteristic of this method is that only two memory locations are used

for the storage of the realisations of the flow field, during every step of the algorithm. Low storage time advancement algorithms are popular for large scale simulations [42, 149, 61] where an economical memory usage is crucial.

In equation (3.40) the vector of the non-linear terms, $\widehat{\boldsymbol{NL}}$, cannot be derived explicitly from the spectral representation of the field variables $\hat{\boldsymbol{X}}$. The unknowns of equation (3.40) are expressed in spectral space, whereas the terms of $\widehat{\boldsymbol{NL}}$ are a function of the field variables expressed in real space. In order to evaluate $\boldsymbol{NL}$ at each time step the field $\hat{\boldsymbol{X}}$ must be transformed to the real or physical space, and $\boldsymbol{NL}$ can then be computed from $\boldsymbol{X}$.

After its calculation in the physical space, the vector of the nonlinear terms $\boldsymbol{NL}$ is transformed back to spectral space, where it is introduced to equation (3.40) for calculation of the approximation of $\hat{\boldsymbol{X}}$ at the time step $\Delta t + t$. This procedure results to two three dimensional Fourier transforms, i.e. one FFT and one FFT^{-1} each time equation (3.40) is evaluated. Thus, using a third order Runge-Kutta algorithm, the three dimensional FFT is called six times per single time step. In fact, the FFT is known to consume most of the computational time in a spectral Navier-Stokes solver [139, 61].

3.2.6 Computer implementation

It has been made clear that an efficient implementation of the Fourier transform is a vital factor for the performance of the spectral solver. Apart from the speed of the calculations the memory requirements need to be considered.

A characteristic of the Fourier representation is the fact that the value of any variable at a specific point in physical space is a function of the weights of all the wavenumbers. This characteristic imposes some difficulties if the field is stored in the spectral space $[k_x, k_y, k_z]$. In a scenario like that, all the values of the flow field in spectral space $\hat{\boldsymbol{X}}$ must be used for the evaluation of the nonlinear terms $\boldsymbol{NL}$ at a single point in physical space. Since this must be done for all points of the physical discretisation, the computational cost is excessive. Another approach would be to evaluate all the points of the physical space instantaneously. However this approach would occupy a double amount of memory.

Following the latter approach one memory allocation is needed to store the field in the physical space $\boldsymbol{X}$ and a second one for the field in spectral space $\hat{\boldsymbol{X}}$. Keeping in mind that DNS is usually operated close to the maximum available memory capacity, such an approach affects the finest resolution of turbulent scales that the solver can achieve.

A popular strategy to tackle the performance problem described in the previous paragraphs is the Rogallo technique, described in figure 3.2. The approach of Rogallo lies between the two scenarios mentioned and balances the CPU time and memory allocation needs. The field variables at time t for the whole computational domain are stored as a single array $\boldsymbol{X}$, expressed in spectral space for the x and y directions and in physical space for the z direction as shown in figure 3.1(c). The array $\tilde{\boldsymbol{X}}$ defined in the (k_x, k_y, z)-space is the starting point of the Rogallo algorithm shown in stage **1** of figure 3.2. The next step is to compute the nonlinear terms $\boldsymbol{NL}$. Having stored the flow field in the above semi-spectral space, any variable in the physical space is a function of the weights of the wavenumbers stored at the same z-coordinate at stage **1**.

Using a loop along the z-axis, (stage **2**), each iso-z plane of $\tilde{\boldsymbol{X}}$ is extracted and then transformed to the (k_x, y, z)-space, (stage **3**), and finally to the physical (x, y, z)-space at stage **4**. At stage **5** the plane contains the field variables in physical space $\boldsymbol{X}$, and $\boldsymbol{NL}$, is evaluated and stored in the plane containing $\boldsymbol{X}$. The plane containing the nonlinear terms is transformed back to the (k_x, y, z)-space, (stage **6**), and stored, (stage **7**). The iso-z loop continues for all the N planes along the z-axis.

At stage **8** the domain is being swiped across the k_x*−direction*. Each iso-k_x plane is transformed to spectral space $[k_x, k_y, k_z]$,(stage **9**). Having expressed the specific plane in purely spectral space $\hat{\boldsymbol{X}}$, the time advancement equation (3.40) can be evaluated, (stage **10**). Then the approximation of the field for the intermediate Runge-Kutta step can be transformed, (stage **11**) and stored back, (stage **12**) using the minimal storage time advancement scheme until the final Runge-Kutta step is achieved, (stage **13**).

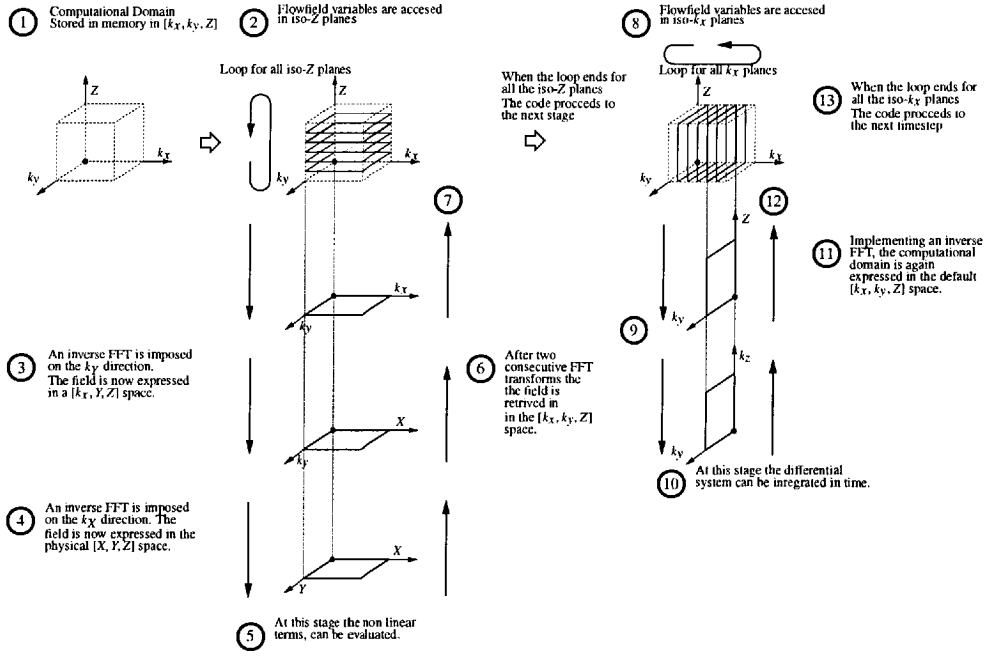

Figure 3.2: Structure of the pseudospectral DNS code.

3.3 The parallel pseudospectral algorithm

It is apparent that computational power is crucial for DNS of turbulent combustion. The need of simulations with Reynolds number as high as possible lead to increased memory and CPU time demands. DNS simulations on single processor machines yield low to moderate Reynolds numbers only. In contrast, modelling methodologies for turbulence and combustion, usually assume that the Reynolds number is high.

Furthermore, the introduction of reactive species for the modelling of combustion processes increases the computation costs significantly if detailed chemistry needs to be used. A realistic investigation of the extinction and re-ignition phenomena means that the flame cannot be modelled by a simple one-step chemistry mechanism, as is often employed for DNS of reacting flows. The four-step mechanism used for the modelling of methane combustion in the present study demands the solution of five additional transport equations together with the three momentum transport equations on a 512^3 grid, resulting in a simulation of 10^9 independent variables.

Given that typical flames configurations involve shear flows like jets and shear

layers, turbulent combustion is best investigated in inhomogeneous transitional flows. Such cases require more computational power because the large velocity gradients in the shear layer that demand reduced computational time steps and thus increased demand for computational power.

A parallel DNS algorithm has therefore been developed that allows for increased computational power and memory allocation, and DNS solutions of relatively high Reynolds number shear flows with multistep chemistry become feasible.

3.3.1 Parallelisation technique

A parallelisation of a computational algorithm aims to split the computational domain into segregated partitions which are to be solved separately by different computers. This reduces the memory allocation needs on each computer to a fraction of the total memory needs. Also, the computational cost for each processor reduces to the solution of each partition, instead of the whole domain. Domain splitting, however, introduces a need of communication between the computers which is an extra computational cost that all parallelised codes share.

Specific issues arise for the parallelisation of pseudospectral codes. Spectral representation lacks spatial characteristics. As mentioned before, the weights of the eigenfunctions for a field expressed in spectral space affect all the points in physical space. This characteristic of the Fourier transform introduces some difficulties for the partitioning of the computational domain. At some point of the computations information from the whole computational domain must be exchanged across the processors. In contrast to finite differences or finite volume algorithms where the communication between the partitions takes place only along the boundaries of the partitions, the weights of the basis functions are important for the evaluation of the governing equations to all the points inside each partition.

It will be shown in the next section that the memory allocation and output storage remain the bottlenecks of the DNS simulations, even for parallel computations. The parallelisation presented in this study has been designed in order to demand the least possible communication of fields and the smallest possible allocation of memory. To achieve this the communication takes place during the calculation of the nonlin-

ear terms, where only $\widehat{NL}$ is returned back to the nodes at the stage **5** of figure 3.2. Furthermore, the structure of the Rogallo technique is respected, so that the memory allocation remains low, not exceeding the limit of $1GByte$ per node for the calculations presented in this study.

Parallel pseudospectral solvers have been used in local and shared memory architectures by Iovieno *et* al. [149], where a maximum grid of 256^3 was achieved. However, for this case a speed oriented strategy had been followed where the matrix of the field is transposed before each time advancement loop. This demands a second array to be allocated for the transpose of the field. The parallel implementation of Itakura *et* al. [61] for the Earth Simulator supercomputer was based on a hybrid memory architecture where clusters of eight nodes share the same memory, whereas these clusters are connected with two switches of $12.3GBytes/sec$ each.

The parallel code is based on the single process DNS code of Kerr [42], written in FORTRAN77. The Message Passing Interface (MPI) has been used for the management of the communication between the nodes. The computations were carried out on non-shared memory Linux computer clusters.

In the case of the Rogallo code used in the present study, the computational domain consists of the flow field variables stored in the hybrid space (k_x, k_y, z)-space. The domain is split along the k_x axis into n_p partitions, where n_p is the number of processors employed. Thus, each partition consists of local domains with dimensions $n_x/n_p, x_y, n_z$ as seen in figure (3.3).

The reason of partitioning along one of the directions only is to avoid any need for communicating information across the processors during the FFT loops that transform real space into spectral space. According to this setup there should be exchange of information only during the stage of the calculation of the non-linear terms, (stage **5**).

The starting point of the parallel algorithm is stage **1** in figure (3.3). At this point, each node has the information for its own partition of the domain expressed in (k_x, k_y, z)-space and this information is stored in the local memory.

Each one of the processors undertakes the task of calculating the non linear terms for one iso-z plane. However, the information of the whole iso-z plane is split among the processors. At this point (stage **2**), all the other processes send the information

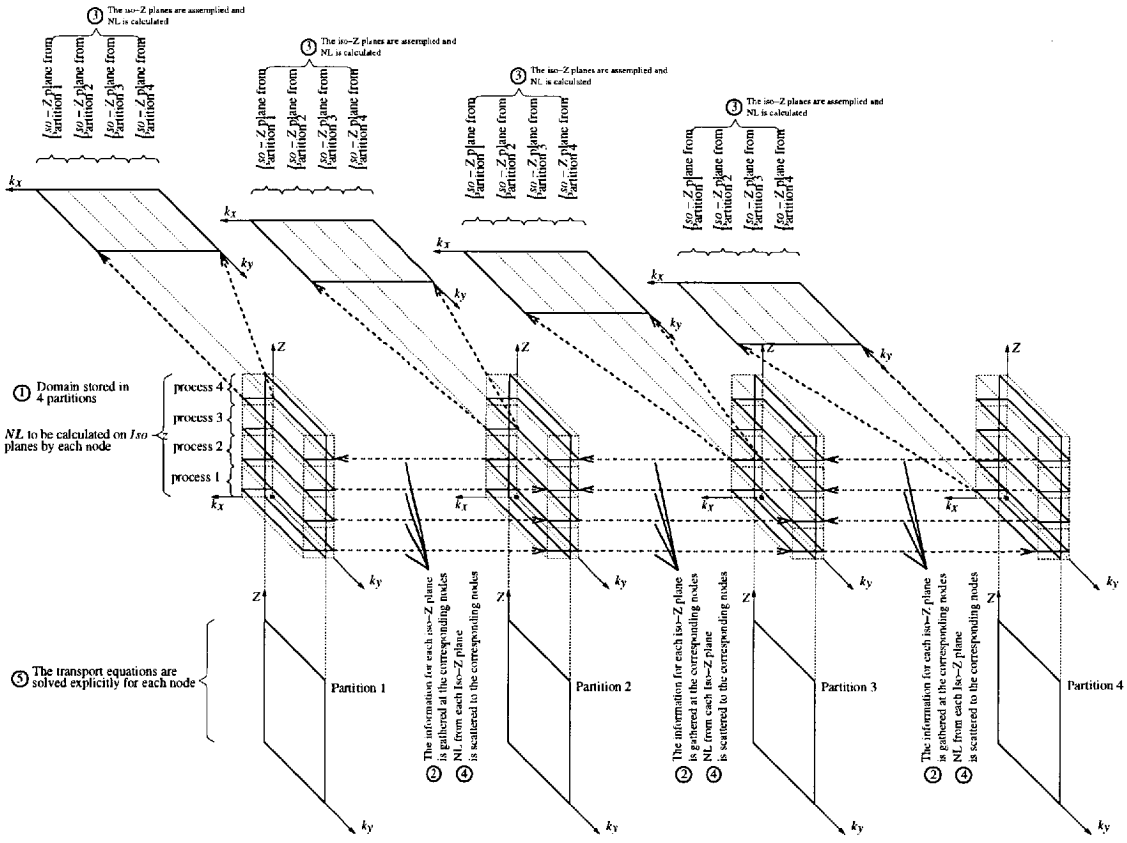

Figure 3.3: Structure of the parallel pseudospectral DNS code.

to the node that has undertaken the calculation of the non-linear terms for the specific plane. The necessary information is gathered and assembled in the node. This exchange of information is implemented for all the nodes.

After this stage all the nodes engaged have obtained an entire plane, stage **3**. Each process can proceed to the transformation of the $k_x - k_y$ planes to physical space $x - y$ and the calculation of the nonlinear terms. After the transformation of the calculated nonlinear terms to the (k_x, k_y, z)-space, the information must be scattered back to the nodes and stored, in order to be used for the calculation of the time evolution of the field, stage **4**. Then a new iso-z plane is appointed to each processor, the iso-z plane is assembled in each node and the calculated non linear terms are stored back to each node.

When all the iso-z planes have been read through, the algorithm proceeds to the next stage where the time evolution equation (3.40) must be evaluated. Each process

undertakes the task of calculating the estimate for the time advancement for one iso-k_x plane. At this point, stage **5**, there is no need for communication among the nodes. The nonlinear terms and the field variables are stored in the local memory of each node. When the calculations for all the N/n_p iso-k_x planes are finished in each processor, the algorithm is ready to advance to the next time step.

3.3.2 Evaluation of the parallelisation

In order to evaluate the efficiency of the parallelisation DNS simulations, on one, two, four, eight, and sixteen processors where performed using two different meshes. The details of the simulations are not of any particular interest here. The specific simulations are DNS computations of homogeneous and isotropic turbulence where only the velocity field is integrated in time. During these calculations the allocated memory and the average time needed for each time step were measured. The CPU time per time step, T_n, and the allocated memory per processor M_n are presented in table 3.1, as functions of the numbers of processors.

Table 3.1: Memory usage per processor, and average CPU time per time step for the two test simulations

	512^3 mesh		256^3 mesh	
Number of processors	Memory Used [Mbytes]	CPU time [sec/cycle]	Memory Used [Mbytes]	CPU time [sec/cycle]
1	4171	771	603	80
2	2151	405	348	38
4	1135	279	220	27
8	638	203	158	25
16	390	171	125	23

The assessment of the parallelisation performance shown in table 3.1 has been carried out on a cluster of AMD Opteron dual processors. The CPU clock frequency for the specific machine is $2393MHz$ while the memory corresponding to each pair of processors is $2GBytes$.

The efficiency of the parallelisation can be expressed in comparison to an ideal parallelisation. An ideal parallelisation of an algorithm on n_p processors is expected to

be exactly n_p times faster and to allocate n_p times less memory than the single process algorithm. Thus, the parallelisation efficiency for the CPU-time e_{CPU}, and the memory allocation e_{MEM} can be defined as a percentage of the ideal values.

$$e_{CPU} = \frac{\frac{1}{T_n}}{n_p \frac{1}{T_1}} \cdot 100\% \ , \ e_{MEM} = \frac{M_n}{\frac{M_1}{n_p}} \cdot 100\% \ . \tag{3.41}$$

As mentioned above, the implementation of a parallel algorithm, introduces additional memory allocation, and extra array manipulations. Moreover, the computational time is increased due to the communication needed across the processors. These extra costs, cause a deviation of the speed and memory allocation from the ideal. The effect of the parallelisation on the performance of the parallel algorithm used in this study can be seen in figures 3.4 and 3.5. As the number of processors increases, the need of communication and extra memory allocation increases, affecting both parallelisation efficiencies.

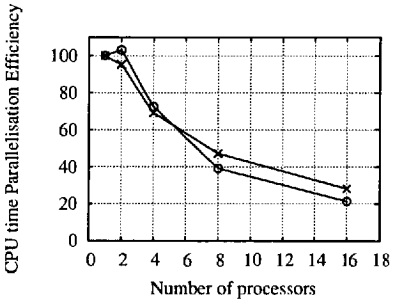

Figure 3.4: Efficiency of the parallelisation for the CPU time. Symbols; ⊙, 256^3 mesh, × 512^3 mesh

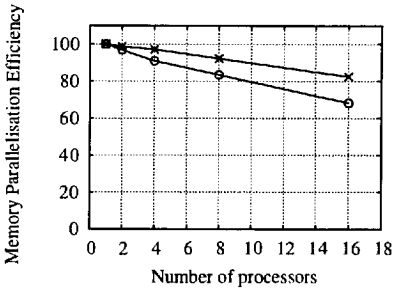

Figure 3.5: Efficiency of the parallelisation for the memory usage. Symbols; ⊙, 256^3 mesh, × 512^3 mesh

As seen in figure 3.4, the increase of communication due to the increase of the number of the nodes, causes a dramatic reduction of the parallelisation efficiency. This is common to pseudospectral codes where all the information for the calculation of the non linear terms must be scattered and gathered among the nodes. In contrast to finite difference codes where information is exchanged only across the boundaries of the partitions, in spectral codes each process needs information from the whole field in order to execute the integration of the flow field.

Given that a typical memory capacity for available Linux clusters is $1GByte$, parallelisation is the only way to achieve DNS of 512^3 nodes, where the use of 8 processors reduces the memory demands to less than $1GByte$ per node. Furthermore, simulations of combustion incorporating a four step chemistry mechanism requires an additional 166% of memory allocation and 16 processors are needed to reduce the memory allocation to less than $1GByte$ per node. Note that e_{MEM} stays above 80%.

Chapter 4

The numerical experiments

The present study includes the DNS of both reacting and non-reacting mixing of methane and air in turbulent flow fields. In this chapter, the details of these simulations are outlined and the results of the simulations are evaluated in comparison to experimental results and theoretical principles.

The turbulent combustion DNS cases are characterised by two types of initialisations for the velocity field, that represent two typical "families" of flow fields. The first is the velocity field of decaying homogeneous and isotropic turbulence. The second is the transition of a double shear layer from laminar to fully turbulent. For the double shear layer case, two simulations with different orifice Reynolds number and momentum thicknesses of the shear layer have been carried out. However, the turbulence intensity does not vary for the homogeneous isotropic turbulence case.

For the non-reacting mixing cases an initial distribution of a single conserved scalar, or contaminant, is assumed. In the simulations of mixing in homogeneous isotropic turbulence the conserved scalar is initialised as pockets of a contaminant surrounded by ambient fluid. For the shear layer simulations the contaminant is contained in the jet, surrounded by quiescent ambient fluid.

The chemistry of the reacting simulations of methane is modelled by a four-step mechanism for hydrocarbon flames. The four-step mechanism has been chosen since it allows for extinction and re-ignition without adding too much overhead to the computations due to an excessive number of reactive species. One should be aware, how-

ever, that a four-step mechanism will certainly not capture all flame dynamics due to extinction and re-ignition, but is likely to approximate the mean and the variance of temperature and major species concentrations rather well [17].

This mechanism is common for all the reacting simulations. However, the pre-exponential factors included in the formulation of the chemistry reaction rates are scaled in order to provide simulations of different levels of extinction. Specifically, four reacting cases with different levels of extinction have been simulated for each one of the two families of velocity initialisations, more detail is given in section 4.1.3.

The initialisation of the species distribution for the reacting cases is based on the initialisation of the mixing problems, where the contaminant is replaced by the mixture fraction. The reacting species distribution is provided as a function of the mixture fraction using a precomputed flamelet solution. This leads to pockets of methane surrounded by oxidiser for the homogeneous turbulence case, and a jet of diluted methane issuing in a quiescent air environment for the planar jet cases.

The momentum and scalar transport is modelled assuming constant density, viscosity and diffusivities. Thus, the solution for the mixture fraction mixing in the reacting cases does not differ from the solution for the mixing of the contaminant in the non-reacting simulations. The solution of the mixing problem is contained in the reacting problem. The reason for running a separate pure mixing case is that more frequent data probing is needed for the capturing the performance of LES micromixing modelling during the transition period.

In the first section of this chapter, the setup of the reacting mixing of homogeneous isotropic turbulence is discussed, starting from the initial conditions for the velocity field and the initialisation of the mixture fraction. Then, the four-step reaction mechanism used is presented along with the initialisation of the reacting species.

Next, three differentiation schemes used for the solution of the reactive species transport are assessed. The performance of each solution is assessed on the basis of performance, (i.e. properly capturing the reaction rates in the flame front), and computational cost. The presentation of the homogeneous simulations is completed with the description of the details of the four methane combustion cases with different levels of extinction that have been carried out.

The last sections of this chapter deal with the cases of pure mixing and methane combustion in a planar jet. The results for the velocity field are compared with experiments, while the proper resolution of the reaction region is also discussed.

The DNS database extracted from the non-reacting cases are used for the investigation of the turbulent mixing and the assessment of the closure techniques used for the turbulent mixing in LES. The simulations with reaction are also used for the investigation of the closure of the reaction rate terms in CMC and the effect of local extinction and re-ignition on the performance of singly and doubly conditioned CMC.

4.1 DNS of reacting mixing in homogeneous isotropic turbulence

Combustion in homogeneous isotropic turbulence and the performance of singly conditioned CMC has been investigated by Mell *et* al. [43], using DNS with a simple one-step reaction. Also, Swaminathan and Bilger [41] have used DNS for the assessment of CMC and SLFM closures in turbulent combustion using a two step reaction mechanism. Furthermore, DNS solutions with two-step chemistry have been used for the investigation of single and double conditioning closures in flames with local extinction and re-ignition by Kronenburg [18]. The homogeneous turbulence simulation presented in this section is similar to the above mentioned simulations as far as the flow field and the mixture fraction initialisations are concerned. However, the chemistry initialisation and the chemistry mechanism is the four step mechanism of Jones and Lindstedt [36], which has been used in the DNS of Kronenburg and Papoutsakis [17]. This relatively more complicated chemistry mechanism is introduced for the more appropriate capture of the local extinction phenomenon.

In short, the momentum transport is solved using the pseudospectral code described in chapter three for a cubic domain, with dimensions $(2\pi)^3$ and periodic boundary conditions. For the species transport, both spectral and finite differences methods are used.

4.1.1 Initialisation of the velocity field

The initial velocity field of homogeneous and isotropic turbulence is achieved in two stages. At first, a synthetic turbulent flow field is constructed using equation (3.37). However, this flow field is not derived from a solution of the Navier-Stokes equations in time. Thus, it is not characterised by an organised inertial range and does not respect high order velocity correlations [42]. In order to derive a homogeneous isotropic turbulent flow field, the synthetic flow field is integrated in time, while the large eddies are forced. The forcing procedure mimics the energy cascade from the large scales and allows the flow field to be integrated in time without reduction of the absolute turbulence levels due to viscosity [42]. In the cases simulated here, the forcing is implemented by artificially increasing the energy of the fluctuations for the two lowest wavenumbers $|\boldsymbol{k}| = 1$ and $|\boldsymbol{k}| = 2$ when the total turbulent kinetic energy becomes smaller than its initial value. This procedure lasts for seven eddy turnover times and the final velocity field is integrated for just half an eddy turnover time without any forcing in order to eliminate the effect of forcing on the large scales. The resulting flow field serves as an initial condition for the simulations presented here and is characterised by a Taylor Reynolds number of $R_\lambda = 54$.

4.1.2 Initialisation of the mixture fraction field

The initialisation of the reacting species and of the temperature field is based on a SLFM solution, where the scalar dissipation rate at the stoichiometric has been matched with the mean scalar dissipation at stoichiometric in the DNS. Following Mell *et* al. [43], the mixture fraction is initialised as a distribution of large scale areas with size close to the integral length scale of the velocity field, where the mixture fraction is constant and equal to zero or unity. On the borders between these areas the mixture fraction decays to zero gradually providing a smooth mixture fraction profile as seen in figure 4.1.

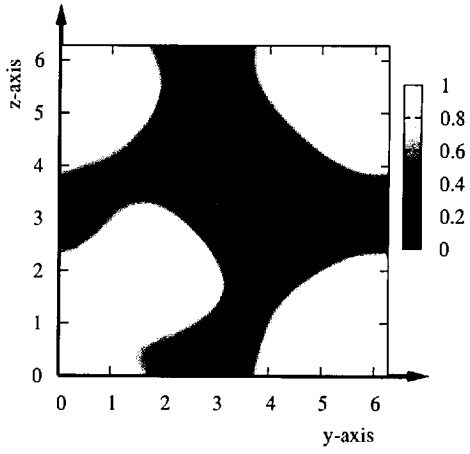

Figure 4.1: Initial distribution of the mixture fraction ξ across a cross-section of the domain used for the homogeneous turbulence simulations.

4.1.3 The reaction mechanism

Although a two step chemistry mechanism has been used to simulate extinction and re-ignition [18], such a choice does not allow a realistic simulation of the phenomenon [17]. When a two step mechanism is used, the temperature remains high and the mixture always re-ignites when the turbulence intensity drops sufficiently. For this reason, the reduced four-step mechanism for hydrocarbon combustion of Jones and Lindstedt [36] is used for the simulations presented here.

The flame modelled in the present simulations is a diluted methane flame. The fuel consists of methane, diluted with nitrogen and argon, while the oxidiser consists of a mixture that corresponds to the composition of air. The reduced reaction mechanism of Jones and Lindstedt [36] consists of the following four reactions,

$$\begin{aligned} CH_4 + \tfrac{1}{2}O_2 &\rightarrow CO + 2H_2 \quad (I) \\ CH_4 + H_2O &\rightarrow CO + 3H_2 \quad (II) \\ H_2 + \tfrac{1}{2}O_2 &\rightleftharpoons H_2O \quad (III) \\ CO + H_2O &\rightleftharpoons CO_2 + H_2 \quad . \quad (IV) \end{aligned} \tag{4.1}$$

The species that appear in the reactions shown above are methane, CH_4, hydro-

gen, H_2, carbon monoxide, CO, oxygen, O_2, water, H_2O, and carbon dioxide, CO_2. According to the stoichiometry of this reaction mechanism the concentrations of the six above species can be expressed as a function of four independent variables. The independent variables chosen are the mass fractions of methane, Y_{CH_4}, hydrogen, Y_{H_2}, carbon monoxide, Y_{CO}, and the mixture fraction, ξ. Following equation (2.41) for Y_O^0 and Y_F^0, the mixture fraction can be expressed as,

$$\xi = \frac{sY_F - Y_O + 1}{s + 1}, \tag{4.2}$$

where s is the stoichiometry ratio, Y_F is the mass fraction of the fuel and Y_O is the mass fraction of the oxidiser. The fuel mixture consists of CH_4, N_2, and Ar with a composition of 15%,34% and 51% respectively. The oxidiser is also a mixture, which consists of O_2 and N_2 with a composition of 30% and 70% respectively. This composition of fuel and oxidiser provides two streams with similar properties close to the ones of air. In addition this combination has been chosen in order to increase the value of the stoichiometric mixture fraction which is equal to $\xi_{st} = \frac{1}{3}$, given that an increased numerical resolution is needed for a smaller value, [41].

Following Jones and Lindstedt [36], the forward reaction rate for each one of the reactions 4.1(I-IV) is provided by the formulae

$$\begin{aligned}
\omega_I^f &= cA_I^f T^{b_I} e^{-E_I/RT}[CH_4]^{1/2}[O_2]^{5/4} \\
\omega_{II}^f &= cA_{II}^f T^{b_{II}} e^{-E_{II}/RT}[CH_4][H_2O] \\
\omega_{III}^f &= cA_{III}^f T^{b_{III}} e^{-E_{III}/RT}[H_2]^{1/2}[O_2]^{9/4}[H_2O]^{-1} \\
\omega_{IV}^f &= cA_{IV}^f T^{b_{IV}} e^{-E_{IV}/RT}[CO][H_2O].
\end{aligned} \tag{4.3}$$

According to the above expressions, the reaction rate is a function of temperature, the ideal gas constant R, the activation energy E_i and the pre-exponential factor A_i^f for each reaction i. The parameters that appear in the expressions (4.3) for the reaction rates, are provided in table 4.1. The backward reaction rates are defined according to the equilibrium constants for each one of the reactions, following Jones and Lindstedt

[36]. Note that the reactions *I* and *II* are supposed unidirectional, and as such, the backward reaction is not considered at all.

Table 4.1: The parameters of the reduced chemistry mechanism for CH_4 combustion.

Reaction	A^f	b	E
I	0.44×10^{-12}	0	3×10^4
II	0.30×10^{-9}	0	3×10^4
III	0.68×10^{-16}	−1	4×10^4
IV	0.275×10^{-10}	0	2×10^4

In equations (4.3) the pre-exponential factor A^f is multiplied by a non-dimensional scaling factor c, which varies between 0.00045 – 0.003 for the homogeneous combustion DNS cases, and between 0.003 – 0.018 for simulations of the jet flames. The introduction of this scaling aims to provide a series of simulations, characterised by different levels of local extinction, a phenomenon governed by the ratio between turbulent and chemical length scales, i.e. the Damköhler number provided in equation (2.52). Reducing the turbulence time scales leads to a prohibitive increase of the computational cost for the DNS. For example, simulations in Sandia Flames D-F give some indication of the local turbulent Reynolds numbers when extinction occurs, and it is estimated to be of the order of $O(10^4)$ [18], whereas in turbulent DNS an order of just $O(10^2)$ can be reached. Following Swaminathan and Bilger [144] or Kim *et* al. [150], the level of extinction can be controlled by adjusting the chemistry scales instead. As a result, using a series of values for the coefficient c, a series of simulations with desired levels of extinction is achieved, that can be used for a qualitative analysis of the phenomenon.

4.1.4 The initialisation of the reacting scalar fields

In all the reacting cases presented here, the initialisation of the reacting scalar fields is based on the initial distribution of the mixture fraction field, and a flamelet solution is used. In the case of methane combustion in a homogeneous turbulent flow field, the initialisation of the reactive species is based on the mixture fraction profile, shown in

figure 4.1. As mentioned in the presentation of the chemistry mechanism, the solution of transport equations for three reactive species are needed. Here methane, hydrogen and carbon monoxide are solved for explicitly. In addition, the evolution of sensible enthalpy h_s or temperature will be computed. The flamelet solution used for the initialisation of the reacting scalar fields is shown in figure 4.2.

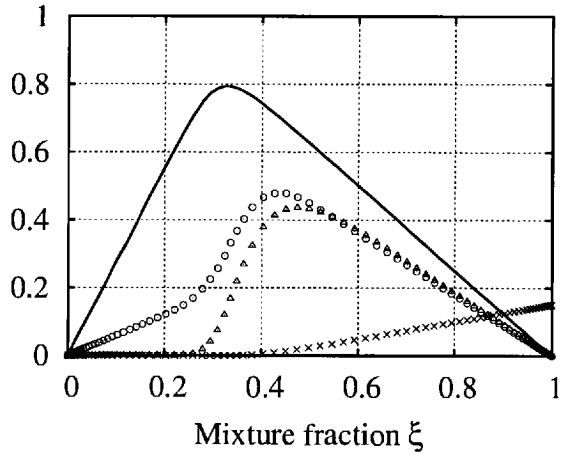

Figure 4.2: The SLFM solution used for the initialisation of the reactive species as a function of the initial mixture fraction distribution. Continuous line, – non-dimensionalised temperature T^*, symbols; × methane Y_{CH_4} ,⊙ carbon monoxide $10 \cdot Y_{CO}$, △ hydrogen $100 \cdot Y_{H_2}$.

For the constant properties simulations carried out, the sensible enthalpy is simply proportional to the temperature of the mixture,

$$h_s = C_p T \,. \tag{4.4}$$

The non-dimensional temperature, T^*, shown in figure 4.2 is normalised by the adiabatic temperature T_{ad} defined in equation (2.49) and the ambient temperature T_0.

$$T^* = \frac{T - T_0}{T_{ad} - T_0} \,. \tag{4.5}$$

Alternatively, a non-dimensional expression for the sensible enthalpy, Θ, can be used

$$\Theta = \frac{C_p(T - T_0)}{C_p(T - T_{ad})}, \tag{4.6}$$

which is equal to T^* for the current constant property simulations.

4.2 Test cases

In order to assess the numerical methods used for the solution of the reacting species transport in DNS, three test cases have been carried out. In each of the test cases, the momentum transport equation is integrated with the same pseudospectral code, described in chapter three. However, two alternative numerical methods have been used for the solution of the reacting species transport problem.

The details of these three test simulations are shown in table 4.2. The first test case, `HReactive-T1`, is solved using the spectral representation for the solution of both the momentum and the species transport equations. As it will be pointed out below, the pseudospectral scheme shows some disadvantages for the solution of the reacting scalars due to over and under shoots beyond the physical limits, and therefore two more test cases, i.e `HReactive-T2`, and `HReactive-T3` that employ finite difference algorithm instead, are also used for the discretisation of the reacting species.

The differentiation scheme for the `HReactive-T2` simulation is a simple central differencing scheme of fourth order, similar to the differentiation scheme used by Cant *et* al. [145] for DNS of reacting flows. The differentiation scheme for the `HReactive-T3` is the implicit sixth order scheme described by Lele [151]. Both differentiation schemes are popular for DNS simulations.

All three cases have common initial conditions and parameters. The mesh used in the finite difference approaches identical to the spectral solver, with 256 equivalent nodes in each direction. The three test cases have been integrated for three eddy turnover times starting from the forced homogeneous turbulence initial conditions at time $t^* = 7.5$. Given that the same problem is modelled, the instantaneous solutions must be identical and deviations due to different algorithms can easily be assessed by comparison of the test cases results.

The predictions of the mixture fraction distribution exhibit minor difference be-

Table 4.2: The parameters of the test cases HReactive-T1, HReactive-T2, and HReactive-T3.

CASE	HReactive-T1	HReactive-T2	HReactive-T3
VELOCITY FIELD			
Re_t	54	54	54
CHEMISTRY			
Scaling c	0.0015	0.0015	0.0015
NUMERICAL			
Mesh	256^3	256^3	256^3
Nodes	16,777,216	16,777,216	16,777,216
Velocity solver	Spectral	Spectral	Spectral
Species solver	Spectral	Finite differences	Finite differences
Differentiation	N/A	Central differences	Implicit Lele

tween the three test cases. In figure 4.3(**a**)-(**b**) the distribution of the mixture fraction is presented along the x-axis, at $y = \pi$ and $z = \pi$, for two instances of all three test simulations at $t^* = 8.32$ and $t^* = 10.53$ eddy turnover times. At both instances the three numerical methods provide the same solution.

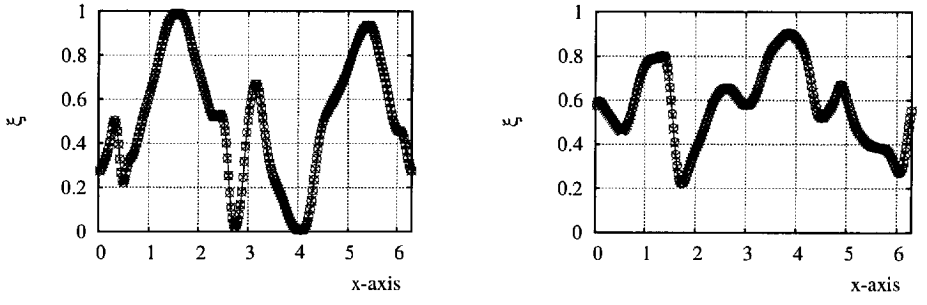

(a) **(b)**

Figure 4.3: Mixture fraction distribution across the x-axis. Symbols; ⊙, implicit scheme, × central differences, and continuous line, − spectral. (**a**) at $t^* = 8.32$ and (**b**) at $t^* = 10.53$

As far as the instantaneous distributions of the reactive species are concerned, the three solvers give the similar results, as seen in figure 4.4(**a**) for the methane mass fraction. However, the spectral method is limited when dealing with reacting scalars,

where the gradients for the reacting species are relatively steeper due to the effect of the flame front [26]. A closer look at the methane distribution provided in figure 4.4(**a**), is presented in figure 4.4(**b**) for $0.4 < x < 0.65$. The spectral representation of a steep gradient causes some overshoot on the lean side of the diffusion flame front, as seen in figure 4.4(**b**). Across this flame front the methane mass fraction reduces rapidly due to the reaction rate term ω_{CH_4}. Given that a central difference scheme is used, negative values may appear for all three test cases. These negative concentrations have very small values of the order of $O(10^{-4})$, and are set to zero for the calculation of the reaction rates [36]. The major difference in the behaviour of the spectral method lies in the positive overshoot of the order of $O(10^{-5}) - O(10^{-6})$ exhibited on the lean side of the flame front and can be attributed to the Gibbs phenomenon. However, as seen in figure 4.5(**a**), this small but positive value is located in areas where the temperature is still high due to convection from other flame fronts. Furthermore, the oxidiser mass fraction is also high and leads to a very high but spurious reaction rate, as seen in figure 4.5(**b**).

In cases where the oxidiser and the fuel are not well mixed, the spurious reaction rates may appear as filaments parallel to the flame front as is shown in figure 4.6. This happens during the initial time steps of the homogeneous and isotropic turbulence simulation and throughout the combustion simulation of a planar jet. In regions where the reactants are mixed, spurious reaction rates appear as spots as seen in figure 4.7.

Due to this inaccuracy of the spectral solver when dealing with reactive species, the finite differences methodology is used for the integration of the reacting species transport equations. Both central differences and implicit differentiation schemes, deliver the same results when used for the solution of simple transport equations of the species as seen in figures 4.4 to 4.5. However, the implicit differentiation scheme demands the solution of an algebraic system of equations to provide the first and second derivatives along each direction. In a parallel code the derivatives along the directions that cross the partition boundaries can be calculated by solving the above mentioned system instantaneously for all the collocation points at each time step. This demands the allocation of memory space for all the first and second derivatives of the field. Solving the algebraic system that is derived from the implicit expression of the deriva-

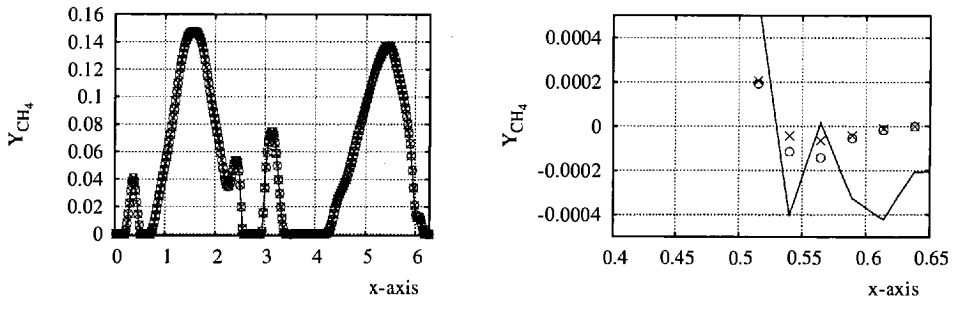

(a) **(b)**

Figure 4.4: Instantaneous distribution of the methane CH_4 concentration at time t^* = 8.32 eddy turnover times. Symbols; ⊙, implicit scheme, × central differences, and continuous line, – spectral.**(a)** along the x-axis **(b)** zoom on the reaction region at $x = 0.5$

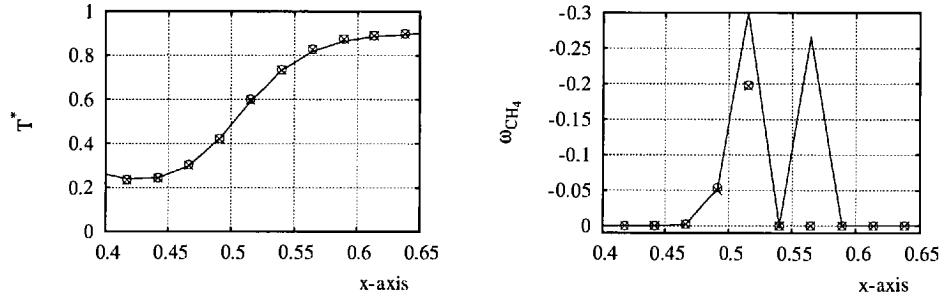

(a) **(b)**

Figure 4.5: Instantaneous distribution of the non-dimensionalised temperature T^* **(a)**, and the methane reaction rate **(b)**, along the x-axis at time t^* = 8.32 eddy turnover times. Symbols; ⊙, implicit scheme, × central differences, and continuous line, – spectral.

tives leads to the transmission of short but frequent messages in the cases of parallel computations. Due to the latency time needed to initiate a communication among computational nodes in a distributed memory cluster, the communication time becomes disproportional to the size of the exchanged information, and has a dramatic effect on the performance of the algorithm. Taking into account that the computational power available is marginal compared to the computational needs of the DNS carried out, the much simpler and economical fourth order central difference method has been chosen here and is used for all computations that are analysed in the remainder of this study.

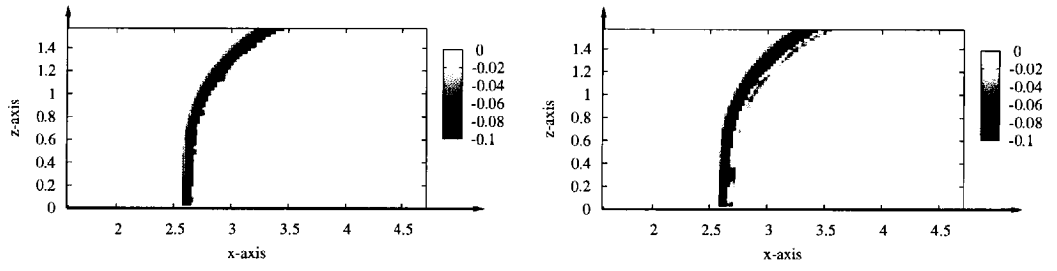

(a) (b)

Figure 4.6: Contour plots of the reaction rate for the methane ω_{CH_4} on the iso-y plane. at $t^* = 8.32$. **(a)** central differences solver **(b)** pseudospectral solver

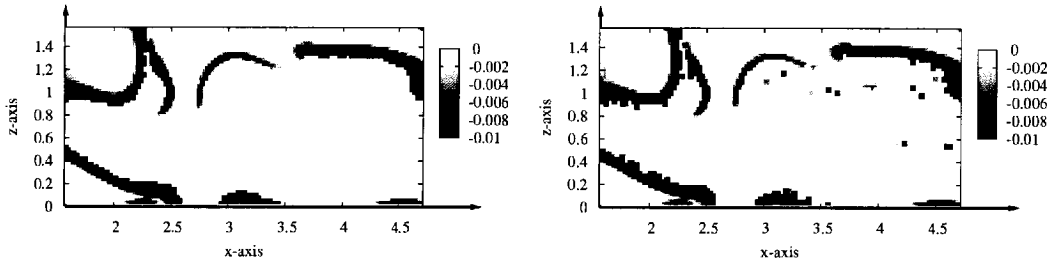

(a) (b)

Figure 4.7: Contour plots of the reaction rate for the methane ω_{CH_4} on the iso-y plane. at $t^* = 10.53$. **(a)** central differences solver **(b)** pseudospectral solver

Although the high accuracy implicit scheme is quite popular in DNS algorithms [152], it is used for the integration of the momentum transport equations in variable density flows. Given the efficiency of the pseudospectral code for the integration of the incompressible momentum transport equations for both homogeneous turbulence and well resolved shear layers and jets [87], this code is retained for the integration of the velocity field. The finite difference methodology is coupled with the pseudospectral code to provide the solution for the much simpler fourth order reactive species transport equations. The resulting hybrid solver is used for the derivation of the final DNS database presented in this study.

4.3 Combustion in homogeneous isotropic turbulence

Four DNS of methane combustion in homogeneous and isotropic turbulence have been carried out. In these simulations, the momentum transport equation is integrated using the parallel pseudospectral code. In this code, a finite differences solver is coupled with the momentum transport solver for the integration of the reacting species, as discussed in the previous section.

In order to study the modelling of local extinction and re-ignition, each case is characterised by different extinction levels. This is controlled by adjusting the pre-exponential scaling coefficient c. The details of the four simulations are presented in table 4.3. Apart from the scaling coefficient, all the other details of the simulation are identical. The initial conditions for these simulations have been achieved from synthetic turbulence initial conditions, forced for $t^* = 7.5$ eddy turnover times, as discussed in section 4.1.1. The initial field for the methane combustion in homogeneous isotropic turbulence is then integrated for four eddy turnover times until $t^* = 11.5$. .

In figure 4.8 the time evolution of the non-dimensional temperature T^* of the mixture located around the area of the stoichiometric mixture fraction, $\xi_{st} - 0.01 < \xi < \xi_{st} + 0.01$, is presented. Depending on the magnitude of the scaling coefficient c each case is characterised by different levels of extinction. Case `HReactive-A` totally extinguishes, whereas `HReactive-B`, and `HReactive-C` show high to medium extinction, while they re-ignite later on. Finally case `HReactive-D` presents very low levels of extinction. Given that the solution of the mixing problem for all the reacting cases is the same, the DNS data containing the solution of the velocity field and the mixture fraction consists the mixing case `HMixing`, which will be used for the investigation of scalar mixing in homogeneous and isotropic turbulence.

4.4 DNS of mixing in a planar jet

The planar jet case is a simulation of a jet stream issuing into an quiescent fluid of the same properties. The jet is supposed to consist of a non-reacting contaminant with mass fraction equal to unity around the centreline and equal to zero within the

Table 4.3: The parameters of the test cases `HReactive-A`, `HReactive-B`, `HReactive-C` and `HReactive-D`.

CASE	`HReactive-A`	`HReactive-B`	`HReactive-C`	`HReactive-D`
VELOCITY FIELD				
Re_t	54	54	54	54
CHEMISTRY				
Scaling c	0.00045	0.00100	0.00150	0.00300
NUMERICAL				
Mesh	256^3	256^3	256^3	256^3
Nodes	16,777,216	16,777,216	16,777,216	16,777,216
Total time	13.7	13.7	13.7	13.7
Timesteps stored	22	22	22	22
Data size	17*Gbytes*	17*Gbytes*	17*Gbytes*	17*Gbytes*
Velocity solver	Spectral	Spectral	Spectral	Spectral
Species solver	Finite differences	Finite differences	Finite differences	Finite differences
Differentiation scheme	Central differences fourth order	Central differences fourth order	Central differences fourth order	Central differences fourth order

quiescent fluid.

The transport equations that have to be solved are the momentum transport for the three components of the velocity field plus the scalar transport equation for the contaminant concentration. The computational domain of this simulation consists of a cube with dimensions $(2\pi)^2$ and is represented in a Cartesian coordinate system of three orthogonal axis.

4.4.1 Initial conditions

The setup of the initial conditions for the planar jet is illustrated in figure 4.9. This figure depicts a cross-section of the initial flow field on the iso-y plane. A hyperbolic tangent profile is used for the initialisation of the velocity and the scalar field distributions. A similar setup has been simulated by Stanley *et* al. [153], where a hyperbolic

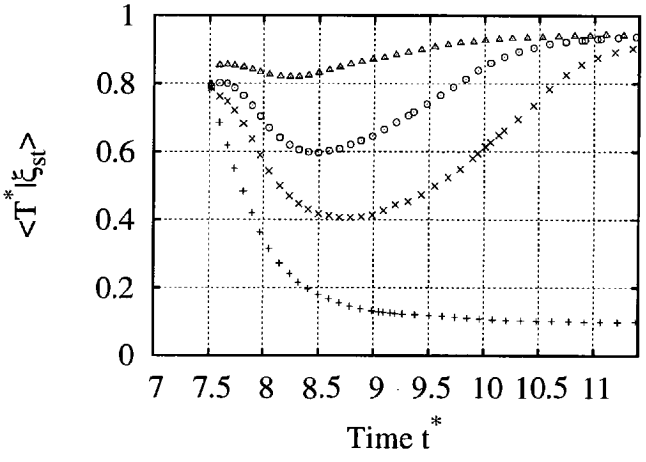

Figure 4.8: Time evolution of the non-dimensionalised temperature T^*, averaged on the stoichiometric mixture fraction $\xi_{st} = 0.333$, for the four combustion simulations in homogeneous and isotropic turbulence. Symbols; + `HReactive-A`, × `HReactive-B`, ⊙ `HReactive-C`, △ `HReactive-D`

tangent profile has been used for the boundary conditions of the DNS for a spatially evolving planar jet. In the case presented in this study the boundary conditions for all the quantities are periodic in all directions as imposed by the spectral algorithm, dictating a simulation of a planar jet evolving in time rather than space. The jet is issuing parallel to the x-axis, along the stream-wise direction, while the profile of the velocity is distributed along the z-axis defining the tranverse direction. This two dimensional velocity field does not vary in the span wise direction along the y-axis.

This setup initially consists of two laminar shear layers. However, this type of flow is unstable, and it is expected to exhibit a transitional stage until it becomes fully turbulent at the later stages of the mixing process, where the two shear layers will start merging into a fully turbulent jet.

The initial velocity field is a parallel flow, characterised by a one dimensional velocity profile. The initial profile is provided by equation 4.7 as a function of the z direction. The u component of the velocity along the x-axis is independent of the x and y directions and is defined as,

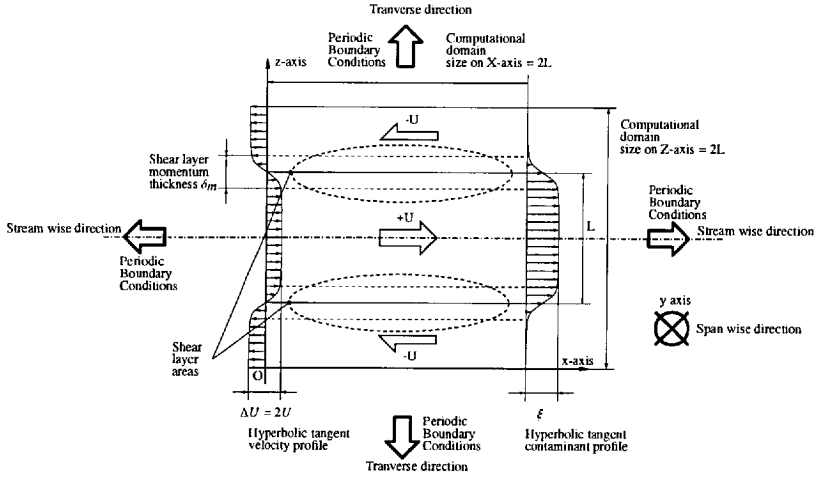

Figure 4.9: Setup of the initial conditions in the case of the planar jet.

$$u(x, y, z; t = 0) = \frac{\Delta U}{2}\left[\tanh\left(\frac{z - L/2}{2\delta_m}\right) - \tanh\left(\frac{z - 3L/2}{2\delta_m}\right) - 1\right], \qquad (4.7)$$

where L is the width of the jet, δ_m is the initial momentum thickness of each mixing layer and ΔU is the difference of the mean initial velocity between the two streams. This is illustrated in figure 4.9. The other two components of the velocity vector i.e. v and w, are zero.

The setup of the initial velocity field as described in equation (4.7) provides a parallel unidirectional laminar flow. A Kelvin-Helmholtz instability is expected to arise [154, 155], and the transition to turbulence is expected to occur [155]. In order to trigger the instability of this shear flow some perturbations have been added to the velocity field. The perturbations consist of the synthetic homogeneous and isotropic turbulent field described in section 3.3.2, and it is superimposed on the laminar planar jet flow field. The magnitude of the added perturbations is constant across the flow field and equal to 2% of the mean velocity field. Similar perturbations are introduced as inflow boundary conditions for the spatially evolving DNS of a planar jet by Stanley *et* al. [153] or as fluctuations included in the initial conditions of the temporally evolving DNS of a mixing layer by Rogers and Moser [154].

The contaminant distribution is initialised in a similar way to the u component of the velocity field according to,

$$\xi(x, y, z; t = 0) = \frac{1}{2}\left[\tanh\left(\frac{z - L/2}{2\delta_m}\right) - \tanh\left(\frac{z - 3L/2}{2\delta_m}\right)\right] . \tag{4.8}$$

The distribution of the contaminant provided by equation (4.8) results in a constant concentration in the core of the jet, which is equal to unity, and smoothly decays to zero in the surrounding air as seen in figure 4.9. This setup provides a spatially correlated initial distribution of the momentum and the scalar concentration.

4.4.2 Cases studied

Two simulations of a non-reacting planar jet have been carried out. The details of the two cases are presented in table 4.4. Each case is characterised by a flow Reynolds number defined as

$$Re = \frac{\Delta U L}{\nu} , \tag{4.9}$$

Case `JMixing-A` is characterised by a low Reynolds number of $Re = 3141.5$ and is resolved on a cubic orthogonal equivalent mesh of 256^3 nodes. The flow Reynolds number for the case `JMixing-B` is, equal to $Re = 6283.0$. The mesh used for the full resolution of case `JMixing-B`, has 512 nodes in each direction.

4.4.3 Velocity field

The planar jet cases presented consist of two mixing layers lying on two iso-z planes, located at positions $z_1 = \pi/2$ and $z_2 = 3\pi/2$ respectively, shown in figure 4.9. The solution of the current DNS simulation can be compared with results from experiments of spatially evolving shear layers [156, 75]. A typical experimental setup of a plane shear layer is presented in figure 4.10. The two streams issue from the orifice or splitter plate and are characterised by almost uniform velocity profiles U_1 and U_2 with low turbulence intensities. Within the mixing region, the time averaged streamwise velocity changes smoothly and monotonically from U_1 to U_2, and a mean convection velocity can be appointed to the mixing layer, defined as the mean of the velocities for each stream $U_m = (U_1 + U_2)/2$. A non-dimensional streamwise velocity is then defined as,

Table 4.4: The parameters of the planar jet mixing cases `JMixing-A` and `JMixing-B`.

CASE	`JMixing-A`	`JMixing-B`
VELOCITY FIELD		
L	π	π
ΔU	10	20
δ_m	1/10	1/20
Re_{jet}	3141.5	6283.0
u'	$0.01\Delta U$	$0.01\Delta U$
u_{rms}	0.015	0.015
NUMERICAL		
Mesh	256^3	512^3
Nodes	16,777,216	134,217,728
Total time	52.7	50.1
Timesteps stored	55	83
Data size	$8.4Gbytes$	$100Gbytes$

$$U^* = \frac{U - U_2}{U_1 - U_2} . \tag{4.10}$$

A characteristic length for each streamwise position x of the shear layer, is the shear layer width $\delta_{0.9}$, defined as the distance on the x-axis between the locations where $U^* = 0.1$ and $U^* = 0.9$. The width $\delta_{0.9}$ increases proportionally to the streamwise distance x from the jet orifice [156]. Thus, a non-dimensional expression for the transverse distance from the shear layer centreline on the z-axis can be written as,

$$\zeta = \frac{z}{x} . \tag{4.11}$$

In contrast to DNS of spatially evolving planar jets [88, 153], the simulation presented in this study evolves in time rather than in space. For this reason the mean velocity at each tranverse position on z-axis is calculated as the mean of the spatial distribution of the the turbulent velocity across the homogeneous directions perpendicular to the z-axis, i.e. the iso-z planes. The shear layer thickness in computations of time evolving jets increases in time [74], whereas it remains constant across the the streamwise direction, as imposed by the periodic boundary conditions. In order to make a

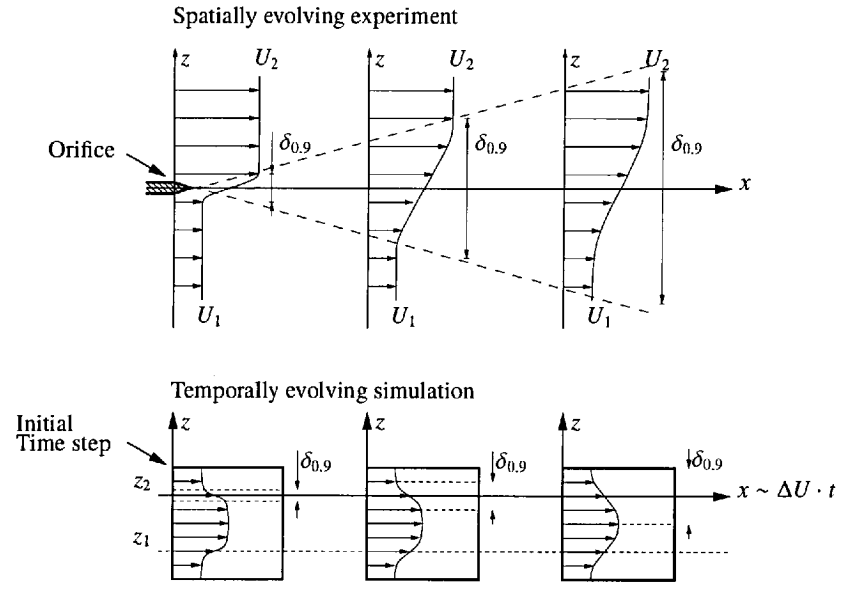

Figure 4.10: Comparison of the experimental configuration, with the time evolving DNS setup.

comparison with experimental results, a virtual distance from the orifice can expressed as the product of the convection speed of the shear layer with the time, thus a similarity variable for the tranverse wise distance from the shear layer is defined as

$$\zeta = \frac{z - z_i}{U_m \cdot t}, \tag{4.12}$$

where t is the time from the beginning of the simulation, and z_i is the position of the shear layer on the z-axis. The current initialisation dictates that the velocity of the jet is $\Delta U/2$, whereas the surrounding fluid is moving in the opposite direction, with the same velocity magnitude. However, it can be supposed that the jet is issuing with a velocity $U_2 = \Delta U$ on the centreline, whereas the surrounding fluid is quiescent i.e. $U_1 = 0$. In this case, the mean velocity introduced in equation (4.10) is the mixing layer convection speed, i.e. $U_m = \frac{U_1 - U_2}{2} = \Delta U/2$. The equivalent length $\Delta U t/2$ is the distance that the shear layer would have conveyed from the start of the mixing, assuming that the surrounding fluid is quiescent, and can be related to the streamwise distance from the orifice in a spatially evolving experimental setup, as seen in figure 4.10.

The typical time scale for a DNS of a turbulent flow is the eddy turnover time. This is defined as the time scale of the large turbulent structures at the initial conditions. For the planar jet case, the initial eddy turnover time definition is based on the velocity difference ΔU and the shear layer initial momentum thickness δ_m as

$$t_0 = \frac{\delta_m}{\Delta U} , \tag{4.13}$$

Time is then normalised by this new eddy turnover time,

$$t^* = \frac{t}{t_0} . \tag{4.14}$$

Given that the experiments for planar jets and shear layers are characterised by relatively high Reynolds numbers, the results from the high Reynolds number simulation case `JMixing-B` are compared with actual experiments. The self similarity of the turbulent mixing layer is exhibited in figure 4.11(**a**). In this figure it can be seen that the mean velocity profiles for a series of time steps of the simulation from the early stages to the final time step, collapse when transformed to ζ-space using equation (4.11). In addition, the velocity profiles are in good agreement with the experimental results of Bell and Mehta, [157] as shown in the same graph.

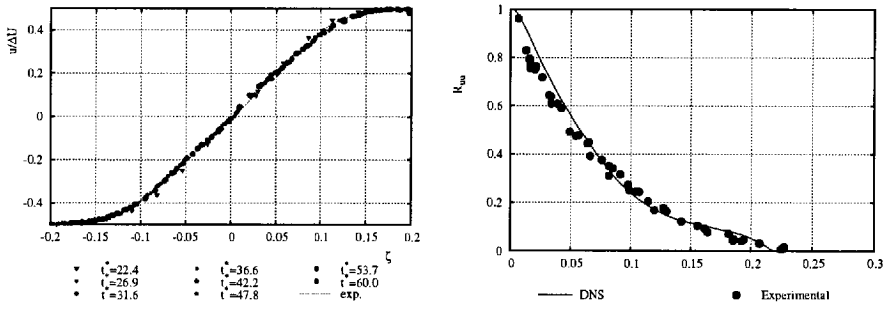

(**a**) (**b**)

Figure 4.11: (**a**) The mean velocity profiles for several time steps as a function of the similarity variable ζ case `JMixing-B`. Dots from the experiment of Bell and Mehta [157]. (**b**) Autocorrelation coefficient as a function of r at $\zeta = 0$, case `JMixing-B`. Dots from the experiment of Wygnanski [75].

The next figure 4.11(**b**) depicts the distribution of the autocorrelation coefficient of

the streamwise component of the velocity field at time $t^* = 60.0$ in comparison to the distribution of the experimental results of Wygnanski [75]. Furthermore, the turbulence intensities at $t^* = 60.0$ are in good agreement with the experimental results of Bell and Mehta [157]. The comparison of the computational results with the outcomes of experimental research shows that the DNS database is a realistic, model free simulation of a shear flow.

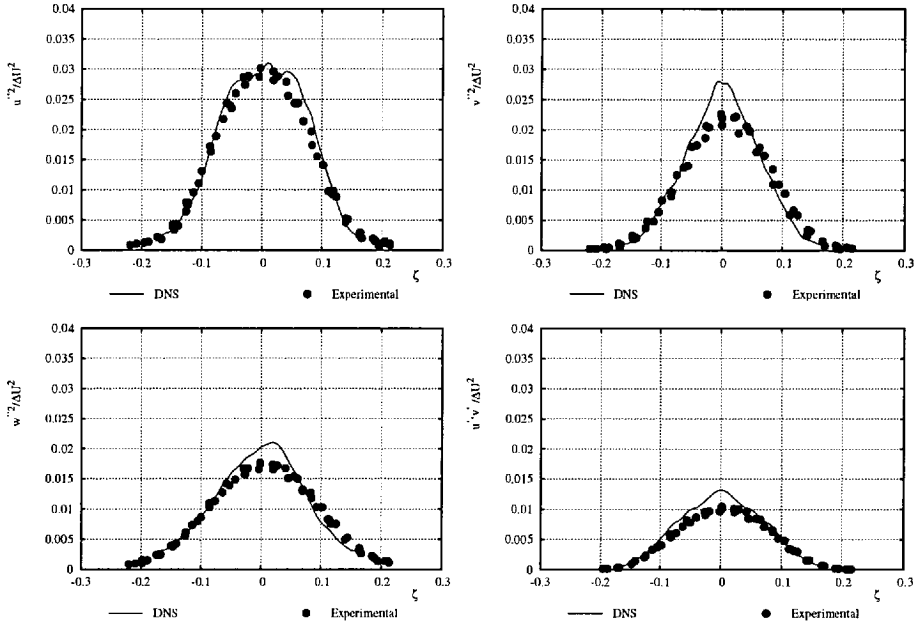

Figure 4.12: Turbulent intensities at time step $t^* = 60.0$ from the case `JMixing-B`, compared to the experiments of Bell and Mehta [157]

The mixing layer is well known for its coherent structures [72]. During the first stage of transition vorticity tubes also known as rollers appear [71]. These cylindrical regions are characterised by large vorticity magnitudes, exhibit a two dimensional structure and extend along the span wise direction as predicted by linear stability analysis for the Kelvin-Helmholtz instability [29]. In the later transitional stage, the vorticity tubes become interconnected with three dimensional structures, the so-called rib vortices as shown in figure 4.13. In this figure the iso-surface of the vorticity magnitude equal to 100 is depicted at $t^* = 17.2$ identifying high vorticity areas in the shear flow. The domain shown in figure 4.13 spans from 0 to $\frac{\pi}{2}$ on the x-axis, from 0 to $\frac{\pi}{2}$ on the y-axis and from $\frac{\pi}{4}$ to $\frac{3\pi}{4}$ on the z-axis, covering one sixteenth of the computational

domain. The pairing and later the cascade of the resulting turbulent structures finally results in a fully turbulent shear layer [154].

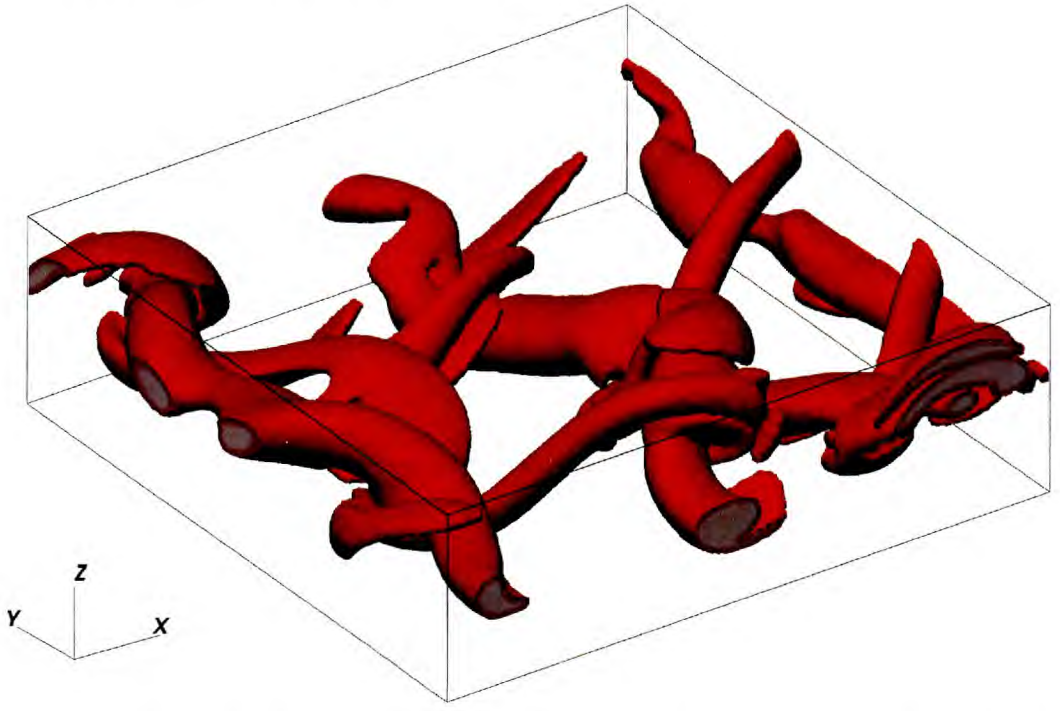

Figure 4.13: Vorticity tubes during the transition period. Case `JMixing-B` at $t^* = 17.2$.

4.4.4 Spectra and turbulence scales

The spectra for the turbulent kinetic energy distribution in the wavenumber space are depicted in figure 4.14, for the high Reynolds simulation at $t^* = 26.9$, $t^* = 36.6$, $t^* = 47.8$ and $t^* = 60.0$. In the same graphs the $-5/3$ exponential decay is also illustrated, expressing the theoretical distribution of the turbulent kinetic energy for the inertial turbulence scales.

These spectra are calculated on planes parallel to the shear layer covering the homogeneous directions of the flow. The drop of turbulent kinetic energy by five orders of magnitude guarantees the proper resolution of the small scales by the pseudospectral code [42]. The absence of a peak near the region of the high wavenumbers indicates that the turbulent kinetic energy dissipates naturally and that the smallest scales present

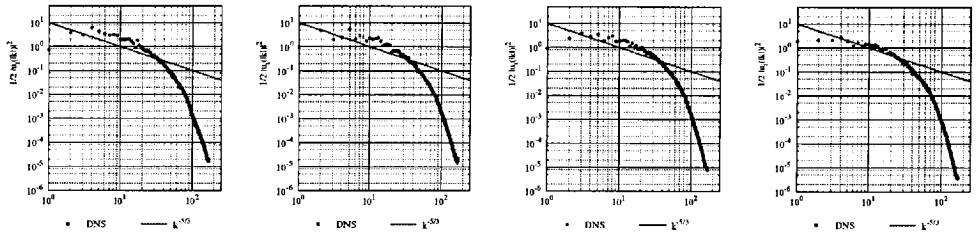

$t^* = 26.9$ $t^* = 36.6$ $t^* = 47.8$ $t^* = 60.0$

Figure 4.14: Turbulent kinetic energy spectra on the shear layer plane, $\zeta = 0$.

negligible fluctuations. The proper resolution of the DNS calculations can also be investigated by calculating the Kolmogorov length scales as defined by expression 2.23.

The turbulent mixing layer is characterised by three turbulence scales, the inertia, the Taylor and the Kolmogorov length scales. The distribution of the turbulence length scales across the z-axis of the planar jet for the case `JMixing-A` is presented in figures 4.15 at two representative times, $t^* = 14.7$ and $t^* = 51.5$. The turbulence scales for case `JMixing-B` are also shown in figure 4.16 for $t^* = 26.9$ and $t^* = 60.0$. The results presented are based on the analysis of the turbulence length scales found in section 2.2. Given that the Kolmogorov scale remains always larger than the mesh spacing for both cases, the proper resolution of the turbulence scales in the DNS computations carried out is demonstrated.

4.5 DNS of reacting planar jets

The initialisation of the velocity field for the reacting jet cases is identical to the non-reacting mixing problem described in the previous section, where the non-reacting scalar field represents the mixture fraction defined in equation (2.41). In addition, the temperature transport equation and the mass fractions of methane, carbon monoxide and hydrogen are also accounted for. Based on the initialisation of the mixture fraction in equation (4.8), the normalised temperature field and the reactive species are initialised using a flamelet solution that corresponds to the scalar dissipation rate for the initial distribution of the mixture fraction on the stoichiometric surface. Given that the initialisation of the mixture fraction is one-dimensional, an example of the initial

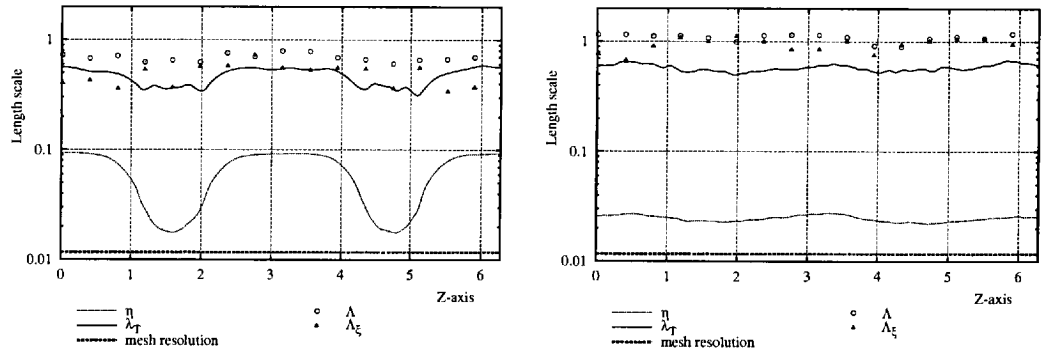

Figure 4.15: The distribution of the integral length scale Λ, the integral length scale Λ_ξ for the mixture fraction distribution, the Taylor length scale λ_T, the Kolmogorov length scale η and the mesh resolution of the simulation for the case `JMixing-A`, across the planar jet. **(a)** at $t^* = 14.7$ **(b)** at $t^* = 51.5$

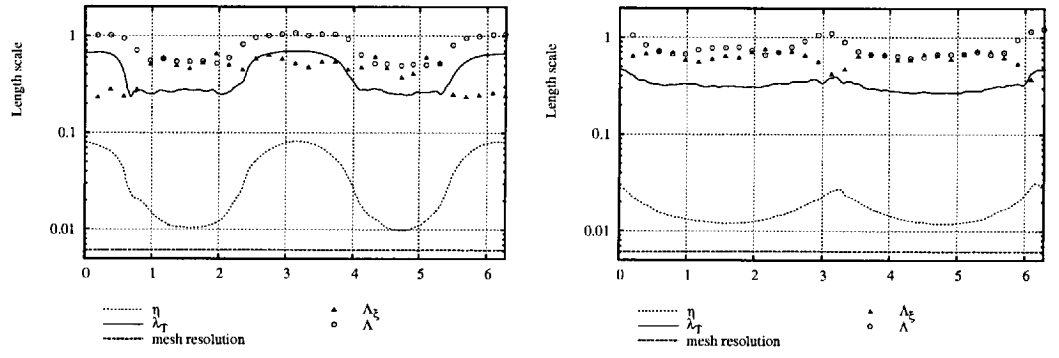

Figure 4.16: The distribution of the Integral length scale Λ, the integral length scale Λ_ξ for the mixture fraction distribution, the Taylor length scale λ_T, the Kolmogorov length scale η and the mesh resolution of the simulation for the case `JMixing-B`, across the planar jet. **(a)** at $t^* = 26.9$ **(b)** at $t^* = 60.0$

distribution along the tranverse direction, of the species, the mixture fraction and the non-dimensional temperature is provided in figure 4.17.

4.5.1 Cases studied

Four simulations of a reacting planar jet have been carried out. The details of the simulations are presented in table 4.5. The velocity field initialisation for cases `JReactive-A` and `JReactive-B` is identical based on the mixing case `JMixing-A` and characterised

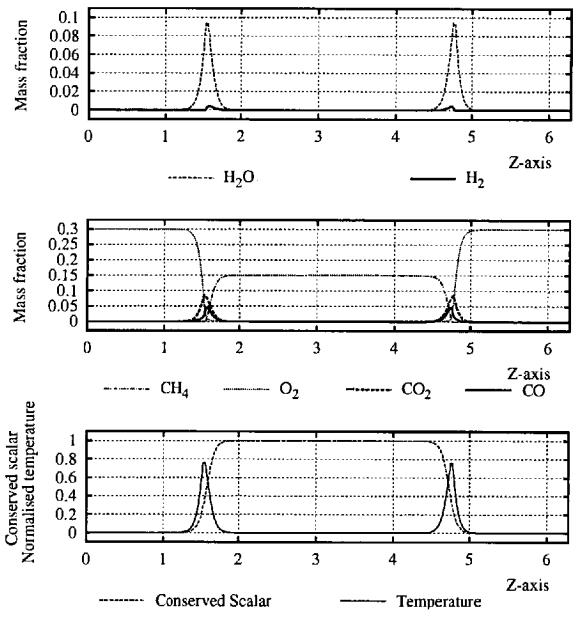

Figure 4.17: Initialisation of the species, the mixture fraction and temperature, along the z-axis.

by a relatively lower flow Reynolds number, $Re = 3141.5$. The flow field initialisation for the cases `JReactive-C` and `JReactive-D` is based on the pure mixing case `JMixing-B` where the Reynolds number is $Re = 6283.0$. Due to the higher Reynolds number a finer mesh of 512^3 nodes has been utilised for the cases `JReactive-C` and `JReactive-D`.

The magnitude of the pre-exponential scaling coefficient, c, varies and this provides a series of cases with different levels of extinction and re-ignition. Cases `JReactive-B` and `JReactive-D` have higher Damköhler numbers in comparison to the equivalent cases `JReactive-A` and `JReactive-C`, respectively. Due to the variation of Da along the simulations, these four simulation present different levels of extinction as shown in the figure 4.18.

The resolution of the flame front can be exhibited with the comparison of the the thickness of the reaction region, ℓ_r, to the mesh resolution of the simulations. Following the analysis of section 2.4.1 the Damköhler number has been calculated based on the relations (2.52) and the theoretical reaction region thickness has been derived using the expression (2.54). Due to the variability of the scalar dissipation rate across

Table 4.5: The parameters of the test cases `JReactive-A`, `JReactive-B`, `JReactive-C` and `JReactive-D`.

CASE	`JReactive-A`	`JReactive-B`	`JReactive-C`	`JReactive-D`
VELOCITY FIELD				
L	π	π	π	π
ΔU	10	10	20	20
δ_m	1/10	1/10	1/20	1/20
Re_{jet}	3141.5	3141.5	6283.0	6283.0
u'	$0.01\Delta U$	$0.01\Delta U$	$0.01\Delta U$	$0.01\Delta U$
u_{rms}	0.015	0.015	0.015	0.015
CHEMISTRY				
Scaling c	0.003	0.006	0.009	0.018
NUMERICAL				
Mesh	256^3	256^3	512^3	512^3
Nodes	16,777,216	16,777,216	134,217,728	134,217,728
Total time	52.7	52.7	73.6	73.6
Timesteps stored	10	10	18	18
Data size	6.4*Gbytes*	6.4*Gbytes*	107*Gbytes*	107*Gbytes*

the stoichiometric mixture fraction, the thickness of the reaction region ℓ_r changes in time as shown in figure 4.19.

The mesh spacing, depicted in the same figure, always remains smaller than the theoretical flame thickness ℓ_r. However, for case `JReactive-D`, which is the case presenting the highest reaction rates, this difference is marginal especially in the initial stages of the flow. The next two figures 4.20 and 4.21 depict the distribution of the four reactive scalars and the mixture fraction across a cross-section of the flow field along the $x-z$ plane for z varying from $\frac{3\pi}{4}$ to $\frac{5\pi}{4}$. This area focuses on one of the two shear layers of the planar jet. In addition, the contour plots of the source terms for each one of the reactive scalars are presented across the regions highlighted in the contour plots of the scalar fields. This area has been blown up so that the mesh starts to be visible. From the reaction rate contour plots it can be stated that the reaction region is captured by at least four DNS cells even in the initial time steps where the theoretical flame thickness has the smallest value.

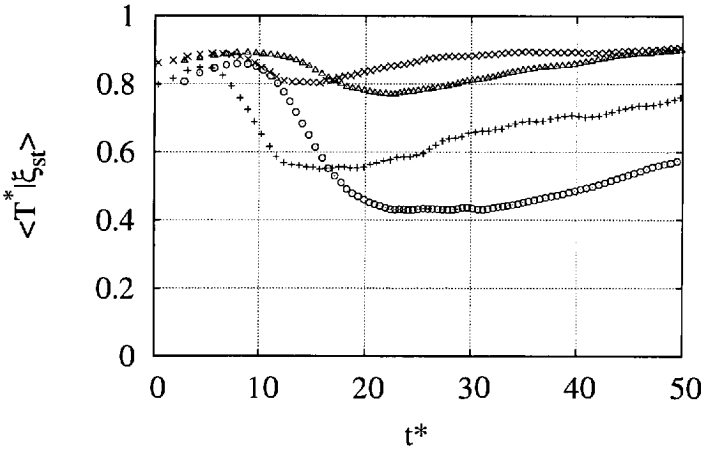

Figure 4.18: Time evolution of the non-dimensionalised temperature T^*, averaged on the stoichiometric mixture fraction ξ_{st} = 0.333, for the four combustion planar jet simulations. Symbols; + JReactive-A, × JReactive-B, ⊙ JReactive-C, △ JReactive-D

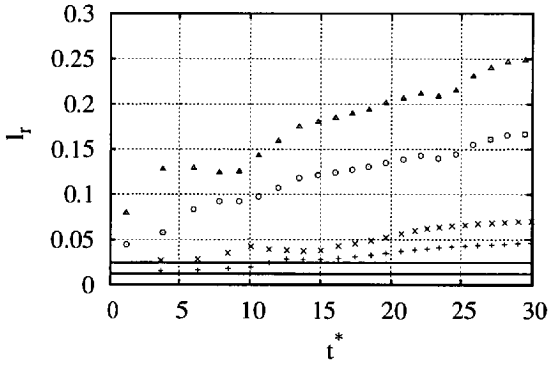

Figure 4.19: Time evolution of the theoretical reaction thickness ℓ_r. Symbols; + JReactive-D, × JReactive-C, ⊙ JReactive-B, △ JReactive-A ,line - mesh size for the 512^3 and 256^3 cases.

4.6 Summary

In this chapter the details of the numerical experiments that have been carried out have been presented. In addition, an analysis of the resolution of the turbulence and chemical scales is also provided. The resulting realisations for selected time steps of

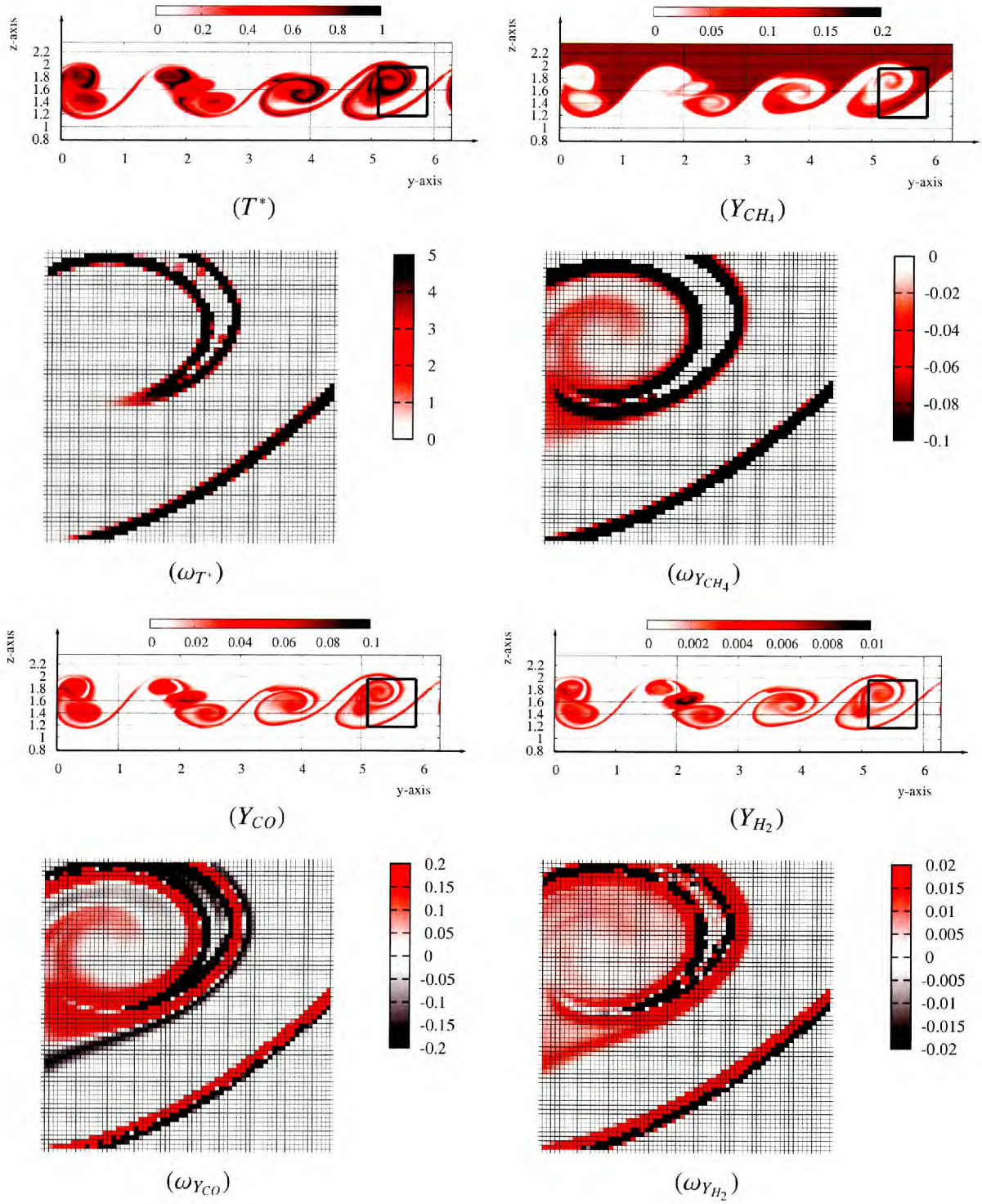

Figure 4.20: Contour plots of the scalar fields for case `JReactive-D` and the corresponding reaction rates for the reacting scalars at $^* = 17.2$.

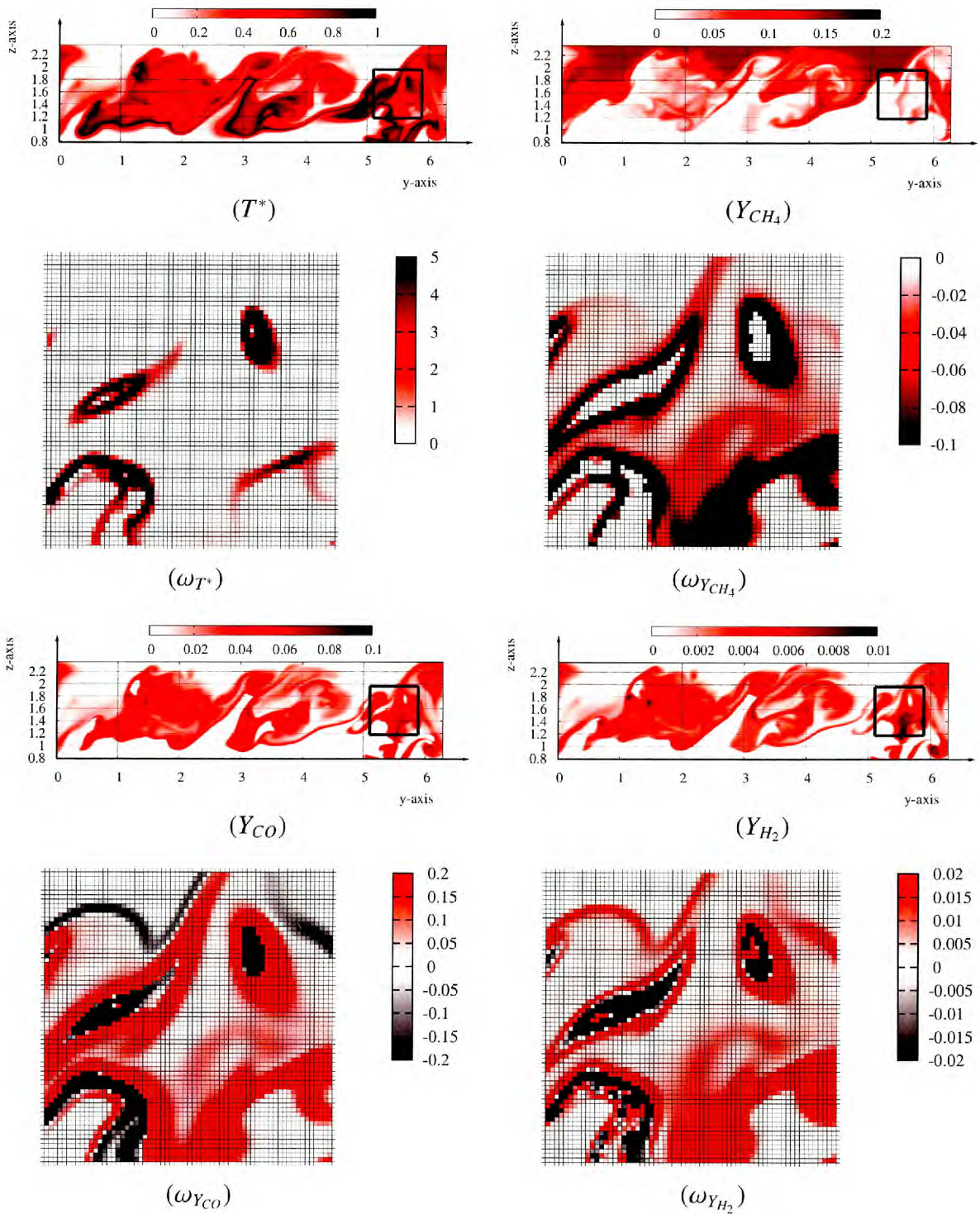

Figure 4.21: Contour plots of the scalar fields for case `JReactive-D` and the corresponding reaction rates for the reacting scalars at $t^* = 36.6$.

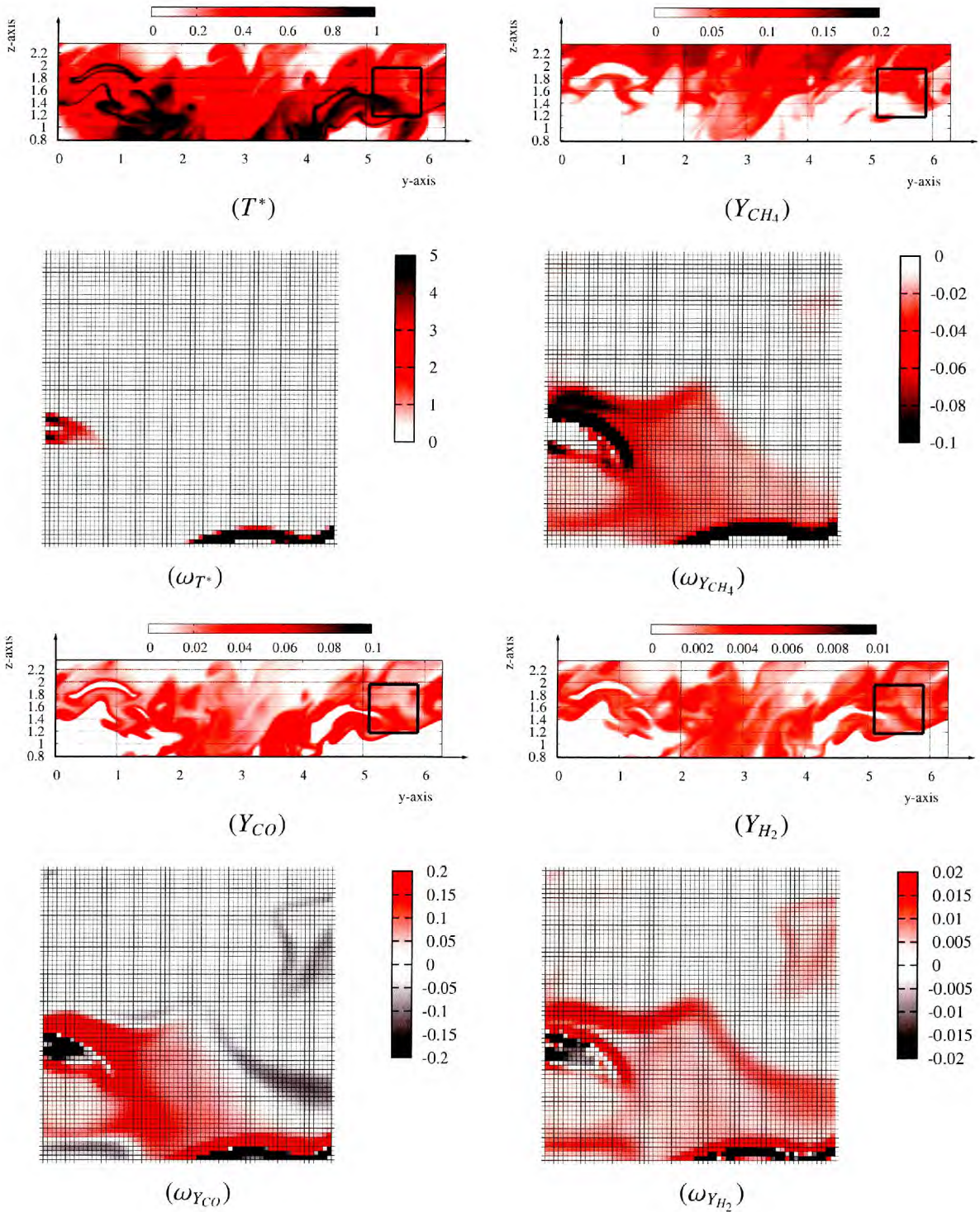

Figure 4.22: Contour plots of the scalar fields for case `JReactive-D` and the corresponding reaction rates for the reacting scalars at $t^* = 72.9$.

the solutions consist the DNS database, which will be used for the assessment of the mixing and combustion models, presented in the next two chapters. The number of the time steps stored for each simulation and the size of each set of files are shown in the tables 4.3, 4.4 and 4.5 for both mixing and reactive simulations. As far as the homogeneous turbulence mixing simulation is concerned, the flow-field data is included in the solution of the reacting simulations outlined in table 4.4.

Chapter 5

"A priori" tests of LES models for the scalar mixing

The modelling methodologies for diffusion flames in turbulent combustion are based on the observation that the mixing of the reactants is the controlling step of the reaction process [1]. In LES of non-premixed flames, the mixing of the resolved scales is modelled by the transport equation (2.78)for the filtered mixture fraction $\widetilde{\xi}$. The closure of the mixture fraction transport requires sub-grid scale (SGS) models to account for the effect of the unresolved scales on the resolved ones. In addition, information for the sub-grid distribution of the mixture fraction is also important for the closure of combustion models. As discussed in the second chapter, the effect of scalar mixing on the chemical reactions in SLFM and CMC is quantified through the SGS scalar dissipation rate, χ_{SGS}, and the SGS scalar variance, $\widetilde{\xi''^2}$, defined in equations (2.101) and (2.102) respectively. This chapter aims at presenting an assessment of the performance of zero equation sub-grid scale models for the two SGS terms.

The assessment of closures for χ_{SGS} and $\widetilde{\xi''^2}$ is based on the filtered DNS solutions of the mixing problems presented in chapter four. The predictions of the models are then compared to the SGS quantities, that can be obtained directly from the DNS data. Given that the assessment is made before any actual LES simulation, this procedure is known as "a priori" testing [158, 159]. "A priori" tests of LES and RANS modelling methodologies have been used to provide an insight in the behaviour of models for

turbulent viscosity [158, 159], scalar mixing [160, 161] and passive scalar turbulent diffusion [83]. In contradiction to "a priori" investigation of closures for turbulent simulations, "a posteriori" assessments involve the comparison of the final results from LES with experimental data or DNS results [158, 162].

In this study the three non reacting DNS presented in chapter four are used for "a priori" testing. The first is the scalar mixing simulation in homogeneous and isotropic turbulence. As discussed in chapter four the solutions of the velocity field and the mixture fraction are not affected by reaction and are common for all cases presented in table 4.3. The velocity and mixture fraction fields of these cases constitute the mixing case `HMixing`. The other two DNS are the planar jet cases `JMixing-A` and `JMixing-B`, where `JMixing-B` has a higher Reynolds number as indicated in table 4.4.

5.1 The filtered DNS flow field

Following the "a priori" testing practice, the filtered velocity and scalar fields are extracted from the the DNS database by applying a spatial filter. The spatial filter imposed is the box filter [163] with a filter width equal to Δ. For this reason a parallel postprocessing code has been developed. The DNS data, being stored in spectral space, are transformed to real space, as described in chapter two. Then, the filtering operation is applied on the flow field. A spectral filtering procedure [112, 74] has not been chosen given that the jet cases studied are spatially localised whereas the Fourier representation is not [29].

The filtering operation presented in equation (2.68) is defined continuously for every point of the turbulent flowfield. Given that the turbulent flow field from the DNS solutions is inevitably discretised on the DNS mesh, the filtering operation provided by equation (2.68) can then be written as,

$$\bar{f}(x_i, y_j, z_k; t) = \left(\frac{\Delta x}{\Delta}\right)^3 \sum_{x_k - x_i = -\Delta/2}^{\Delta/2} \sum_{y_l - y_j = -\Delta/2}^{\Delta/2} \sum_{z_m - z_k = -\Delta/2}^{\Delta/2} f(x_k, y_l, z_m; t)\,, \qquad (5.1)$$

where a box filter with width Δ is assumed. In the above equation, $\Delta x = \frac{2L}{N_{DNS}}$

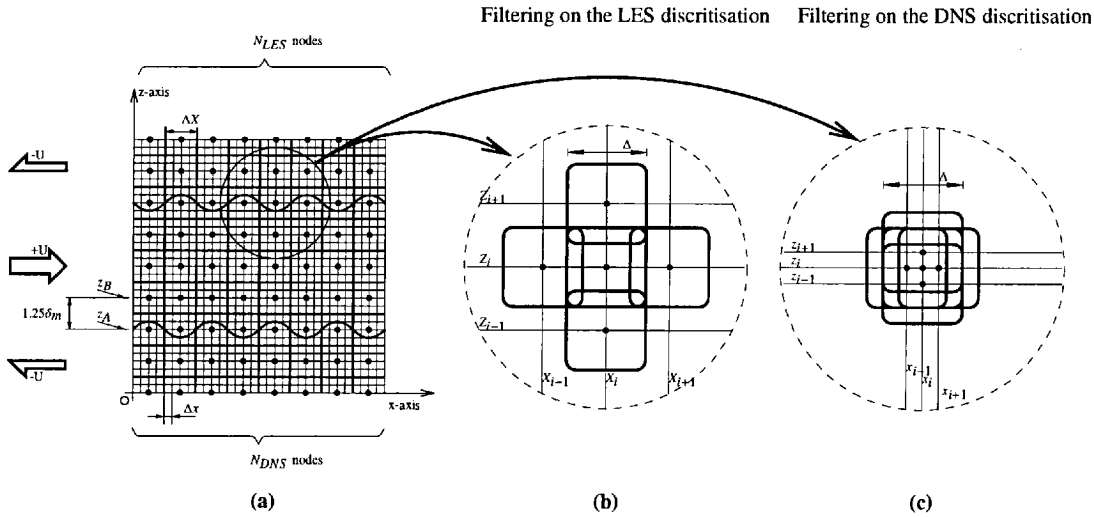

Figure 5.1: LES and DNS meshes for the jet configuration

is the grid spacing of the DNS mesh and N_{DNS} is the number of nodes for the DNS discretisation in each direction. The discrete values $f(x_i)$, which are defined on the spatial discretisation $x_1 \ldots x_i \ldots x_{N_{DNS}}$ of the x-axis, represent the distribution of an arbitrary variable of the DNS solution. For the orthogonal structured grid with equal spacing which is used here, the x-axis is discretised as $x_i = \Delta x \cdot (i - \frac{1}{2})$. The control volumes of the filtering operation shown in equation (5.1) are depicted in the figure 5.1(c).

However, in the present study an alternative discretisation of the filtered flow field is also used. For reasons of computational cost the filtering operation is not always applied to all the cells of the DNS discretisation. Instead, a coarser mesh, that can be assumed to correspond to an LES configuration, is introduced. The turbulent flowfield from the DNS database consisting of N^3_{DNS} nodes is reduced to a filtered field with N^3_{LES} nodes. The filtered field defined in equation (5.1) is discretised on the coarser LES mesh $X_1 \ldots X_i \ldots X_{N_{LES}}$, where the filtered value $\overline{f}(X_i, Y_j, Z_k)$ is computed for each cell with its centre located at X_i. This coarser mesh of the filtered field is discretised as $X_i = \Delta X \cdot i$. Finally, the definition for the discretisation X_i forces the centre of the LES cells to be located in the shear layers at, $z = L/2$ and $z = 3L/2$. The two discretisations of the filtered field are compared for an one dimensional setup, in figure 5.2.

The calculated filtered values correspond on this orthogonal mesh that covers the

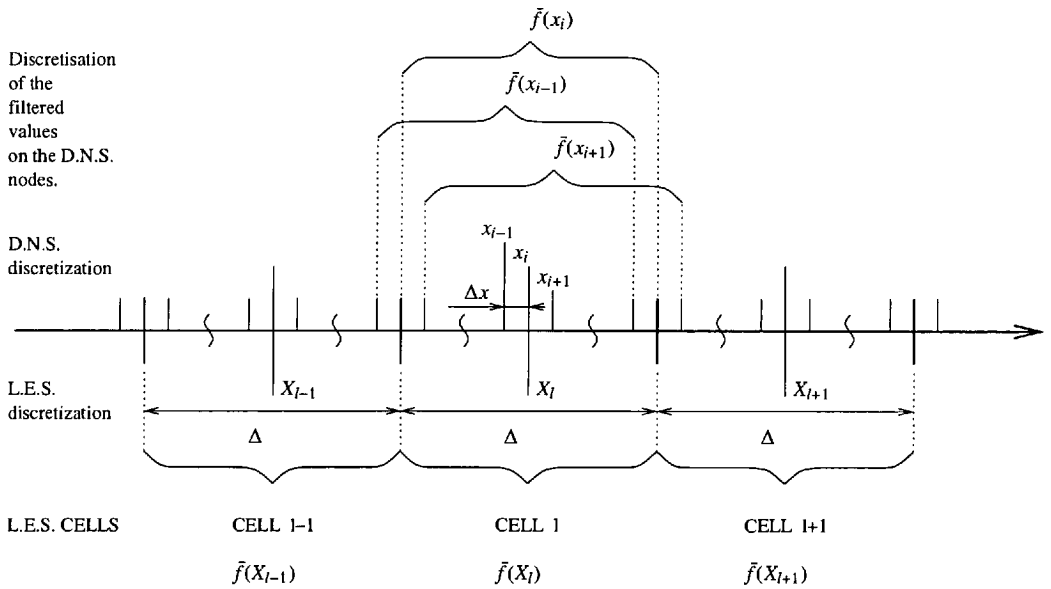

Figure 5.2: Notations of the DNS and the LES discretisation

DNS domain. This configuration is shown in figure 5.1(**a**) for the planar jet configuration. However, the same setup is used for the homogeneous turbulence simulation too.

5.1.1 Energy resolution

The flow field of each of the three mixing simulations has been filtered on three LES grids characterised by a different number of nodes, N^3_{LES}. Case `JMixing-B` is filtered on three different meshes with $N^3_{LES} = 64^3, 32^3$ and 16^3 nodes each. The low Reynolds number jet simulation `JMixing-A` and the homogeneous mixing case `HMixing` are filtered on three meshes of $N_{LES} = 32^3$, 16^3, and 8^3 nodes, respectively. Thus, three filtered fields with fine, intermediate and coarse resolutions are extracted from each DNS simulation.

The planar jet simulations are characterised by homogeneous directions located on the iso-Z planes, parallel to the stream and span-wise directions. The turbulent kinetic energy resolution, α, for the homogeneous plane located at $z = Z_0$ on the LES discretisation, is defined as,

$$\alpha(Z_0) = \frac{\frac{1}{2}\left[|\overline{u}|^2\right]_{z=Z_0} - \frac{1}{2}\left[|\overline{u}|\right]^2_{z=Z_0}}{\frac{1}{2}\left[|u|^2\right]_{z=Z_0} - \frac{1}{2}\left[|\overline{u}|\right]^2_{z=Z_0}}\,, \tag{5.2}$$

which is the ratio of the resolved over the total turbulent kinetic energy where the kinetic energy due to the mean jet velocity along a homogeneous direction, i.e. $\frac{1}{2}\left[|\overline{u}|\right]^2_{z=Z_0}$, has been subtracted. The brackets $[\cdot]_{z=Z_0}$ imply averaging over the iso-Z_0 homogeneous plane, viz.

$$\left[\overline{f}\right]_{z=Z_0} = \frac{1}{N^2_{LES}} \sum_{i=1}^{N_{LES}} \sum_{j=1}^{N_{LES}} \overline{f}(X_i, Y_j, Z_0)\,. \tag{5.3}$$

The time evolution of the energy resolution for the case `JMixing-A`, averaged along the LES nodes located on the homogeneous plane in the shear layer, i.e. at $z_A = z_1 = \frac{L}{2}$, is presented in figure 5.3(a), for each one of the three LES discretisation on 8^3, 16^3 and 32^3 LES nodes. The energy resolution on the shear layer, for the high Reynolds number case `JMixing-B`, filtered on 16^3, 32^3 and 64^3 LES nodes, is presented in the next figure 5.4(a). Each one of the coarse, intermediate and fine discretisation of the LES flow field results in filtered DNS fields, which are characterised by the same approximately levels of energy resolution, i.e. 0.8-1.0 for the finest grid, 0.6-0.8 for the intermediate grid and 0.2-0.6 for the coarse grid at the end of the simulation.

In addition to the planes at $z_A = \frac{L}{2}$, the "a priori" tests carried out are also focused on iso-Z planes located outside the shear layer. For the planar jet simulation `Mixing-A` this plane is at $z_A = \frac{2L}{8}$, while, for the case `Mixing-B` the position is at $z_B = \frac{3L}{8}$. These positions have been selected so that their distance from the shear layer equals 5/4 of the momentum thickness δ_m. The time evolution of the turbulent kinetic energy resolution for the three LES discretisations on the z_B planes, is presented in figures 5.3(b) and 5.4(b) for the cases `Mixing-A` and `Mixing-B`, respectively. Again the same levels of energy resolution are observed for each type of LES grid.

The homogeneous and isotropic turbulence mixing case `HMixing` is not characterised by mean flow velocity, and the energy resolution is therefore defined as the ratio of the kinetic energy of the filtered velocity flow field over the kinetic energy of the DNS flowfield,

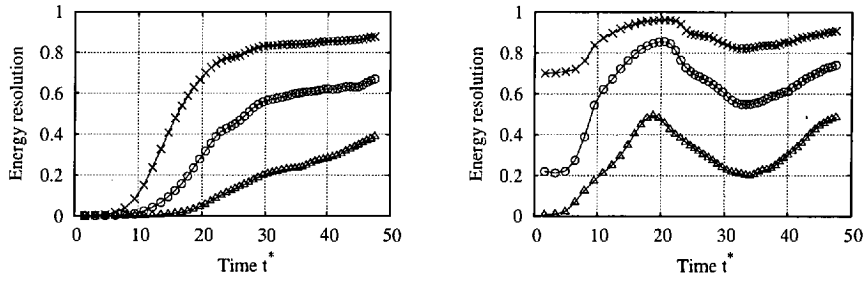

Figure 5.3: Time evolution of the energy resolution for the case Mixing-A on 32^3 nodes (×), 16^3 nodes (⊙) and 8^3 nodes (△). **(a)**, for $Z_i = z_A$, **(b)**, for $Z_i = z_B$.

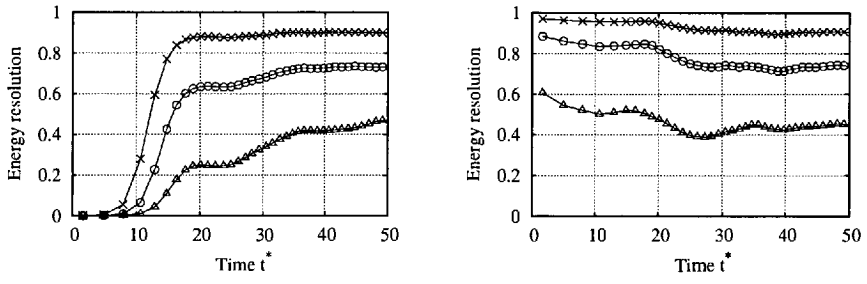

Figure 5.4: Time evolution of the energy resolution for the case Mixing-B on 64^3 nodes (×), 32^3 nodes (⊙) and 16^3 nodes (△). **(a)**, for $Z_i = z_A$, **(b)**, for $Z_i = z_B$.

$$\alpha = \left[\frac{\frac{1}{2}|\overline{u}|^2}{\frac{1}{2}\overline{|u|^2}} \right], \tag{5.4}$$

where the brackets $[\cdot]$ in the homogeneous turbulence case imply averaging over the whole DNS domain. The time evolution of α for case `HMixing`, filtered on 8^3, 16^3 and 32^3 LES nodes is presented in figure 5.5.

Given that an acceptable energy resolution for an LES simulation is thought to be around 0.80 [95, 96, 26], the LES fields extracted from the filtering of the DNS field on the fine, intermediate and coarse LES meshes would correspond to relatively poor, acceptable and over resolved LES discretisations.

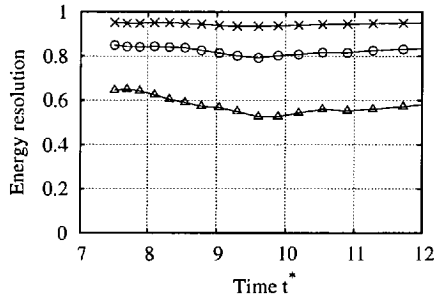

Figure 5.5: Time evolution of the energy resolution for the case `HMixing` on 32^3 nodes ($\times$), 16^3 nodes ($\odot$) and 8^3 nodes ($\triangle$).

5.1.2 Double filtering

Apart of the box filtering defined by equation (5.1), additional test filtering of the LES field is required for the dynamic and similarity models. The definition of the test filtering operation presented in equation (2.112) is based on the non discrete filtered turbulent flow field. However, following the common practice in DNS "a priori" testing [118], the test filtered field $\widehat{\bar{f}}$ is calculated from the box filtered flow field $\bar{f}$, discretised on the LES mesh, as

$$\widehat{\bar{f}}(X_i, Y_j, Z_k) = \sum_{\ell_1=-1}^{1} \sum_{\ell_2=-1}^{1} \sum_{\ell_3=-1}^{1} \bar{f}_{X_i+\ell_1, Y_j+\ell_1, Z_k+\ell_3} \cdot A_{\ell_1,\ell_2,\ell_3} \,. \tag{5.5}$$

From the above equation it can be noted that the test filtered field is the weighted average of the filtered values $\bar{f}$ of the neighbouring cells around the i, j, k cell, shown in figure 5.6. The three dimensional matrix $A_{i,j,k}$ contains the weight coefficients for the test filtering operation. Following Zang [118], the matrix A for the test filter with width $\hat{\Delta}$ equal to twice the box filter width Δ, is defined as

$$A_{i,j,-1} = A_{i,j,1} = \begin{bmatrix} \frac{1}{64} & \frac{2}{64} & \frac{1}{64} \\ \frac{2}{64} & \frac{4}{64} & \frac{2}{64} \\ \frac{1}{64} & \frac{2}{64} & \frac{1}{64} \end{bmatrix}; A_{i,j,0} = \begin{bmatrix} \frac{2}{64} & \frac{4}{64} & \frac{2}{64} \\ \frac{4}{64} & \frac{8}{64} & \frac{4}{64} \\ \frac{2}{64} & \frac{4}{64} & \frac{2}{64} \end{bmatrix} . \tag{5.6}$$

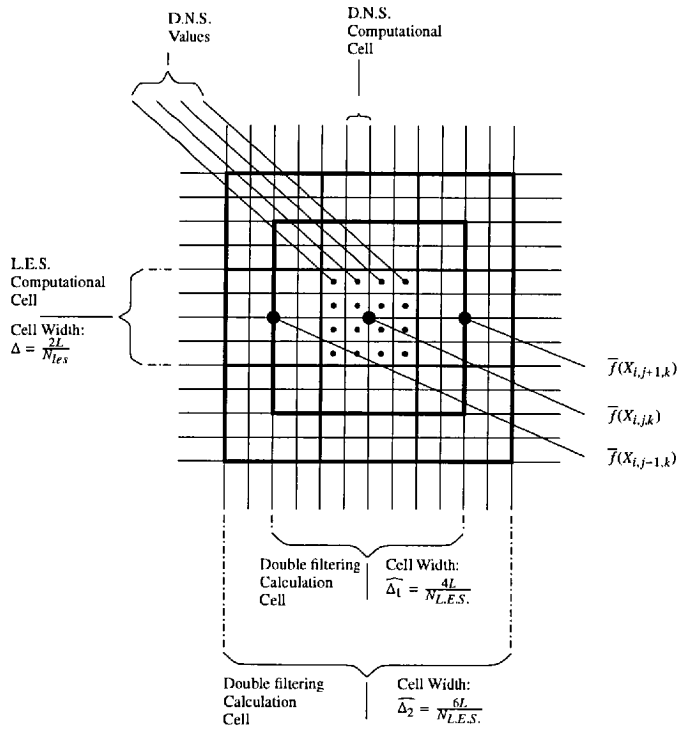

Figure 5.6: Setup of a single box filtering and the test filtering of the DNS data.

5.1.3 Spatial derivatives and commutation error

The spatial derivatives of the filtered flow field are computed using the finite difference formulation discretised on the LES mesh,

$$\left.\frac{\partial \overline{f}}{\partial x}\right|_{x=X_l} = \frac{\overline{f}(X_{l+1}) - \overline{f}(X_{l-1})}{2\Delta X}, \tag{5.7}$$

as shown in the figure 5.1(**b**). However, the differentiation error introduced invalidates the commutation of the spatial derivatives with the filtering operation, even for equally spaced LES meshes [164]. In cases where the differentiation error has to be kept to a minimum, the computation of the spatial gradients using the equation 5.7 should be avoided and the spatial derivatives are computed from filtered values on the DNS field $f(\bar{x}_i)$. Following this approach the spatial derivatives are computed as

$$\left.\frac{\partial \overline{f}}{\partial x}\right|_{x=X_l} = \frac{\overline{f}(x_{i+1}) - \overline{f}(x_{i-1})}{2\Delta x}, \tag{5.8}$$

where x_i corresponds to the X_I coordinate on the LES discretisation as shown in figure 5.2 and 5.1(**c**). Due to the smaller grid spacing Δx which is used in expression 5.8 the differentiation error is minimised, so that the spatial derivative commutes with filtering as shown in the figure 5.7. In this figure, the filtered value of first spatial derivative of the mixture fraction, along the tranverse direction $\widetilde{\frac{\partial \xi}{\partial z}}$ is presented for each LES cell. The first spatial derivative of the filtered distribution of the mixture fraction $\widetilde{\xi}$ for each LES cell calculated numerically using the finite difference expressions (5.8) and (5.8) is also presented. From this graph it is obvious that the differentiation on the LES mesh invalidates the commutation for the spatial derivatives with the filtering operation. As a result, in cases where the commutation error is important the expression (5.8) is used for the calculation of the first and second spatial derivatives.

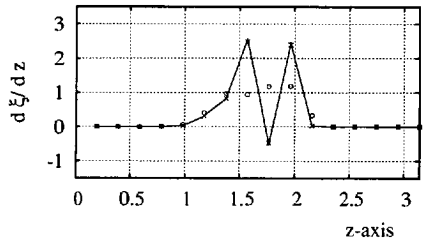

Figure 5.7: First spatial derivative of the mixture fraction distribution along the transverse axis discretised on 32 nodes, case `JMixing-A` at $t^* = 23.8$. Symbols; $\frac{d\tilde{\xi}}{dz}$ from equation (5.7)(⊙), $\frac{d\tilde{\xi}}{dz}$ from equation (5.8) (×) and continuous line, (−) $\overline{\frac{d\xi}{dz}}$ from the DNS solution.

5.2 Scalar variance transport

The scalar variance transport equation (2.107) is the starting point for the derivation of zero equation models for the scalar dissipation rate [114]. From this equation, the *production equals dissipation* assumption can be derived, if local equilibrium is assumed. The local equilibrium assumption is not confined to cases of homogeneous and isotropic turbulent flows only. Given the universal character of the small unresolved

scales in LES, the local equilibrium assumption is also applied to non-homogeneous flows. The hypothesis of local equilibrium between the large and the small scales of motion in turbulent flows is one of the most frequently used in turbulence modelling [165]. In this section an investigation of the scalar variance transport equation and an assessment of the local equilibrium assumption is presented, and it focuses on the transitional period of the planar jet simulations.

The time evolution of each one of the terms of the scalar variance transport equation (2.107) is presented in figures 5.8 to 5.10. The variance transport equation is evaluated on the filtered DNS flow field from the three mixing cases on 32^3 LES nodes. For the planar jet cases, equation (2.107) has been averaged along the homogeneous planes z_i parallel to the mixing layer, giving

$$\underbrace{\left[\overline{\rho}\frac{\partial\left(\overline{\xi^2}-\overline{\xi}^2\right)}{\partial t}\right]_{z=Z_i}}_{\text{Rate}} \underbrace{+\overline{\rho}\left[\overline{u_i\frac{\partial\xi^2}{\partial x_i}}-\overline{u_i}\frac{\partial\overline{\xi}^2}{\partial x_i}\right]_{z=Z_i}}_{\text{Convection}} \underbrace{-\left[D\overline{\rho}\frac{\partial^2\left(\overline{\xi^2}-\overline{\xi}^2\right)}{\partial x_i^2}\right]_{z=Z_i}}_{\text{Diffusion}}$$

$$\underbrace{+\left[2D\overline{\rho}\left(\overline{\frac{\partial\xi}{\partial x_i}\frac{\partial\xi}{\partial x_i}}-\frac{\partial\overline{\xi}}{\partial x_i}\frac{\partial\overline{\xi}}{\partial x_i}\right)\right]_{z=Z_i}}_{\text{Dissipation}} \underbrace{-\left[2\frac{\partial\overline{\xi}\tau_i}{\partial x_i}\right]_{z=Z_i}}_{\substack{\text{Diffusion}\\ \text{of large}\\ \text{scales}}} \underbrace{+\left[2\tau_i\frac{\partial\overline{\xi}}{\partial x_i}\right]_{z=Z_i}}_{\substack{\text{Production}\\ \text{by large}\\ \text{scales}}} = \underbrace{[R]_{z=Z_i}}_{\text{Residual}}, \tag{5.9}$$

whereas the results for the homogeneous cases have been averaged on the whole DNS domain. In the above equation, R, is the residual from the numerical evaluation of the above scalar variance transport equation on the flow field. In order to keep the magnitude of the residual R low, the first and second derivatives are calculated using the finite difference formulation (5.8).

For both planar jet cases, `JMixing-A` and `JMixing-B`, the magnitudes of the production and the dissipation terms is kept at the same levels as seen in figures 5.8(**a**) and 5.9 (**a**). However, during the transitional period and until $t^* = 15$ eddy turnover times, where the flow field is not fully turbulent, the production term is close to zero and the *production equals dissipation* assumption does not hold. In addition, the other

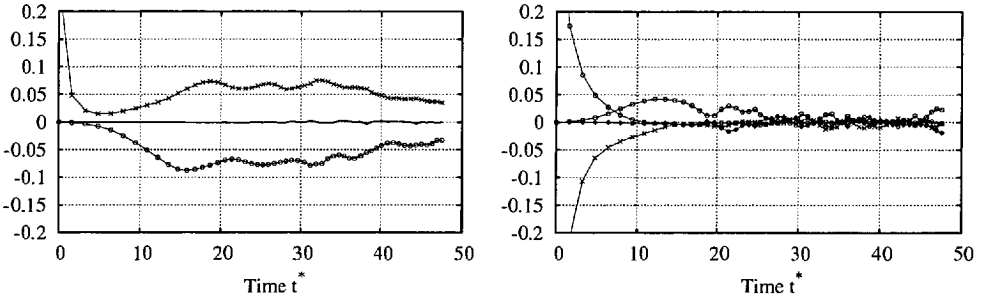

Figure 5.8: Time evolution of the terms of equation (5.9), from case `JMixing-A` filtered on 32^3 LES nodes at $Z_i = z_A$, **(a)** production ($\odot$), dissipation ($\times$) and residual ($-$), of the variance transport equation, **(b)** time derivative ($\times$), convection ($\odot$), diffusion ($\triangle$) and diffusion of large scales ($\diamond$).

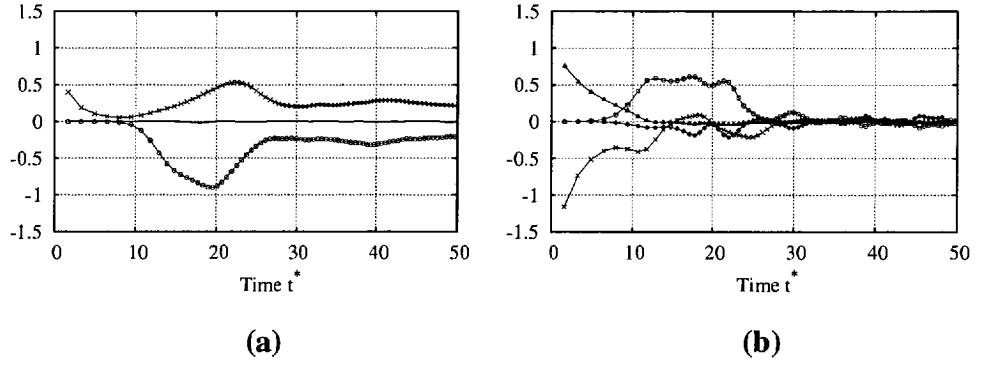

Figure 5.9: Time evolution of the terms of equation (5.9), from case `JMixing-B` filtered on 32^3 LES nodes at $Z_i = z_A$, **(a)** production ($\odot$), dissipation ($\times$) and residual ($-$), of the variance transport equation, **(b)** time derivative ($\times$), convection ($\odot$), diffusion ($\triangle$) and diffusion of large scales ($\diamond$).

terms of the scalar variance equation, i.e. the convection, the time derivative and the diffusion terms remain high, and are comparable in magnitude to the the levels of the production and dissipation terms as seen in the figures 5.8(**b**) and 5.9(**b**). This contradicts the local equilibrium assumption described in the section 2.8.2, where the small scales are considered to be homogeneous in space, and all terms incorporating spatial derivatives should reduce to zero.

In the homogeneous and isotropic turbulence mixing case the production equals

dissipation assumption seems to hold, and the two terms have the same magnitude from the initial stages of the simulation, as seen in figure 5.10(**a**). Furthermore, the homogeneity of the flow leads to relatively small values for the rest of the terms of equation (5.9), (see figure 5.10(**b**)).

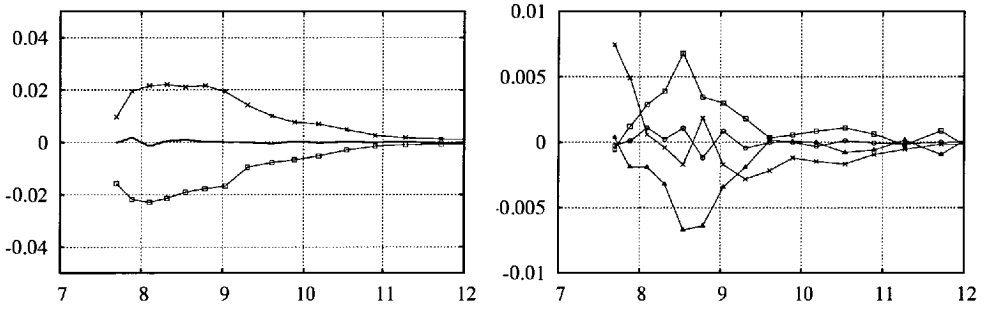

Figure 5.10: Time evolution of the terms of equation (5.9), from case `HMixing` filtered on 32^3 LES, **(a)** production ($\odot$), dissipation ($\times$) and residual ($-$), of the variance transport equation, **(b)** time derivative ($\times$), convection ($\odot$), diffusion ($\triangle$) and diffusion of large scales ($\diamond$).

Figure 5.11 depicts the time evolution of the terms of equation (5.9), based on the DNS data from the high Reynolds number planar jet case `Mixing-B`, averaged over the homogeneous direction outside the shear layer, at $Z_i = z_B$. In this case, the turbulent shear layers of the jet expand and reach the laminar core of the jet at around $t^* = 20$ eddy turnover times. At this position of the jet domain the production and the dissipation terms increase together to the same levels, thus the *production equals dissipation* assumption holds. However, the other four terms of equation (5.9) are not small. Although the time derivative, the convection and the diffusion terms are characterised by high magnitudes, comparable to the production and dissipation rate terms, they seem to cancel each other and the local equilibrium hypothesis seems to hold at all times.

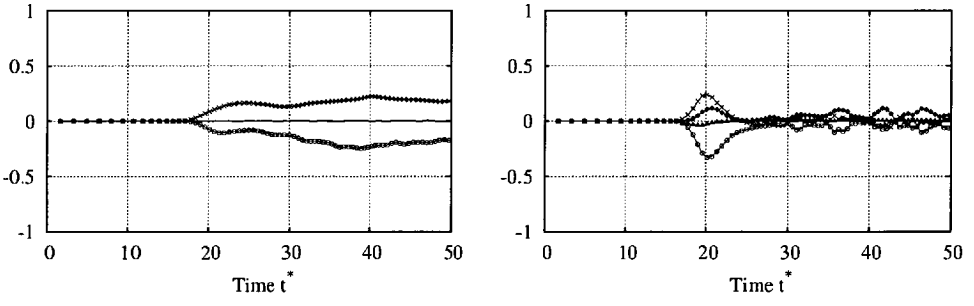

Figure 5.11: Time evolution of the terms of equation (5.9), from case `JMixing-B` filtered on 32^3 LES nodes at $Z_i = z_B$, **(a)** production ($\odot$), dissipation ($\times$) and residual ($-$), of the variance transport equation, **(b)** time derivative ($\times$), convection ($\odot$), diffusion ($\triangle$) and diffusion of large scales ($\diamond$).

5.3 Micromixing modelling

In this section, SGS scalar dissipation rate and scalar variance models are assessed. As mentioned above, the scalar variance represents the energy of the turbulent fluctuations of the mixture fraction, within an LES cell. Given that in LES most of the energy spectrum is resolved, its sub-grid contribution can be extracted by similarity arguments from the resolved scales [121]. On the other hand, virtually all the dissipation of the the scalar field occurs within the smallest unresolved scales [114], leading to modelling techniques based on local equilibrium assumptions.

The spectrum of the energy of the fluctuations of the scalar distribution for the mixing case `JMixing-B` at time $t^* = 42.2$ is presented in figure 5.12(**a**). In the same figure the turbulent kinetic energy spectrum (scaled by a factor of 10^{-5}) is also presented for comparison. The vertical lines represent the cut off wavenumbers k for the three filters imposed on the planar jet case `JMixing-B`.

From this figure, it is evident that the cutoff wavenumbers for the three box filters, are located within the inertial subrange of the turbulent kinetic energy spectrum. Thus, most of the energy of the scalar fluctuations are resolved. The energy spectrum for the scalar dissipation fluctuations is presented in figure 5.12(**b**), but here only the finest LES discretisation captures the ranges where the dissipation of the scalar fluctuations

take place.

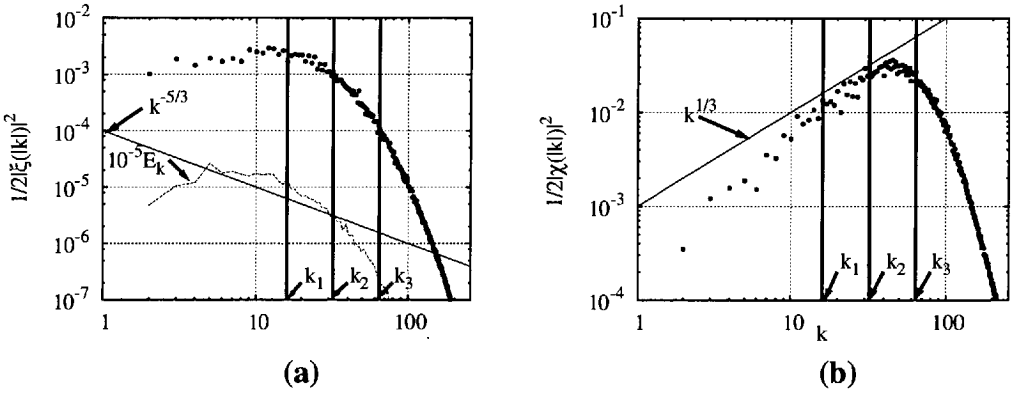

Figure 5.12: Energy spectrum for the mixture fraction fluctuations (**a**), and for the scalar dissipation rate (**b**).

The fine structure of the scalar dissipation rate as exhibited in its spectral distribution can also be identified in the figure 5.12. For the planar jet case, the high values of the scalar dissipation rate appear as thin structures around the vorticity tubes on the shear layer as seen in figure 5.13. The domain depicted in figure 5.13 is the same domain shown in the figure 4.13. The scalar dissipation rate isosurfaces shown in white are plotted at $\chi = 5$, surrounding the the vorticity tubes of figure 4.13 at an angle of around 45^o. Similar behaviour has been observed in measurements of the scalar dissipation rate in a non reacting turbulent jet by Everest *et* al. [166], and in the LES results of Pitsch *et* al. [103].

5.3.1 Scalar dissipation rate modelling

The assessment of the scalar dissipation rate modelling is based on the comparison of the filtered scalar dissipation rate, χ_{SGS}^{DNS}, extracted from the filtered DNS flow field, with the estimates of the zero equation models presented in section 2.8.2. The zero equation models are evaluated on the filtered flow field which represents the resolved scales in an LES simulation. The spatial derivatives are calculated using a second order central difference approximation based on the expression 5.7. The test filtering operation is carried out as described in the section 5.1.2 where a test filter with twice

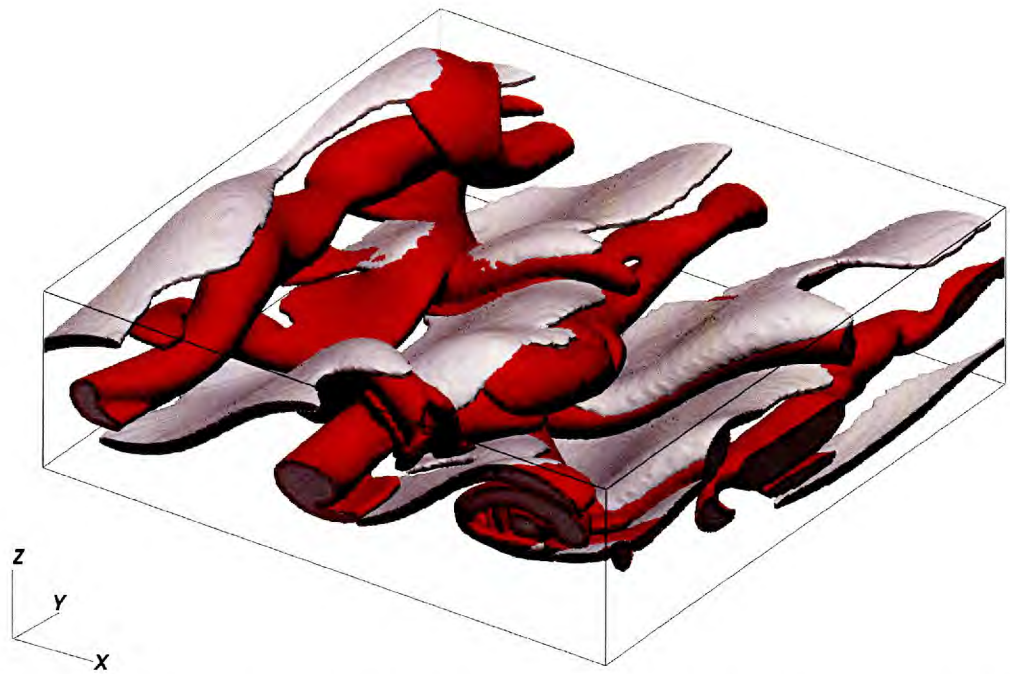

Figure 5.13: Vorticity tubes shown in red during the transition period, surrounded by scalar dissipation structures shown in gray. Case `JMixing-B`.

the filter width is chosen.

At this point it must be mentioned that the predictions of SGS modelling are stochastic in nature [167] and a perfect match between model and DNS cannot be expected for a particular instance in time and space. The instantaneous scatter plot for the pairs for the filter scalar dissipation rate and the predictions of the gradient model for the LES cells at one homogeneous plane located in the shear layer is presented in figure 5.14. The SGS scalar dissipation rate for each LES cell in the shear layer is characterised by a wide range of values. However, from this figure it can be concluded that a value of χ_{SGS}^{DNS} in a specific LES cell may be over or under estimated by at least one order of magnitude. For small unimportant values of χ_{SGS} this deviation is even greater.

Given the stochastic nature of the SGS modelling, the assessment of each model is not focused on the predictions for each one of the individual LES cells. The performance of each SGS model is assessed by comparison of the mean values for all the LES cells on each homogeneous plane [162]. In addition, a sub-grid term may

range within an interval where extremely high values may be observed. In the case of scalar dissipation rate, these extreme values may account for local extinction of a flame. Thus, an SGS model must be able to predict the number of the LES cells which are characterised by such extreme values. For this reason the PDF of the predictions and the DNS results are also compared.

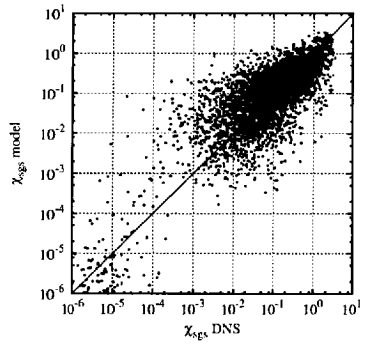

Figure 5.14: Scatter of the pairs χ_{SGS}^{DNS} and χ_{SGS}^{Model} for the predictions for the gradient model, case `JMixing-B`

Gradient model

The gradient model for the scalar dissipation rate is described by equations (2.109) and (2.110). The values of the constants C_s and Sc_t incorporated in the gradient model have been chosen as

$$Sc_t = 0.7 \quad \text{and} \quad C_s = 0.2\,. \tag{5.10}$$

Figure 5.15(**a**) depicts the scatter of the predictions of the gradient model $\left[\chi_{SGS}^{Model}\right]_{z=Z_i}$ and the corresponding DNS results $\left[\chi_{SGS}^{DNS}\right]_{z=Z_i}$, averaged over all homogeneous planes Z_i. The pairs of predictions shown in the scatter plot 5.15(**a**) are extracted from all the timesteps of the three mixing simulations for all homogeneous planes.

These predictions of the mean SGS values can be interpolated by a simple linear function as $y = ax$ using linear regression. The deviation of the proportionality coefficient a from unity quantifies the predictive behaviour of the model. Furthermore, the linear correlation coefficient c describes the scatter of the model predictions from the

linear fit. For the gradient model, the values of a and c for each mixing case and grid resolution are presented in table 5.1.

Table 5.1: The values of the correlation coefficient c for the predictions of the gradient model and the corresponding proportionality coefficient a of the the linear interpolation.

Gradient model for χ_{SGS}						
Mesh	Fine		Intermediate		Coarse	
	a	c	a	c	a	c
HMixing	0.9385	0.9186	0.6922	0.8279	0.4483	0.6473
JMixing-A	1.7418	0.6888	1.7352	0.7141	1.7488	0.8087
JMixing-B	1.4836	0.7339	1.3204	0.7427	1.3102	0.8177

Dynamic model

The dynamic model for χ_{SGS} is described by equations (2.109) and (2.121) and results are shown in figure 5.15(**b**). In this figure, the pairs of the predictions and the DNS results for the scalar dissipation rate averaged over the homogeneous directions of each mixing DNS case, i.e. $\left[\chi_{SGS}^{Model}\right]_{z=Z_i}$ and $\left[\chi_{SGS}^{DNS}\right]_{z=Z_i}$, are presented for all the simulations and for all the three LES grid resolutions. The results of the linear interpolation of the dynamic model predictions, for each simulation and each grid resolution are presented in table 5.2.

Table 5.2: The values of the correlation coefficient c for the predictions of the dynamic model and the corresponding proportionality coefficient a of the the linear interpolation.

Dynamic model for χ_{SGS}						
Mesh	Fine		Intermediate		Coarse	
	a	c	a	c	a	c
HMixing	1.5649	0.9375	1.6078	0.8455	1.1357	0.7887
JMixing-A	1.2684	0.8985	0.9043	0.8368	0.4453	0.6945
JMixing-B	1.3515	0.8876	1.2221	0.8663	0.5881	0.8586

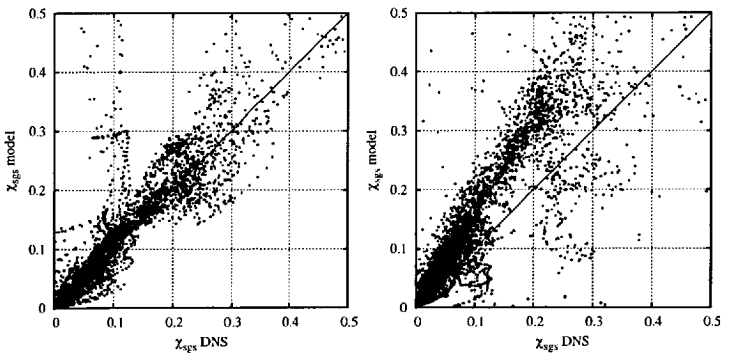

Figure 5.15: Scatter plot of the predictions for the scalar dissipation rate, averaged over the homogeneous directions, at all the time steps and for all mixing simulations, **(a)** gradient model **(b)** dynamic model.

5.3.2 Comparison of the gradient and the dynamic models and discussion of their performance

The time evolution of the SGS scalar dissipation rate from the DNS data averaged along the homogeneous plane in the shear layer is presented in the figures 5.17 to 5.18. In these figures, the results from the two planar jet cases `JMixing-A` and `JMixing-B`, filtered on the three different types of grids are presented. In the same plots, the time evolution of the predictions of the gradient and the dynamic models is also depicted. Figures 5.19 to 5.20 depict the time evolution of the same terms averaged along the homogeneous plane outside the mixing layer, i.e. for $z = z_B$. In addition to the scalar dissipation rates, the production term $2\tau_i \frac{\partial \overline{\xi}}{\partial x_i}$ is also shown in figures 5.17 to 5.20.

As seen in table 5.1, the gradient model performs well for the homogeneous, isotropic mixing case `HMixing`. The correlation between the prediction and the DNS results is very high for the fine discretisation and deteriorates as the resolution reduces, remaining above 0.8 for the intermediate LES grid. Furthermore, its proportionality is very close to unity for the fine LES filter where the energy resolution is around 0.95 but the model becomes under-predictive for the coarser grids.

For the planar jet cases, the gradient model is always overpredictive not being able to adjust to the high rate of strain tensor observed in the shear layer. Surprisingly, the correlation coefficient for the predictions of the gradient model in both planar jet cases

improves as the grid gets coarser. This behaviour can be attributed to the extremely over predictive behaviour of the model around the shear layer which can be observed in the figures 5.17(**a-c**) to 5.18(**a-c**). As the grid becomes coarser the resolved gradient of the shear layer reduces, thus providing a reduced over prediction of the scalar dissipation rate and improving the correlation of the model.

The dynamic model for the scalar dissipation rate is over-predictive for the homogeneous cases, and the proportionality coefficient falls close to unity for the coarse filtered field. The correlations of the predictions of the model remain high for the homogenous case, becoming smaller as the resolution decreases. Although the correlation, c, for the dynamic model remains at the same levels with the gradient model, it does not exhibit the same sensitivity to the grid resolution remaining close to 0.8 for the coarsest grid.

For the two jet cases the dynamic model performs clearly better than the gradient model as seen in the tables 5.1 and 5.2. For the fine and the intermediate meshes, the correlation coefficient remains larger than 0.8 while the proportionality of the predictions is close to unity. As expected, its performance declines rapidly for the coarse grid.

It can be concluded that the gradient model performs well for the homogeneous and isotropic turbulence case using $C_s = 0.2$, however, it fails to predict SGS dissipation in the shear flow, accurately. In contrast the dynamic model manages to adjust to the different types of flows, but it is overpredictive for the homogeneous turbulence case.

The behaviour of the gradient model can be analysed in more detail in figures 5.16 to 5.20. In both types of flow, the gradient model succeeds to predict the trends of the time evolution of the sub-grid scalar dissipation rate. However, in the planar jet cases and for the planes located on the mixing layer, see in the figures 5.17 (**a-c**) and 5.18(**a-c**), the gradient model is dramatically overpredictive during the transition period and until around 25 eddy turn over times for both planar jet simulations.

On the other hand, the dynamic model follows the trends of χ_{SGS}^{DNS} in all types of flow. During the transitional period for the planar jet simulations the dynamic model follows the trends of the production term rather than the dissipation rate. This be-

haviour can be attributed to the failure of the *production equals dissipation* assumption, for the first 15 eddy turnover times.

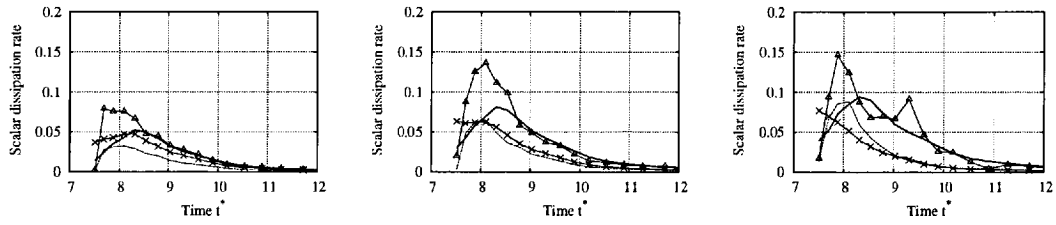

Figure 5.16: Time evolution of the sub-grid scale scalar dissipation rate (−), the production (−−), the predictions of the gradient model (×), and the dynamic model (△), case HMixing, **(a)** on 32^3, **(b)** on 16^3 and **(c)** on 8^3 nodes.

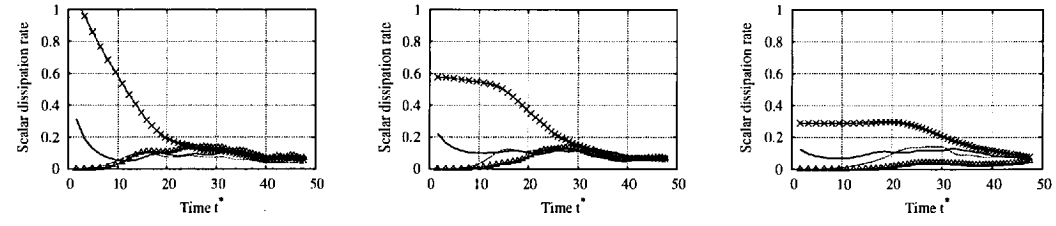

Figure 5.17: Time evolution of the sub-grid scale scalar dissipation rate (−), the production (−−), the predictions of the gradient model (×), and the dynamic model (△), case JMixing-A, **(a)** on 32^3, **(b)** on 16^3 and **(c)** on 8^3 nodes.

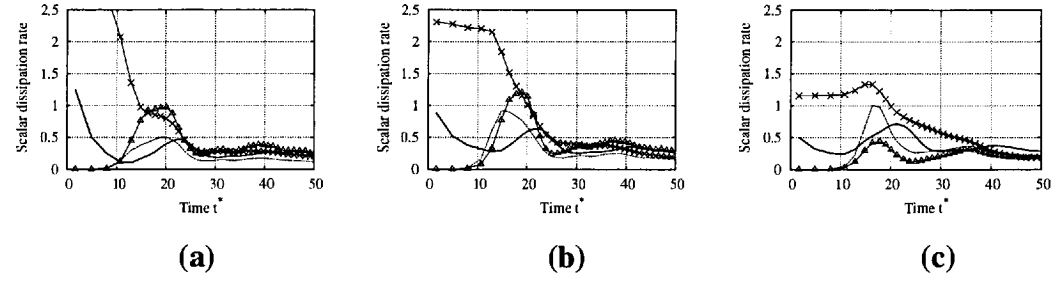

Figure 5.18: Time evolution of the sub-grid scale scalar dissipation rate (−), the production (−−), the predictions of the gradient model (×), and the dynamic model (△), case JMixing-B, **(a)** on 64^3, **(b)** on 32^3 and **(c)** on 16^3 nodes.

The probability density function (PDF) for the logarithm of scalar dissipation rate $P(\chi_{SGS}^{DNS})$ across the LES cells filtered on the finest mesh for the homogeneous turbu-

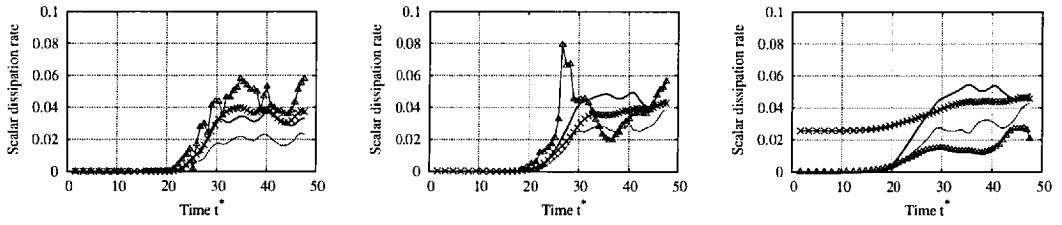

Figure 5.19: Time evolution of the sub-grid scale scalar dissipation rate (−), the production (−−), the predictions of the gradient model (×), and the dynamic model (△), case JMixing-A, **(a)** on 64^3, **(b)** on 32^3 and **(c)** on 16^3 nodes.

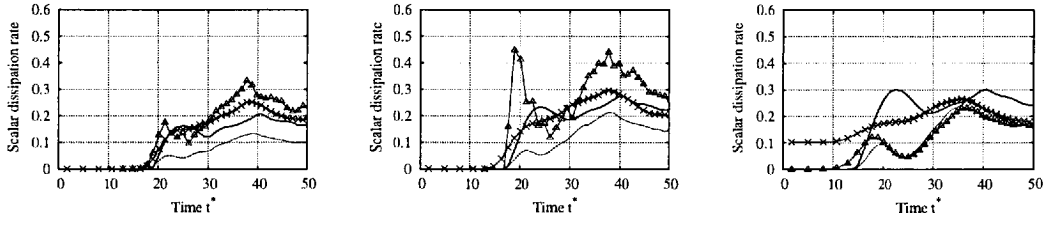

Figure 5.20: Time evolution of the sub-grid scale scalar dissipation rate (−), the production (−−), the predictions of the gradient model (×), and the dynamic model (△), case JMixing-B, **(a)** on 64^3, **(b)** on 32^3 and **(c)** on 16^3 nodes.

lence simulation, is presented in the next figure 5.21(**a**) at $t^* = 8.09$ and in the figure 5.21(**b**) at $t^* = 9.03$. In the same graph, the PDFs of the predictions $P(\chi_{SGS}^{Model})$ for the scalar dissipation rate by the gradient and the dynamic models are also presented. The PDF functions depicted in the figure 5.22, are extracted from the distribution of the scalar dissipation rates across the LES cells on the mixing layer at $t^* = 17.2$ and $t^* = 26.9$, respectively.

As discussed before, the SGS models fail to predict the SGS scalar dissipation rate for every LES cell exhibiting a wide scatter of predictions, as seen in the figure 5.14. Nevertheless, both models capture the distribution of the PDF for χ_{SGS}^{DNS}, as seen in the figures 5.21 to 5.22. This means that the SGS model fails to provide a correct value for the sub-grid distribution of the scalar field in turbulent mixing. However, the SGS models predict the number of nodes characterised by specific value of the scalar dissipation rate.

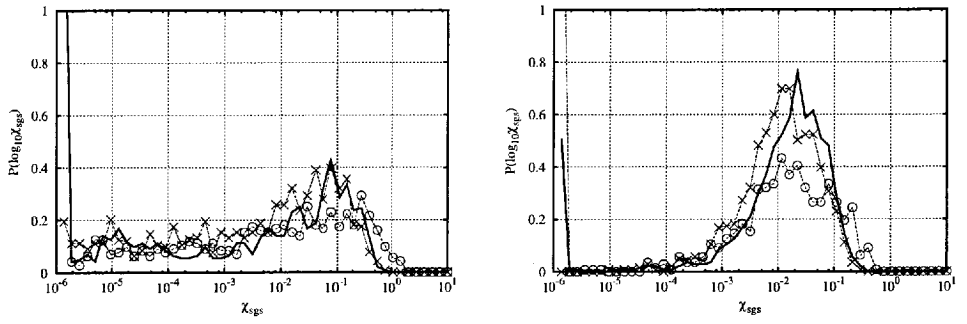

(a) (b)

Figure 5.21: Probability density function of χ_{SGS} for the DNS field of case `HMixing` filtered on 32^3 nodes. Symbols; (⊙) dynamic model (×) gradient model and continuous line (−) DNS result, **(a)** at $t^* = 8.09$ and **(b)** at $t^* = 9.03$.

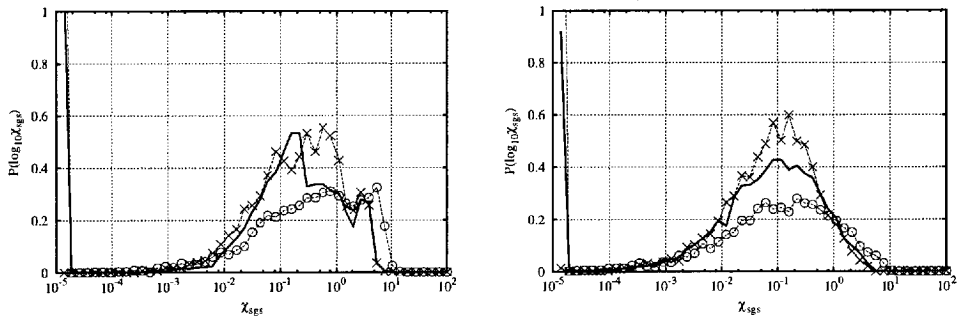

(a) (b)

Figure 5.22: Probability density function of χ_{SGS} for the DNS field of case `JMixing-B` filtered on 64^3 nodes, across homogeneous plane on the shear layer. Symbols; (⊙), dynamic model (×) gradient model and continuous line, (−) DNS result, **(a)** at $t^* = 17.2$ and **(b)** at $t^* = 26.9$.

It can be concluded that the gradient model provides a PDF distribution relatively close to the DNS result, In contrast, the dynamic model yields a wider distribution with significantly lower probability of the most likely SGS dissipation values and increased probability for very large dissipation.

5.3.3 Scalar variance modelling

The procedure followed for the the assessment of models for the scalar dissipation rate is also followed for the investigation of the performance of the scalar variance modelling. The scalar variance for the filtered fields $\widetilde{\xi''^2}^{DNS}$ is extracted from the DNS

data. The zero equation models for the scalar variance presented in the section 2.8.2 are then evaluated on the resolved scales of the filtered field. The assessment of the models is based on the comparison of $\widetilde{\xi''^2}^{DNS}$ and $\widetilde{\xi''^2}^{Model}$ for each model assessed, separately. The spatial derivatives are calculated using a second order central difference approximation on the LES discretisation, using equation (5.7).

Gradient model

The scalar variance gradient model has been introduced by equation (2.111). Now, a constant of $C_v = 0.2$ has been used to evaluate $\widetilde{\xi''^2}$ for the filtered DNS results. The comparison of the gradient model with the values from the DNS scalar field is presented in the figure 5.23(**a**). This scatter plot depicts pairs of scalar variance $\left[\widetilde{\xi''^2}^{Model}\right]_{z=Z_i}$ and $\left[\widetilde{\xi''^2}^{DNS}\right]_{z=Z_i}$, for all simulations, grid resolutions and timesteps.

Table 5.3: The values of the correlation coefficient c for the predictions of the gradient model for the scalar variance and the corresponding proportionality coefficient a of the the linear interpolation.

Gradient model for $\widetilde{\xi''^2}$						
Mesh	Fine		Intermediate		Coarse	
	a	c	a	c	a	c
`HMixing`	1.5510	0.9921	0.9742	0.9568	0.6840	0.8935
`JMixing-A`	1.1986	0.9523	0.7193	0.9040	0.4740	0.8885
`JMixing-B`	1.2114	0.9672	0.7128	0.9370	0.5158	0.9278

Imposing a linear fit on the scatter of the predictions presented in figure 5.23(**a**), the proportionality coefficients a for each grid resolution and for each DNS mixing case are calculated. The results of the linear regression and the linear correlation coefficient c for the gradient model are presented in the table 5.3.

Similarity model

The similarity model for the scalar variance is given by equation (2.126). For the first implementation of the model, named "similarity model I" the constant C_z is defined as

$$C_z = 0.2\frac{\hat{\Delta}}{\Delta}, \tag{5.11}$$

where the test filter $\hat{\Delta}$ is taken as twice the LES filter width Δ.

Table 5.4: The values of the correlation coefficient c for the predictions of the similarity model I for the scalar variance and the corresponding proportionality coefficient a of the the linear interpolation.

Similarity model I for $\widetilde{\xi''^2}$						
Mesh	Fine		Intermediate		Coarse	
	a	c	a	c	a	c
HMixing	1.2098	0.9849	0.7355	0.9403	0.4830	0.8768
JMixing-A	0.9241	0.9075	0.5195	0.8446	0.3055	0.8228
JMixing-B	0.9393	0.9391	0.5322	0.9007	0.3751	0.8826

The assessment of the similarity model defined by equations (2.126), (2.128) and (2.129), named "similarity model II" is presented in the table (5.5).

Table 5.5: The values of the correlation coefficient c for the predictions of the similarity model II for the scalar variance and the corresponding proportionality coefficient a of the the linear interpolation.

Similarity model II for $\widetilde{\xi''^2}$						
Mesh	Fine		Intermediate		Coarse	
	a	c	a	c	a	c
HMixing	1.4999	0.9767	1.4140	0.9282	1.4734	0.8682
JMixing-A	0.8199	0.9125	0.6154	0.8075	0.5784	0.6858
JMixing-B	1.1848	0.9702	1.0394	0.9476	1.1127	0.9289

Figures 5.23(**b**) and 5.23(**c**) present the scatter plot of the predictions of the two similarity models averaged on homogeneous planes, i.e. $\left[\widetilde{\xi''^2}^{Model}\right]_{z=Z_i}$ and $\left[\widetilde{\xi''^2}^{DNS}\right]_{z=Z_i}$.

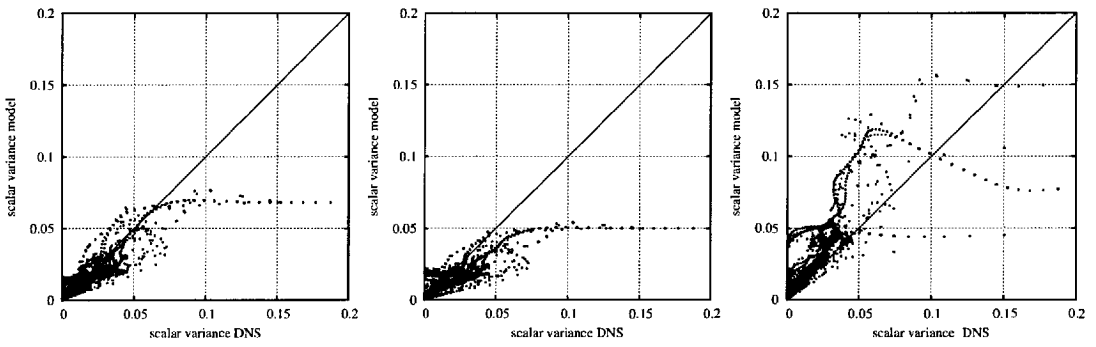

Figure 5.23: Scatter plot of the prediction for the scalar variance averaged over homogeneous planes, **(a)** gradient model, **(b)** similarity model I, **(c)** similarity model II.

5.3.4 Comparison of the gradient and the similarity models of scalar variance and discussion of their performance

The gradient model predictions present a high linear correlation coefficient c for the prediction of the scalar variance, which remains close or higher than 0.9 for all the flow geometries and all grid resolutions as seen in table 5.3. Although the scalar variance in the homogeneous flow field is overpredicted, the proportionality factor, a, for the gradient model does not vary significantly for the different flow geometries. However, it reduces with the grid resolution.

The same behaviour is observed for the "similarity model I", where the correlations of the predictions of the model remains high, regardless of the grid resolution. However, the proportionality of this model shows a strong dependence on the grid resolution, while being insensitive to Reynolds numbers. This behaviour is very similar to the gradient model. The "similarity model II", also shows a high linear correlation coefficient, which also declines as the grid resolution becomes coarser. However, the proportionality coefficient is much more sensitive to the grid resolution when compared to the gradient model and the similarity model I.

Figures 5.25 to 5.26 depict the time evolution of the scalar variance $\left[\widetilde{\xi''^2}^{DNS}\right]_{z=z_A}$ and the predictions of the three models $\left[\widetilde{\xi''^2}^{Model}\right]_{z=z_A}$ presented in this section, averaged over the homogeneous plane at $Z_i = z_A$, for `JMixing-A` and `JMixing-B`. Figures 5.24 **(a)** to **(c)** show the results from the DNS simulation `HMixing`.

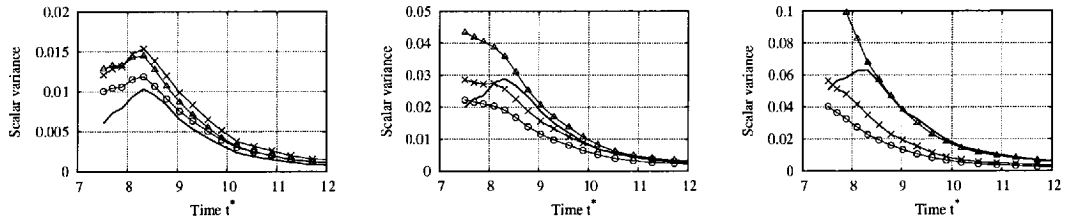

Figure 5.24: Time evolution of the scalar variance (−), the predictions of the gradient model (×), the similarity model I (⊙) and the similarity model II (△), case HMixing, **(a)** on 64^3, **(b)** on 32^3 and **(c)** on 16^3 nodes.

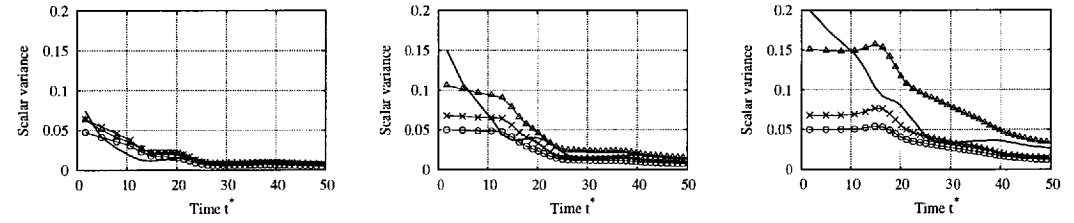

Figure 5.25: Time evolution of the scalar variance (−), the predictions of the gradient model (×), the similarity model I (⊙) and the similarity model II (△), case JMixing-B, on the mixing layer, **(a)** on 64^3, **(b)** on 32^3 and **(c)** on 16^3 nodes.

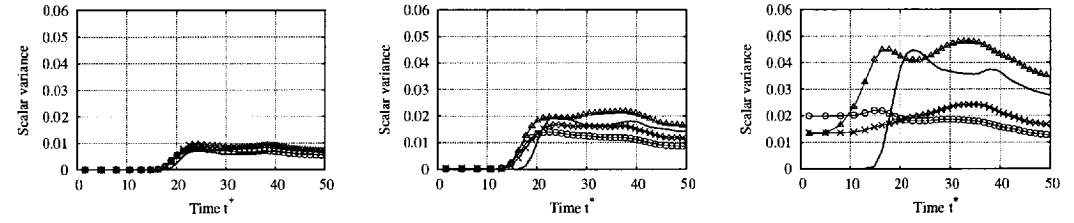

Figure 5.26: Time evolution of the scalar variance (−), the predictions of the gradient model (×), the similarity model I (⊙) and the similarity model II (△), case JMixing-B, off the mixing layer, **(a)** on 64^3, **(b)** on 32^3 and **(c)** on 16^3 nodes.

In contrast to the SGS scalar dissipation rate, the magnitude of the scalar variance exhibits a strong dependence on the grid resolution. It can be seen in figures 5.16 to 5.20 that for each one of the DNS realisations, χ_{SGS}^{DNS} remains at the same level when

the grid resolution changes. However, the scalar variance from the DNS simulations increases proportionally to the filter width Δ, as seen in the plots 5.24 to 5.26 of time evolution of $\widetilde{\xi''^2}$. This behaviour can be attributed to the reduction in resolution leads to a large increase in SGS energy of the scalar fluctuations, as seen in figure 5.12(**a**).

In contrast, most of the scalar dissipation rate arises from fluctuations with length scale smaller than the filter width, as seen in figure 5.12(**b**) and differences between the coarse and the intermediate are indeed minor. Thus, a decrease in resolution demands the capability of the variance model to capture a wide range of length scales and their different characteristics while the modelling of scalar dissipation needs to account for a smaller range of scales only.

5.4 Effect of the differentiation error on SGS scalar dissipation rate modelling

In section (5.1.3) it has been pointed out that finite differences approximation of the spatial derivatives on the LES grid introduces a differentiation error. However, following the common practice in the LES methodology and in "a priori" testing, the zero equation SGS models have been assessed using the LES discretisation depicted in figure (5.1)(**b**). In this section the performance of the gradient model for the scalar dissipation rate is assessed using the finite difference approximation provided by equation (5.8) calculated on the discretisation shown in figure (5.1)(**c**).

In figures (5.27)(**a**) and (5.27)(**b**) the scatter plot of the predictions of the gradient model when the filtered field is discretised on the DNS mesh is compared with the predictions of the model evaluated on the LES mesh. The comparison of the scatter of the predictions with the straight lines depicted in the figures 5.27(**a-b**) shows that the discretisation depicted in the graph (5.1)(**b**) provides overpredictive results by two or three times, depending on the filter width. This behaviour of the gradient model when the fine discretisation is used can be attributed to the better capture of the high gradients of the shear layer.

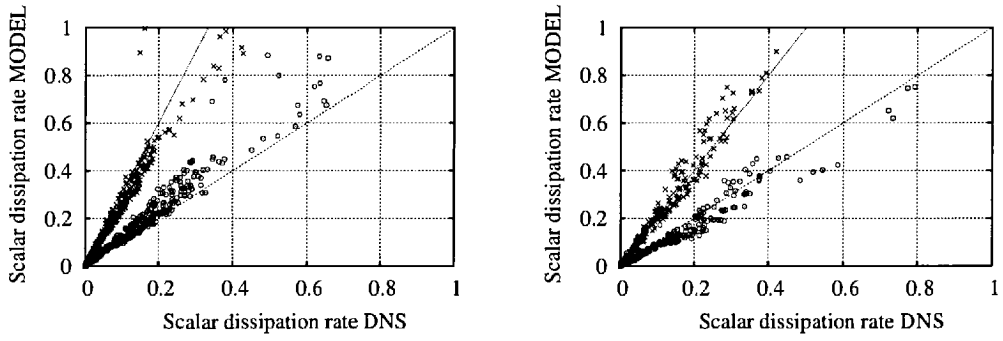

(a) **(b)**

Figure 5.27: Scatter plot of the predictions for the scalar dissipation rate, averaged over the homogeneous direction at $Z = z_A$, at all the time steps of the simulation `JMixing-B` **(a)** on the fine mesh **(b)** on the intermediate mesh. Symbols; (×) the filtered field discretised on the DNS mesh, (⊙) The filtered field discretised on the LES mesh.

5.5 Summary

In this section, the main findings for the investigation of the turbulent mixing problem carried out in this chapter, are presented.

The production equals dissipation assumption has been found to be valid for all cases with the exception of the shear layer regions of the planar jet simulations, during the initial stages of the flow field evolution. In addition, for the non-homogeneous simulations and for the areas outside the mixing layers, the rest of the terms of the scalar variance transport equation exhibit large magnitudes which are comparable to the ones of the production and the dissipation terms in contradiction to the local equilibrium assumption, however they cancel each other. The approximation of the spatial derivatives for the transport equation of $\widetilde{\xi''^2}$ has been carried out on the DNS mesh. Using a coarser LES mesh with grid spacing comparable to the filter width introduces a differentiation error that results in a high residual for the terms of the scalar variance transport equation.

This discretisation error causes a significant divergence of the spatial derivatives of the filtered quantities to the corresponding filtered derivatives from the DNS. This behaviour influences the final predictions of the models, as shown for the case of the gradient model. The gradient model becomes systematically over-predictive when the

differentiation error is avoided. It must be noted, though, that a simple reduction of the model constant would correct the final predictions.

The "a priori" tests of the gradient and the dynamic scalar dissipation models has shown that they provide reasonable predictions. However, during the initial time period in the planar jet simulations the models deviate from the DNS results. The gradient model overestimates the SGS contribution of χ due to the high resolved gradients of the transitional flow field. The dynamic model, being able to adapt to laminar flows [114], predicts the production of the energy of the scalar fluctuations rather than the dissipation term. In addition, the gradient model exhibits better predictions of the PDF of the scalar dissipation rate, in relation to the similarity model. Finally, the predictions of the models for the scalar variance show sensitivity to the energy resolution, with the exemption to the similarity model II, where the distribution for the energy of the fluctuations of the scalar field is modelled by the Oboukhov-Corrsin spectrum.

Chapter 6

CMC modelling of extinction and re-ignition in turbulent non-premixed flames

In chapter four the details of the simulations for diluted methane combustion in homogeneous and turbulent shear flows were presented. In this chapter, the singly and the doubly conditioned CMC methodologies are used to model the reaction rates and the time evolution of the conditioned mass fractions for the simulated flow field. Since the DNS database comprises of flames with varying Damköhler numbers, the relative performance of the two CMC methodologies can be assessed for flames with varying degrees of local extinction and re-ignition.

6.1 Singly conditioned CMC

The difficulties of turbulent combustion modelling arise from the fact that the rates of reaction are highly non-linear functions of temperature and species concentrations [15]. Given that large spatial and temporal fluctuations of the scalar quantities occur in turbulent flames, the efforts to express average rates of reaction in terms of average values of the scalars prove to be inadequate. The CMC methodology is based on the representation of the scalar quantities conditioned on selected variables such as

the mixture fraction. Taking into account that the fluctuation of the scalar quantities can be associated with the fluctuations of one key quantity, the fluctuations around the conditionally averaged or conditionally filtered variable provided by the equation (2.145) are reduced.

The variation of carbon monoxide mass fraction inside a filtering volume of the LES discretisation, as presented in chapter five, is depicted in figure 6.1 as a function of the mixture fraction. As it can be seen that the unconditioned fluctuations of Y_{CO} are high, however the fluctuations around the conditional average are reduced. For the carbon monoxide mixture fraction, the conditionally averaged value, $\langle Y_{CO}|\eta\rangle$, is also presented in figure 6.1.

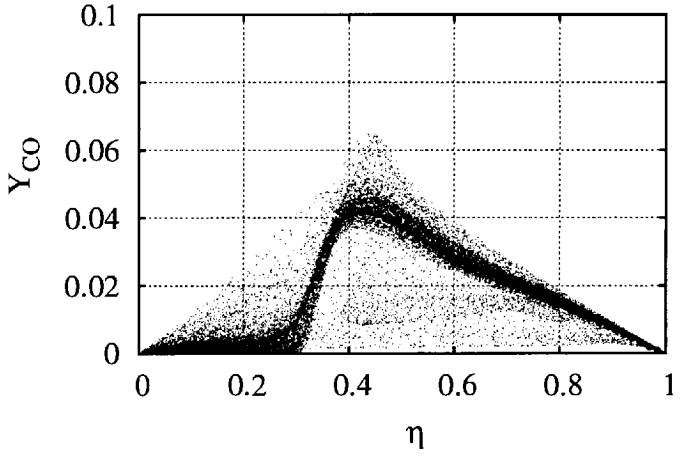

Figure 6.1: Scatter of Y_{CO} on η space from case `HReactive-D`. Continuous line (–), $\langle Y_{CO}|\eta\rangle$.

The singly conditioned CMC closure for the DNS simulations presented here is based on the averages of the scalar field conditioned on the mixture fraction for the whole computational domain. Following Klimenko *et* al. [15], the conditional average of the field quantity Φ can be expressed as

$$\langle \Phi(x;t)|\eta\rangle = \frac{1}{P(\eta)} \int_{-\infty}^{\infty} \phi P(\phi,\eta) d\phi \,, \tag{6.1}$$

where, η and ϕ are the sample space ξ and Φ, respectively and P is the joint PDF

of ξ and Φ. As mentioned in chapter two, the field variable Φ represents the enthalpy or temperature field or any other reacting scalar, which transports within the flow field. Taking into account that in the present study a diluted methane flame has been simulated and constant properties are assumed, the conditional average defined in equation (6.1) is equal to the expression of the conditionally filtered variable shown in equation (2.145), i.e. $\langle \Phi|\eta \rangle = \tilde{\Phi}_{\eta}$, assuming a box filter function G that covers the whole DNS domain. This results in the following expression for the singly conditioned CMC equation (2.156) (SCMC),

$$\frac{\partial \langle \Phi|\eta \rangle}{\partial t} = \langle \omega_{\Phi}|\eta \rangle + \langle N|\eta \rangle \frac{\partial^2 \langle \Phi|\eta \rangle}{\partial \eta^2} \ . \tag{6.2}$$

In the above equation the spatial gradients of the conditioned moments have been neglected since the CMC cell covers the whole DNS domain and the boundary conditions of the simulated flow field are periodic. In addition to the differential equation (6.2), the boundary conditions for the species mass fractions and the conditional enthalpy are written as,

$$\langle \Phi|\eta = 0 \rangle = \Phi^{O} \ , \ \langle \Phi|\eta = 1 \rangle = \Phi^{F} \ , \tag{6.3}$$

where Φ^{O} and Φ^{F} are the values of the scalar Φ in the areas of the pure oxidiser and fuel, respectively. Equations (6.2) and (6.3) define an initial value problem. The initial conditions $\langle \Phi|\eta \rangle(t = 0)$ consist of the same flamelet solution used for the derivation of the initial distributions of the scalars fields for the DNS simulations shown in figure 4.2.

In order to evaluate the performance of the SCMC model, equation (6.2) is solved in time using a finite difference numerical algorithm for the simulations, with reactions that are listed in tables 4.3 and 4.5. The conditional fields are solved implicitly in space while time advancement is solved explicitly. In addition, a fractional step algorithm [168] is used for the implicit evaluation of the conditional reaction rate. The conditional reaction rate is evaluated using a first order closure,

$$\langle \omega_{\Phi}|\eta \rangle = f\left(\langle Y_{CH_4}|\eta \rangle, \langle Y_{CO}|\eta \rangle, \langle Y_{H_2}|\eta \rangle, \langle \Theta|\eta \rangle\right) \tag{6.4}$$

based on the the singly conditioned mass fractions and enthalpy using the four-step chemistry mechanism presented in chapter four. The remaining unclosed quantity is the conditional scalar dissipation term $\langle N|\eta\rangle$. For the assessment of the SCMC modelling methodology, the $\langle N|\eta\rangle$ term is closed using the data from the DNS simulation.

The time evolution of the mean distribution for the methane mass fraction $< Y_{CH_4} >$, which is defined as

$$< Y_{CH_4} >= \int_0^1 \langle Y_{CH_4}|\eta\rangle P(\eta) d\eta \,, \tag{6.5}$$

is presented in figure 6.2(**a**) for the low extinction case `HReactive-D`. In this figure, the results from the solution of the SCMC model are compared with $< Y_{CH_4} >$ calculated from the DNS. In figure 6.2(**b**), the results from the planar jet simulations `JReactive-B` and `JReactive-D` are also presented.

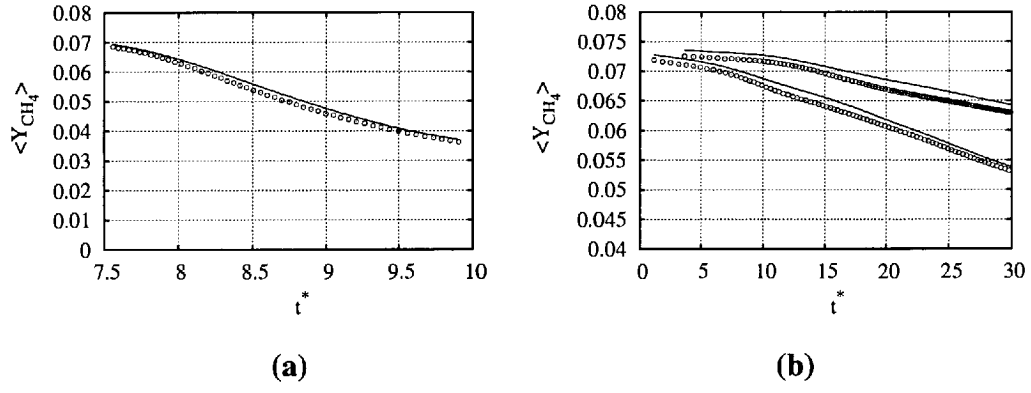

Figure 6.2: Time evolution of $< Y_{CH_4} >$ Symbols; ($\odot$) SCMC model and continuous line ($-$) DNS result. (**a**) for the case `HReactive-D`. (**b**) for the case `JReactive-B` and `JReactive-D`

Although the SCMC model provides good predictions for the low extinction simulations, this is not the case for the simulations that present significant local extinction i.e. `HReactive-B`, `JReactive-A` and `JReactive-C` as seen in figure 6.3. In the cases with high rates of extinction, the SCMC model predicts a faster depletion of the methane mass fraction. This behaviour can be attributed to the inability of the SCMC model to capture the dependence of the reaction rates on the temperature [17]. Finally, the SCMC model provides good predictions for the case `HReactive-A`, which

presents total extinction.

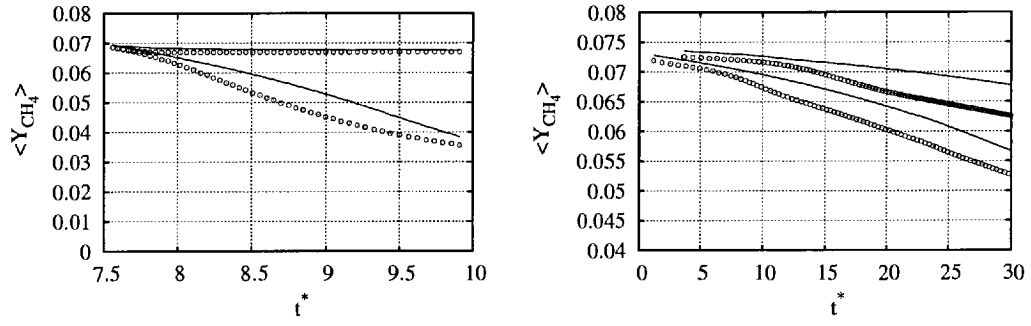

Figure 6.3: Time evolution of $< Y_{CH_4} >$ Symbols; (⊙) SCMC model and continuous line (−) DNS result. **(a)** for the cases `HReactive-A` and `HReactive-C`. **(b)** for the cases `JReactive-B` and `JReactive-D`

6.2 Doubly conditioned CMC

Important combustion phenomena like flammability limits, flame stabilisation and wall quenching, require accurate modelling of extinction and re-ignition events [17]. Conventional CMC methodologies are based on the fact that fluctuations of the reactive scalars can be associated with those of one key quantity. However, this is not valid in flames with local extinction. The scatter plot, presented in figure 6.4 **(a)**, depicts the carbon monoxide mass fraction as a function of the mixture fraction for the DNS cells within an LES filtering volume. In contrast to figure 6.1, this plot is from the case `HReactive-B`, which is characterised by high extinction. As it can be seen, the fluctuations of the mass fraction around the conditional value are much higher than the ones observed in case `HReactive-D`, where the extinction is smaller. These high fluctuations around the singly conditioned mean $\langle Y_{CO}|\eta\rangle$ introduce large errors for a first order closure of the reaction rates using the expression (2.159) [17].

However, the fluctuations of $\langle Y_{CO}|\eta\rangle$ are correlated with the normalised sensible enthalpy Θ, since they are caused by the local extinction of the flame. In places where the flame is extinct within the filtering volume, the flame structure cannot be repre-

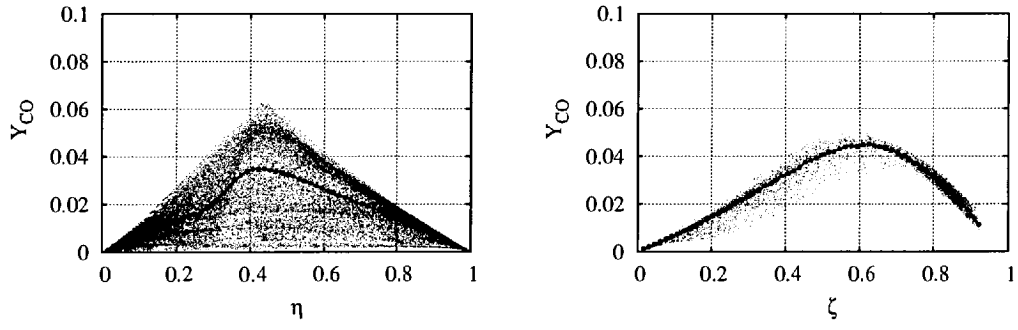

(a) **(b)**

Figure 6.4: **(a)** Scatter of Y_{CO} on η space from case `HReactive-B`. Continuous line $\langle Y_{CO}|\eta\rangle$. **(b)** Scatter of $\langle Y_{CO}|\eta\rangle$ on ζ space for $\eta = \xi_{st}$ from case `HReactive-B`. Continuous line $\langle Y_{CO}|\eta,\zeta\rangle$.

sented by a unique distribution of the mass fractions in η-space. Introducing a second conditional direction, i.e. the ζ-space as discussed in chapter two, the field variables can be in addition conditioned on the normalised enthalpy as,

$$\langle\Phi(\boldsymbol{x};t)|\eta,\zeta\rangle = \frac{1}{P(\eta,\zeta)}\int_{-\infty}^{\infty}\phi P(\phi,\eta,\zeta)d\phi\,, \tag{6.6}$$

following the expression (6.1) of the singly conditioned field. The fluctuations around the resulting doubly conditioned (DCMC) mass fraction $\langle Y_{CO}|\eta,\zeta\rangle$ become smaller in relation to the fluctuations around the singly conditioned value, as seen in the scatter plot (6.4)(**b**) of Y_{CO} against ζ for $\eta = \xi_{st}$. The DCMC equations (2.186) for the constant property simulations discussed in this chapter can be expressed as,

$$\begin{aligned}\rho\frac{\partial\langle\Phi|\eta,\zeta\rangle}{\partial t} = \langle\omega_\Phi|\eta,\zeta\rangle - \langle\omega_\Theta|\eta,\zeta\rangle\frac{\partial\langle\Phi|\eta,\zeta\rangle}{\partial\zeta} &+ \rho D\langle\nabla\xi\cdot\nabla\xi|\eta,\zeta\rangle\frac{\partial^2\langle\Phi|\eta,\zeta\rangle}{\partial\eta^2} \\ +\rho D\langle\nabla\Theta\cdot\nabla\Theta|\eta,\zeta\rangle\frac{\partial^2\langle\Phi|\eta,\zeta\rangle}{\partial\zeta^2} &+ 2\rho D\langle\nabla\xi\cdot\nabla\Theta|\eta,\zeta\rangle\frac{\partial^2\langle\Phi|\eta,\zeta\rangle}{\partial\eta\partial\zeta}\end{aligned} \tag{6.7}$$

where the spatial gradients have been neglected, a box filtering operation is assumed, and the e_Φ and e_D terms, along with the convection term, have been discarded. Although expression (6.7) has been derived by the conditional filtering operation de-

fined in equation (2.165), it is worth noting that it is identical to the DCMC equations for the conditional averages derived by the decomposition method [17].

The DCMC model is used for the modelling of the time evolution of the conditional mass fractions for the reacting DNS simulations. Following a similar approach to SCMC, equation (6.7) is integrated numerically in time using the same algorithm as for the solution of equation (6.2). A finite difference scheme is used for the discretisation of the doubly conditioned values on the two dimensional conditional space. In addition, the fractional step algorithm is used for the evaluation of the chemical source term, and the time step advancement is calculated explicitly. The boundary conditions of each one of the conditional fields are expressed as:

$$\begin{aligned} \langle \Phi|\eta = 0, \zeta\rangle = \Phi^O \quad , \quad & \langle \Phi|\eta = 1, \zeta\rangle = \Phi^F \\ \langle \Phi|\eta, \zeta = 0\rangle \;\; = \;\; & \Phi^O + \eta(\Phi^F - \Phi^O) \\ \langle \Phi|\eta, \zeta = 1\rangle \;\; = \;\; & \begin{cases} 0 & \text{if } \eta < \xi_{st} \\ \frac{\eta - \xi_{st}}{1 - \xi_{st}} \Phi^F & \text{if } \eta \geq \xi_{st} \end{cases} , \end{aligned} \tag{6.8}$$

where frozen chemistry is assumed for $\zeta = 0$ and fast chemistry for $\zeta = 1$. The initial conditions $\langle \Phi|\eta, \zeta\rangle(t = 0)$ are synthesised using the initial flamelet solution, shown in figure 4.2, and is therefore consistent with the initial conditions of the DNS simulations. Given that the flamelet solution provides a one dimensional expression of enthalpy as a function of mixture fraction, a spline interpolation [18] is used to interpolate the initial conditions in the two dimensional conditional domain, as shown in figure 6.5.

The remaining unclosed terms of equation (6.7) are the three dissipation terms. Their distribution in η-ζ-space is shown in figure (6.6). In order to evaluate the primary modelling assumption the unclosed terms, $\langle \nabla\xi \cdot \nabla\xi|\eta, \zeta\rangle$, $\langle \nabla\Theta \cdot \nabla\Theta|\eta, \zeta\rangle$ and $\langle \nabla\xi \cdot \nabla\Theta|\eta, \zeta\rangle$ are evaluated from the DNS simulation and modelling is not attempted here. Models based on the Multiple Mapping Conditioning (MMC) approach have recently been tested [169] but the evaluation of conditional dissipation is beyond the scope of this thesis.

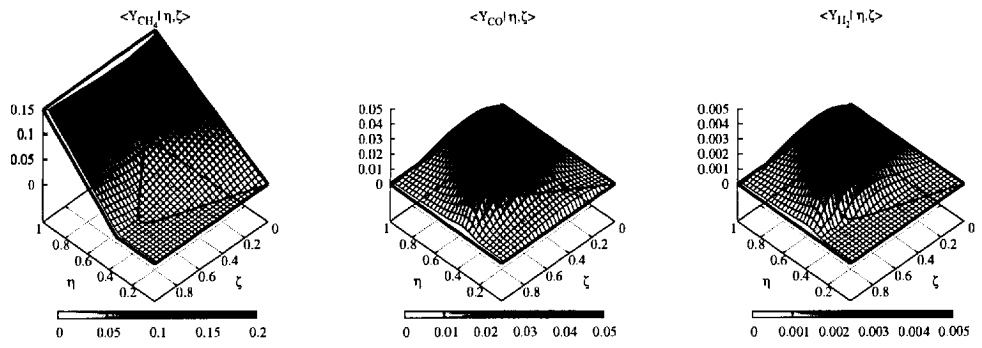

Figure 6.5: Initial conditions for the doubly conditioned fields interpolated from the flamelet solution.

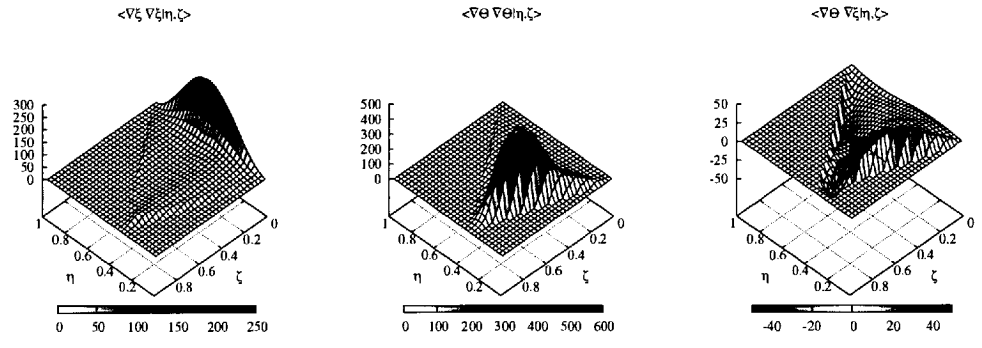

Figure 6.6: Distribution of the unclosed dissipation terms of the DCMC equation.

The solution of the DCMC model in time provides the time evolution of the doubly conditioned fields for the whole DNS domain. The depletion of the methane mass fraction due to combustion is presented in figure 6.7. In this plot, the time evolution of the average of the methane mixture fraction defined as,

$$< Y_{CH_4} >= \int_0^1 \int_0^1 \langle Y_{CH_4}|\eta,\zeta\rangle P(\eta,\zeta) d\eta d\zeta \ , \tag{6.9}$$

is presented for both homogeneous turbulence and planar jet simulations. Comparison of the DCMC results with the values in figure 6.3 shows that the DCMC model manages to provide the correct time evolution for the methane mass fraction in both homogeneous and inhomogeneous turbulent fields, regardless of the amount of local extinction in each flame.

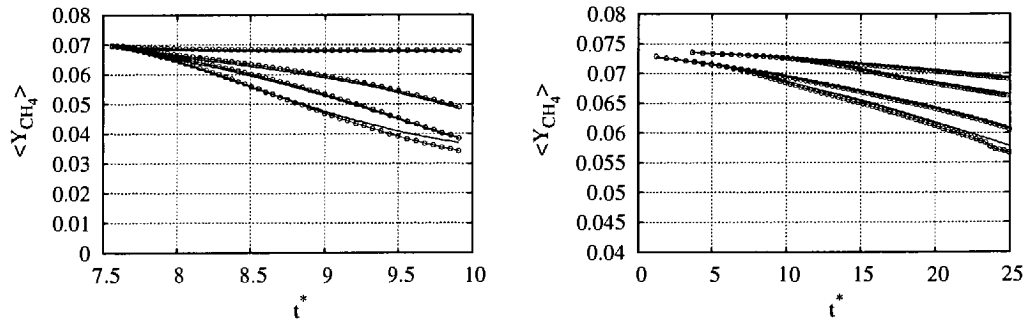

(a) **(b)**

Figure 6.7: Time evolution of $< Y_{CH_4} >$. Symbols; (⊙) DCMC model and continuous line (−) DNS result. **(a)** for the cases `HReactive-A` to `HReactive-D`. **(b)** for the cases `JReactive-A` to `JReactive-D`.

6.3 Comparison of the SCMC and DCMC predictions

The SCMC predictions, i.e. $\langle \Phi|\eta \rangle^{SCMC}$, can be compared to the equivalent prediction $\langle \Phi|\eta \rangle^{DCMC}$ of the DCMC model. Results are conditioned on the η-space only, using the expression

$$\langle \Phi|\eta \rangle^{DCMC} = \int_0^1 \langle \Phi|\eta, \zeta \rangle P(\eta, \zeta) d\zeta \, . \tag{6.10}$$

In figure 6.8 the DNS results for the progress rates of the four chemical reactions at $t^* = 37.60$ from the high extinction jet simulation `JReactive-C` are compared with the SCMC and DCMC predictions. Due to the high fluctuations around the singly conditioned mean, the SCMC model fails to account for local extinction, thus over predicting the rates $\langle \omega|\eta \rangle$ for all four reactions of the four step chemistry mechanism. This behaviour leads to the underprediction of the conditional averages for the species mass fractions shown in the figure 6.9, where the methane mass fraction is depleted on the lean side. In addition, the mass fractions of the intermediate species, i.e. CO and H_2, are under predicted. However, The predictions of the DCMC model provided in the same figures are close to the DNS results, given that the conditional fluctuations of the doubly conditioned values are reduced.

A more general comparison of the SCMC and DCMC models is presented in the

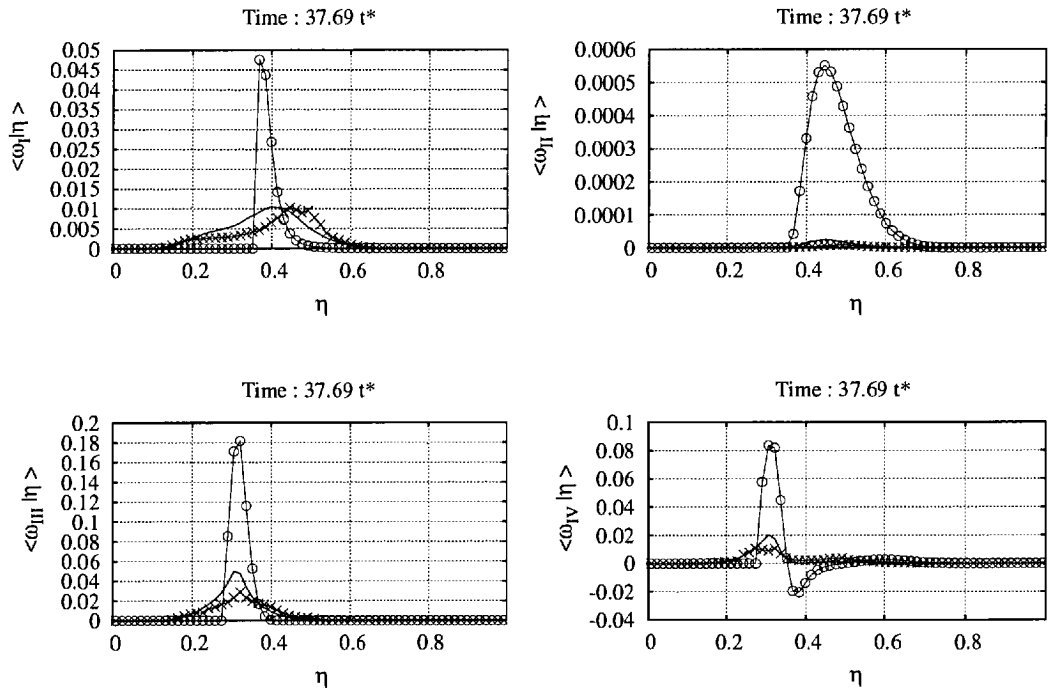

Figure 6.8: Case JReactive-C. Conditional average of the chemical reaction rates for the four step chemistry mechanism. Symbols; (⊙), single conditioning, (×) double conditioning, and continuous line, (−) DNS results.

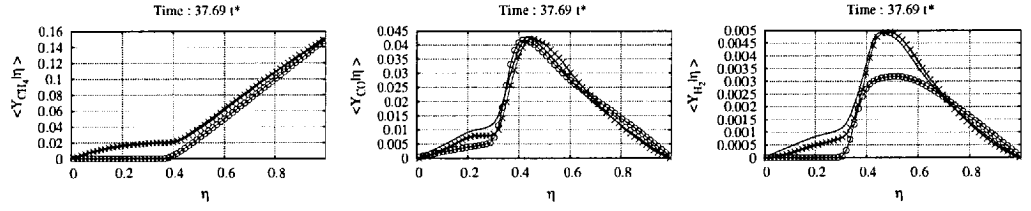

Figure 6.9: Case JReactive-C. Conditional average of the methane, carbon monoxide and hydrogen mixture fraction plotted against the mixture fraction. Symbols; (⊙), single conditioning, (×) double conditioning, and continuous line, (−) DNS results.

figures 6.10 to 6.12. In these figures the time evolution of the predicted mass fractions on the stoichiometric mixture fraction is compared to the DNS result for the cases JReactive-C, JReactive-D and HReactive-D respectively. As it can be seen, even for the low extinction case JReactive-D the SCMC model fails to capture the time evolution of the species mass fractions accurately. The DCMC model manages to cap-

ture the evolution of the species mass fractions for all the cases of different extinction levels.

Finally the case HReactive-D both models provide satisfactory results. As seen in the figure 4.8 this case exhibits minor extinction, thus the SCMC assumption for reduced conditional fluctuations around the singly conditioned average holds.

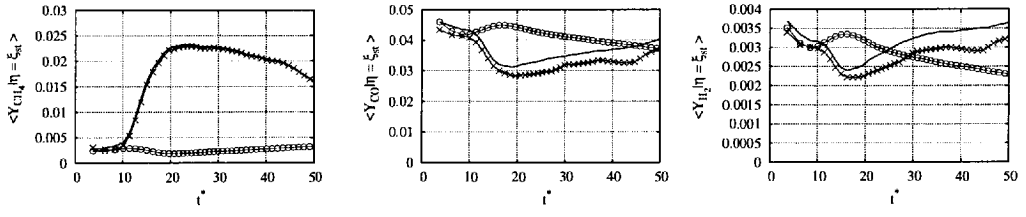

Figure 6.10: Case JReactive-C. Time evolution of the reactive species close to the stoichiometric mixture fraction. Symbols; (⊙), single conditioning, (×) double conditioning, and continuous line, (−) DNS results.

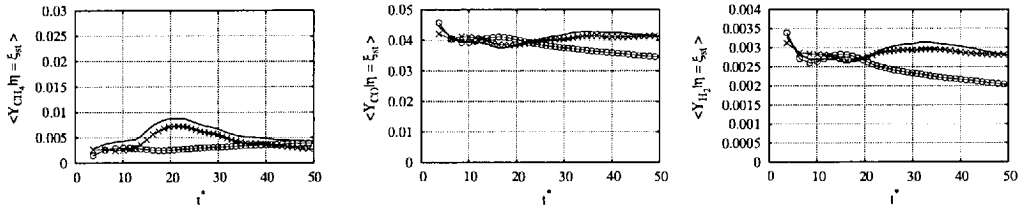

Figure 6.11: Case JReactive-D. Time evolution of the reactive species close to the stoichiometric mixture fraction. Symbols; (⊙), single conditioning, (×) double conditioning, and continuous line, (−) DNS results.

Figure 6.13 **(a)** shows the distribution of the $P(\eta, \zeta)$ at $\eta = \xi_{st}$ for the homogeneous turbulence simulations. As it can be seen for the cases HReactive-B and HReactive-C the shape of the PDF presents two peaks for the low and the high enthalpy areas. The intermediate interval, i.e. for $0.3 < \zeta < 0.7$, is sparsely populated. It can be said that this interval consists of cells that transit from the high to the low temperature areas during extinction or to the opposite direction during the re-ignition. As expected the PDF for the fully burning case HReactive-D and the extinct simula-

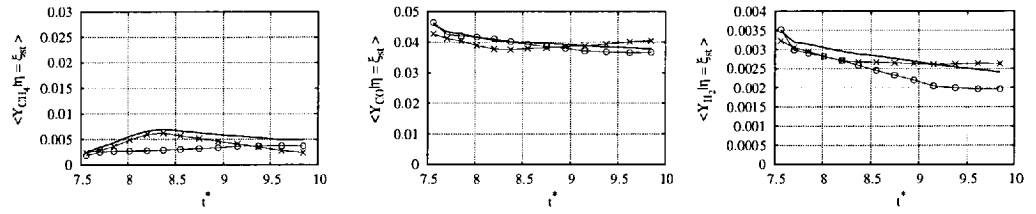

Figure 6.12: Case HReactive-D. Time evolution of the reactive species close to the stoichiometric mixture fraction. Symbols; (⊙), single conditioning, (×) double conditioning, and continuous line, (−) DNS results.

tion HReactive-A does not present this shape. The PDF for the planar jet simulations shows the same bimodal shape. As seen in the next figure 6.13 **(b)** the maximum reaction rates are located in this sparsely populated area around $\zeta = 0.6$. As a result the SCMC model which implicitly assumes a Dirac PDF distribution along the ζ-space distribution, which is located at the value of the singly conditioned enthalpy or temperature, provided in the figure 4.8 is bound to overpredict the depletion of the methane mass fraction as shown in this chapter.

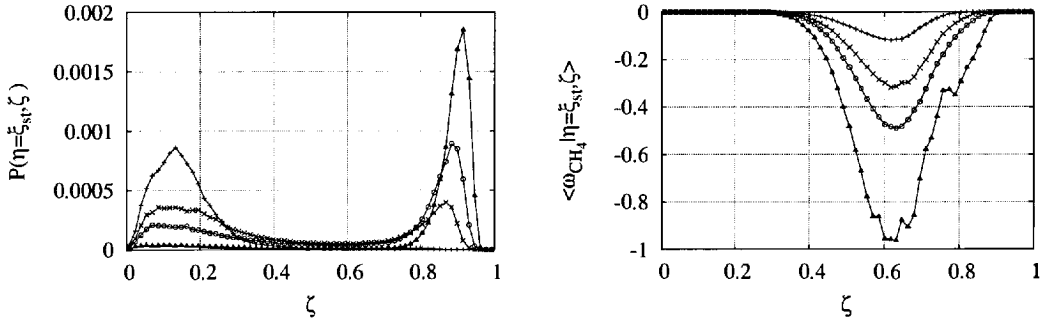

Figure 6.13: **(a)** The distribution of the joint probability density function, $P(\eta, \zeta)$ for $\eta = \xi_{st}$, from the homogeneous turbulence simulations at $t^* = 8.5$. **(b)** The distribution of the doubly conditioned methane chemical source term, at $t^* = 8.5$. Symbols; + HReactive-A, × HReactive-B, ⊙ HReactive-C, △ HReactive-D

6.4 Summary

The SCMC and DCMC methodologies presented in the second chapter of this thesis have been tested as far as the closure of the chemical reaction rates of a diluted methane flame is concerned. It was shown that the SCMC methodology fails to predict the reaction rate for flames with significant local extinction, leading to the over prediction of the fuel depletion. In contrast, the DCMC methodology manages to capture the effect of local extinction and re-ignition, thus providing better results for flames with different Damköhler numbers.

Chapter 7

Closure

The work presented in this thesis has dealt with the numerical investigation of scalar mixing and combustion modelling in turbulent flows. In this chapter the main findings are summarised and suggestions are made for future work.

7.1 Summary

The work carried out in the present study can be summarised as follows:

- The background on turbulent combustion modelling in CFD has been presented. In addition, a review of the evolution of DNS for the solution of turbulent reacting and non-reacting flows has been described. Finally, a derivation of the governing equations for the filtered doubly conditioned moments has been presented, that is based on the conventional filter function used in LES.

- A parallelisation approach for a pseudospectral solver has been derived and presented in chapter two, that allows the realisation of DNS of turbulent reactive flows with low memory allocation.

- The problems arising from the spectral representation of reactive species in the DNS of turbulent combustion have been identified, and a finite differences solver has been used for the integration of the reactive species in time. In addition, a series of DNS solutions of reacting and non-reacting flows has been carried out

constituting a DNS database of diluted methane combustion with different rates of extinction and re-ignition.

- Zero equation models for the scalar variance and the scalar dissipation rate have been assessed based on the DNS solutions.

- Finally the suitability the SCMC and DCMC models for the solution of the diluted methane combustion with varying degrees of extinction by comparison with the DNS results.

7.2 Suggestions for future work

Open questions and un-investigated topics have arisen from the present study. More specifically, some of the areas that should be subject of future research are:

- The diluted methane combustion DNS database can be used for the investigation of alternative turbulent combustion models other than the CMC, such as the multiple mapping conditioning (MMC).

- "A posteriori" tests are expected to provide better insight into the predictive capabilities of the micromixing models and they can answer questions on the effect of the discretisation on the LES modelling and the nature of the filtering operator in LES.

- A CMC solver that accounts for possible spatial variation of the conditional moments may be used for the modelling of the reactive species evolution. A finer discretisation of the conditional averages is expected to provide better results to the singly conditioned closure.

- The modelling of the doubly conditioned scalar dissipation, dissipation of enthalpy and cross dissipation terms. These terms remain unclosed for the doubly conditioned CMC equations.

7.3 Conclusion

The results of the present study have been assessed and discussed in the previous chapters. In the following, the most important conclusions are summarised.

- It has been shown that the derived DNS database is characterised by proper resolution of the turbulent scales, and the flame front thickness is captured well. Furthermore, the comparison of the DNS results to similar experiments for the velocity fields shows that the DNS solutions are realistic representations of the turbulent flow field.

- The "a priori" tests of the zero equation models for the scalar mixing showed that - with the exception of the transitional period - the models tested provide reasonable results when averaged over homogeneous directions. The probability distribution of scalar dissipation rates predicted by the gradient model approximate the corresponding PDF for the DNS well. In addition, the gradient model does not show sensitivity to the mesh size and resolution. The main inefficiency of the gradient model in relation to the dynamic model derives from the inability of the model to adapt to shear flows during the transitional period. The need of a modelling constant for the gradient model is an additional drawback. The differentiation error plays a significant role in the predictive capabilities of all scalar dissipation models changing its behaviour significantly.

- The singly conditioned CMC equation fails to predict the evolution of the reactive species mass fractions for flames with mild extinction. The reason of this performance for the singly conditioned model lays on the inability to capture the distribution of the flame structure for flames with extinction. The doubly conditioned CMC model works well for all the simulations with various degrees of extinction.

Bibliography

[1] N. Peters. *Turbulent Combustion*. Cambridge Univercity Press, 2000.

[2] Department of Trade and Industry. The energy challenge. *Energy Review Report*, 2006.

[3] J. M. Beer. Combustion technology developments in power generation in response to environmental challenges. *Progress in Energy and Combustion Science*, (26):301–327, 2000.

[4] H. J. Herzog and E. M. Drake. Long-term advanced CO_2 capture options. Technical report, Cheltenham, UK, IEA/93/0E6 Greenhouse Gas R&D Program, 1993.

[5] Hein and R.G. Klaus. Combustion at a crossroads: Status and prospects. *Proceedings of the Combustion Institute*, 29:393–398, 2002.

[6] F.B. Blackmore, C. Davies, and J.G. Isaac. The effects of changes in the uk energy demand and environmental legislation on atmoshperic pollution by carbon dioxide. *Applied energy*, 59:273–303, 1998.

[7] R.W. Bilger, S.B. Pope, K.N.C. Bray, and Driscoll J.F. Paradigms in turbulent combustion research. *Proceedings of the Combustion Institute*, 30:21–42, 2005.

[8] R.S. Turns. *An introduction to combustion: Concepts and Applications*. McGraw-Hill, New York, 1996.

[9] N. Peters. Laminar diffusion flamelet models in non-premixed turbulent combustion. *Progress in Energy and Combustion Science*, 10:319–340, 1984.

[10] F. Maus, D. Keller, and N. Peters. A lagrangian simulation of flamelet extinction and re-ignition in turbulent jet diffusion flames. *Proceedings of the Combustion Institute*, 22:569–597, 1988.

[11] D.C. Haworth, M.C. Drake, R.J. Pope, and R.J. Blint. The importance of time-dependent flame structures in stretched laminar flamelet models for turbulent jet diffusion flames. *Proceedings of the Combustion Institute*, 22:569–597, 1989.

[12] C. Dopazo and E. E. O'Brien. An approach to the autoignition of a turbulent mixture. *Acta Astronaut.*, 1:1239–1266, 1974.

[13] S. B. Pope. The implications of the probability equations for turbulent combustion models. *Combustion and Flame*, (27):299–312, 1976.

[14] A. Y. Klimenko. Multicomponent diffusion of various mixtures in turbulent flow. *Fluid Dynamics*, 25:327–334, 1990.

[15] A. Y. Klimenko and R. W. Bilger. Conditional moment closure for turbulent combustion. *Progress in Energy and Combustion Science*, 25:595–687, 1999.

[16] M. R. Roomina and R. W. Bilger. Conditional moment closure (CMC) predictions of a turbulent methane-air jet flame. *Combustion and Flame*, 125:1176–1195, 2001.

[17] A. Kronenburg and A. E. Papoutsakis. Conditional moment closure modelling of extinction and re-ignition in turbulent non-premixed flames. *Proceedings of the Combustion Institute*, 30:759–766, 2005.

[18] A. Kronenburg. Double conditioning of turbulent scalar transport equations in turbulent non-premixed flames. *Physics of Fluids*, 16(7):2642–2648, 2004.

[19] A. Y. Klimenko and Pope S. B. The modelling of turbulent reactive flows based on multiple mapping conditioning. *Physics of Fluids*, 15(5):1907–1925, 2003.

[20] T. Poinsot and D. Veynante. *Theoretical and Numerical Combustion*. R.T. Edwards, Inc, 2001.

[21] K. K. Kuo. *Principles of Combustion.* John Wiley, 1986.

[22] J. O. Hinze. *Turbulence.* McGraw-Hill, 1987. First edition 1959, Second 1975.

[23] L. F. Richardson. Athmospheric diffusion shown on a distance-neighbour graph. *Proc. Roy. Soc. A*, 110:709, 1926.

[24] J. Bardina, J. H. Ferzinger, and W. C. Reynolds. Improved subgrid-scale models for large-eddy simulation. *AIAA Journal*, (1357), 1980.

[25] H. Tennekes and Lumley J. L. *A First Course in Turbulence.* MIT Press, 1972.

[26] S. B. Pope. *Turbulent Flows.* Cambridge University Press, 2001.

[27] A.N. Kolmogorov and V.M. Tikhomirov. *Selected works of A. N. Kolmogorov: Volume I: Mathematics and Mechanics.* Kluwer Academic Publishers, 1991.

[28] P. K. Yeung and S. B. Pope. Langrangian statistics from direct numerical simulations of isotropic turbulence. *Journal of Fluid Mechanics*, 207:531–586, 1989.

[29] P. A. Durbin. *Statistical theory and Modelling for turbulent flows.* John Wiley, 2001.

[30] P. G. Saffman. The large-scale structure of homogeneous isotropic turbulence. *Journal of Fluid Mechanics*, 27:581–593, 1967.

[31] L. G. Loitsyansky. Some basic laws for isotropic turbulent flows. Technical report, Moscow Centr. Aero. Hydrodyn. Inst. Rep. No 440, 1993, (NACA Tech. Memo. 1079 (1939)), 1939.

[32] N. Branley. *Large eddy simulation of non-premixed turbulent flames.* PhD thesis, Department of Chemical Engineering and Chemical Technology, Imperial College of Science, Technology and Medicine, 1999.

[33] G. K. Batchelor. Small-scale variation of convected quantities like temperature in a turbulent fluid, Part 1. *Journal of Fluid Mechanics*, 5:113–133, 1959.

[34] A. M. Oboukhov. Structure of the temperature field in turbulent flows. *Izvestiya Akademii Nauk SSSR, Geogr. and Geophys. Ser.*, 13:58, 1949.

[35] S. Corrsin. On the spectrum of isotropic temperature fluctuations in isotropic turbulence. *Journal of Applied Physics*, 22:469, 1951.

[36] W. P. Jones and R. P. Lindstedt. Global reaction schemes for hydrocarbon combustion. *Combustion and Flame*, 73:233–249, 1988.

[37] N. Peters. Fifteen lectures on laminar and turbulent combustion. Technical report, Ercoftact Summer School, RWTH Aachen, 1996.

[38] L. Vervisch and T. Poinsot. Direct numerical simulation of non-premixed turbulent flames. *Annual Review of Fluid Mechanics*, 30:655–691, 1998.

[39] Liñan A. and Crespo A. An asymptotic analysis of unsteady diffusion flames for large activation energies. *Combustion Sci. Tech.*, 14(95), 1976.

[40] B. Cuenot and T. Poinsot. Asymptotic and numerical study of diffusion flames with variable lewis number and finite rate chemistry. *Combustion and Flame*, (104):111–37, 1996.

[41] N. Swaminathan and R. W. Bilger. Direct numerical simulation of turbulent nonpremixed hydrocarbon reaction zones using a two step reduced mechanism. *Combust. Sci. Technol.*, 127:167–196, 1997.

[42] R.M. Kerr. Higher-order derivatives correlations and the alignment of small-scale structures in isotropic numerical turbulence. *Journal of Fluid Mechanics*, 153:31–58, 1985.

[43] W. E. Mell, V. Nilsen, G. Kosaly, and J. J. Riley. Investigation of closure models for nonpremixed turbulent reacting flows. *Physics of Fluids*, 6(3):1331–1355, 1994.

[44] W. C. Reynolds. *The Pontential and Limitations of Direct and Large Eddy Simulations*. Springer-Verlag, Berlin, 1990.

[45] P. Givi. Model-free simulations of turbulent reactive flow. *Progress in Energy and Combustion Science*, 15, 1989.

[46] S. A. Orszag and G. S. Patterson. *Lecture Notes in Physics, in Statistical Models and Turbulence*. Springer-Verlag, New York, 1972.

[47] S. A. Orszag and G. S. Patterson. Numerical simulation of three-dimensional homogeneous isotropic turbulence. *Physical Review Letters*, 28(2), 1972.

[48] E.D. Siggia. Numerical study of small scale intermittency in three-dimensional turbulence. *Journal of Fluid Mechanics*, 107:375, 1981.

[49] M.E. Brachet, D.I. Meiron, S.A. Orszag, B.G. Nickel, R.H. Morf, and U. Frisch. Small-scale structure of the Taylor-Green vortex. *Journal of Fluid Mechanics*, 130:411, 1983.

[50] S. Kida and Y. Murakami. Kolmogorov similarity in freely decaying turbulence. *Physics of Fluids*, 30:2030, 1987.

[51] Moin P. and M. Krishnan. Direct numerical simulation. a tool in turbulence research. *Annual Review of Fluid Mechanics*, 30:539–578, 1998.

[52] Rogallo R. S. Numerical expreriments in homogeneous turbulence. *AIAA Journal*, (NASA TM-81315), 1981.

[53] A. Vincent and M. Meneguzzi. The spatial structure and statistical properties of homogeneous turbulence. *Journal of Fluid Mechanics*, 225:1, 1991.

[54] S. Chen, K.R. Sreenivasan, M. Nelkin, and N. Cao. Refined similarity hypothesis for transverse structure functions in fluid turbulence. *Phys. Rev. Lett*, 79:2253, 1997.

[55] Jimenez J. On small scale vorticies in turbulent flows. *Physics of Fluids A*, 4:652–654, 1991.

[56] J. Jimenez and P. Moin. The minimal flow unit in near wall turbulence. *Journal of Fluid Mechanics*, 225:213–240, 1991.

[57] J. Jimenez, A.A. Wray, P.G. Saffman, and R.S. Rogallo. The structure of intense vorticity in isotropic turbulence. *Journal of Fluid Mechanics*, 225:213–240, 1991.

[58] N. Chakraborty and R. S. Cant. Unsteady effects of strain rate and curvature on turbulent premixed flames in an inflow-outflow configuration. *Combustion and Flame*, (137):129–147, 2005.

[59] V. Eswaran and S.B. Pope. An examination of forcing in direct numerical simulations of turbulence. *Comput. Fluids*, 16:25778, 1988.

[60] D. Fukayama, T. Oyamada, T. Nakano, T. Gotoh, and K. Yamamoto. Longitudinal structure functions in decaying and forced turbulence. *J. Phys. Soc. Japan*, 69:701, 2000.

[61] K. Itakura, A. Uno, M. Yokokawa, T. Ishihara, and Y. Kaneda. Scalability of hybrid programming for a CFD code on the earth simulator. *Parallel Computing*, 30:1329–1343, 2004.

[62] J.J. Riley and R.W. Metcalfe. Direct numerical simulation of a perturbed, turbulent mixing. *AIAA paper*, (800274), 1980.

[63] R.D. Moser and P. Moin. The effects of curvature in wall-bounded turbulent flows. *Journal of Fluid Mechanics*, 175:479–510, 1987.

[64] Moser RD. Kim J, Moin P. Turbulence statistics in fully-developed channel flow at low Reynolds number. *Journal of Fluid Mechanics*, 177:133–136, 1987.

[65] H. Le and P. Moin. Direct numerical simulation of turbulent flow over a backwardfacing step. *Report TF-58, Thermosci. Div., Dept. Mech. Eng. Stanford Univ.*, 1994.

[66] Y Na and P. Moin. Direct numerical simulation of turbulent boundary layers with adverse pressure gradient and separation. *Report TF-68, Thermosci. Div., Dept. Mech. Eng. Stanford Univ.*, 1996.

[67] R. W. Metcalfe, S. A. Orszag, M. E. Brachet, and Riley J. J. Secondary instability of a temporally growing mixing layer. *Journal of Fluid Mechanics*, 184:207–243, 1987.

[68] A. B. Cortesi, G. Yadigaroglu, and S. Banerjee. Numerical investigation of the formation of three-dimensional structures in stably-stratified mixing layers. *Physics of Fluids*, 10(6):1449, 1998.

[69] A. B. Cortesi, B. L. Smith, B. Sigg, and S. Banerjee. Numerical investigation of the scalar probability density function distribution in neutral and stably stratified mixing layers. *Physics of Fluids*, 13(4):927, 2001.

[70] M. M. Rogers and D. M. Robert. Direct simulations of a self-similar turbulent mixing layer. *Physics of Fluids*, 6(2):903–922, 1993.

[71] M. M. Rogers and R. D. Moser. The three dimensional evolution of a plane jet mixing layer: the Kelvin-Helmholtz rollup. *Journal of Fluid Mechanics*, 243:183–226, 1992.

[72] M. M. Rogers and R. D. Moser. Direct simulation of a self-similar turbulent mixing layer. *Physics of Fluids*, 6(2):903–922, 1994.

[73] B. J. Geurts and J Frohlich. A framework for predicting accuracy limitations in LES. *Physics of Fluids*, 14(6):L41, 2002.

[74] R. Akhavan, S. Ansari, S. Kang, and N. Mangiavacchi. Subgrid-scale interactions in a numerically simulated planar turbulent jet and implications for modelling. *Journal of Fluid Mechanics*, 408:83–120, 2000.

[75] I. Wygnanski and H. E. Fiedler. The two-dimensional mixing region. *Journal of Fluid Mechanics*, 41:327, 1970.

[76] M. Klein, A. Sadiki, and J. Janicka. Investigation of the influence of the Reynolds number on a plane jet using direct numerical simulation. *Heat and Fluid Flow*, (24):785–794, 2003.

[77] S. A. Stanley, S. Sarkar, and J. P. Mellado. A study of the flow-field evolution and mixing in a planar turbulent jet using direct numerical simulation. *Journal of Fluid Mechanics*, (450):377–407, 2002.

[78] B. Knaepen, O. Debliquy, and Carati D. DNS and LES of a shear-free mixing layer. *Center for turbulence research*, 2003.

[79] P. Brancher, J. M. Chomaz, and Huerre P. Direct numerical simulations of round jets: Vortex induction and side jets. *Physics of Fluids*, 6(5):1768–1773, 1993.

[80] R. Verzicco and P. Orlandi. Direct simulations of the transitional regime of a circular jet. *Physics of Fluids*, 6(2):751, 2001.

[81] J. Mathew and A. J. Basu. An economical method for direct numerical simulation studies of transitional round jets. *Computers and Fluids*, 3:0543–0554, 2001.

[82] W. J. Feiereisen, W. C. Reynolds, and J. H. Ferziger. Numerical simulation of a compressible homogeneous turbulent shear flow. *Report TF-13, Thermosci. Div., Dept. Mech. Eng. Stanford Univ.*, 1981.

[83] S. S. Girimaji and S. Balachandar. Analysis and modelling of buoyancy-generated turbulence using numerical data. *Int. J. Heat Mass Transfer*, 41:915929, 1998.

[84] W. E. Mell, V. Nilse, G. Kosaly, and J. J. Riley. Direct numerical simulation investigation of the conditional moment closure model for nonpremixed turbulent reacting flows. *Combustion Science and Technology*, (91):179–186, 1993.

[85] T. Poinsot and S. K. Lele. Boundary conditions for direct simulations of compressible viscus flows. *Journal of Computational Physics*, 101:104–129, 1992.

[86] S. M. de Bruyn Kops, J. J. Riley, and G. Kosaly. Direct numerical simulation of reacting scalar mixing layers. *Physics of Fluids*, 13(5):1450, 2001.

[87] J. J. Riley, R. W. Metcalfe, and S. A. Orszag. Direct numerical simulations of chemically reacting turbulent mixing layers. *Physics of Fluids*, 29:406–422, 1986.

[88] C. Pantano. Direct simulation of non-premixed flame extinction in a methane-air jet with reduced chemistry. *Journal of Fluid Mechanics*, 514:231–270, 2004.

[89] E. R. Hawkes, R. Sankaran, J. C. Sutherland, and J. H. Chen. Scalar mixing in direct numerical simulations of temporally evolving plane jet flames with skeletal CO/H_2 kinetics. *Proceedings of the Combustion Institute*, 31:1633–1640, 2007.

[90] E. Mastorakos, T. A. Baritaud, and Poisont T. J. Numerical simulations of autoignition in turbulent mixing flows. *Combustion and Flame*, 109:198–223, 1997.

[91] Favre A. *Statistical equations of turbulent gases.*, pages 231–266. Physics of hydrodynamics and continum mechanics. Society for industrial and applied mathematics, PA. USA.

[92] Jones W. P. *Turbulence modelling and numerical solution methods for variable density and combustion flows.*, chapter 6, pages 309–374. P.A. Libby; F.A. Williams, 1994.

[93] P. Sagaut. *Large Eddy Simulation of incompressible flows.* Springer-Verlag, Berlin, Heidelberg, New York, 2002.

[94] W. Deardorff, J. On the magnitude of the subgrid scale eddy coefficient. *Journal of Comp. Physics*, 7:126–133, 1971.

[95] A. M. Kempf, F. Flemming, and J. Janicka. Investigation of lengthscales, scalar dissipation and flame orientetation in a piloted diffusion flame by LES. *Proceedings of the Combustion Institute*, 2004.

[96] S. B. Pope. Ten questions concerning the large-eddy simulation of turbulent flows. *New Journal of Physics*, (6):35, 2004.

[97] J Smagorinsky. General circulation experiments with the primitive equations, Part I: the basic experiment. *Monthly Weather Review*, 91:99–164, 1963.

[98] V. J. Boussinesq. Essai sur la thorie des eux courantes. *Mémoires prsents par divers savants á l'Acadmie des Sciences*, 23:46, 1877.

[99] U. Schumann. Subgrid-scale model for finite difference simulations of turbulent flow in plane channels and annuli. *Journal of Computational Physics*, (18):376–404, 1975.

[100] D. K. Lilly. The representation of small scale turbulence in numerical simulation experiments. *Proc. of IBM Scientific Computing Symp. on Env. Sciences*, page 195, 1967.

[101] R. A. Clark, J. H. Ferziger, and W. C. Reynolds. Evaluation of subgrid-scale turbulence models using a fully simulated turbulent flow. *Journal of Fluid Mechanics*, 91:1–16, 1979.

[102] D. W. Kwak, J. H. Ferziger, and W. C. Reynolds. Three-dimensional time-dependent simulation of turbulent flow. *Report TF-5, Thermosci. Div., Dept. Mech. Eng. Stanford Univ.*, 1975.

[103] H. Pitsch and H. Steiner. Scalar mixing and dissipation rate in large-eddy simulations of non-premixed turbulent combustion. *Proceedings of the Combustion Institute*, (28):41–49, 2000.

[104] S. M. de Bruyn Kops, J. J. Riley, G. Kosaly, and A. W. Cook. Investigation of modelling for non-premixed turbulent combustion. *Flow, Turbulence and Combustion*, (60):105–122, 1998.

[105] N. Branley and W. P. Jones. Large eddy simulation of a turbulent non-premixed flame. *Combustion and Flame*, (127):1914–1934, 2001.

[106] C. Jimenez, F. Durcos, B. Cuenot, and B. Bedat. Subgrid scale variance and dissipation of a scalar field in large eddy simulation. *Physics of Fluids*, 13(6):1748–1754, 2001.

[107] E. Effelsberg and N. Peters. Scalar dissipation rates in turbulent jets and jet diffusion flames. *Proceedings of the Combustion Institute*, (22):693–700, 1988.

[108] G. Blanquart and H. Pitsch. Modelling autoignition in non-premixed turbulent combustion using a stochastic flamelet approach. *Proceedings of the Combustion Institute*, 30(2):2745–2753, 2005.

[109] S. K. Liew, K. N. C. Bray, and J. B. Moss. A stretched laminar flamelet model of turbulent non-premixed combustion. *Combustion and Flame*, 56:199, 1984.

[110] H. Pitsch, M. Chen, and N. Peters. Unsteady flamelet modelling of turbulent hydrogen-air diffusion flames. *Proceedings of the Combustion Institute*, (27):1057–1064, 1998.

[111] J. P. H. Sanders and I. Gokalp. Scalar dissipation rate modelling in variable density turbulent axisymmetric jets and diffusion flames. *Physics of Fluids*, 10(4):0938–0948, 1998.

[112] S. S. Girimaji and Y. Zhou. Analysis and modelling of subgrid scalar mixing using numerical data. *Physics of Fluids*, 8(5):1224–1236, 1996.

[113] C. Jimenez, L. Valino, and C. Dopazo. A priori and a posteriori tests of subgrid scale models for scalar transport. *Physics of Fluids*, 13(8):2433–2436, 2001.

[114] C. D. Pierce and P. Moin. A dynamic model for subgrid-scale variance and dissipation rate of a conserved scalar. *Physics of Fluids*, 10(12):3041–3044, 1998.

[115] P. Moin, K. Squires, W. Cabot, and S. Lee. A dynamic subgrid-scale model for compressible turbulence and scalar transport. *Physics of Fluids A*, 3:2746, 1991.

[116] M. Germano, U. Piomelli, P. Moin, and W. H. Cabot. A dynamic subgrid-scale eddy viscosity model. *Physics of Fluids A*, 3(7):1760–1765, 1991.

[117] A. Yoshizawa. Statistical theory for compressible turbulent shear flows, with the application to subgrid modelling. *Physics of Fluids*, 29(7):2152–2164, 1986.

[118] Y. Zang, L. S. Robert, and R. K. Jeffrey. A dynamic mixed subgrid-scale model and its application to turbulent recircualting flows. *Physics of Fluids A*, 5(12):3186–3196, 1993.

[119] D. K. Lilly. A proposed modification of the Germano subgrid-scale closure method. *Physics of Fluids A*, 4(3):633–635, 1992.

[120] S. Ghosal, T. S. Lund, P. Moin, and K. Akselvoll. A dynamic localization model for large-eddy simulation of turbulent flows. *Journal of Fluid Mechanics*, 286:229–255, 1995.

[121] A. W. Cook and J. J. Riley. A subgrid model for equilibrium chemistry in turbulent flows. *Physics of Fluids*, 6(8):2868–2870, 1994.

[122] J. Reveillon and L. Vervisch. Response of the dynamic LES model to heat release induced effects. *Physics of Fluids*, 8(8):2248–2250, 1996.

[123] A. W. Cook. Determination of the constant coefficient in scale similarity models of turbulence. *Physics of Fluids*, 5(9):1485–1487, 1997.

[124] S. Corrsin. Further generalisations of Onsager's cascade model for turbulent spectra. *Physics of Fluids*, 7(1156), 1964.

[125] A. E. Papoutsakis, A. Kronenburg, and W. P. Jones. Assessment of sub-grid scale modelling for large eddy simulation during transition from laminar to turbulent flow. *European Combustion Meeting*, 2005.

[126] R. W. Bilger. Conditional moment closure for turbulent reacting flow. *Physics of Fluids A*, 5(2):436–444, 1993.

[127] R. W. Bilger. Conditional moment methods for turbulent reacting flow using crocco variable conditions. Technical report, The University of Sydney, 1991.

[128] N. S. A. Smith, R. W. Bilger, C. D. Carter, R. S. Barlow, and J. Y. Chen. Comparison of CMC and PDF modelling predictions with experimental nitric oxide lif/raman measurements in a turbulent H2 jet flame. *Combustion Science and Technology*, 105:357, 1995.

[129] S. H. Kim, C. H. Choi, and K. Y. Huh. Second order conditional moment closure modelling of a turbulent CH4/H2/N2 jet diffusion flame. *Proceedings of the Combustion Institute*, 30:735–743, 2005.

[130] F. G. Cerru, A. Kronenburg, and R. P. Lindstedt. A systematically reduced reaction mechanism for sulphur oxidation. *Proceedings of the Combustion Institute*, 30:1227–1235, 2005.

[131] A. Kronenburg, R. W. Bilger, and J. H. Kent. Second-order conditional moment closure for turbulent jet diffusion flames. *Proceedings of the Combustion Institute*, 27:1097–1104, 1998.

[132] W. K. Bushe and Helfried Steiner. Conditional moment closure for large eddy simulation of nonpremixed turbulent reacting flows. *Physics of Fluids A*, 11:1896–1906, 1999.

[133] S. Navarro-Martinez, A. Kronenburg, and F. Di Mare. Conditional moment closure for large eddy simulations. *Turbulence and Combustion*, 75:245–247, 2005.

[134] S. H. Kim and Kang Y. Huh. Second -order conditional moment closure modelling of turbulent piloted jet diffusion flames. *Combustion and Flame*, 138(4):336–352, 2004.

[135] A. Kronenburg, R. W. Bilger, and J. H. Kent. Computation of conditional average scalar dissipation in turbulent jet diffusion flames. *Flow, Turbulence and Combustion*, 64:145–159, 2000.

[136] E. Mastorakos and R. W. Bilger. Second order conditional moment closure for the autoignition of turbulent flows. *Physics of Fluids*, 10(6):1246–1248, 1998.

[137] R. W. Bilger. *Advanced Laser Diagnostics: Implications of Recent Results For Advanced Combustor Models*, pages 3–16. R.S.L. Lee; J.H. Whitelaw; T.S. Wung, 1991.

[138] C. M. Cha, G. Kosaly, and H. Pitsch. Modelling extinction and re-ignition in turbulent non-premixed combustion using a doubly-conditioned moment closure approach. *Physics of Fluids*, 13:3824, 2001.

[139] M. Y. Hussaini and Zang T. A. Spectral methods in fluid dynamics. *Annual Review of Fluid Mechanics*, 19:339–367, 1987.

[140] N. Blinova, E. Hydrodynamic theory of pressure and temperature waves and center of action of the atmospere. *Physics of Fluids*, 27:1345–1347, 1944.

[141] E. Eliasen, E. Machenmauer, and Rasmussen E. Atmospheric flow patterns and their representation by spherical surface harmonics. Technical Report 14, AFCRL Geophys. Res. Pap., 1952.

[142] I. Silberman. Planetary waves in the atmosphere. *J. Meteorol.*, 11:27–34, 1954.

[143] S. A. Orszag. Numerical methods for the simulation of turbulence. *Physics of Fluids*, 12:250–257, 1969.

[144] N. Swaminathan and R. W. Bilger. Assesment of combustion submodels for turbulent nonpremixed hydrocarbon flames. *Combustion and Flame*, 116:519–545, 1999.

[145] R. S. Cant and K. N. C. Bray. Strained laminar flamelet calculations of premixed turbulent combustion in a closed vessel. *Proceedings of the Combustion Institute*, 22:791–799, 1988.

[146] R.S. Rogallo and P. Moin. Numerical simulation of turbulent flows. *Annual Review of Fluid Mechanics*, 16:99–137, 1984.

[147] William H. Press, Saul A. Teukolsky, William T. Vettering, and Brian P. Flannery. *Numerical Recipes in C.* Cambridge University Press, 1997.

[148] Alan A. Wray. Minimal storage time advancement schemes for spectral methods. unpublished.

[149] M. Iovieno, C. Cavazzoni, and D. Tordella. A new techique for a parallel dealised pseudospectral Navier-Stokes code. *Computer Physics and Communications*, 141:365–374, 2001.

[150] S. H. Kim, K. Y. Huh, and R. W. Bilger. Second-order conditional moment closure modelling of local extinction and reignition in turbulent non-premixed hydrocarbon flames. *Proceedings of the Combustion Institute*, (29):2131–2137, 2002.

[151] S. K. Lele. Compact finite difference schemes with spectral like resolution. *Journal of Computational Physics*, 103:16–42, 1992.

[152] C. Pantano, S. Sarkar, and F. A. Williams. Mixing of a conserved scalar in a turbulent reacting shear layer. *Journal of Fluid Mechanics*, (481):291–328, 2003.

[153] S. A. Stanley, S. Sarkar, and J. P. Mellado. A study of the flow-field evolution and mixing in a planar turbulent jet using direct numerical simulation. *Journal of Fluid Mechanics*, 450:0377–0407, 1999.

[154] M. M. Rogers and R. D. Moser. The three dimensional evolution of a plane jet mixing layer: pairing and transition to turbulence. *Journal of Fluid Mechanics*, 247:275–320, 1993.

[155] F. O. Thomas and Goldschmidt V. W. Structural characteristics of a developing turbulent planar jet. *Journal of Fluid Mechanics*, (163):227–256, 1986.

[156] S. Tavoularis and S. Corrsin. The structure of a turbulent shear layer embedded in turbulence. *Physics of Fluids*, 30(10):3025–3033, 1987.

[157] J. H. Bell and R. D. Mehta. Development of a two-stream mixing layer from tripped and untripped boundary layers. *AIAA Journal*, 28:2034, 1990.

[158] C. Hartel and Kleisner. Analysis and modelling of subgrid-scale motions in near wall turbulence. *Journal of Fluid Mechanics*, 356:327–352, 1998.

[159] M. V. Salvetti and S. Banerjee. A *priori* tests of a new dynamic subgrid-scale model for difference large eddy simulations. *Physics of Fluids*, 7(11):2831–2847, 1995.

[160] V. Eswaran and S.B. Pope. Direct numerical simulations of the turbulent mixing of a passive scalar. *Physics of Fluids*, 31:506520, 1987.

[161] A. W. Cook and W. K. Bushe. A subgrid-scale model for the scalar dissipation rate in nonpremixed combustion. *Physics of Fluids*, 11(3):746–748, 3 1999.

[162] C. Jimenez, L. Valino No, and C. Dopazo. A *piori* and a *posteriori* tests of subgrid scale models for scalar dissipation. *Physics of Fluids*, 13(8):2433–2436, 2001.

[163] J. Jimenez, A. Linan, M. M. Rogers, and F. J. Higuera. A priori testing of subgrid models for chemically reacting nonpremixed turbulent shear flows. *Journal of Fluid Mechanics*, 349:149–171, 1997.

[164] B.J. Geurts. *Elements of Direct and Large-eddy Simulation.* Edwards, 2003.

[165] C. D Silva and C. F. Pereira. On the local equilibtium of the subgrid scales: The velocity and scalar fields. *Journal of Fluid Mechanics*, 17(108103):1–4, 2005.

[166] D. A. Everest, D. A. Feikema, and J. F. Driscoll. Images of the strained flammable layer used to study the liftoff of turbulent jet flames. *Proceedings of the Combustion Institute*, (26):129–136, 1996.

[167] N. Park, Yoo Y. Y., and Choi H. Toward improved consistency of a priori tests with a posteriori tests in large eddy simulation. *Physics of Fluids*, 17(015103), 2005.

[168] N.N. Yanenko. *The method of fractional steps: solution of problems of mathematical physics in several variables.* Springer-Verlag, New York, 1971.

[169] M. J. Cleary and A. Kronenburg. "Hybrid" multiple mapping conditioning on passive and reactive scalars. *Combustion and Flame*, 2007. Article in Press.